Pure and acid-functionalized ordered mesoporous silicas: Hosts for metallo-supramolecular coordination polymers

vorgelegt von
Diplom-Chemikerin
Dilek Akçakayıran
geboren in Istanbul-Türkei

Von der Fakultät II – Mathematik und Naturwissenschaften –
der Technischen Universität Berlin
zur Erlangung des akademischen Grades

Doktor der Naturwissenschaften
– Dr. rer. nat. –

genehmigte Dissertation

Promotionsausschuss:

Vorsitzende: Prof. Dr. R. von Klitzing
Gutachter: Prof. Dr. G. H. Findenegg
Gutachter: Prof. Dr. R. Schomäcker

Tag der wissenschaftlichen Aussprache: 11. 11. 2008

Berlin 2009

D 83

Für Kai

Erfolg hat drei Buchstaben: TUN!

Goethe

Zusammenfassung

Native und funktionalisierte Silika Materialien, die periodisch und mesoporös sind, wurden synthetisiert und mittels N_2-adsorption, SAXD, SEM/TEM, CHNS-Analyse, NMR, TGA/DTA, XPS, FT-IR und potentiometrischer Titration charakterisiert. Die Funktionalisierung wurde nach den Grafting und Co-Kondensation Methoden durchgeführt. Die funktionalisierten Silikas wurden (i) für die Untersuchung der Oberflächeneigenschaften von MCM-41 und SBA-15, (ii) für Aciditätsmessungen in wasserfreien Poren und (iii) als Wirtsysteme für MEPE verwendet.
Die Verteilung der Silanol Gruppen an den Porenwänden wurde durch Grafting von di- und tripodalen funktionellen Reagenzien ***F*** ($((CH_3)_2Si(OCH_3)_2$, $CH_3Si(OCH)_3$) an die Oberfläche untersucht. Die Anzahl der kovalenten Bindungen zwischen der Silikaoberfläche und ***F*** wurde durch ^{29}Si CPMAS NMR Spektroskopie bestimmt. Für hoch geordnete MCM-41 können di- und tripodale ***F*** nur eine kovalente Bindung zur Oberfläche bilden. Im Fall von SBA-15 ist auch die Bildung von zwei kovalenten Bindungen zur Oberfläche möglich, was auf einen kleineren Abstand zwischen den Silanolgruppen hinweist.

Die Co-Kondensation Methode wurde verwendet, um SBA-15 mit Carboxlysäure (CA), Phosphonsäure (PA) und Sulfonsäuregruppen (SA) zu funktionalisieren. Die Reaktionsbedingungen für die Maximierung des Funktionalisierungsgrades von SBA-15 unter Beibehaltung seiner strukturellen Ordnung werden wesentlich durch die Kinetik der Self-assembly bestimmt. Für ein tieferes Verständnis des Effektes der Hydrolyse und Kondensation der Silikaprecursors (TEOS oder ***F***) sowie deren Wechselwirkung mit Templatmolekülen wurden verschiedene Parameter wie der Anteil des funktionellen Silans ϕ, der prehydrolysierte Silikaprecursor (TEOS oder ***F***) und die Zeit der Prehydrolyse variiert. Die Erhöhung von ϕ senkt den Anteil des Templats in der funktionalisierten Silika und bewirkt dabei eine bessere Entfernung des Polymers durch die H_2SO_4 Behandlung. Die höchsten Oberflächenbedeckungen von SBA-15 mit CA, PA und SA sind jeweils 50%, 40% und 30% mit einer ähnlichen Abnahme der Ausbeute der Funktionalisierungsreaktionen. Aciditätsmessungen der funktionalisierten Materialien wurden mit der ^{15}N NMR Methode durchgeführt. Die erhaltenen chemischen Verschiebungen der Pyridin Molekülen zeigen, dass SA, PA and CA Gruppen durch Pyridin Moleküle deprotoniert werden können, was auf ein hohes Protondonorvermögen von diesen festen Säuren hinweist. FT-IR Messungen von CA-SBA-15 beweisen, dass die CA Gruppen im wässrigen Medium bei pH 8 deprotoniert werden.

Der Effekt der Säurefunktionalisierung auf die Adsorptionseigenschafen von SBA-15 wurde für Fe-MEPE untersucht, welches ein metallo-supramolekulares Koordinationspolymer ist und durch die Komplexierung von Fe(II)-Acetat mit einem neutralen Bis-Terpyridin Liganden entsteht. Die Adsorptionsaffinität und Kinetik der MEPE-Ketten wird stark erhöht, wenn (i) die Poren mit CA Gruppen funktionalisiert sind oder (ii) der pH Wert der Lösung oder die Temperatur steigt. Das Adsorptionsgleichgewicht von MEPE lässt sich gut durch die Langmuir Isotherme beschreiben. Die große Adsorptionskonstante weist dabei auf eine starke Wechselwirkung zwischen Fe-MEPE und CA dekorierten Porenwänden hin. Die MEPE Aufnahme in die Poren kann als eine Überlagerung eines langsamen und eines schnellen Prozesses erster Ordnung dargestellt werden. Der schnelle Prozess ist mit einer Erniedrigung des pH Werts verbunden, die durch einen Ionenaustauschprozess verursacht wird. Der langsame Prozess dauert über mehrere hundert Stunden. MEPE-Aufnahme ist ein diffusionskontrollierter Prozess, und die Aufnahme ist ihrerseits kontrolliert durch Oberflächenschicht-Resistenz. Die Stöchiometrie von MEPE in den Poren (XPS) ist unabhängig von der Beladung. Die Länge der ^{15}N markierten MEPE-Ketten wurde vor und nach der Einlagerung in die CA-SBA-15 durch ^{15}N CPMAS NMR untersucht. Demnach bewirkt die Einlagerung eine Abnahme der Kettenlänge, wenn der Komplex in die Poren eingelagert wird.

Abstract

Pure and functionalized periodic mesoporous silicas were synthesized and characterized by N_2 adsorption, SAXD, SEM, TEM, CHNS analysis, NMR, TGA/DTA, FT-IR and potentiometric titration. Functionalization was performed by grafting and by the co-condensation route. The functionalized silicas were used (i) for examination of the surface properties of MCM-41 and SBA-15 silicas, (ii) for acidity measurements in waterless confined geometry, and (iii) as hosts for MEPE.

The arrangement of the silanol groups at the pore walls was studied by grafting di- and tripodical functional reagents ***F*** ($((CH_3)_2Si(OCH_3)_2$, $CH_3Si(OCH)_3$) to the surface. The number of covalent bonds to the surface formed by ***F*** was studied by pyridine adsorption using ^{15}N CPMAS NMR spectroscopy. For high-quality MCM-41, di- and tripodical ***F*** can form only one covalent bond to the surface. In case of SBA-15 the formation of two covalent bonds to the surface is possible as well, indicating a closer mean distance between the silanol groups at the surface.

The co-condensation route was used to functionalize of SBA-15 with carboxylic acid (CA), phosphonic acid (PA) and sulfonic acid (SA) groups. Reaction conditions for maximizing the degree of functionalization of SBA-15 without losing structural order are strongly affected by the kinetics of self-assembly. To better understand the influence of the hydrolysis and condensation steps of the silica sources and their interaction with template, the percentage of the functional silane ϕ the prehydrolyzed silica source (TEOS or ***F***), and the prehydrolysis time were varied. Increasing ϕ decreases the amount of template in the functionalized SBA-15 and results in a better polymer removal by H_2SO_4 treatment. The highest surface coverages of SBA-15 by CA, PA, and SA groups are 50%, 40% and 30%, respectively, with a similar decrease in the yields of the corresponding functionalization reactions. Acidity measurements of the functionalized SBA-15 materials performed via ^{15}N NMR. Chemical shifts measurements of pyridine indicate that SA, PA as well as CA groups are deprotonated by pyridine, suggesting a high proton donor ability of all three solid acids. FT-IR measurements of CA functionalized SBA-15 show that the carboxylic acid groups are deprotonated in aqueous media at pH 8.

The effect of surface functionalization on the adsorption properties of SBA-15 was investigated for Fe-MEPE, a metallo-supramolecular coordination polyelectrolyte formed by complexation of Fe(II)-acetate with an uncharged ditopic bis-terpyridine ligand. The adsorption affinity and kinetics of the MEPE chains is strongly enhanced when the pore walls are doped with CA, and when the pH of the aqueous medium or temperature is increased. The adsorption equilibrium of MEPE in the pores conforms to the Langmuir isotherm with a high adsorption constant, indicating a strong interaction between Fe-MEPE and the CA-decorated pore walls. The uptake of MEPE into the pores can be represented by a superposition of a slow and a fast first-order process. The fast process is connected with a decrease of pH of the aqueous solution, indicating an ion-exchange mechanism. The slow process extends over hundreds of hours. MEPE uptake is a diffusion controlled process, and uptake is controlled by the surface layer resistance. The stoichiometry of MEPE in the pores (determined by XPS) is independent of the loading and similar to that of the starting material. The mean chain length of MEPE before and after embedding in the CA-SBA-15 was studied by solid-state ^{15}N NMR using ^{15}N-labeled MEPE. The average chain-length is reduced when the complex is incorporated in the pores.

Contents

Chapter 1

Introduction

Porous materials play an important role in nature. For example, porosity of soils is crucial for water permeability and also for water and fossil oil and gas storage. In a different direction, the heat insulation of building materials is mainly effected by their porosity.

Porosity is defined by the ratio of the volume of void-space and the total volume of the material, including the solid and void components. According to the IUPAC definition porous materials are categorized in three groups depending on their pore dimensions. Materials having pore diameter less than 2 nm are denoted by **microporous**. The diameter of **mesoporous** materials is between 2 and 50 nm, whereas **macroporous** materials have diameters bigger than 50 nm.

In material science microporous materials, also known as molecular sieves, make up an important class of materials. First there are zeolites belonging to the class of aluminosilicates which are crystalline structures with micropore channels. Besides about 50 naturally occurring zeolites more than 150 synthetic zeolite types have been manufactured and are used in various fields including adsorption (water purification and production of medical-grade oxygen), ion exchange (water softening, detergents, soil treatment in agriculture), size selective molecular separation (chromatography) and in catalysis (fluid catalytic cracking and hydro-cracking in the petrochemical industry)[1]. More recently, metallo-organic framework (MOF) compounds have been gained interest for various applications including hydrogen gas storages [2]. However, for many other applications microporous materials are not suitable due to their small pore size.

These constrains were overcome by the discovery of periodic mesoporous materials such as MCM-41 and SBA-15 [3, 4]. These materials constitute a 2D hexagonal arrangement of cylindrical pores with a diameter tunable in a range from 2 to 12 nm. Due to their wide pore openings, narrow pore size distribution and large internal surface area, these

materials have a high potential for applications in many fields. Although the larger size of the pores is a prerequisite for many applications, it is by itself often not sufficient when specific surface properties are desired. Specific surface sites for metal-ion binding, catalysis, or controlled sorption can be introduced through surface functionalizations. Surface functionalization can be performed by different routes. Two of them, *surface grafting* and *co-condensation* methods, are employed in this Thesis.

It is well known that high-quality MCM-41 silica constitutes quasi-ideal arrays of uniform-size pores with thin pore walls and a smooth surface, while SBA-15 silica has thicker pore walls with framework and surface defects (roughness) [5]. However, more detailed information about the structure of the pore walls and inner surfaces of these materials is lacking. Such details are relevant for applications of these materials as catalysts and host materials. The clear need to gain further insight into the surface characteristics of these silica materials has been one of the motivations for this thesis. To this end, the surface of MCM-41 and SBA-15 silicas were functionalized by the *grafting route* using $(CH_3)_2Si(OCH_3)_2$ and $(CH_3)Si(OCH_3)_3$ as grafting agents. The arrangement of surface silanol groups at the silica surfaces before and after the functionalization was then studied by solid-state NMR methods.

Acid-functionalized SBA-15 materials are promising solid-state catalysts for various applications in the field of heterogenous catalysis [6]. Our aim was to study the acidity of the functional groups inside the mesopore channels of SBA-15 silica via solid-state NMR, in order to find out whether the proton-donor ability is effected by the confined geometry. Pyridine was used as a probe molecule to measure the acidity of the functional groups. This approach exploits the specific dependence of the ^{15}N chemical shift of hydrogen-bonded pyridine on the length of the corresponding $N\cdots H$ distance [5, 7]. For such experiments, high-quality SBA-15 materials with a large number of acid groups are needed. Our synthesis of choice was the *co-condensation route* because the high surface coverage of silica by acid groups could not be achieved by the grafting method. SBA-15 materials containing carboxylic acid, phosphonic acid and sulfonic acid groups, with increased acidy in the liquid phase, were synthesized by the *co-condensation route* (see Figure 1.1). In this method, a fraction of the silica precursor tetraethoxysilane (TEOS) is replaced by the functional silane. In order to obtain a high degree of functionalization relatively large proportions of functional silane have to be used. However, increasing the proportion of the functional silane beyond a certain extent leads to the formation of disordered materials or to materials with morphologies different from the typical worm-like structures of SBA-15. Therefore, during the synthesis of functionalized materials various

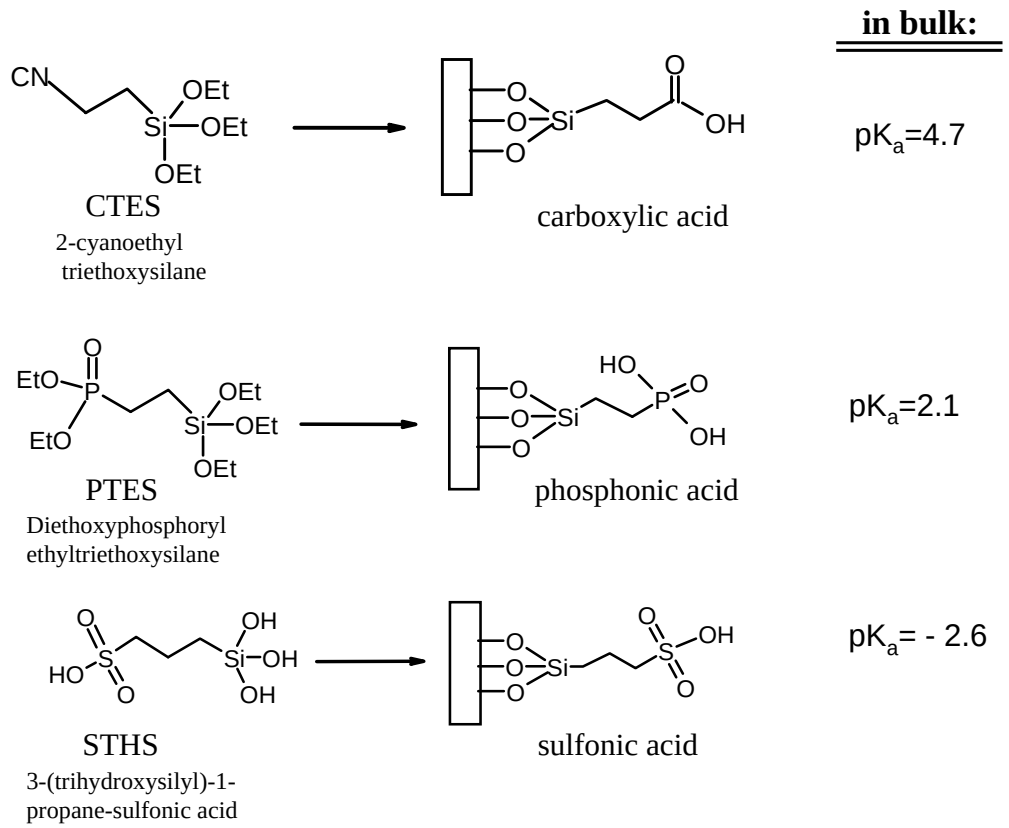

Figure 1.1: Functional silanes used in the preparation of acidic SBA-15 materials by co-condensation route.

parameters had to be changed stepwise in order to understand the formation mechanism and to optimize the reaction conditions for the desired functionalization.

The modified and functionalized porous silica materials have potential applications in the field of heterogenous catalysis [8, 6] and photocatalysis involving bulky grafted catalysts, for example enzymes (enzyme immobilization) and/or the conversion of large substances [9, 10]. Other potential applications include ion exchange and separation, removal of heavy metals, chromatography, stabilization of quantum wires, stabilization of dyes and polymer composites [11]. With an eye on such applications we studied the incorporation of **Me**tallo-supramolecular coordination **p**olyel**e**ctrolyte (MEPE) such as Fe-MEPE **(2)** in the pores of SBA-15 (see Figure 1.2).

Fe-MEPE is a poly-cationic, water soluble organometallic complex assembled from Fe(II)-acetate and 1,4-bis-(2,2´:6´2´´-terpyridine-4´-yl)-benzene **(1)** by the coordinative bonds [12]. The quasi-rigid chain molecules with their stereochemically well-defined octahedral coordination geometry can be regarded as cylinders of diameter 1.5 nm. More-

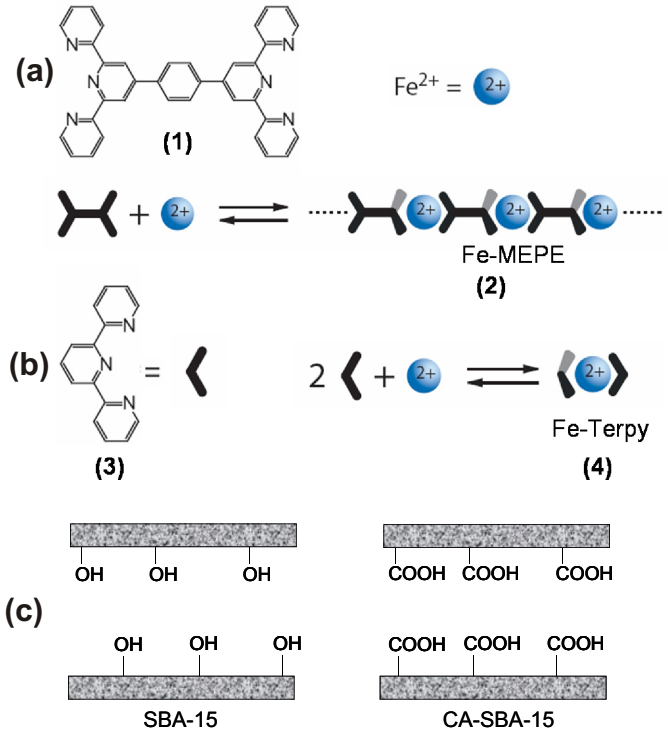

Figure 1.2: a) Metallo-supramolecular coordination polyelectrolyte (MEPE) formed by self-assembly of Fe(II) ions with the ditopic ligand 1,4-bis-(2,2´:6´2´´-terpyridine-4´-yl)-benzene (1). (b) Monotopic Fe-Terpy (4) formed by complexation of Fe(II) ions and 2,2´:6´2´´-terpyridine (3). (c) Cartoon of the cylindrical mesopores of SBA-15 and CA-SBA-15, in which the pore walls are decorated by propionic acid groups, here indicated by -COOH.

over, Fe-MEPE is a *supramolecular polymer*, meaning that the bonds between the monomers are not covalent but based on weaker, reversible interactions. For example, some proteins in biological cells such as actin, fibrinogen and tubulin polymerize into long filaments by supramolecular interactions. Such a polymerization is important for cell rigidity, cell motility, and intercellular transport [13]. In the case of Fe-MEPE, the reversible interactions based on the coordinative bonds between the ligand and the metal ion are caused the *living-polymer* character of Fe-MEPE. This means that the chains brake and recombine on the experimental timescale. As a consequence, the chain length distribution may vary depending on the conditions, and it is possible to tune the properties of these polymers by changing the concentration, solvent, pH, temperature, or other parameters. In addition to dynamic properties coming from labile metal ion ligand interactions, Fe-MEPE ex-

hibits other potentially useful properties such as electro-chromic behavior and molecular magnetism [14].

In this Thesis the uptake of Fe-MEPE into the mesopores of pure and acid-functionalized SBA-15 was studied as an example for the adsorption behavior of charged bulky supramolecular molecules into the silica pores. The adsorption was performed under varying conditions of pH, temperature and the chemical properties of the pore wall. The latter was accomplished through the use of SBA-15 functionalized by carboxylic acid groups (CA-SBA-15, see Fig. 1.2c) which are similar to the acetate ions forming the counter ions of Fe-MEPE in solution. We studied in detail the adsorption kinetic and the adsorption equilibrium in water. In addition, the main chain length of Fe-MEPE before and after the adsorption into the pores was examined by means of ^{15}N solid-state NMR. In this experiment the monotopic Fe-Terpy complex (4) formed by complexation of Fe(II) ions and 2,2´:6´2´´-terpyridine (3) (see Fig. 1.2b) is used for the assignment of the different ^{15}N resonances of Fe-MEPE. The solid-state NMR proved to be a useful method for estimating the chain lengths.

1.1 Outline of this thesis

This Thesis is divided into two parts. The first part concentrates on the preparation and characterization of pure and functionalized MCM-41 and SBA-15 silica materials, while the second part focuses on the uptake of the supramolecular coordination polymer Fe-MEPE into the pores of SBA-15 silicas.

Part I deals with synthesis and characterization of functionalized silica materials synthesized both by the co-condensation and grafting routes. The main results of Part I are presented in Chapter 5 and Chapter 6. In **Chapter 5**, MCM-41 and SBA-15 silicas with hydrophobized pore walls prepared by the grafting route using $(CH_3)_2Si(OCH_3)_2$ and $(CH_3)Si(OCH_3)_3$ reagents are presented. The ^{29}Si NMR method is applied to obtain the ratio of numbers of single-, double-, and triple surface-bonded species for each reagent. These results in turn provide qualitative information about the arrangement of the surface silanol groups, from which the surface properties of MCM-41 and SBA-15 silicas can be assessed. **Chapter 6** concentrates on the characterization of SBA-15 materials containing different acid groups (carboxylic, phosphonic, and sulfonic acid) tethered to the pore walls, which were synthesized by co-condensation route in acidic medium. The effect of several synthesis parameters, such as the relative amount of the functional silane, the sequence in which the silica precursors (TEOS or functional silane) were added to the

synthesis solution, and the time allowed for prehydrolysis of that component on the morphology and on the acidity of SBA-15 were investigated by various methods. After the characterization of the products, the proton donor ability of the different acid functionalities inside the pores was studied by ^{15}N CPMAS NMR after pyridine adsorption into the pores.

Part II deals with the investigation of the Fe-MEPE uptake into the pores of SBA-15. The main results of Part II are presented in Chapter 9 and Chapter 10. In **Chapter 9** it is shown that the uptake can be increased considerably at higher temperatures, at higher pH values and also by using carboxylic acid functionalized SBA-15 as adsorbent. It turns out that the ion exchange process plays a role on the adsorption. In addition, the chain lengths of Fe-MEPE in the pores estimated by ^{15}N CPMAS NMR are shorter than those in solution. From this we concluded that Fe-MEPE chains break into smaller entities in the pores. **Chapter 10** outlines the sorption kinetic and sorption equilibrium of MEPE in the pores of carboxylic acid functionalized SBA-15. The Fe-MEPE uptake curves can be represented by a sum of two exponential decay functions, for the fast initial process and a subsequent slow uptake process which leads to the adsorption equilibrium. The diffusion is controlled by the surface layer resistance and the solid-liquid equilibrium of Fe-MEPE can be described by the Langmuir adsorption isotherm satisfactorily.

The work presented here arose from a cooperation with two other research groups in the framework of *Sonderforschungsbereich 448 Mesoskopisch struktruierte Verbundsysteme*. All solid-state NMR measurements were performed in the group of Prof. Limbach and Dr. Shenderovich of FU-Berlin, whereas the supramolecular coordination polymer Fe-MEPE was provided by the group Prof. Möhwald and Dr. Kurth of MPI of Colloids and Interfaces in Potsdam-Golm.

Chapter 2

Experimental Background

2.1 UV-vis spectra of metal-ligand complexes

The different types of electron transitions in an octahedral coordinated metal complex ML_6 with π acceptor ligands by means of the molecule orbital scheme are shown in a simplified form in 2.1a [15].

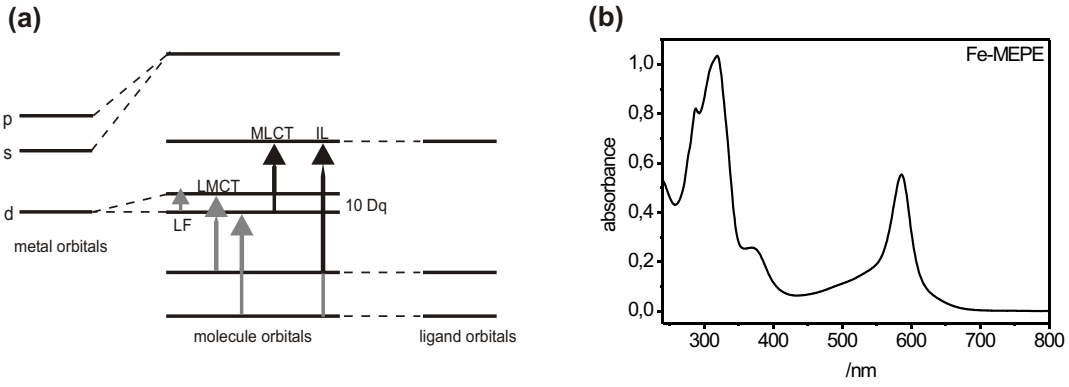

Figure 2.1: (a) MO scheme for a simple octahedral coordinated metal complex ML_6; (b) the UV-vis absorption spectrum of 0.2 mM Fe-MEPE in water.

The molecule orbitals of the complex are formed by the combination of metal orbitals (s, p and d) and ligand orbitals (σ, π and π^*). The following transitions can be observed:

1. *Ligand field* (LF) transitions take place between orbitals which basically have metal character ($d \rightarrow d$ transition)

2. *Charge transfer* (CT) transitions take place between metal and ligand orbitals. If the transition occurs from a filled metal orbital to a empty ligand orbital, it is called

Metal-to-Ligand-Charge-Transfer (MLCT) transition. In the opposite case, if the transition occurs from a filled ligand orbital to a empty metal orbital, this is denoted as *Ligand-to-Metal-Charge-Transfer* (LMCT) transition.

3. *Intra ligand* (IL) transitions take place between orbitals essentially having ligand character ($\pi \rightarrow \pi^*$ transition)

These transitions can be detected by UV-vis spectroscopy. In Figure 2.1b a UV-vis absorption spectrum of 0.2 mM Fe-MEPE in water is shown. The bands centered at 288 nm and 319 nm are assigned to IL transitions. The peak at 585 nm is attributed to the MLCT transition. The small peak at 368 nm which appears as a shoulder comes from a LF transition and is assigned to the transition of Fe^{2+} electrons between the d-orbitals splitted in the octahedral ligand field.

The absorption of light follows the Lambert-Beer law. Accordingly, the intensity of transmitted light decreases exponentially with increasing molar concentration of the absorbing species c and the thickness d of the sample . The equation has the following form

$$log\frac{I}{I_0} = -\varepsilon \cdot c \cdot d \tag{2.1}$$

where I_0 is the incident intensity, I is the intensity after passage through the sample, and ε is the molar absorption coefficient of the species at the frequency of the incident radiation. It depends on the frequency of the radiation, and its dimension (length.concentration)$^{-1}$ is usually expressed in *L mol*$^{-1}$ *cm*^{2}. The dimensionless quantity $A = \varepsilon \cdot c \cdot d$ is called *absorbance* (formerly extinction or optical density) of the sample, and the ratio I/I_0 is called the *transmittance* T. These two quantities are connected by the equation

$$logT = -A. \tag{2.2}$$

2.2 Atom absorption spectroscopy (AAS)

The **A**tom **A**bsorption **S**pectroscopy (AAS) is a proven and fast method for qualitative and quantitative analysis of many elements in (mostly) aqueous solutions [16]. The basis of AAS is the ability of the atoms to absorb electromagnetic radiation of a certain wavelength in their initial state and to go thereby into an excited state. For analytical use of this principle in AAS the atoms are often generated by thermic splitting of suitable compounds. In this work an atomizer-burner system with air/acetylene flame ($T \approx 1800°C$) is used for the atomization. This process is called flame AAS method (FAAS). During the passageway through the flame various processes occur consecutively:

- The solvent (mostly water or aqueous systems such as dilute acids) evaporates from the aerosol (i.e., the droplets of sample solution)
- The resulting solid particles evaporate
- The molecules dissociate into atoms
- A very small number of atoms is excited thermally or ionized.

In the Figure 2.2 the schematic construction of a flame AAS spectrometer is shown. For AAS it is essential to maximize the proportion of atoms converted into gas state and minimize the number of excited or ionized atoms. Because the elements differ from each other in their electronic structure they absorb radiation at strictly characteristic wavelengths. For this reason the resulting "atom cloud" in the flame is illuminated with light characteristic for the element to be determined. To this end light with the intensity I_0 is radiated

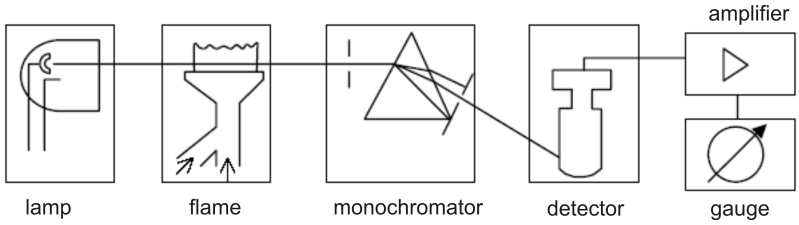

Figure 2.2: Schematic construction of a flame AAS spectrometer.

into the flame in the atomizer. Subsequently, owing to the resonance process, light with the same wave length is emitted. However the emission occurs in all directions of the room so that a decrease of the incident intensity to the value I is detected. This decrease is proportional to the concentration of the element in the sample and can be calculated by the Beer-Lambert law (Equation 2.1).

AAS is a relative method. This means that for the determination of the element concentration it is necessary to measure the extinction of calibration standards of known concentration. In this work the *standard addition method* [17] is used for the calibration. Because of the short time span during which the atoms are exposed to radiation in the AA spectrometer the sensitivity of the flame technique is not very high. This technique has a detection limit in the range from a few mg/L up to a few $\mu g/L$, depending on the element.

2.3 X-ray photoelectron spectroscopy (XPS)

Photoelectron spectroscopy (PES) is the examination of energy levels of molecules by determining the kinetic energies of electrons ejected by absorption of high-frequency monochromatic radiation. If the incident radiation is in the X-ray region, then the technique is called XPS or ESCA (electron spectroscopy for chemical analysis). In XPS, the sample is irradiated with low-energy(1.5 keV) X-rays, in order to provoke the photoelectric effect. The kinetic energy of photoejected electron E_{kin} is approximately equal to the difference between the energy of X-rays $h\nu$ and the binding energy of the electron E_b:

$$E_{kin} = h\nu - E_b. \tag{2.3}$$

Therefore, a determination of E_{kin} will give the value of E_b and hence, via Koopmans' theorem, the energy of the orbital from which the electron was ejected. Because the core electrons are largely (but not entirely) independent of the state of the bonding atom, the binding energies are characteristic of specific electron orbital in specific atoms. This can be used to identify the elements present in the sample.
The following processes can occur after the photo-ionization [18]:

- Generation of Auger-electrons, which takes place after the escape of the photoelectron. An electron from a higher energetic level drops into the resulting gap. The corresponding energy causes the release of a third electron from the atom. This process predominates in case of light elements. The kinetic energy of Auger electrons is independent on the energy of X-rays. Therefore they can be distinguished from photoelectron lines by measurements at two different X-ray excitation energies.

- Absorption of X-ray radiation followed by emission of characteristic X-rays (X-ray fluorescence). This process predominates in case of heavy elements.

- Auto ionization.

Both *XPS-electrons* and *Auger-electrons* are analyzed with regard to their kinetic energy. From these data it can be established, after comparison with tabulated values, which element is ionized by the X-ray radiation. Hydrogen and helium are missing from such tables, because they are essentially impossible to detect by XPS. Helium does readily form solid compounds and its 1s orbital has a tiny cross-section for photo emission. Hydrogen also has a tiny cross-section and suffers from having to share its only electron in forming compounds, which then resides in a valence-like orbital with varying energy

from compound to compound.

Chemical Shift

In XPS, the term chemical shift is used to describe the shift in binding energy of electrons dependent on the chemical surrounding such as state of binding, valency and type of surrounding ligands. In compounds of elements with different electronegativity (e.g. metals with oxygen) the valence electrons are shifted the more electronegative partner. This leads to an increase of effective core charge, so that the core electrons of metal atoms stay in a stronger Coulomb field and thus are stronger bonded. These electrons leave the sample surface with lower kinetic energy, so that the signal in the spectrum is shifted towards higher binding energies.

The comparison of the N1s spectrum of embedded Fe-MEPE with that of bulk Fe-

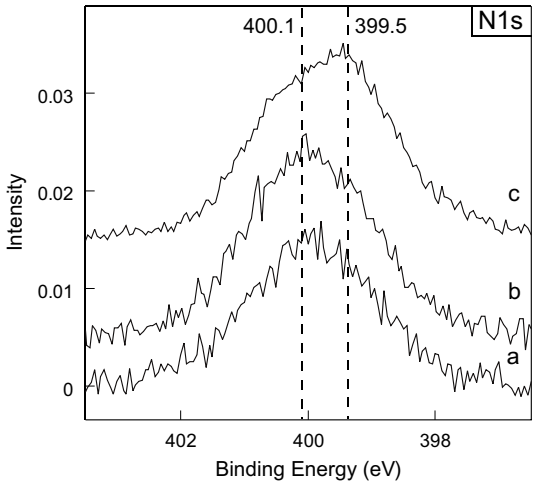

Figure 2.3: X-ray photoelectron N1s spectra of 20-CA loaded with Fe-MEPE (a) 0.4 mM (b) 0.6 mM as well as (c) bulk Fe-MEPE normalized in intensity to spectrum b.

MEPE shows an intensity shift to higher binding energies. For pyridine a binding energy of 399.5 eV was reported [19]. This upshift may therefore indicate the increased number of nitrogen atoms participating in Fe coordination.

Escape depth of photo electrons

X-rays can easily penetrate into materials to a depth of some μm. The use of XPS as a surface investigation method results from the limited escape depth of photo electrons. This escape length was determined for different materials. Thereby it was shown, that the mean free path of the electrons λ_m is dependent on their kinetic energy E_{kin}. Seah and Dench [20] give the following empirical equations describing the mean free path

$$\lambda_m = \frac{538}{E_{kin}^2} + 0.41\sqrt{aE_{kin}} \tag{2.4}$$

$$\lambda_m = \frac{2170}{E_{kin}^2} + 0.72\sqrt{aE_{kin}} \tag{2.5}$$

where λ_m is expressed in nm and E_{kin} is expressed in eV. The factor a in the root represents the layer thickness in nm. Equation 2.4 applies to elements and Equation 2.5 to anorganic substances. These relations are used to plot the mean free path of an electron against its kinetic energy. In a range from 10 eV to 1100 eV the values of λ_m are in a range of approximately 1 to 3 nm, e.g., photoelectrons with this energy mainly come from the top layers of the sample. Therefore XPS is very surface sensitive. For this reason the sample analysis is conducted in a vacuum chamber under the best vacuum conditions achievable, typically ca. 10^{-10} torr. This facilitates the transmission of the photoelectrons to the analyzer and, more importantly, minimizes contamination of the sample.

2.4 Solid-state NMR spectroscopy

The elementary particles (neutrons and protons) composing an atomic nucleus, have the intrinsic quantum mechanical property of *spin*. The overall spin of the nucleus is determined by the spin quantum number *I*. If the number of both the protons and neutrons in a given isotope are odd then $I \neq 0$, i.e. there is an overall spin. This non-zero spin, I, is associated with a non-zero magnetic moment, μ, via

$$\mu = \gamma \cdot I \tag{2.6}$$

where the proportionality constant, γ, is the gyromagnetic ratio. It is this magnetic moment that is exploited in NMR. The spin, and hence the magnetic moment, of the nucleus may lie in $2I + 1$ different orientations relative to an arbitrary axis (usually z-axis). In the stationary state, all orientations have equivalent energies. However, in an external magnetic field B_0 these $2I + 1$ orientations of the nucleus have different energies. The energy

difference ΔE between the affected energy levels is proportional to the applied magnetic field, and the resonance is achieved by excitation of the sample with electromagnetic radiation in the radio frequency region [21].

In solution NMR, spectra consist of a series of sharp lines due to averaging of anisotropic interactions by rapid random tumbling of the molecules. By contrast, solid-state NMR spectra are very broad (up to several kHz), as the full effects of anisotropic or orientation-dependent interactions are observed in the spectrum. Thus in solid state the chemical shielding becomes anisotropic due to the different orientation of molecules relative to the external magnetic field. Therefore the chemical shielding is characterized by a shielding tensor. Molecular orbitals and crystallographic symmetry dictate the orientation and magnitude of chemical shielding tensors [22]. In the solid state the interactions between the magnetic active nuclei become anisotropic as well. These can be dipolar interactions resulting from interaction of the nuclear spin with a magnetic field generated by another nuclear spin, and vice versa. This is a direct through space interaction depending on the magnetogyric ratio γ of each nucleus as well as on the distance between the nuclei. If the sample contains nuclei with a quadrupol moment ($I \geq 1$), the anisotropic interactions of quadrupol with the electric field gradient affect the line form and the number of resonance lines.

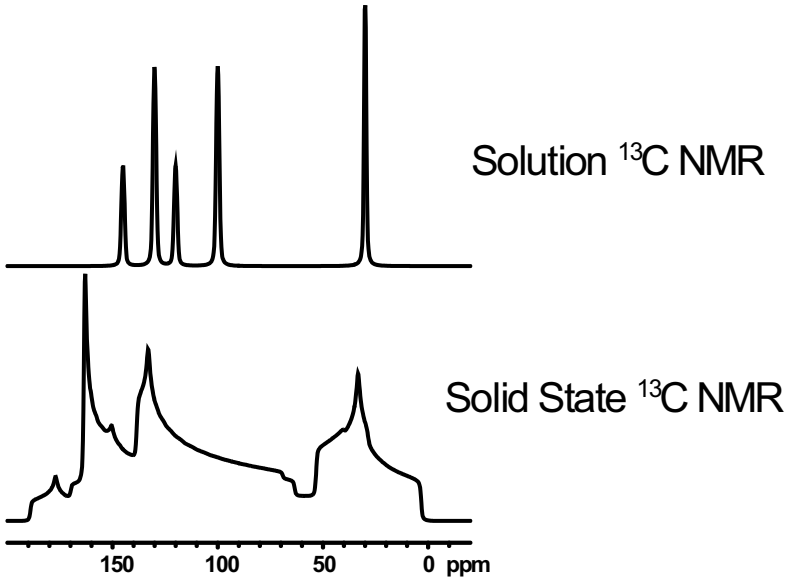

Figure 2.4: Comparison of ^{13}C NMR spectra in solution and solid state [22].

In a NMR experiment a directed macroscopic magnetization is induced. Its time dependent decay is described by two independent time constants T_1 and T_2. The relaxation time T_1 is called as longitudinal relaxation time. It gives information about reestablishment of Boltzmann-distribution of the energy levels of a nucleus. In this process an energy exchange of the nucleus with its surroundings takes place. ("spin-lattice" relaxation). The relaxation time T_2, the so-called "transversal" relaxation time, characterizes the decay of the intensity of the induced magnetization, and it is an entropic process. Thus the constant T_2 describes the line width of the resonance signals whereas T_1 determines repetition rate of the NMR experiment.

The potential of NMR measurements in solid state is affected in three different ways, which do not pose serious problems in liquid state:

- Chemical shielding anisotropy
- Strong anisotropic dipolar interactions, i.e., short transversal relaxation time T_2
- Long longitudinal relaxation time T_1.

The first two lead to the distribution of the signal intensities over a wide frequency range of several kHz. On the other hand, a rapid accumulation of several spectra is not possible because T_1 is long. High resolution solid state NMR spectra can provide the same type of information that is available from corresponding solution NMR spectra, but special techniques and equipment are needed, including magic-angle spinning and cross polarization.

2.4.1 Magic angle spinning (MAS)

Each magnetic active nucleus produces a local magnetic field $B_0 \propto \frac{1}{R^3}(1 - 3cos^2\theta)$, where R is the distance from the nucleus and θ is the angle between the applied field B_0 and the principal axis of the molecule. The anisotropy of the chemical shift also varies with the angle θ as $(1 - 3cos^2\theta)$. For this reason the line widths of solid samples can be reduced by spinning the sample with high speed at the *magic angle* $\theta = 54.74°$ at which the factor $(1 - 3cos^2\theta) = 0$. At adequate rapid spinning in time average all vectors in the sample take the magic angle to the external magnetic field.

In order for the MAS method to be successful, spinning has to occur at a rate equal or greater than the one corresponding to the dipolar line width. In our measurements the rotation frequency was $6 - 8$ kHz, corresponding to a rotation rate of up to 8000 rps. In this case the anisotropic interactions between the nuclei among themselves and between the nuclei and the external magnetic field will be ineffective. Thus by MAS the problem

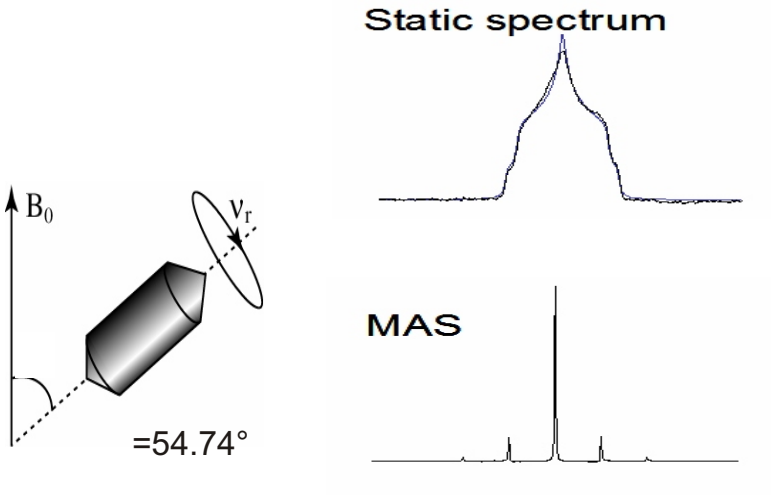

Figure 2.5: The principle of Magic Angle Spinning NMR spectroscopy (MAS-NMR) and spectra before and after MAS [22].

of anisotropy of chemical shielding is solved and at the same time the weak heteronuclear and strong homonuclear dipolar interactions are eliminated or reduced.

2.4.2 Cross polarization (CP)

Cross polarization is a very important technique in solid state NMR. In this technique, polarization from abundant spins such as ^1H or ^{19}F is transferred to dilute spins such as ^{13}C, ^{29}Si or ^{15}N. The overall effect is to enhance the signal-to-noise ratio:

1. Cross polarization enhances the signal from dilute spins potentially by a factor of γ_I/γ_S, where γ_I and γ_S are the magnetogyric ratios of the abundant and the dilute spin. For instance, by transfer of the spin polarization from ^1H to ^{13}C the signal of the latter can be enhanced by the factor 4.

2. Since abundant spins are strongly dipolar coupled, they are subject to large fluctuating magnetic fields resulting from motion. This induces rapid spin-lattice relaxation at the abundant nuclei. As a result, the repetition rate for the accumulation of the spectra is no longer dependent on the T_1 of the dilute spin but on that of the abundant spin. For instance, $T_1(^1H)$ is in the region of seconds, and thus it is in general significantly shorter than $\mathrm{T}_1(S)$ for many nuclei S.

A major problem in the application of the CP technique is that, owing to the strong magnetic moment of I nuclei the anisotropic interactions between S and I are strong as well,

and this leads to a widening of the resonance signals of S nuclei. However, this problem can be solved by the so-called "spin locking" method, by which the I nuclei are decoupled from S nuclei.

Cross polarization requires that nuclei are coupled to one another by dipolar interactions, and it even works while samples are being spun at the magic angle. Hence the acronym CPMAS NMR (**C**ross **P**olarization **M**agic-**A**ngle **S**pinning NMR). By CPMAS the time of the measurement can be reduced drastically. The disadvantage of this method is that information about the concentration of the respective species is lost.

2.4.3 Analysis of ^{29}Si MAS NMR spectra of functionalized silicas

When applying the MAS NMR technique to mesoporous silicas such as SBA-15 and MCM-41, three peaks can be observed in the spectrum which may be assigned to three kind of silicon atoms. Silicon atoms with 4 $O - Si$ neighbors are denoted as Q^4. These atoms are located inside the silica framework. Analogously, Q^3 and Q^2 silicon atoms have 3 and 2 $O - Si$ neighbors (and 1 or 2 OH neighbors), respectively. These silicon atoms are situated at the pore walls, as shown in Figure 2.6a.

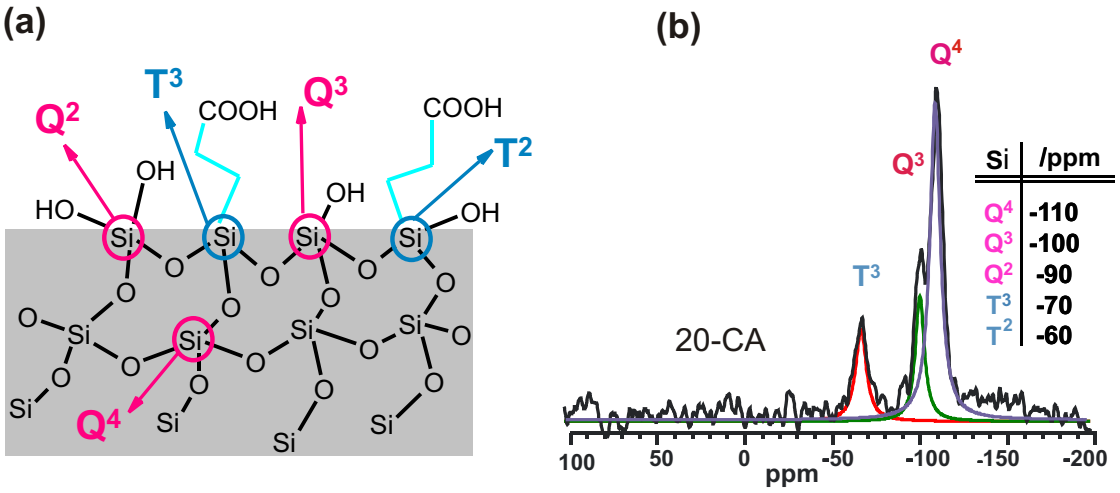

Figure 2.6: Cartoon of a silica framework (a) and a ^{29}Si MAS NMR spectrum of carboxylic acid doped SBA-15, 20-CA (b).

Silicon atoms carrying an alkyl chain are denoted by T. Again the exponent indicates the number of O-Si neighbors of a silicon atom. The different Q and T silicon atoms have different chemical shifts in the ^{29}Si spectra as can seen in the small table in Figure 2.6b. Also shown in Fig. 2.6b is the silicon NMR spectrum of a SBA-15 doped with carboxylic

acid (20-CA). The three peaks of this spectrum are assigned to Q^4, Q^3 and T^3 silicon atoms. The number of silicon atoms directly connected to functional groups *F* (propionic acid) is proportional to the integral intensities of the peaks $T^3 + T^2$, while the number of silicon atoms bearing $-OH$ groups is proportional to the peak intensities $Q^3 + 2Q^2 + T^2$. Accordingly, the mole fraction of functional groups in the mixture of surface groups (here $-OH$ and $-COOH$) at the pore walls is given by:

$$\frac{N_F}{N_{OH} + N_F} = \frac{T^2 + T^3}{2Q^2 + Q^3 + 2T^2 + T^3} \tag{2.7}$$

To determine the mole fraction of F groups, the spectrum is fitted by a deconvolution method. The data for the individual peaks are normalized to the Q^4 peak and adjusted to the ratios of the integrals of the T and Q regions. Since in some cases it was not possible to separate the peaks T^3 and T^2, or Q^3 and Q^2 in the spectra, the fraction x of surface silica atoms carrying a functional group is used as an approximate measure of the degree of the surface coverage by functional groups at the pore walls:

$$x_F = \frac{T^2 + T^3}{Q^2 + Q^3 + T^2 + T^3} \tag{2.8}$$

Moreover, the yield of a synthesis by co-condensation route can be estimated from a comparison of the ratio T/Q with the ratio of functional groups and TEOS in the synthesis mixture, where T/Q is given by

$$\frac{T}{Q} = \frac{T^2 + T^3}{Q^2 + Q^3 + Q^4} \tag{2.9}$$

2.5 Small-angle X-ray diffraction (SAXD)

Periodic mesoporous silica materials exhibits a periodic arrangement of mesopores while the silica matrix is amorphous at the atomic scale. The periodic arrangement of the mesopores produces characteristic Bragg reflexes in the small-angle diffraction, as shown in the SAXD spectrum in Figure 2.7a. Specifically, MCM-41 and SBA-15 comprise a two-dimensional hexagonal pore lattice (space group p6*mm*) as indicated in Figure 2.7b.

The walls of the mesoporous materials investigated in this work are amorphous in the atomic level. Moreover, as seen in Figure 2.7a, while examining these materials with SAXD we observe Bragg-reflexes which suggest an order of the materials in the mesoscopic scale. The reason for the appearance of Bragg-reflexes is that the mesopores in the materials are well ordered. The peaks are to be attributed to the 2D hexagonal unit cell

with the lattice constant a_0. For this reason a crystallographic formulation can be used for the small angle X-ray scattering on these materials.

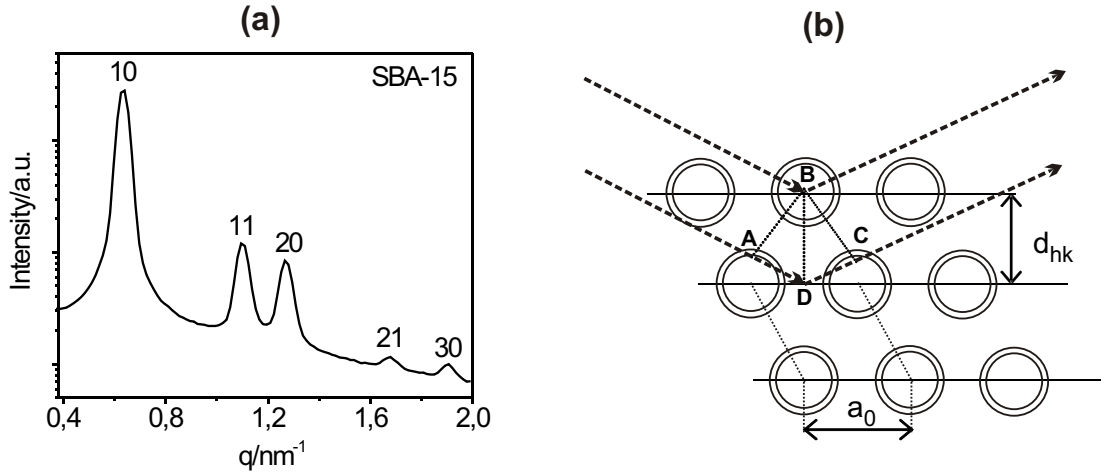

Figure 2.7: SAXD spectrum of a SBA-15 (a) and derivation of Bragg's law for X-ray diffraction on hexagonal ordered materials (b).

Figure 2.7b illustrates the principle of diffraction of monochromatic X-rays of wavelength λ by the lattice planes of a 2D hexagonal crystal lattice. If the lattice planes are considered as semipermeable mirrors a portion of incident X-rays is reflected and the rest is transmitted. A Bragg-reflex originates if X-rays reflected at numerous parallel lattice planes interfere constructively. This happens when the pathlengths of the X-rays reflected at two neighboring lattice planes differ by an integer multiple of λ, i.e. $\overline{ADC} = n \cdot \lambda$. This is described by the Bragg equation. For our 2D ordered pore system where the lattice planes can be labeled with Miller indices hk one has

$$n \cdot \lambda = 2 \cdot d_{hk} \cdot sin(\theta_{hk}). \tag{2.10}$$

The Bragg equation is the basic equation of diffractometry. It ties together the wavelength λ, the lattice plane spacing d_{hk} and the glancing angle θ_{hk} between the incident wave and the lattice plane d_{hk}; n is an integer and its physical interpretation is the interference order. Thus at a given wavelength first-order reflection of X-rays by lattice planes occurs only at a certain angle θ_{hk}. If the wavelength is known, the interplanar spacing d_{hk} can be calculated by measuring of the glacing angle θ_{hk}. For its determination in this work diffraction in small angle region is applied. In small angle scattering the scattering angle 2θ lies in range of $0.05° < 2\theta < 5°$.

X-ray scattering at ordered crystal lattices represents a special case of the scattering at an array of scattering centers. The origin of X-ray scattering is illustrated in Figure 2.8.

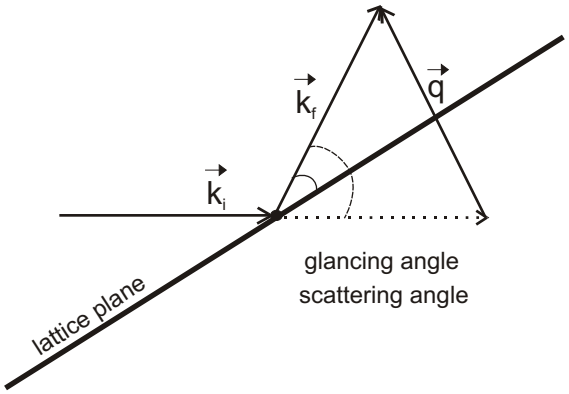

Figure 2.8: The origin of X-ray scattering and the relation between glacing angle and scattering angle. k_i: incident wave, k_f: final wave, q: scattering vector.

X-ray scattering takes place if the electrons of the scattering particle oscillate in resonance with the frequency of the incident X-ray and after this interaction a coherent secondary X-ray wave is emitted. The wave vector of a wave with the wavelength λ is defined by

$$|\overrightarrow{k}| = \frac{2\pi}{\lambda} \tag{2.11}$$

Elastic scattering represents an interaction between X-rays and the sample in which no energy transfer occurs but an impulse exchange of $\Delta\overrightarrow{p} = \hbar(\overrightarrow{k_f} - \overrightarrow{k_i})$ takes place. The term $\overrightarrow{q} = (\overrightarrow{k_f} - \overrightarrow{k_i})$ is referred to as scattering vector (see Fig. 2.8). In elastic scattering the normal of the wave vector remains unchanged after the interaction process, i. e.:

$$|\overrightarrow{k_f}| = |\overrightarrow{k_i}| = \frac{2\pi}{\lambda} \tag{2.12}$$

Combination of this relation with Equation 2.10 results in the following important relations between the wave vector, glancing angle and interplanar spacing d_{hk}.

$$q_{hk} = \frac{4\pi}{\lambda} \cdot sin\theta_{hk} = \frac{2\pi}{d_{hk}} \tag{2.13}$$

In MCM-41 and SBA-15, the individual crystal domains contain approximately 100 and 1000 pores, respectively. The Bragg-reflexes are determined by the type of crystalline system and the *lattice parameter* a_0 of the unit cell. For a 2D hexagonal lattice, the lattice parameter is obtained by the following equation from the interplanar spacing

$$a_0 = \frac{2}{\sqrt{3}} \cdot d_{hk} \cdot \sqrt{h^2 + hk + k^2}. \tag{2.14}$$

Information about the pore diameter D and the nature of the pore walls can be determined by SAXD structure modeling. This can be achieved by applying the so called-continuous

density function (CDF) technique [23] in combination with the derivative difference minimization (DDM) method [24]. Alternatively, the intensities of the Bragg-reflections may be fitted by modeling the form factor of the cylindrical pores in an appropriate way [25, 26]. Both of these techniques yield quantitative information about the pore diameter D and the wall thickness w along the pore center-to-center line, which are related to the lattice parameter a_0 by $a_0 = D + w$.

2.6 Nitrogen adsorption

The physisorption of gases at solid surfaces and in porous solids represents a classical method for characterizing the surface properties and porosity of the materials [27]. It is based on weak interactions of the gasses with the material which in simple cases leads to reversible adsorption. Due to the weak interaction, substantial adsorption takes place only at relatively low temperatures, typically at or below the normal boiling temperature T_b of the fluid. Nitrogen ($T_b = 77.3K$) is used as the adsorptive gas in many routine studies. Typically, an adsorption isotherm is measured by increasing the pressure in small steps up to the saturation pressure. Subsequently a desorption isotherm is measured by gradually decreasing the pressure in the system.

Analysis of an adsorption isotherm

The form of adsorption isotherms strongly depends on the structure of the adsorbent and on the interaction between adsorbent and adsorptive. Adsorption isotherms are classified into six different types by IUPAC. Mesoporous samples including SBA-15 and MCM-41 often show an isotherm of type IV [28]. In this type of isotherms pore condensation of the fluid occurs. In some cases, such as SBA-15, this is accompanied by a hysteresis, i.e. pore evaporation takes place at a lower pressure than pore condensation. Three important quantities can be obtained by analysis of the adsorption isotherm of a porous material:

1. Pore size distribution and mean pore size
2. Specific surface area (BET area)
3. Specific pore volume.

In Figure 2.9 a typical adsorption isotherm of nitrogen in a SBA-15 silica is shown. Also indicated in the figure are the pressure ranges from which the different quantities are

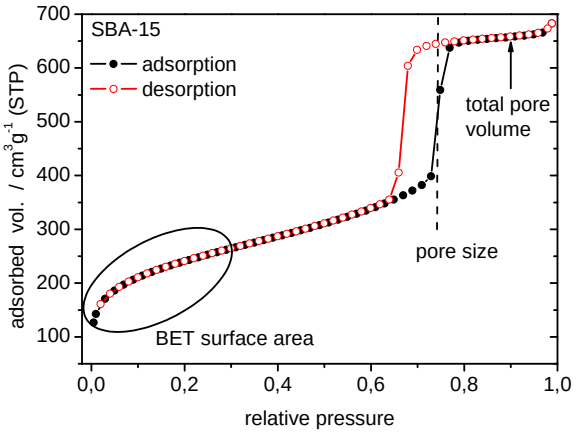

Figure 2.9: Analysis of a typical nitrogen adsorption isotherm for a SBA-15 silica.

derived. The calculation of these quantities from the experimental isotherms is explained in detail in the following sections.

2.6.1 Specific surface area

An important quantity, which can be obtained from nitrogen adsorption isotherms is the specific surface area a_s in $m^2\ g^{-1}$ of the porous solid. It is calculated according to the theory of Brunauer, Emmet and Teller (BET). They developed an equation from which the amount of the gas necessary for the formation of a complete monolayer at the surface can be determined. In gas-volumetric measurements this amount is often expressed by the respective gas volume V_{mono} under standard conditions (STP). By measuring the amount of adsorbed gas V_{ads} as a function of relative pressure p/p_0 the typical adsorption curve is obtained which can be described by the BET equation. After linearization the BET equation has the form

$$\frac{p/p_0}{V_{Ads}(1-p/p_0)} = \frac{1}{V_{mono}\cdot C} + \frac{C-1}{C\cdot V_{mono}}\cdot\frac{p}{p_0}. \tag{2.15}$$

Here C is the scalar BET constant which is dependent on the isotherm shape. It characterizes the strength of the interaction between the gas molecules and the solid surface. Large values of C (C>100) indicate relatively strong adsorption energy of molecules in the first adsorption layer with regard to the condensation energy of the adsorptive. According to the BET equation a linear relation is obtained if $\frac{p/p_0}{V_{Ads}(1-p/p_0)}$ is plotted against $\frac{p}{p_0}$ (*BET plot*). In this manner it is possible to obtain the parameters V_{mono} and C. The range of

linearity of the BET plot is always restricted to a limited part of the isotherm usually to the region $0.01 < p/p_0 < 0.3$.

The BET specific surface area is calculated from V_{mono} according to following formula

$$a_s = V_{mono} \cdot \sigma(N_2) \cdot N_A. \tag{2.16}$$

Here N_A is the Avogadro constant, and $\sigma(N_2)$ is the average area (molecular cross-sectional area in m^2/molecule) occupied by each adsorbed molecule in a complete monolayer. It is usually assumed that BET nitrogen monolayer is closed-packed, giving 0.162 nm^2 at 77 K. This value of σ is used in the present work for the calculations of specific surface area of the silica materials. However, it must be kept in mind that a constant value of $\sigma(N_2)$ is unlikely and that caution needs to be exercised in dealing with surfaces which give rise to either especially strong or weak adsorbent-adsorbate interactions that are able to influence the packing.

In case of porous solids the BET method yields the whole surface of the solid, i.e., the external plus the internal surface. For determining the mesopore surface area it is also necessary to take into account the presence of micropores. In this case the micropore surface area can be determined, for example, by the $t - plotmethod$ [29, 30] and can be subtracted from the whole surface area. Details of the calculation of microporosity by t-plot method will be presented in the following section.

2.6.2 Analysis of microporosity

Microporosity can be assessed by tracing comparison plots with reference isotherms, usually called *t-plots*. This method of isotherm data analysis was introduced by de Boer. It assumes that in a certain isotherm region, the micropores are already filled whereas the adsorption in larger pores occurs according to some simple equation characteristic for a large class of solids. This equation should approximate adsorption in mesopores, macropores and on a flat surface in a narrow pressure range just above complete filling of micropores, but below critical vapor pore condensation pressure in mesopores. The adsorption within this pressure region may be described by a simple linear dependence

$$V(p/p_0) = V_{micro} + k \cdot a_{ext} \cdot t_(p/p_0). \tag{2.17}$$

Here $V(p/p_0)$ is the adsorbed volume, V_{micro} is the maximum adsorption in micropores, k is a coefficient which depends on the units used for the values of adsorption and a_{ext} is the *external surface area*, i.e., the surface area of pores larger than micropores. $t(p/p_0)$ is

the statistical thickness of adsorbed layer in meso- and macropores which is estimated by the Harkins and Jura (HJ) [31] or by the Frenkel-Halsey-Hill (FHH) [32] equations. The t-layer required for the analysis of microporosity is calculated by the HJ-equation in the following form

$$t(p/p_0)/nm = 0.1\sqrt{\frac{13.99}{0.034 - log(p/p_0)}}. \tag{2.18}$$

This equation is commonly applied to a range of relative pressure from 0.1 to 0.2, corresponding to t values from 0.354 to 0.5 nm. Thus, according to the Equation 2.17 the t-plot analysis consists of plotting the adsorbed volume V as a function of the calculated film thickness t as determined by Equation 2.18. In the absence of micropores, when a multilayer of adsorbate is formed unhindered on the solid surface, the adsorbed volume V is a linear function of t passing through the origin. The total surface area is then given by the slope of the t-plot. In the presence of micropores, the graph of V vs. t will be linear at higher pressures (higher t) and an extrapolation of this linear region to $t = 0$ will give a positive intercept corresponding to the micropore volume. In this case, negative deviations from linearity of $V(t)$ will occur at lower t. On the other hand, positive deviations from linearity will occur at higher relative pressure (higher t-values) in case of capillary condensation in mesopores. In this case the y-intercept gives the micropore volume and the slope gives the 'external' area which is equal to mesopore + macropore area. Here the micropore area corresponds to the difference of the whole specific surface area and external area.

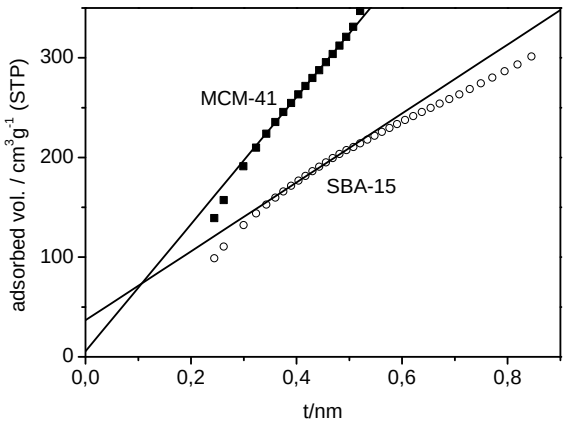

Figure 2.10: Comparison of t-plots of MCM-41 and SBA-15 silica.

In Figure 2.10 t-plots for MCM-41 and SBA-15 materials are displayed. In both cases

the graph shows a positiv y-intercept indicating microporosity of the samples. However, the intercept for SBA-15 (37 cm^3g^{-1}) is nearly 7 times higher than that for the MCM-41 (5.6 cm^3g^{-1}) sample. These values correspond to micropore volumes of 0.057 cm^3g^{-1} and 0.009 cm^3g^{-1} for SBA-15 and MCM-41, respectively. It is well known that SBA-15 materials have a higher microporosity than MCM-41. The micropores in SBA-15 arise from comparatively strong interactions of EO blocks of block copolymer with silica precursor TEOS. During the synthesis the EO blocks penetrate into the silica matrix and remain partially in it even after the aging. These leave small holes (micropores) in the silica wall after burning out the organic material by calcination at 550°C.

2.6.3 Specific pore volume

In contrast to adsorption on flat surfaces, the amount of the fluid adsorbed in pores is limited by the volume of the pore space. When neglecting adsorption at the outer surface of the porous particles, the amount of adsorbed gas in the plateau region of the isotherm represents the total pore volume of the sample. In the absence of micropores this is also called the mesopore volume. But the adsorption isotherm often exhibits a further increase above the pore condensation pressure step. In this case, the specific pore volume can be roughly estimated from the amount of adsorbed gas directly after the pore condensation step.

In nitrogen adsorption measurements by the gas volumetric method the amount of adsorbed nitrogen is indicated as gas volume under standard conditions (STP) in cm^3 g^{-1}. STP stands for **S**tandard **T**emperature and **P**ressure (273.15 K and 1 bar). Under these conditions nitrogen is a nearly ideal gas. The adsorbed gas volume of the nitrogen can be converted into the volume of liquid at the normal boiling temperature (77.3 K) by using the following equation:

$$V_l = \frac{V_{STP} \cdot M \cdot P}{\rho \cdot R \cdot T} = V_{STP} \cdot 1.547 \cdot 10^{-3} cm^3 g^{-1}. \tag{2.19}$$

Here P and T denote the standard pressure and temperature, respectively, R is the gas constant, M is the molar mass of a nitrogen molecule, and ρ is the density of liquid nitrogen equal to 808.6 kg m^{-3}.

2.6.4 Pore size

A typical phenomenon for the adsorption of fluids in mesoporous materials is pore condensation. It is characterized by a condensation in the pore at a relative pressure $p/p_0 < 1$

which is characteristic of the pore size. Pore condensation in pores of uniform size and shape is quantitatively described by the Kelvin equation. This equation applies only for mesopores, i.e., pores with a pore diameter bigger than 2 nm. For cylindrical pores the Kelvin equation has the form

$$RT\, ln(p/p_0)_{pc} = -\frac{2\gamma V_M \cos\theta}{r_p}. \tag{2.20}$$

This equation relates the pore condensation pressure $(p/p_0)_{pc}$ for a certain pore radius r_p with macroscopic properties of the fluid, namely the surface tension γ, molar volume of liquid adsorptive V_M and the and contact angle θ of the fluid with the pore wall. For nitrogen at its boiling temperature and standard pressure, γ=8.85 mN m^{-1} and V$_M$=34.71 cm^3 mol^{-1}. According to Equation 2.20 the pressure at which the pore condensation occurs is a function of pore radius. The smaller the radius r_p the smaller is relative pressure $(p/p_0)_{pc}$ at which the pore condensation takes place. For complete wetting of the wall the so called Kelvin radius can be determined by the following equation:

$$r_K/nm = \frac{-0.415}{log(p/p_0)_{pc}}. \tag{2.21}$$

In the case of complete wetting, at the onset of pore condensation the pore walls are covered with an adsorbed film of thickness t, so that the Kelvin radius is smaller than the real pore radius. Such a correction is considered in the modified Kelvin equation, viz.

$$r(p/p_0) = r_K + t(p/p_0). \tag{2.22}$$

In order to determine the effective pore size the thickness t of this adsorbed film must be added to the Kelvin radius. This so-called statistical film thickness is dependent on the pressure and is usually determined by gas adsorption measurements on chemically similar but flat (nonporous) surfaces. Several empirical approaches for determining the statistical film thickness have been proposed [33]. Nevertheless all of them are tainted with uncertainty and none of them can be used universally for any adsorbent. For this reason no singular method exists for determining the correct pore radius. When indicating a pore diameter it is necessary to specify the method through which the t layer was calculated.

For ordered masoporous solids like MCM-41 the pore diameter can be estimated from the lattice parameter a_0 and the specific pore volume v_p by the relation

$$D = \sqrt{\frac{2\sqrt{3}}{\pi}}\, a_0 \sqrt{\frac{v_p\rho_s}{1 + v_p\rho_s}} \tag{2.23}$$

where ρ_s is the matrix density of silica $\rho_s = 2.2$ g cm^{-3}. Based on values of D obtained by this relation and the respective pore condensation pressures $(p/p_0)_{pc}$ for a set of MCM-41 materials, Kruk et al. [34] obtained an empirical correlation known as the KJS relation. It has the form

$$D = \frac{-a}{log(p/p_0)_{pc}} + 2t + c. \tag{2.24}$$

where $a = 2 \cdot r_K$ and c is the constant that fits Equation 2.24 to the experimental dependence of D versus $(p/p_0)_{pc}$ obtained for the MCM-41 samples studied; t is the statistical film thickness adopted from Harkins-Jura equation [31] which used in following form:

$$t(p/p_0)/nm = 0.1 \, (\frac{60.65}{0.03071 - log(p/p_0)})^{0.3968}. \tag{2.25}$$

which quite accurately represents the film thickness of adsorbed nitrogen on flat surfaces in a pressures range from 0.1 to 0.95. Later, Jaroniec and Solovyov (2006) used X-ray diffraction modeling (see Section 2.5) to determine the pore diameter of SBA-15 materials independently of the adsorption measurements. As in the work of KJS [35] they obtained a set of data $D(p/p_0)_{pc}$ and fitted these data by a relation

$$D = \frac{-A}{log(Bp/p_0)_{pc}} + 2t + C \tag{2.26}$$

where A, B, C were obtained by data fitting (best fit parameters: $A = 1.15$, $B = 0.875$ and $C = 0.27$) and t is given by Equation 2.25.

Hence the imp. KJS equation has following form:

$$D/nm = \frac{-1.15}{log(0.875p/p_0)_{pc}} + 0.2 \, (\frac{60.65}{0.03 - log(p/p_0)_{pc}})^{0.397} + 0.27. \tag{2.27}$$

With the aid of this expression the pore size of hexagonal ordered mesoporous materials with pore condensation pressure between 0.1 and 0.8 can be described very well.

2.7 Thermogravimetric analysis (TGA/DTA)

Thermogravimetric analysis, (TGA) is an analytical technique used to determine a material's thermal stability and the fraction of volatile components in the material by monitoring the weight change that occurs as a sample is heated [36]. In this method the weight of the sample is recorded as a function of increasing temperature. For the determination of thermal decomposition (pyrolysis) of a sample the measurement is carried out in an inert atmosphere such as helium, argon or nitrogen, whereas for examination of thermo-oxidative degradation (oxidation) of a sample the measurement is performed in oxygen or air atmosphere.

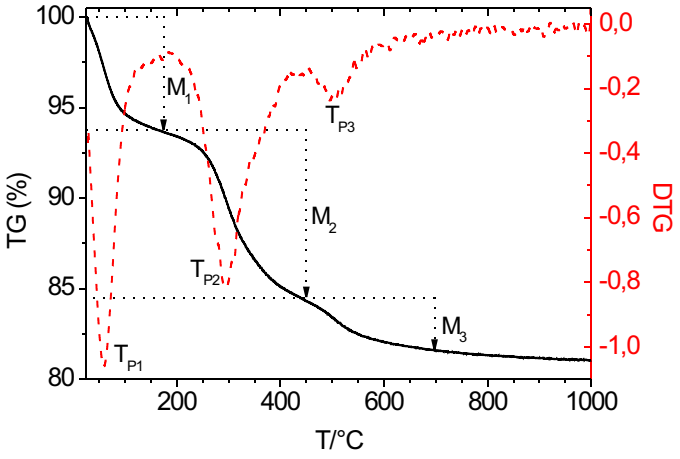

Figure 2.11: Analysis of a typical TG curve (full line) exhibiting three overlapping steps by means of the DTG signal (dashed line). M_1, M_2 and M_3 are weight losses during the steps 1, 2 and 3; T_{P1},T_{P2} and T_{P3} are the peak temperatures of DTG curve for the respective processes.

Many thermal changes in materials (e.g. phase transitions) do not involve a change of mass. For this reason, in addition to weight changes, some instruments also record transient temperature differences between the sample and one or more reference pans as a function of temperature (differential thermal analysis, DTA). When the sample undergoes a physical or chemical change, the temperature increase differs between the inert reference and the sample, and a peak or a dip is detected in the DTA signal.

Typical heating rates employed in TGA measurements with silica materials are in the 5-10 K min^{-1} range. Owing to closely spaced or overlapping the weight changes multiple step TGA curves often show no regions of a constant weight. In this case the differenti-

ated signal dm/dt (where m is the sample mass) delivers secondary information. Figure 2.11 shows a TGA curve with a three-step weight decrease. Here the border between two successive steps on the TG curve can be determined by the minimum value of the DTG curve between these two steps. In this case the silica materials were studied up to 1000°C, and the TGA curve is analyzed up to 700°C. Above this temperature, due to the condensation of isolated silanol groups, the amount of the siloxane bridges ($Si-O-Si$) is increased leading to a further small loss of mass.

Part I

Ordered Mesoporous Silicas: Self-assembly and Functionalization

Chapter 3

State of Knowledge

Ordered mesoporous silica materials of the type MCM-41 (**M**obil **C**omposition of **M**atter) [3] and SBA-15 (University of California at **S**anta **Ba**rbara) [4] are synthesized by a cooperative assembly of surfactant or block copolymer micelles and associated silica species in aqueous media. The products are disordered on the atomic scale but ordered on the mesoscopic scale. Due to their well-defined mesopore structure and high surface area these materials have gained much interest.

During the formation of such materials the matching of charge density at the surfactant (S)/inorganic (I) interfaces governs the assembly process. In the case of the 2D hexagonal formed MCM-41 the assembly process is controlled by electrostatic complementarity between the anionic inorganic ions in solution and the positively charged surfactants (S^+I^-). The isoelectric point of silica is at pH 2. Basic conditions are therefore necessary to form negatively charged silicate particles and to promote the hydrolysis of silica precursor tetraethylorthosilicate (TEOS). The use of tetramethylorthosilicate (TMOS) is possible as well. It can even be more beneficial in some advance preparations such as functionalization of MCM-41 using organoalkoxysilanes. Namely, TMOS hydrolyzes faster than TEOS does, due to the steric hindrance at ethoxide moieties and reduced solvation of resulting ethanol [37]. The anionic surfactant cetyltrimethylammoniumbromid (CTAB) is a quaternary ammonium compound with a long chain alkyl group. The pore size of MCM-41 materials can be varied by changing the alkyl chain length of this cationic surfactant. MCM-41 with 2D hexagonally ordered pores can be obtained in a chain length range between C10 and C18. On the other hand, non-ionic amphiphilic polyethylene oxide-polypropylene oxide-polyethylene oxide (PEO-PPO-PEO) triblock copolymers such as P123, P103, etc. are used as structure-directing agents for the synthesis of SBA-15. The formation of SBA-15 in acidic media, above pH=2, occurs by a pathway involving hy-

drogen bonding interactions among block copolymers and protonated silica species. The main interaction for the self assembly of the polymer micelle and silica precursor should be the ($S^0H^+X^-I^+$) type interaction, where X^- is the counter ion. Under acidic conditions, the PPO block is more hydrophobic than the PEO block upon heating from 35°C to 80°C. Accordingly, hydrophilic silicate species interact preferentially with the more hydrophilic PEO block. In the absence of sufficiently strong hydrogen-bonding interactions at pH values 2-7 no precipitation occurs and amorphous or otherwise disordered silica are formed. However, Kim et al. succeeded in preparing SBA-15 over a wide range of pH (0-9) by controlling the relative rates of hydrolysis and condensation of silica species using fluoride and TMOS [38]. The authors suggest that fully hydrolyzed monomeric silica species are needed for an attractive interaction with the block copolymer template for obtaining ordered mesostructures. This is due to a competition between the condensation of partially hydrolyzed silica species and the hydrolysis of alkoxysilane moieties associated with the silica precursors. Above pH 4, silica oligomers may contain the organic moieties from incomplete hydrolysis due to relatively rapid condensation compared to the rate of hydrolysis. The presence of such residual organic moieties leads to weaker interactions between hydrophilic block polymer and silica oligomers, resulting in poorly organized mesocomposites. So the reaction mixtures above pH 4 without fluoride yield gel-like precipitation and disordered or amorphous silica structures. On the other hand, addition of fluoride results in the formation of white precipitates and well ordered mesostructures up to pH 9. This indicates that hydrolysis of TMOS can be completed before significant condensation of the silica species occurs, which is consistent with the catalytic activity of fluoride for hydrolysis. The more rapid hydrolysis of TMOS thus makes it a preferable silica precursor to TEOS for producing ordered mesostructures. Nevertheless, such ordered mesostructures can be produced using TEOS, provided the silica sol is pre-hydrolyzed near pH 2 where the hydrolysis rate is fast and the condensation rate is slowest. It has also been reported that the addition of inorganic salts lead to a better order in mesostructured systems [39, 40, 41]. This is attributed to specific interactions between non-ionic amphiphiles and metal ions [42]. In this manner, Li et al. were for example able to synthesize highly ordered Fe-SBA-15 materials under weak acidic conditions [41].

SBA-15 materials have thicker pore walls than MCM-41 materials making them hydrothermally more stable. Higher temperatures or longer reaction times result in larger pore sizes and thinner pore walls. This may be caused by protonation or temperature-dependent hydrophilicity of the PEO block under the acidic synthesis conditions, or a combination of both effects. Resulting moieties are expected to interact more strongly

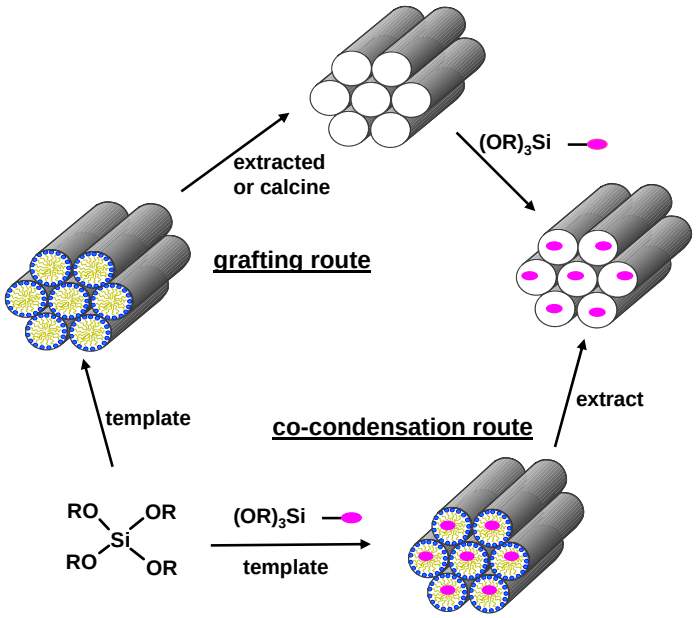

Figure 3.1: Schematic representation of the co-condensation and grafting routes for functionalization of ordered mesoporous silica materials [6].

with the silica species and thus are more closely associated with the inorganic wall than the more hydrophobic PPO block. At higher temperatures however, the PEO blocks become more hydrophobic, resulting in increased hydrophobic domain volumes, smaller lengths of PEO segments associated with the silica wall, and increased pore size.

While the structural properties of MCM-41 and SBA-15 are interesting for many potential applications involving host-guest interactions, it is often necessary to modify the surface composition of these materials, e.g., by attaching inorganic and organic components to the surface. Organic functionalization can be achieved either by covalently grafting of various organic species to surface silanol groups, or by incorporating functionalities directly during the preparation.

The first approach, the grafting process, has been widely employed to anchor specific organic groups onto surface silanols of a variety of silica supports. Typically, hydrolyzable moieties such as $RSiX_3$, where X=Cl, OCH_3 or OCH_2CH_3, are used as silica precursors for the surface functionalization. Moreover, different disilazane reagents $NH(SiR_2)$ can also be used for grafting in a gas phase reaction, as done in this work. Due to the relatively week N-Si bonds, these reagents are unstable at higher temperature and decompose releasing two functional group and NH_3. However, the grafting method has several drawbacks:

1. It is difficult to control the extent of the functionalization and the position of the anchored functional groups in an adequate way. The grafting rates depend on the reactivity of the precursors, diffusion limitations, steric factors and accessibility of surface silanol groups. For these reasons, variable and often rather low loadings are obtained. In this context, Brunel at al. reported that calcination of micelle templated silicas produces hydrophilic and hydrophobic zones on the surface and that grafting occurs only on the hydrophobic zones, leading to clustering of the functional silane even at relatively low loadings [43].

2. Post-synthesis grafting is time-consuming, as two steps are needed to accomplish the goal. In particular, the steps required to obtain the functionalized product are extensive, often requiring thorough drying of both the silica and the reaction solvent before the grafting reaction in order to avoid the formation of unwanted by-products.

3. To reach a high degree of modification it is often necessary to employ a large excess of functional silane.

4. Post-synthesis modification may lead to reduced pore size due to the attachment of a layer of the functional moiety on the surface.

These drawbacks my be overcome by a direct single-step process, i.e. incorporation of organic groups during the synthesis of the mesoporous silica by co-condensing siloxane and organosiloxane precursors in a templating environment. It is believed that this approach enables a higher and more homogeneous surface coverage of organosilane functionalities [44], although little direct evidence is available for the latter point. Evidence based on the kinetics of bromination of grafted and co-condensated vinyl-MCM-41 reported by Lim et al. indicates that vinyl groups are located predominantly on external surfaces and around the pore openings of grafted materials, but more homogenously distributed in materials prepared by co-condensation. Moreover, Fiorilli et. al studied the reactivity of the carboxylic acid (CA) groups of CA-SBA-15 synthesized by co-condensation method in reactions with ammonia in gas phase by following changes in the IR-spectra [45]. They concluded that the acid groups are well-dispersed, not clustered and behave independently of one another. In that work the materials were synthesized with a F/(F+TEOS) mole ratio of 10%. But the synthesis of well-ordered SBA-15 materials with 20 mole % is possible as well. However, to the best of our knowledge, similar investigations for silica samples which are loaded with functional silane higher than 10 mole % in the initial synthesis mixture are not existent yet.

On the other hand, Yokoi et al. provided evidence suggesting that some functional silanes may in fact be contained within the pore walls of MCM-41 materials prepared using the co-condensation method [46]. The authors found that materials synthesized using 3-aminopropyltrimethoxysilane, 1-(2-aminoethyl)-3-aminopropyl trimethoxysilane and 1-[3-(trimethoxysilyl)propyl]diethylenetriamine as functional silanes contained similar amounts of nitrogen, but that the accessibility of the amine centers to metal cations in solution decreased as the length of the organic chain increased. By comparing the results from the elemental analyses and the argentometric titrations of the surfactant-extracted samples, they concluded that not all amino moieties incorporated were present on the surface, but some of them were located in the walls of the hexagonal channels.

Another significant difference between grafted functionalities and functionalities generated by the co-condensation route is their stability. Materials obtained by post-synthesis modification are less stable than those prepared by co-condensation. This comes from the fact that the of Si-O-C bonds formed in the grafting process are readily cleaved at elevated temperatures. By contrast, in hybrid materials prepared by co-condensation method the functional group is attached to the matrix by Si-C bonds. So co-condensation results in very strong unhydrolyzable Si-C bonds which are substantially more stable than Si-O-C bonds.

The co-condensation method was first reported by two research groups in 1996 [44, 47] for the functionalization of MCM-41 materials. A variety of functional groups have been incorporated into mesoporous materials such as aliphatic hydrocarbons [44, 48, 49, 50], thiol groups [51, 52, 53], vinyl groups [54, 48, 55], phenyl groups [44, 49, 48], amine groups [56, 57, 50], etc. Most of these works have been conducted with M41S designated materials under basic synthesis conditions. These functionalized materials have potential for applications in different areas such as adsorption and separation processes, enzyme immobilization and catalysis.

An immobilized enzyme attached to an inert, insoluble material, provides increased resistance to changes in conditions such as pH or temperature. Immobilization also allows enzymes to be held in place throughout the reaction. After completion they are easily separated from the products and may be used again. It is a far more efficient process and so is widely used in industry for enzyme catalyzed reactions. For example, the amine, vinyl, thiol and carboxylic acid moieties are important functionalities for enzyme immobilization on porous supports. Chong et al. have found that vinyl functionalized SBA-15 is a candidate as a support material for penicillin acylase because of its high enzyme uptake and high initial activity of the biocatalyst [58]. Similarly, studies of Yiu et al. have shown

that trypsin immobilized on SBA-15 functionalized by thiol and carboxylic acid moieties displayed very high specific activities [10, 59].

On the other hand, there has been increasing interest in the development of heterogeneous solid acid catalysts to avoid the use of traditional homogeneous acid catalytic systems (H_2SO_4, HF, $AlCl_3$, BF_3, etc.) which present serious drawbacks including hazards handling, production of toxic waste, corrosiveness, and difficulties in separation. It has been shown that the type of support material used is a critical factor in the performance of the resulting supported catalyst. Two main factors must be considered when employing a material as a support. First, the material needs to be stable, both thermally and chemically, during the reaction process. Secondly, the structure of support needs to be such that the active sides are well dispersed on its surface in order that these sites are easily accessible. Aluminium substituted MCM-41 has been tested in acidic catalysis, though it shows week acidity in comparison to conventional acid zeolites. As an alternative, the covalent attachment of alkyl sulfonic acid groups to the surface of MCM-41 and other HMS (**h**exagonal **m**esoporous **s**ilica) molecular sieves has been proposed by several groups and successfully tested in several acid catalyzed reactions, including esterification, and condensation [52, 60, 61]. In post-synthesis grafting, 3-mercaptopropyltrimethoxysilane has been used as the key precursor, and the thiol groups were treated with H_2O_2 to obtain sulfonic groups. Margolese et al. used the same method to synthesize propyl sulfonic acid functionalized SBA-15 by the co-condensation route. Subsequently, Melero et al. reported the synthesis of arenesulfonic acid containing SBA-15 having increased acidity compared to propyl sulfonic acid functionalized SBA-15 [62]. These materials proved to be good catalysts for a variety of reactions [8] such as alcohol coupling to ethers [60], Friedel-Crafts-acylation of aromatic compounds [63], Fries rearrangement of phenyl acetate [64], Beckmann rearrangement of cyclohexanone oxime to ϵ-caprolactam [65] and etherification of benzyl alcohol [66]. The catalytic activities of HMS materials functionalized with phosphonic acid have been tested as well. Kawi et al. found that H_3PO_4-MCM-41 synthesized by impregnation of H_3PO_4 in MCM-41 through simply mixing is a promising selective catalyst for specific reactions that need only Brønsted acidity such as dehydration of isopropanol to propylene [67]. Le et al. immobilized tungsten species onto the surface of SBA-15 functionalized by diethylphosphatoethyltriethoxysilane. This catalyst shows high conversion and selectivity in the selective oxidation of cyclopentene to produce glutaraldehyde using H_2O_2 as the oxidant, and can preserve high activity after several cycles of reaction [68].

In the present work, functionalized silica materials were synthesized both by co-condensation and by the grafting route. In Chapter 5, the preparation of MCM-41 and SBA-15 materials with hydrophobized pore walls by the grafting route is described using $(CH_3)_2Si(OCH_3)_2$ and $(CH_3)Si(OCH_3)_3$ reagents. These materials were used for investigating the surface characteristics of MCM-41 and SBA-15 silicas. For this purpose solid-state ^{29}Si NMR methods were employed to obtain the ratio of numbers of single-, double-, and triple surface-bound species for each reagent. These results ratio provide qualitative information about the arrangement of the surface silanol groups at the pore walls from which the surface properties of MCM-41 and SBA-15 silicas can be gathered. Chapter 6 deals with the synthesis of SBA-15 materials containing different acid groups inside the pores prepared by the co-condensation route in acidic medium. SBA-15 functionalized with carboxylic acid, phosphonic acid and sulfonic acid groups were prepared by this route. Several parameters, such as amount of the functional silane and the sequence of prehydrolyzed component (TEOS or functional silane), were varied and the resulting material were characterized by various methods. The acidity of the acids in the aqueous solutions increases in the order carboxylic acid, phosphonic acid and sulfonic acid. Our aim was to examine of the acidity inside the mesopore channels of SBA-15 materials containing the aforementioned acid groups in its walls. The proton donor ability of these acid sides were studied by ^{15}N CPMAS NMR after pyridine adsorption into the pores.

Chapter 4

Materials and Methods

4.1 Materials

The synthesis of ordered mesoporous silica materials of the SBA-15 and MCM-41 type is accomplished with organic structure-directing agents (templates) and proceeds in the way illustrated in Figure 4.1. Template molecules of different kind are used in the synthesis of the two silicas. In the case of SBA-15, nonionic amphiphilic block copolymers are employed. Due to the stronger interactions between silica precursor TEOS and nonionic block copolymer at a pH below the isoelectronic point of silica (pH$\sim$2) the synthesis is performed in acidic medium with pH$<$2. In case of MCM-41, C_nTAB type cationic surfactants are used, where n is the number of carbon atoms in the hydrophobic chain. In this case the reaction is performed in basic media, above the isoelectronic point of silica, because of the cationic character of template molecules. In the following section the synthesis of these silica materials is described in detail.

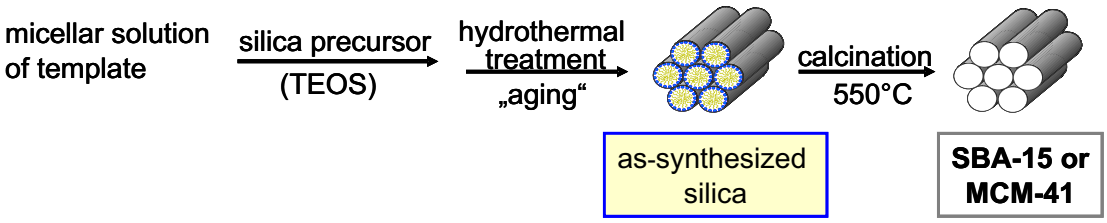

Figure 4.1: General route for SBA-15 and MCM-41 synthesis.

4.1.1 Pure SBA-15

SBA-15 was prepared by the method reported in ref. [4] using technical grade poly(ethylene oxide)-poly(propyleneoxide)- poly(ethylene oxide) triblock copolymer (Pluronic P123, BASF USA, Mount Olive, NJ) as the structure-directing agent. The molar composition of the reaction mixture was 1 TEOS : 5.9 H_2SO_4 : 323 H_2O : 0.017 P123. In a typical synthesis 13 ml of H_2SO_4 (97%) was added to a solution of 4 g of P123 in 240 ml milli-Q water to adjust pH < 2. This solution was transferred to a glas bottle with SL screw cap (1000 ml) and 9.2 ml tetraethoxysilane (TEOS, 99%, ABCR) was added under vigorous stirring at 40°C. The polymer-silica composite, formed as a fine precipitate, was kept in the reaction solution at 40°C for 20 h under constant stirring and then transferred to an autoclave for aging (20 h at 105°C). The product was filtered, washed with milli-Q water, dried at 60°C and finally calcined in air at 550°C.

4.1.2 Pure MCM-41

MCM-41 was synthesized as described in ref.[69], using hexadecyltrimethylammonium bromide (C_{16}TAB) as structure-directing agent (template). The molar composition of the reaction mixture was 1 TEOS : 5.6 NH_3 : 248 H_2O : 0.122 C_{16}TAB. In a typical synthesis 47 ml of aqueous ammonia (25 wt.%) was added to a solution of 5 g C_{16}TAB (Fluka, purity 99 %) in 500 ml Milli-Q water. 25 ml TEOS (ABCR, purity 97%) was added to this solution under vigorous stirring at 40°C. The surfactant-silica composite was formed as a fine precipitate after a few minutes and was kept in the reaction solution for 4 h at 40°C under constant stirring and then transferred into an autoclave for 48 h at 105°C. The material was filtered, washed with Milli-Q-H_2O and dried at 60°C for 6 h and finally calcined in air at 550°C.

4.1.3 Functionalization by grafting

4.1.3.1 HMDS and DCDMS

Hydrophobization of the pore walls of SBA-15 was performed with hexamethyldisilazane ($HN(Si(CH_3)_3)_2$, HMDS) or dichlorodimethylsilane ($(CH_3)_2SiCl_2$, DCDMS). In both cases, the modification was carried out by gas phase reaction. 1 g of SBA-15 was weighed into an open tube which was then placed in the glass flask of the device shown in Figure 4.2. The sample was heated to 120°C and then evacuated to a pressure of 10^{-2} mbar for several hours to remove adsorbed water from the pores. Afterwards the liquid reagent

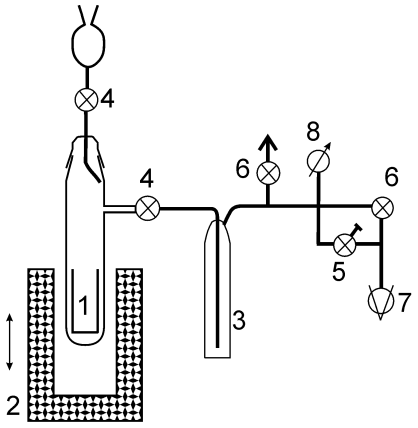

Figure 4.2: Equipment for the gas phase modification of the silicas [70]: **1** small sample tube, **2** oven, **3** N_2-cryo trap, **4** glass tap, **5** dosing valve, **6** blocking valve, **7** oil pumpe, **8** manometer.

(HMDS or DCDMS, both from Fluka) was introduced dropwise into the glass flask where it evaporates and the vapor reacts with the surface silanol groups of mesoporous silica material. The sample was kept in the reaction chamber for 24 h at room temperature (HMDS) or at 100°C (DCDMS). The non-reacted excess amount of the reagent was then removed by heating to 120°C and pumping at 10^{-2} mbar via a N_2-cryo trap.

4.1.3.2 DMDMS and MTMS

Modification of MCM-41 and SBA-15 with dimethyldimethoxysilane ($(CH_3)_2Si(OCH_3)_2$, DMDMS) and methyltrimethoxysilane $(CH_3)Si(OCH_3)_3$, MTMS) was performed by liquid phase reactions. 0.5 g of dry MCM-41 or SBA-15 were suspended in dry toluene in a N_2-atmosphere. An excess of the reagents DMDMS or MTMS (from Sigma Aldrich) was then added slowly through a dropping funnel under constant stirring. The suspension was then heated to 80°C under reflux for 24 h. After the reaction the solid material was vacuum-filtrated and washed each with 25 ml toluene and chloroform. Afterwards the solid was dried in a drying closet at 80°C.

4.1.3.3 Condensation of DMDMS and MTMS without silica

Hydrolysis and condensation of DMDMS and MTMS in the absence of silica was performed in water in acidic conditions, using an excess of 2 mole water per mole of methoxy-groups. The compositions of the reaction system were: 2.0 ml DMDMS (14.6 mmol) with 1.0 ml (58.4 mmol) of 0.1 M HCl, and 2.0 ml MTMS (14.6 mmol) with 1.5 ml (84.6

mmol) 0.1 M HCl. After 2 days of stirring at room temperature the condensation resulted in a clear, slightly viscous liquid in case of DMDMS, and a cloudy gel-like product in the case of MTMS.

4.1.4 Acid-functionalized SBA-15 by co-condensation route

Acid functionalized ordered mesoporous silicas were prepared by a one-pot synthesis method. In this method, a part of the silica precursor TEOS is replaced by a functional silane reagent. The molar composition of the systems used in this work was [71]

(1-x) TEOS (T) : x functional silane (F) : 5.8 HCl : 193 H_2O : 0.017 P123

where x was chosen between 0.1 and 0.3. The synthesis scheme is illustrated in Figure 4.3. Starting from a micellar hydrochloric acid solution of block copolymer (P123), the

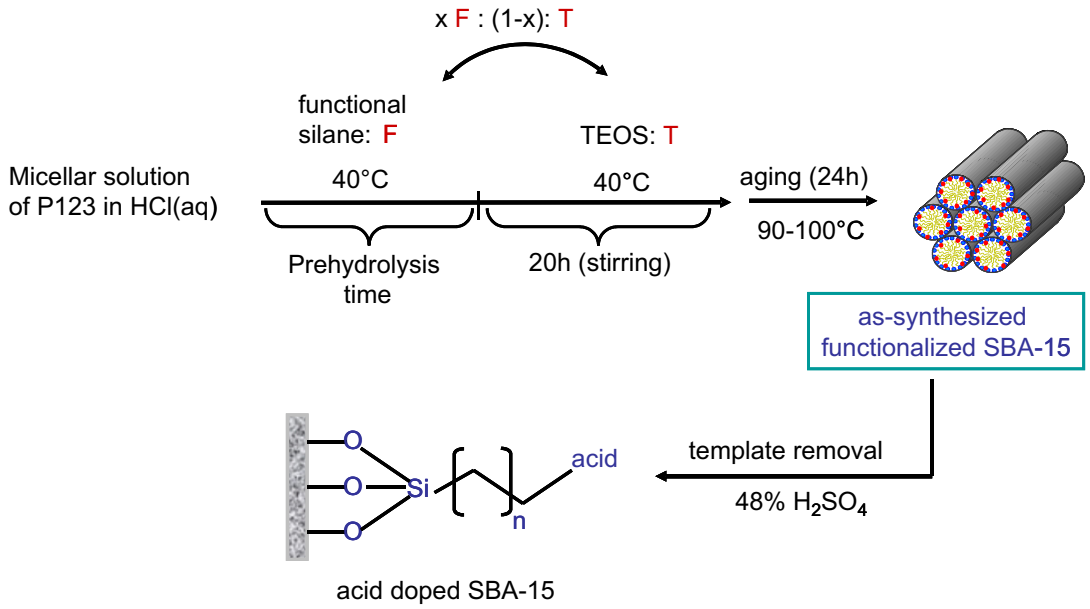

Figure 4.3: One pot synthesis functionalization route of SBA-15.

predetermined amount of functional silane is added, and a certain prehydrolysis time of that component is allowed at 40°C under stirring before adding the respective amount of TEOS. In some cases, TEOS was added first and the functional silane second, in order to asses the effect of the prehydrolysis. Aging occurred at 90-100°C for 24 h. After filtering and washing of the white precipitate *as-synthesized* functionalized SBA-15 materials were obtained. They were treated with 48% sulfuric acid solution to remove the template and produce the final acid containing SBA-15. Freshly prepared diluted H_2SO_4 was used for the template removal, by slowly diluting in an ice bath under stirring. The use of freshly

prepared 48% H_2SO_4 was found to be important for effective removal of the sample. Typically, 1 g of as-synthesized SBA-15 was suspended in 200 ml of 48% H_2SO_4 solution and refluxed at 95°C for 24 h under stirring. The treated powders were filtered and washed extensively, first with acetone and ethanol and later with water until the pH of the eluent was neutral. Finally the product was dried at 80°C.

Acid-doping of SBA-15 with carboxylic acid (CA), phosphonic acid (PA) and sulfonic acid (SA) was performed by this synthesis route. Only three parameters were varied in the synthesis procedure. These were:

1. Pre-hydrolyzed component of silica precursor mixture, i. e. either the functional silane (F) or TEOS (T) is prehydrolyzed with the acidic P123 solution.

2. *y*: Prehydrolysis time of the pre-mixed component expressed in minutes,

3. ϕ: Molar percentage of functional silane (F) in the silica precursor mixture.

$$\phi = \frac{F}{F+T} \cdot 100$$

Throughout this work the acid-functionalized materials are denoted as

ϕ-CA-*y*-**F**, ϕ-PA-*y*-**F** and ϕ-SA-*y*-**F**.

The as-synthesized materials are denoted as

ϕ-CN-*y*-**F**, ϕ-P-*y*-**F** and ϕ-S-*y*-**F**

when the functional silane (F) was the prehydrolized component of the silica precursor. In materials in which TEOS was used as the prehydrolized component, the **F** is replaced by **T**. However, in several cases abbreviated notations will be used as explained below.

4.1.4.1 Carboxylic acid doped SBA-15 (CA-SBA-15)

Materials were prepared by the synthesis route described above. Here the optimized synthesis conditions were taken from the work of Yang et. al [71]. The functional silane 2-cyanoethyltriethoxysilane, *CTES*, (98%, Aldrich) was used in the synthesis of CA-SBA-15. Molar composition of (1-x) T : x F with x = 0.1 and 0.2 were used *(ϕ = x.100)*. In the synthesis of these materials, the functional silane (F) was always used as the prehydrolyzed component, and a prehydrolysis time of 60 min was used in all cases. For this reason an abbreviated nomenclature is used for these materials: The as-synthesized products are called 10-CN and 20-CN, and the respective end products are denoted by 10-CA and 20-CA. The end products are formed by the hydrolysis of CN-groups through the H_2SO_4 treatment during the template removal.

4.1.4.2 Phosphonic acid doped SBA-15 (PA-SBA-15)

For the synthesis of PA-SBA-15 materials by the co-condensation route diethoxyphosphorylethyltriethoxysilane, *PTES*, (95%, ABCR) was chosen as the functional silane. Materials with molar compositions (1-x) T : x F with x = 0.1, 0.15, and 0.2 were prepared. Either TEOS (T) or the functional silane (F) was used as the prehydrolyzed component. The prehydrolysis time was varied between 0 and 95 min. The as-synthesized products are called ϕ-P-*y*-F/T. The products containing phosphonate ester after polymer removal by treatment with H_2SO_4 are denoted as ϕ-POEt-*y*-F/T. Phosphonic acid functionalities were formed by dealkylation of the phosphonate ester groups. To complete the cleavage of phosphonate ester the samples were fluxed in concentrated HCl. For this purpose, ca. 1 g of the H_2SO_4 treated material was suspended in 300 ml of 37% HCl and refluxed under stirring at 95°C for 24 h. After filtering the solid was extensively washed with water until the eluent was pH neutral. Throughout this work samples containing free phosphonic acid groups are referred to as ϕ-PA-*y*-F/T.

4.1.4.3 Sulfonic acid doped SBA-15 (SA-SBA-15)

For the synthesis of SA-SBA-15 materials the functional silane 3-(trihydroxysilyl)-1-propane-sulfonic acid, *STHS*, (30-35% in water, ABCR) was used. Molar compositions (1-x) : x F with x = 0.1 , 0.2, and 0.3 were used, and both TEOS and F was used as the prehydrolyzed component. Notice that in case of STHS, the term 'hydrolysis' is not really appropriate because it already exists in the hydrolyzed form. Rather we are dealing with 'precondensation' of the functional silane. For the sake of a uniform notation the term will nevertheless be used. The prehydrolysis time was varied between 0 and 1480 min. The as-synthesized products are called ϕ-S-*y*-F/T, and the products after treatment with H_2SO_4 are denoted as ϕ-SA-*y*-F/T.

4.2 Methods

4.2.1 Nitrogen adsorption

The pore structure of the silica materials was characterized by N_2 adsorption and small-angle X-ray diffraction. Adsorption isotherms of nitrogen at 77 K were measured by gas volumetry using a Gemini 2375 volumetric gas adsorption analyzer (Micromeritics). The samples were dried and outgassed at 120°C for 45 min at a pressure below 0.1 mbar

and reweighed before the gas adsorption measurement, to determine the net mass of the sample. For the measurements the standard Micromeritics sample tubes were used. For thermal isolation of Dewar vessel in which the sample tube is immersed in liquid nitrogen, the original top of Dewar vessel is replaced by a styrofoam top. In this way it was guaranteed that evaporation of the nitrogen was slow enough to maintain the temperature of the sample constant for the full time of 12 h measurement. Because the barometric pressure was measured only at the beginning of the adsorption ran subsequent variations of air pressure and thus the actual saturation pressure p_0 of nitrogen could not be taken into account.

4.2.2 SAXD

Small-angle X-ray diffraction (SAXD) measurements were made in the Max-Planck Institut für Kolloid- und Grenzflächenforschung in Potsdam/Golm. The SAXD profiles were recorded in a range of the scattering vector q from 0.3 to 2 nm^{-1} by a Bruker SAXS Nanostar machine, using a 2D HI Star area detector and CuKα radiation (λ=1.54 Å). The calibration of q scale was performed using silver behenate as reference. For the measurements the mesoporous silica materials are filled in small glass tubes (Mark Röhrchen) of 1 mm diameter and 80 mm length, and a wall thickness of approximately 0.01 mm. After loading with the powders the tubes were sealed in a flame.

4.2.3 TGA

Weight loss curves due to thermal decomposition in air of functionalized SBA-15 materials was measured on a TG/DTA Netzsch STA 409 simultaneous thermal analysis instrument in the laboratory of inorganic chemistry at TU Berlin. Samples were heated at a rate of 10 K min^{-1} in a stream of synthetic air.

4.2.4 ^{13}C, ^{29}Si and ^{15}N solid-state NMR

^{13}C, ^{29}Si and ^{15}N NMR measurements were performed in cooperation with the group of Prof. H.-H Limbach at the Chemistry department of FU Berlin using a Bruker MSL-300 instrument operating at 7 Tesla, and equipped with a Chemagnetics-Varian 6 mm pencil CPMAS probe. All samples were spun at 6-8 kHz under magic angle spinning (MAS) conditions.

The ^{29}Si MAS spectra were recorded employing a $\pi/12$ pulse-sequence and a recycle delay of 180 s. The $\{^1H\}$-^{29}Si CPMAS spectra were recorded using a relatively long cross polarization (CP) contact time (8 ms), which ensures sufficient polarization transfer to all different Si species of silica, i.e. Q^2, Q^3 and Q^4; further parameters were a recycle delay of 5 s. The ^{29}Si chemical shifts of spectra shown in Chapter 5 are referenced to liquid TMS (Tetramethylsilane), whereas those presented in Chapter 6 are referenced to solid TSP (3-(Trimethylsilyl)propionic acid sodium salt).

The ^{13}C NMR measurements were performed employing the $\{^1H\}$-^{13}C CPMAS technique with a CP contact time of 2 ms and a recycle delay of 5 s. The typical 90°-pulse length in the CP experiments was 3.5 sec for ^{1}H. The ^{13}C chemical shift values are referenced to solid TSP.

The ^{15}N MAS spectra were recorded employing a $\pi/2$ pulse-sequence, with a 90°-pulse length of 4.5 μsec. The room- temperature and low-temperature $\{^1H\}$-^{15}N CPMAS spectra were recorded using a cross polarization contact time of 5 ms. The typical 90°-pulse length was 3.5 μsec for ^{1}H. All ^{15}N chemical shift values are referenced to solid $^{15}NH_4Cl$. In this scale, the ^{15}N nucleus of pyridine resonates at 275 ppm and that of protonated pyridinium below 170 ppm.

4.2.5 FT-IR

FT-IR measurements of CA-SBA-15 samples were recorded using a Bruker Tensor 27 spectrometer in the Max-Volmer laboratory of TU-Berlin. For this purpose a thin silicone spacer (10 mm diameter, 10 μm thick) was placed on a CaF_2 slide and an appropriate amount of the silica powder was put into the ring. A small volume of D_2O or a phosphate buffer solution in D_2O was then added by a microliter pipette in argon atmosphere. The suspension was homogenized with a spatula and the excess solution was removed by waiting in argon atmosphere. Subsequently the cell was closed under argon atmosphere.

4.2.6 Potentiometric titration

Potentiometric titrations were performed by a Metrohm Titrando 836 automatic potentiometer. Aliquots of ca. 50-70 mg of acid functionalized SBA-15 samples were added to ca. 15 g of 2 M NaCl solution and equilibrated for 45 min to assist the proton release via a cation exchange process. The solution obtained in this way was potentiometrically titrated against 0.02 M NaOH (in case of SA-SBA-15) or 0.01 M (in case of CA-SBA-15) solutions. The first derivative curve was used for computation of acidic capacity. Each titration was performed twice at least. Typical titration curves obtained for the CA-SBA-15 and SA-SBA-15 materials are shown in the Figure 4.4.

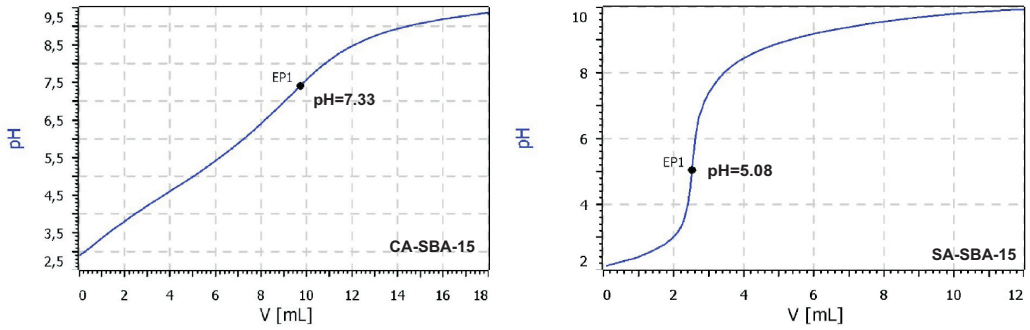

Figure 4.4: Titration plots of CA-SBA-15 and SA-SBA-15 (pH vs. V_{NaOH}).

4.2.7 Scanning electron microscopy (SEM)

SEM images were made in ZELMI at TU Berlin using a Hitachi S-4000 microscope. The dry silica samples were directly attached to carbon-coated Cu grids by dispersing small amounts of the powder using a spatula, to avoid contact to any solvents.

Chapter 5

Functionalization by Grafting*

Abstract

MCM-41 and SBA-15 silicas were studied by ^{29}Si and ^{15}N solid state NMR in the presence of ^{15}N-pyridine with the aim to formulate generic structural parameters which may be used as a checklist for atomic-scale structural models of this class of ordered mesoporous materials. High-quality MCM-41 silica constitutes quasi-ideal arrays of uniform-size pores with thin pore walls, while SBA-15 silica has thicker pore walls with framework and surface defects. The numbers of silanol (Q^3) and silicate (Q^4) groups were found to be in the ratio of about 1:3 for MCM-41 and about 1:4 for our SBA-15 materials. Combined with the earlier finding that the density of surface silanol groups is about 3 per nm^2 in MCM-41 [5] this allows to discriminate between different atomic-scale models of these materials. The arrangement of Q^3 groups at the silica surfaces was analyzed using postsynthesis surface functionalization. It was found that the number of covalent bonds to the surface formed by the functional reagents is affected by the surface morphology. It is concluded that for high-quality MCM-41 silicas the distance between neighboring surface silanol groups is greater than 0.5 nm. As a result, di- and tripodical reagents like $(CH_3)_2Si(OCH_3)_2$ (DMDMS) and $(CH_3)Si(OCH_3)_3$ (MTMS) can form only one covalent bond to the surface. The residual hydroxyl groups of surface bonded functional reagents either remain free or interact with other reagent molecules. Accordingly, the number of surface silanol groups in a given MCM-41 or SBA-15 silica may not decrease but increase after treatment with $CH_3Si(OH)_3$ reagent. On the other hand, nearly all surface silanol groups could be functionalized when $HN(Si(CH_3)_3)_2$ (HMDS) was used.

*In modified form published as: Shenderovich, I. G.; Mauder, D.; Akcakayiran, D.; Buntkowsky, G.; Limbach, H.-H.; Findenegg, G. H. *J. Phys. Chem. B.* **2007**, *111*, 12088

5.1 HMDS and DCDMS grafted samples

Many potential applications of ordered mesoporous silica result from the surface silanol groups at the pore walls. The proton donor ability of the surface hydroxyl groups is similar to that of acids exhibiting a pKa of about 4 in water [5]. Thus, the surface of pure silica is slightly acidic. The chemical activity of the surface can be selectively modified via the grafting method leading to novel hybrid materials. The simplest way to convert the weakly acidic surface of pure silica into a hydrophobic one is to coat it with hexamethyldisilazane (HMDS) by a simply gas phase reaction in room temperature described in Section 4.1. In this case the functionalization reagent contains the only reactive group which can interact with the surface silanols to form Si-O-Si covalent bond as illustrated schematically in Figure 5.1.

Grafting of dichlorodimethylsilane $(CH_3)_2SiCl_2$, (DCDMS) onto the surface of SBA-15

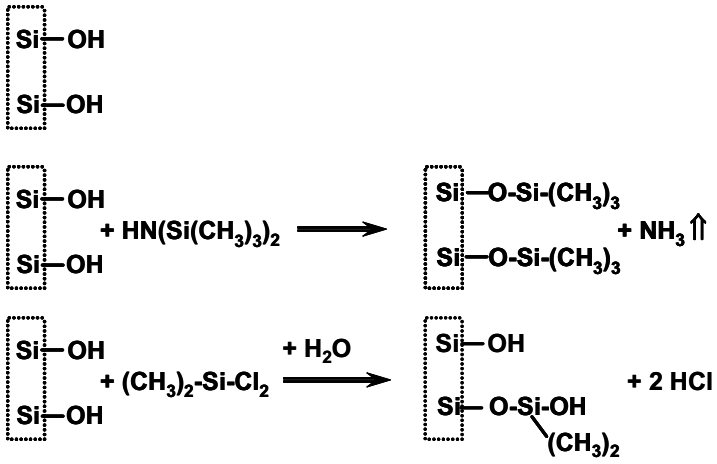

Figure 5.1: Schematic illustration of the chemical structures of the surfaces before and after the functionalization.

was also performed by a gas phase reaction at elevated temperatures (Section 4.1). Here the functional reagent carries two reactive groups. Accordingly, it can form bonds to either one or two silanol groups.

The functionalization and its efficiency were investigated by ^{29}Si and ^{15}N CPMAS NMR spectroscopy. Experimental spectra obtained for the pure and modified SBA-15 are presented in Figure 5.2. After modification a line assigned to the functional silane (Q_R) appears in the ^{29}Si NMR spectra displayed in Fig. 5.2b and Fig. 5.2c. The level

of modification could be roughly estimated from the ^{29}Si spectrum of the modified silica by analyzing the reduction of the corresponding Q^3 peak. For both modified SBA-15 samples the ratio of the Q^3:Q^4 intensities are smaller than for the pure SBA-15 (cf. Fig. 5.2a, Fig. 5.2b, and Fig. 5.2c on the left)

^{15}N CPMAS NMR spectrum of HMDS modified SBA-15 shows a strong reduction of the amount of pyridine bound to the surface hydroxyl groups via hydrogen bonds, (cf. Fig. 5.2a and 5.2b right). Therefore, it appears that HMDS causes a nearly quantitative

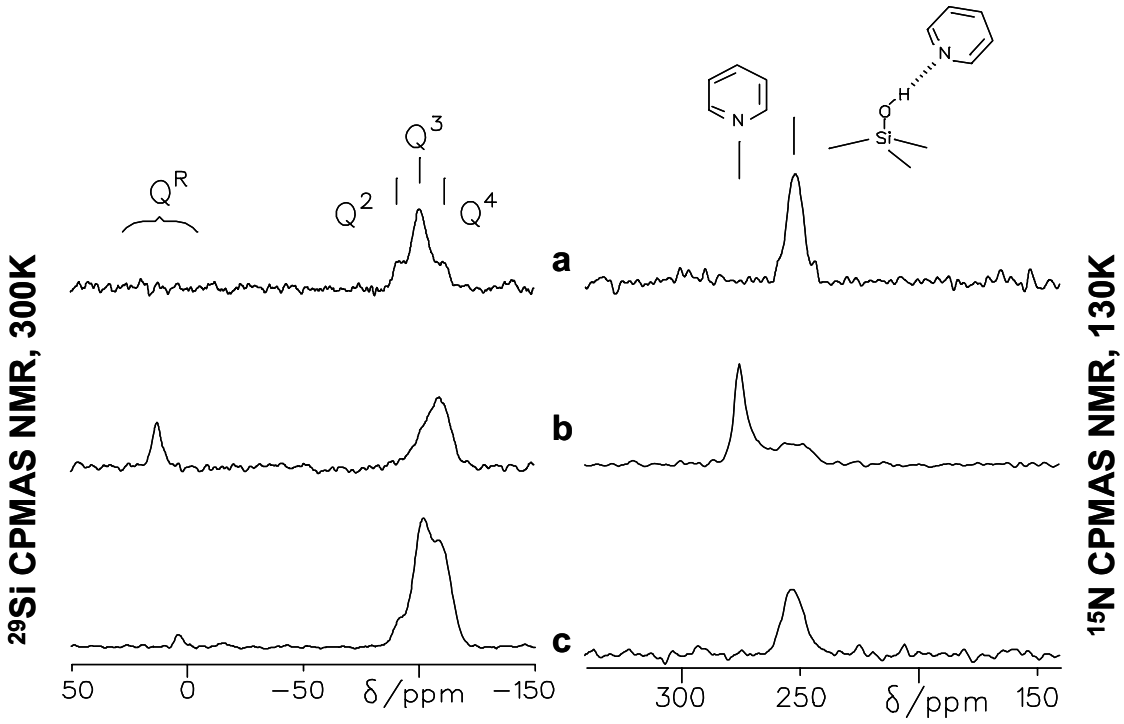

Figure 5.2: Left: ^{29}Si CPMAS NMR of pure (a) and functionalized (b, c) SBA-15 silica, Right: ^{15}N CPMAS NMR at 130 K of the same samples loaded with an equal amount of ^{15}N-pyridine. The functionalization reagents were $HN(Si(CH_3)_3)_2$, HMDS (b), and $(CH_3)_2SiCl_2$, DCDMS (c).

functionalization of the surface. In contrast, the ^{15}N spectrum of DCDMS modified SBA-15 did not display a reduction of the available hydroxyl groups, (cf. Fig. 5.2a and Fig. 5.2c right). This finding indicates that some of the reactive groups of such reagents do not form covalent bonds to the surface but are only hydrolyzed. Since the hydrolysis is the step preceding surface functionalization, we conclude that not all hydrolyzed groups were able to meet surface hydroxyl groups to form covalent bonds. This fact has been employed to analyze the arrangement of the surface hydroxyl groups.

Table 5.1: Abbreviations of samples used and relative intensities of NMR signals corresponding to surface functional groups of different podality.

sample	abbreviation	$D^1 : D^2$	$T^1 : T^2 : T^3$
DMDMS+HCl	DM	5 : 100	
MTMS+HCl	TM		22 : 100 : 354
MCM-41-DMDMS	M-DM	223 : 100	
SBA-15-DMDMS	S-DM	91 : 100	
MCM-41-MTMS	M-TM		62 : 100 : -
SBA-15-MTMS	S-TM		7 : 100 : 38

S: SBA-15; M: MCM-41, DM: DMDMS; TM: MTMS

5.2 DMDMS and MTMS grafted samples

In order to simplify the comparison between HMDS and reagents having two or three reactive groups we studied silica samples modified by the simplest possible reagents, namely dimethyldimethoxysilane (DMDMS) and methyltrimethoxysilane (MTMS). The preparation of these samples is described in Section 4.1.3. Figure 5.3 shows ^{29}Si NMR spectra of these reagents after hydrolysis and condensation as well as spectra of functionalized silica materials (samples: DM, M-DM, S-DM, and TM, M-TM, S-TM). Abbreviations of the modified samples used in this chapter are summarized in Table 5.1. The spectra of the functionalized materials were obtained using the cross-polarization transfer technique. Thus the relative intensities of different peaks of the same spectrum may not precisely coincide with the relative concentration of the corresponding species. However, a long contact time was used and each silicon nucleus carried at least one methyl group that minimized the difference. For these reasons, it is justified to compare the relative intensities of these peaks in order to estimate the relative concentrations of the different Si species. The hydrolysis of pure DMDMS in aqueous 0.1 M HCl solution (DM) resulted mostly in the condensation. The residual amount of silicon atoms carrying one hydroxyl group (D1 species) was small (see Fig. 5.3a). In contrast, the D1:D2 ratio was close to 2 when this reagent was used to modify MCM-41 silica (M-DM) and about 1 for SBA-15 silica (S-DM) as shown in Fig. 5.3b and Fig. 5.3c. The condensation of pure MTMS in 0.1 M HCl solution (TM) was less efficient. About 20% of the silicon atoms were still carrying one hydroxyl group (T^2 species, Fig. 5.3d). At the pore walls of MCM-41, only about 60% of the reagent molecules were forming two covalent bonds to the surface and

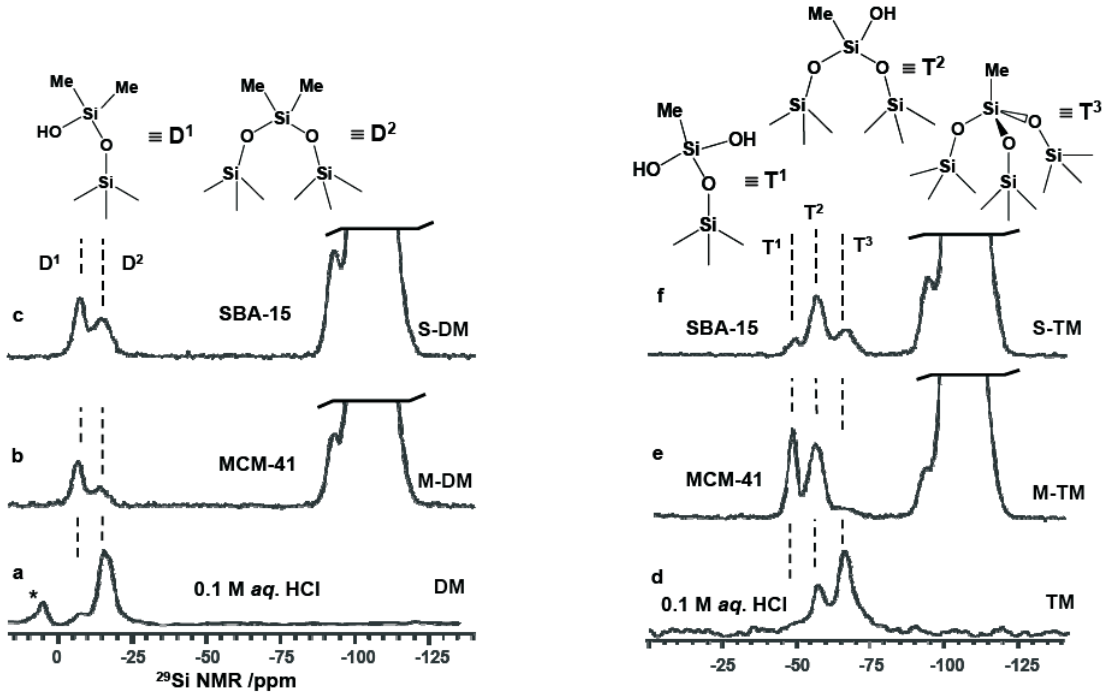

Figure 5.3: Left: ^{29}Si NMR of hydrolysed dimethyldimethoxysilane (DMDMS), sample DM (a) and ^{29}Si CPMAS NMR of MCM-41, sample M-DM (b) and SBA-15, sample S-DM (c) silica samples functionalized using DMDMS as reagent. Right: ^{29}Si NMR of hydrolyzed methyltrimethoxysilane (MTMS), sample TM (d) and ^{29}Si CPMAS NMR of MCM-41, sample M-TM (e) and SBA-15, sample S-TM (f) silica samples functionalized using MTMS as reagent.

almost no molecules forming three bonds (M-TM, Fig. 5.3e). The T1:T2:T3 ratio on the surface of SBA-15 was about 1:10:4 (S-TM, Fig. 5.3f). The resulting T1:T2:T3 ratios are summarized in Table 5.1.

5.3 Arrangement of the surface silanol groups

We showed that silica functionalization using HMDS as reagent allows to obtain practically hydroxyl-free surfaces. This means that groups such as $Si(CH_3)_3$ being immobilized on the surface do not prevent functionalization of neighboring silanol groups. The diameter of a $Si(CH_3)_3$ group at the surface is about 0.5 nm. The mean surface density of the silanol groups is about 3 per nm^2, corresponding to a mean distance of about 0.58 nm between the neighboring silanol groups. However, this estimation does not allow to

conclude whether or not the silanol group at the surface of ordered mesoporous silica are distributed uniformly. This question might be answered by analyzing the rotational dynamics of the immobilized functional groups. They predict only the lower limit for the distance between the neighboring silanol groups on the idealized MCM-41-like surface. The latter indicates that any functionalization reagent of the $(CH_3)_{4-n}$-Si-$(OH)_n$ type could form only one covalent bond to the surface and the residual chemically active groups could be used only to form a new silica layer.

A closer look at spectra of functionalized silica in Fig. 5.3 shows that the half-widths of the NMR peaks corresponding to D^1 and T^1 species is only about one half of the width of D^2, T^2 and T^3 species. In contrast, the half-width of the NMR peaks corresponding to T^2 and T^3 species formed in aqueous solution after $CH_3Si(OMe)_3$ hydrolyzation was approximately the same as that of the D^1 and T^1 species on the silica surface. We ascribe this effect to inhomogeneous broadening due to some variations in the geometry of different D^2, T^2 and T^3 species bonded to the silica surface. These deviations could be caused either by mutual bonding between the functional groups or their multiple bonding to the surface. Which of these two reasons plays the dominant role may be different for MCM-41 and SBA-15 silica. When the surface was functionalized using $CH_3Si(OMe)_3$ as the reagent, we did not observe T^3 bonded species on the MCM-41 surface. This finding is at variance with data reported in other studies [72, 73]. However, in these studies the degree of functionalization was higher than for our samples. Accordingly, the formation of covalent bonds to further reagent molecules cannot be excluded. Indeed, the fact that the number of T^2 species on the MCM-41 surface was much higher than the number of D^2 species, when $CH_3Si(OMe)_3$ reagent was used instead of $(CH_3)_2Si(OMe)_2$, could hardly be explained exclusively in terms of covalent bonding to the surface. The hydroxyl group of the surface-bonded $(CH_3)_2Si(OH)$ species should be directed closer to the surface than one of the hydroxyl groups of the surface-bonded $(CH_3)Si(OH)_2$ species, and this provides a better access of another reagent to the latter hydroxyl group. Thus, the surface of MCM-41 silica did not contain silanol groups which would be able to react with the same molecule of the $(CH_3)_{4-n}$-Si-$(OH)_n$ type reagent. If the formation of mutually bonded functional groups could be suppressed, such a surface would contain exclusively single surface bonded species. On the other hand, each surface silanol group could carry the functional group.

The amount of D^2, T^2 and T^3 species strongly increases when the rough surface of SBA-15 was used instead of the quasi-ideal surface of MCM-41. It is not clear whether T^3 species observed on SBA-15 silica could be formed exclusively by the covalent bonding

to the surface or by bonding to other functional groups as well. We assume that the latter case is more realistic. In Figure 5.4 the situation is summarized in a pictorial way. For simplicity let us assume a uniform arrangement of the silanol groups on the surface (Fig. 5.4a). When the $(CH_3)_2Si(OMe)_2$ reagent is used to functionalize such a surface, it may

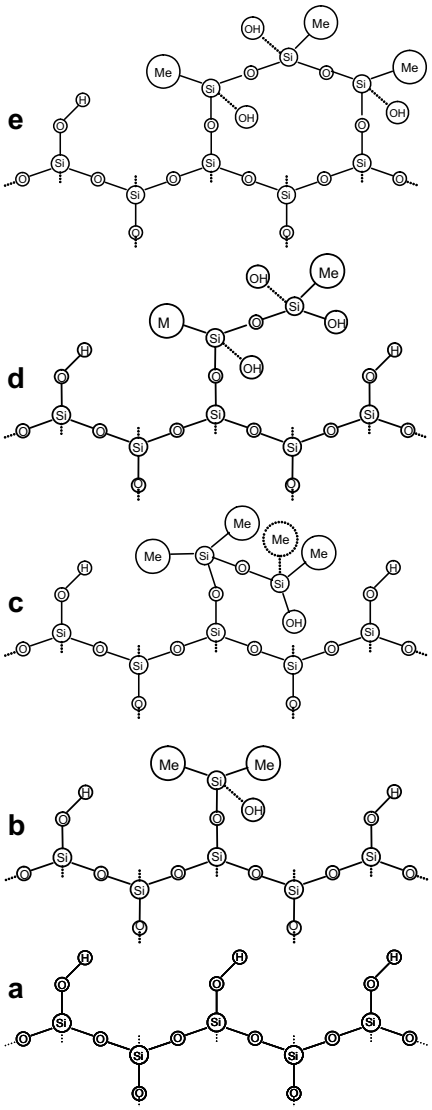

Figure 5.4: Cartoon of the surface structures of a silica before (**a**) and after its treatment with a small (**b**, **d**) and large (**c**, **e**) amount of $(CH_3)_2Si(OCH_3)_2$ and $(CH_3)Si(OCH_3)_3$ reagents.

form only one covalent bond and the second active group is just converted to hydroxyl (Fig. 5.4b). It is hard to imagine how this group could form a second covalent bond to the surface. Potentially, it might react with another reagent molecule (see Fig. 5.4c), but the

experimental spectra indicate that such a reaction was not very effective, as shown in Fig. 5.3b. When the $CH_3Si(OMe)_3$ reagent is used, it may also form only one covalent bond to the surface, but at least one of the two residual free hydroxyl groups can easily be attacked by another reagent (Fig. 5.4d). If no further reaction would take place, the T^1:T^2 ratio would be about 1:1. In contrast, the experimental data for this reagent on MCM-41 silica reveal a ratio of about 2:3 (Fig. 5.3e). This may indicate that a third reagent molecule becomes involved, leading to the double surface bonded species (Fig. 5.4e). The presence of surface defects will allow more complex structures with reduced numbers of unreacted hydroxyl groups, as was indeed observed for SBA-15 silica.

5.4 Conclusions

The main results of the experiments described in this chapter can be summarized as follows. The arrangement of Q^3 silicon atoms on the silica surfaces was analyzed using surface functionalization by grafting route. In particular, it was shown that $Si(CH_3)_3$ groups attached to the surface do not prevent reactions with the neighboring surface silanol groups. This fact indirectly suggests that the distance between neighboring surface silanol groups is greater than 0.4-0.5 nm. ^{29}Si CPMAS NMR measurements of functionalized silicas indicated that the number of covalent bonds formed by the reagents $(CH_3)_2Si(OH)_2$ and $CH_3Si(OH)_3$ depends on the surface roughness. The experiments show that these reagents can form only one covalent bond to the surface of high-quality MCM-41 silica. The residual hydroxyl groups of the surface-bonded reagents either remain free or interact with other reagent molecules. Hence, the surface of MCM-41 did not contain neighboring silanol groups which would be able to form covalent bonds with the same molecule of $(CH_3)_2Si(OH)_2$ or $CH_3Si(OH)_3$ type. On the other hand, it appears that multiple covalent binding to the surface is possible to some extent on the rough pore walls of SBA-15 silica, at least for the $CH_3Si(OH)_3$ reagent. In other words, the number of covalent bonds formed by the functional reagents to the silica surface is affected by the surface morphology. The pore walls can be almost fully functionalized when HMDS is used as the functionalization agent. In contrast, at the same surface the number of silanol groups may even increase by the functionalization under certain conditions when $CH_3Si(OH)_3$ is used as grafting agent.

Chapter 6

Acid-Functionalization by Co-condensation

Abstract

Functionalized SBA-15 silica materials with acidic groups of different pKa values in the liquid phase such as carboxylic acid, phosphonic acid and sulfonic acid are synthesized by the co-condensation route in order to study the effect of confined geometry on acidity. The functional silanes used are 2-cyanoethyltriethoxysilane (CTES) for carboxylic acid functionalization of SBA-15 (CA-SBA-15), diethoxyphosphorylethyltriethoxysilane (PTES) for phosphonic acid functionalization of SBA-15 (PA-SBA-15), and 3-(trihydroxysilyl)-1-propane-sulfonic acid (STHS) for sulfonic acid functionalization of SBA-15 (SA-SBA-15). The structure of the functionalized materials is affected by the amount of the functional silane (*F*), by the prehydrolyzed silica source (TEOS or *F*) and by the prehydrolysis time. Reaction conditions for a high-degree of functionalization under preservation of mesoscopic well-ordered structure of silica changes with the functional silane used. The results suggest that the structural order of the materials are strongly affected by assembly kinetics which involve the hydrolysis and the condensation of silica species and their interaction with template. Nitrogen adsorption isotherms indicate that the functionalized SBA-15 materials have pore diameters larger than 7 nm. Moreover, the microporosity of acid containing SBA-15 samples is lower than that of pure SBA-15. The ^{13}C CPMAS NMR and TGA/DTA measurements show that the higher the percentage of the functional silane ϕ in the synthesis mixture, the lower the amount of polymer template in the as-synthesized functionalized SBA-15, and the higher the degree of the polymer removal by sulfuric acid treatment. In SBA-15 materials synthesized with a molar percentage of functional reagent *F* of ϕ = 20 the polymer template can be removed completely. The

highest surface coverages of SBA-15 by carboxylic acid, phosphonic acid, and sulfonic acid groups are 50%, 40% and 30%, respectively. Also the yields of the functionalization reactions correspond to that decreasing sequence. The acidity measurements of functionalized SBA-15 materials were performed via ^{15}N CPMAS solid-state NMR after adsorption of pyridine into the pores. The pK_a values corresponding to the ^{15}N chemical shifts for the protonated pyridine indicate a high proton donor ability of all three solid acids. The dependence of the proton-donor ability of the 10-CA-SBA-15 (10-CA) and 20-CA-SBA-15 (20-CA) silicas on the pH of the solution by FT-IR measurements show the deprotonation of COOH groups at pH 8. The results suggest that in the 10-CA material with 20% surface coverage nearly all COOH groups are separated and accessible, while in the 20-CA material with 50% surface coverage only a part of the COOH groups is accessible.

6.1 Template removal: calcination vs. acid treatment

The effectiveness of template removal by treatment with 48% H_2SO_4 was studied with pure (non-functionalized) SBA-15 by measuring the weight loss in TGA. The TGA curves of SBA-15 as synthesized (as-S), SBA-15 after H_2SO_4 treatment (S-acid) and after calcination at 550°C (S-cal) are displayed in Figure 6.1. The TGA curves indicate that as-S

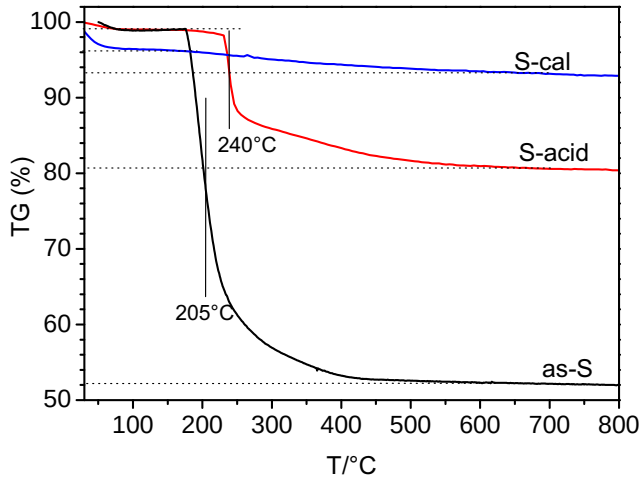

Figure 6.1: TGA curves of as-SBA-15 (as-S), SBA-15 after H_2SO_4 treatment (S-acid) and after calcination at 550°C (S-cal).

contains approx. 47% of polymer template. After template removal with H_2SO_4 the sample S-acid still contains 18% polymer, whereas the mass loss of the sample calcined at 550°C (S-cal) is only 3%. Hence template removal from as-S by acid treatment is not as effective as calcination. A possible explanation for this behavior is that the polymer rests are occluded in the silica matrix and are not accessible to the acid. Figure 6.1 also shows that the decomposition temperature of P123 in acid treated SBA-15, S-acid, (240°C) is slightly higher than that in as-SBA-15, S-as, (205°C). Another finding obtained from the TGA curves is that the content of physisorbed water in S-cal is ca. 3%, but less than 1% in the sample containing a rest of the polymer template. The latter effect can be explained by the hydrophobicity of the polymer groups.

To completely remove the polymer, the acid-treated sample was calcined at 250°C for 3 h in air. The maximum calcination temperature used was 250°C in order to avoid shrinkage during the high-temperature treatment. To check the degree of polymer removal

in the acid treated sample, CHN elemental analysis was performed at BAM (Berlin). In this process the carbon content in the samples S-cal, S-acid, and the acid treated sample after calcination at 250°C for 3 h (S-acid-cal) were analyzed. The outcome of this analysis is presented in Table 6.1. According to these results the acid-treated SBA-15 has the highest carbon content and thus the highest polymer content, but after calcination at 250°C for 3 h the sample loses nearly 97% of the carbon content. However, comparing the carbon contains in the samples calcined at 250°C and 550°C shows that the latter still contains less carbon than the further. Hence, for polymer removal calcination at 550°C is more effective than acid treatment and subsequent calcination at 250°C.

Table 6.1: Characterization of SBA-15 silicas by N_2 adsorption, SAXD and CHN elemental analysis.

sample	a_s/m^2g^{-1}	v_p/cm^3g^{-1}	v_m/cm^3g^{-1}	$(p/p_0)_{pc}$	D/nm	a_0/nm	C wt%
S-cal	947	1.18	0.21	0.743	8.5	11.0	0.04
S-acid-cal	807	1.35	0.12	0.807	10.2	12.5	0.31
S-acid	483	1.0	< 0	0.794	9.8	12.6	9.25

a_s: specific surface area, v_p: pore volume, v_m: micropore volume from t-plots according to the Harkins-Jura equation, $(p/p_0)_{pc}$: pore condensation pressure of nitrogen (77 K), D: pore diameter (imp. KJS, Eq. 2.27, a_0: lattice parameter, C wt%: carbon weight percent.

Nitrogen adsorption measurements corroborate these results. Figure 6.2a shows nitrogen adsorption isotherms in S-cal, S-acid, and , S-acid-cal. A t-plot analysis of these isotherms for determining the micropore volume of the three samples is shown in Fig. 6.2b. The results of this analysis are presented in Table 6.1. It can be seen that the sample calcined at 550°C has the smallest pore diameter (D), which can be attributed to a shrinkage of the matrix during the high-temperature treatment. The pore diameter of this sample is about 1 nm smaller than that of acid treated SBA-15. By contrast, the pore volume (v_p) as well as the specific surface area (a_s) of acid treated SBA-15 sample are much smaller, than the calcined sample because of the polymer content (18%) in the sample. Moreover, calcination of the acid-treated SBA-15 at 250°C for 3 h (S-acid-cal) causes an increase of the pore diameter, the specific area and the pore volume. The pore volume of this sample is even bigger than that of SBA-15 calcined at 550°C (S-cal). The lattice parameter a_0 obtained from SAXD measurements is 11.0 for S-cal, and 12.6 nm for S-acid. From these values and the pore diameter the wall thickness ($w=a_0$-D) can be calculated as 2.5 nm and 2.8 nm, respectively. Thus the wall thickness of S-cal is slightly less than that of S-acid.

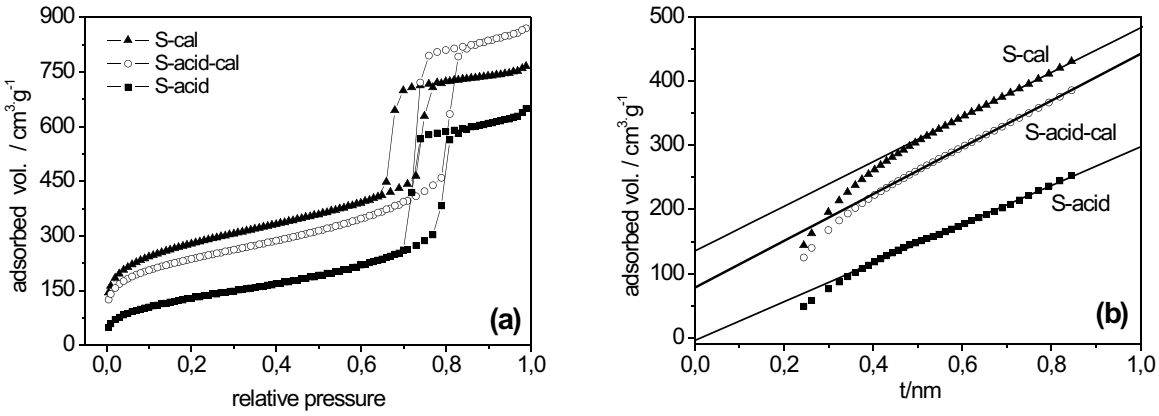

Figure 6.2: Nitrogen adsorption isotherms in three SBA-15 materials: S-cal, S-acid and S-acid-cal (a); t-plots of these three isotherms (b).

The results from CHN elemental analysis could be confirmed by the determination of microporosity by the t-plot method. The data are also included in Table 6.2. In the micropore region, the t-plot for the sample S-cal gives a straight line for values between 0.55 and 0.75 nm, for S-acid-cal between 0.4 and 0.8 nm, and for S-acid between 0.5 and 0.85 nm. As can be seen in Fig. 6.2b, the y-intercept and thus the micropore volume increases when increasing the calcination temperature. This indicates that the micropore volume is related to the amount of polymer left in the materials. Namely, the higher the polymer content the smaller is the micropore volume. This trend can be attributed to the fact that the microporosity of calcined samples is due to the removal of polymer from narrow pores in the matrix, so that these pores become available for gas adsorption.

Figure 6.3 shows SAXD spectra of four samples: as-S, S-cal, S-acid and S-acid-cal. Differences in the relative peak intensities are observed in the four samples. For example, in polymer-filled sample (as-S) the (20) peak is higher than the (11) peak, and the (30) peak is hardly observable. After acid treatment (S-acid) and after its calcination at 250°C (S-acid-cal) the (11) peak is higher than (20) peak. The relative peak intensities of these two samples are similar except for the (30) peak. Its intensity in sample S-acid-cal is weaker than in the sample only treated with acid (S-acid). The peak intensities of the sample S-cal appear to be higher than those of the other samples, presumably because of its lower Porod scattering. For this sample the intensity of the (20) and (30) peaks starts to increase again relative to those of the acid-treated materials.

In conclusion, the template removal studies with 'pure' SBA-15 materials show that template removal by treatment with 48 wt.% H_2SO_4 followed by a mild calcination at 250°C is an alternative method to direct calcination at 550°C. SBA-15 materials obtained

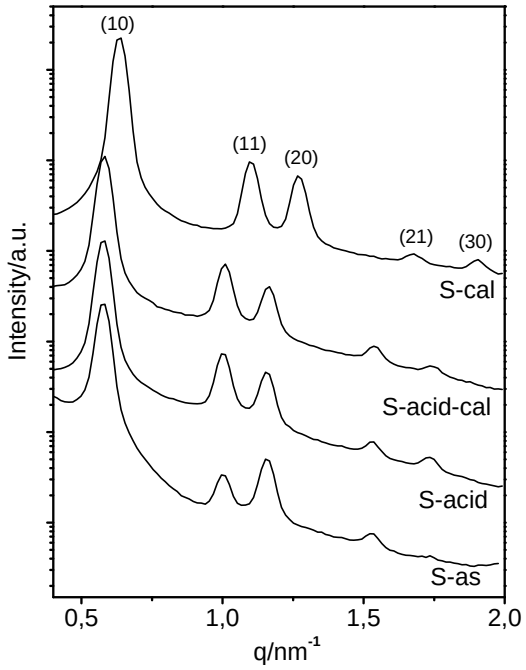

Figure 6.3: SAXD spectra of four samples: as-S, S-cal, S-acid and S-acid-cal. The spectra are shifted against each other.

in this way have larger pore sizes and pore volumes than the respective SBA-15 calcined at 550°C. Moreover, a small fraction of the polymer template remains which reduces the micropore volume and thus the specific surface area of porous sample. With regard to catalytic applications of the materials this is an undesirable situation. On the other hand, a polymer coated silica surface can have some advantages too. For example, nitrogen adsorption measurements of SBA-15 samples kept in air have shown that samples containing some polymer are less affected by aging than samples calcined at 550°C. The changes of relative peak intensities in the SAXD spectra are most probably related to the polymer content in the pore channels. The different amounts of polymer can be considered as organic films of different thickness at the pore walls. A determination of the film thickness from the SAXD profiles is possible on the basis of appropriate models of the electron density in the unit cell [74].

6.2 Carboxylic acid functionalization

SBA-15 functionalized with carboxylic (propionic) acid materials were synthesized according to a prescription by Yang et al. [71]. The polymer filled CN-SBA-15 materials were examined by TGA measurements and compared with as-synthesized SBA-15 (see Figure 6.4). The TGA curves of the CN-SBA-15 materials show two exothermic decomposition steps at 185°C and ca. 330 °C which are attributed to the block copolymer template P123 and cyanoethyl groups, respectively. Hence the decomposition temperature of P123 in as-SBA-15 is slightly higher (about 20 °C) than in CN-SBA-15. As seen in Fig. 6.4 the 20-CN material exhibits a weight loss of about 40%, whereas the content of the organic material in the 10-CN and as-SBA-15 leads to a weight loss of approx. 50%. Hence, the amount of P123 in 20-CN is lower than in the two latter silica materials.

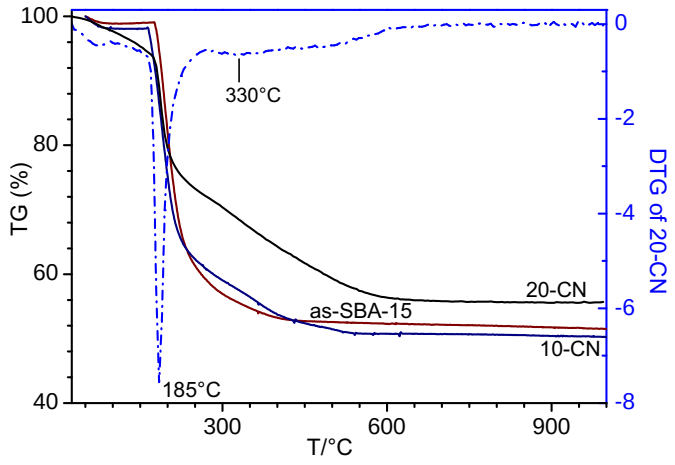

Figure 6.4: TGA analysis of as-synthesized SBA-15, 10-CN and 20-CN. The DTG curve of 20-CN is shown by the dashed-dotted curve.

6.2.1 Morphology, structure and porosity

The structure and porosity of the carboxylic acid-containing SBA-15 materials was characterized by SEM, SAXD, and N_2 adsorption measurements.

The SEM images (Figure 6.5a and Fig. 6.5b) reveal that the acid-containing SBA-15 material consists of worm-like bent particles of hexagonal cross-section which seem to stick together. Moreover, the images indicate that the outer surface of the particles is not

smooth but exhibits of hairy structures which make the contour of the particles diffuse. In image (c) the arrangement of individual pores which run parallel each other is visible. The direction of the view is perpendicular to the pore axes.

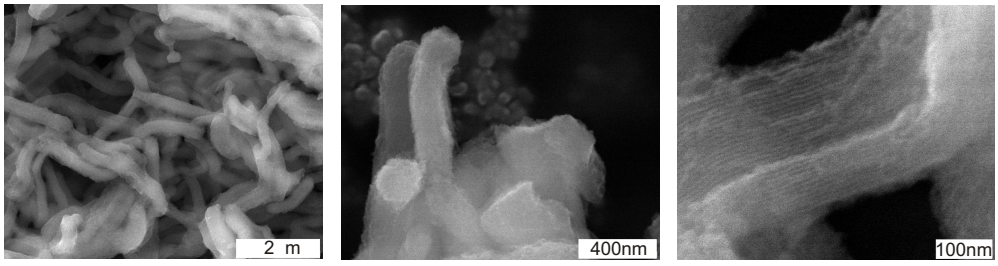

Figure 6.5: SEM images of 20-CA in different magnifications. At the magnification of 100 nm the parallel ordered mesopores appear.

Nitrogen adsorption isotherms and SAXD profiles of 10-CA and 20-CA are shown in Figure 6.6 together with the data of pure SBA-15.

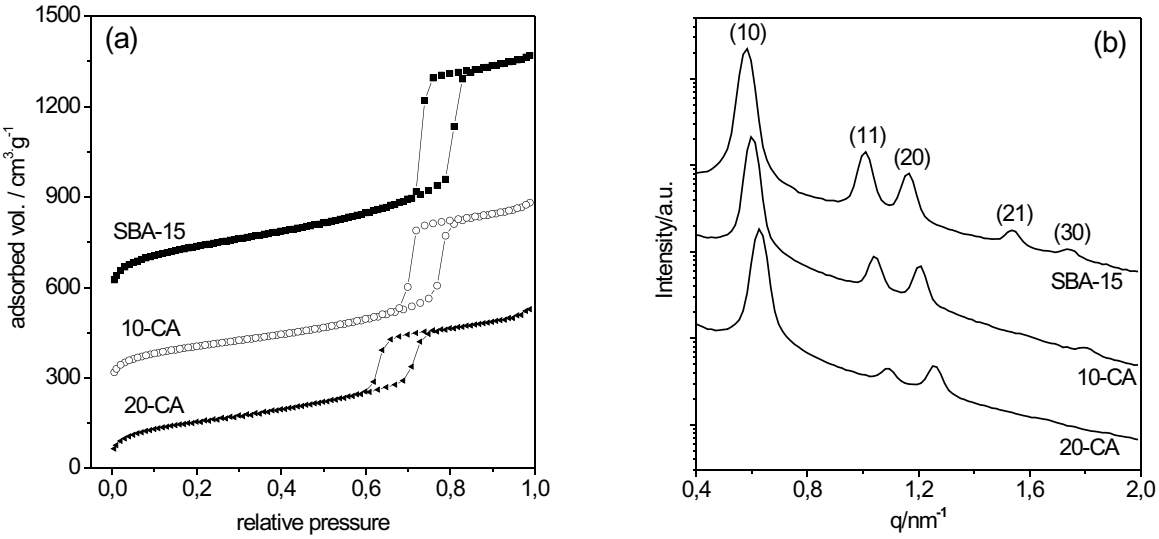

Figure 6.6: Nitrogen adsorption isotherms (a) and SAXS spectra (b) of SBA-15 (S-acid-cal), 10-CA calcined at 250°C for 3h, and of 20-CA. Isotherms and SAXD spectra are shifted against each other for clarity.

The measured typ IV adsorption isotherms of CA-SBA-15 materials show sharp pore condensation steps with H1 type hysteresis loops corresponding to the filling of the ordered mesopores. The pore size distribution is calculated from the adsorption branch according to the imp. KJS equation (Eq. 2.27 in Section 2.6).

Table 6.2: Properties of pure and carboxylic acid functionalized SBA-15.

sample	a_s/m^2g^{-1}	v_p/cm^3g^{-1}	v_m/cm^3g^{-1}	$(p/p_0)_{pc}$	D/nm	a_0/nm	w/nm
SBA-15†	807	1.35	0.10	0.807	10.2	12.5	2.3
10-CA‡	544	0.98	0.02	0.778	9.4	12.1	2.7
20-CA	533	0.82	0.01	0.716	8.0	11.4	3.4

†S-acid-cal, template removal by sulfuric-acid treatment followed by the calcination at 250°C for 3 h; ‡sample is calcined at 250°C for 3 h; a_s: specific surface area, v_p: pore volume, v_m: micropore volume, $(p/p_0)_{pc}$: pore condensation pressure of nitrogen, D: pore diameter, a_0: lattice parameter.

Physicochemical properties of pure and carboxylic acid-functionalized silica are summarized in Table 6.2. It can be seen that the average pore diameter, the pore volume and the pore area all decrease when the molar percentage (ϕ) of functional reagent (CTES) in the synthesis mixture is gradually increased. Also SAXD spectra show peaks which can be assigned to a 2D hexagonal ordered pore system. The cell parameter is also decreases when increasing the percentage ϕ of functional reagent, whereas the wall thickness increases. The smaller pore diameter and the lower amounts of P123 used in the synthesis of 20-CA materials suggest a smaller aggregation number of P123 in the formation of 20-CN compared to that for pure as-SBA-15. In the SAXD spectra of the three samples (Fig. 6.6b) the relative intensities of the Bragg peaks are different. We think that, this can be attributed to the different amount of organic material present inside the pore channels.

6.2.2 Polymer removal and microporosity

The removal of the template P123 by treatment with sulfuric acid was monitored by ^{13}C NMR and TGA measurements. The ^{13}C CPMAS NMR spectra are shown in Figure 6.7. The spectra of materials before acid treatment contain lines attributed to P123 (71, 74, 76 and 18 ppm) and the cyanoethyl groups (122 and 18 ppm). The appearance of the small peaks at 122 and 39 ppm indicates that some of the -CN groups have already been hydrolyzed to COOH groups before the acid treatment. In the ^{13}C CPMAS NMR spectra of acid treated samples three resonance lines assigned to the $(CH_2)_2$-COOH groups (at 179, 27 and 5 ppm) are dominating. Whereas the spectrum of 20-CA indicates complete removal of the polymer template, the spectrum of 10-CA exhibits small lines stemming from remaining EO chains of P123 despite calcination at 250°C. As discussed in Section 6.1, due to the low accessibility of the EO chains in the silica matrix for sulfuric acid, acid-treated SBA-15 still contains ca. 20% of P123 template. Thus the ^{13}C NMR results

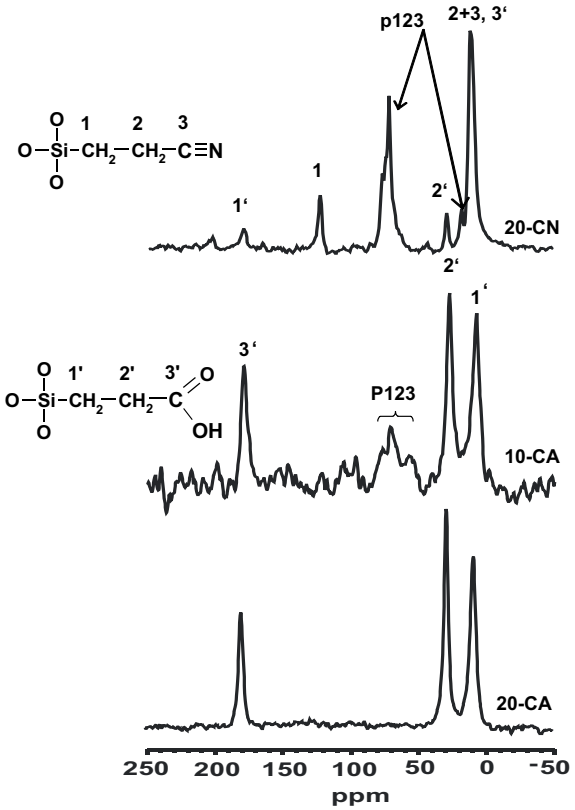

Figure 6.7: ^{13}C CPMAS NMR of the samples 20-CN, 10-CA (after calcination at 250°C for 3 h), and 20-CA.

suggest that by increasing the proportion of functional reagent ϕ in the synthesis mixture the accessibility of EO chains of the polymer for sulfonic acid is increased. Presumably in 20-CN materials the EO chains are either not incorporated or weakly bonded in the silica matrix.

TGA/DTA measurements confirm the results of the ^{13}C CPMAS NMR experiments: TGA curves of 10-CA and 20-CA materials both show that the CH_2-CH_2-COOH surface functional groups decompose at about 350°C and 450° (Figure 6.8). However, the peak at 350°C is not always observable and is rather obscured by the broad peak at 420-450°C. In the case of 10-CA a further peak at ca. 235°C appears which can be assigned to the remaining polymer in the silica matrix. This behavior is consistent with the microporosity analysis of the materials by the t-plot method. t-Plots of the nitrogen adsorption in SBA-15, 10-CA and 20-CA are displayed in Figure 6.9 and the resulting data are included in Table 6.2. From this analysis one concludes that only mesopores and nearly no micropores exists in all the CA-SBA-15 samples after acid treatment. The t-plots were obtained

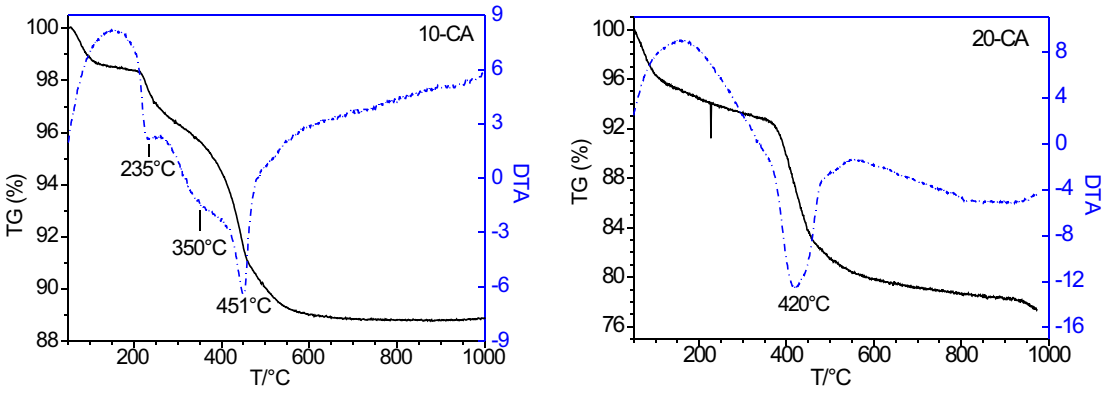

Figure 6.8: TGA and DTA measurements of the samples 10-CA and 20-CA.

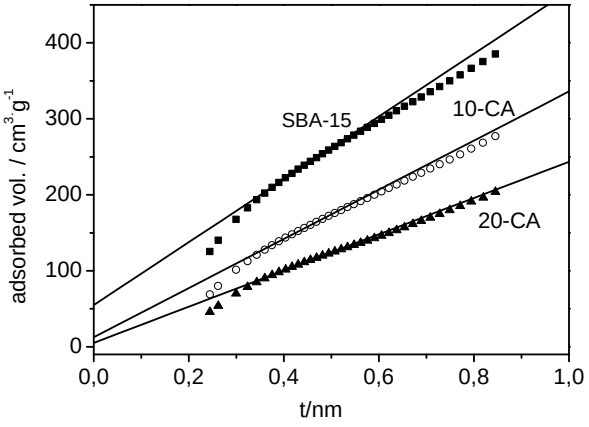

Figure 6.9: Nitrogen t-plots of samples SBA-15-cal250, 10-CA-cal250 and 20-CA.

in the micropore region from t= 0.36 nm to t=0.5 nm. As seen in Fig. 6.9, in spite of small polymer content still remaining in the matrix, the y-intercept of SBA-15 sample has the highest value, indicating that the sample has the highest microporosity. The micropore volume of 10-CA is three times higher than that of 20-CA. This shows that the micropore volume is related to the amount of polymer left in the silica materials after the acid treatment, which is in turn affected by the molar ratio of functional group ϕ present in the synthesis mixture.

6.2.3 Reaction yield and the degree of the functionalization

The degree of acid functionalization of SBA-15 materials synthesized by co-condensation method was studied by TGA/DTA and ^{29}Si NMR measurements, and potentiometric titrations. Under the synthesis conditions the sample 10-CA (with ϕ=10) released about 1.38 mmol functional silane (F) per g SiO_2 while a loss of 1.66 mmol of F/g SiO_2 is expected. For the sample 20-CA (with ϕ=20) a weight loss of 2.79 mmol F/g SiO_2 was measured, while a loss of 3.66 mmol F/g is expected. Thus, both values indicate a high degree (ca. 80%) of carboxylic acid groups incorporated in these samples (see Table 6.3).

The extent of functional silane incorporation in the mesoporous materials was also monitored by ^{29}Si NMR. Figure 6.10 shows ^{29}Si MAS NMR spectra of materials containing different amount of functional groups. The analysis of such spectra of functionalized silica materials is explained in Section 2.4.

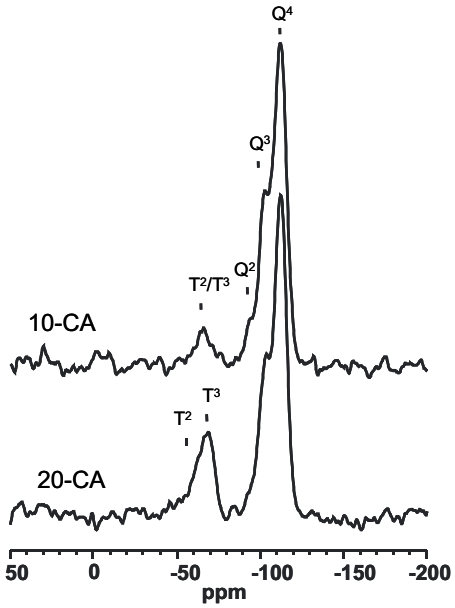

Figure 6.10: ^{29}Si MAS NMR spectra of 10-CA and 20-CA.

The spectra of acid-treated materials in Fig. 6.10 indicate that an increase in the concentration of functional silane (ϕ) in the initial mixture yields increasing the amount of $(CH_2)_2$-COOH groups in the silica wall. The relative integrated intensities of siloxane (Q^n) and organosiloxane (T^m) NMR signals (T^m/Q^n) (Equation 2.9) allow a quantitative assessment of the degree of functionalization of the silica. Table 6.3 shows the data for the individual peaks normalized to the Q^4 peak and adjusted to the ratios of the integrals of the T and Q regions.

Table 6.3: Expected quantities and the corresponding experimental values obtained from ^{29}Si NMR, TGA/DTA and potentiometric titration.

	expected		NMR			TGA		titration	
sample	(T/Q)	n	x	(T/Q)	Y	n	Y	n	Y
10-CA	0.11	1.66	20%	0.08	75%	1.38	82%		
20-CA	0.25	3.32	42%	0.21	83%	2.79	84%	2.53	76%

(T/Q): Expected and experimental ratio of organosiloxane (T) and siloxane (Q) groups; n: Expected and experimental amount of functional silane per unit mass of SiO_2 (in mmol g^{-1}); x: Degree of surface functionalization; Y: Reaction yield.

Hence in the case of 10-CA 20% of the surface groups (-OH and $(CH_2)_2$-COOH) are carboxylic acid groups, whereas in the case of of 20-CA the respective percentage is 42%. Moreover the reaction yield of the incorporation of carboxylic acid groups for 10-CA and 20-CA is 75% and 83%, respectively. Hence, within the error margin these values are in good agreement with those determined from solid-state NMR.

The functionalization degree of the 20-CA sample is also determined by potentiometric titration (for experimental detail see Section 4.2). Although the resulting amount of functional silane in the sample and reaction yield are lower (see Table 6.6), within the error margin these values are consistent with those obtained from NMR and TGA/TDA measurements.

6.2.4 Water stability of CA-SBA-15 materials

Water stability is an important issue in many potential applications of porous materials. For testing water stability the 20-CA-SBA-15 materials were exposed to water at ambient temperature for 4 h, 6 h and 30 d. The effect of the water exposure on the structural ordering of the material was monitored by nitrogen adsorption and SAXD measurements (see Figure 6.11). No changes in the SAXD spectra before and after water treatment were observed, indicating that no degradation of 20-CA occurs during this long-term exposure. As shown in the inlet of Fig. 6.11a, no observable shrinkage of material occurs. In Figure 6.11b nitrogen adsorption isotherms of the same materials are shown. The values of the pore diameter, specific surface area and specific pore volume derived from these isotherms are given in Table 6.4. The adsorption isotherms confirm the result that the pore structure of the 20-CA silica materials is not affected by the treatment of the materials with water. Also the pore diameter is not significantly changed, but the pore volume of the 20-CA

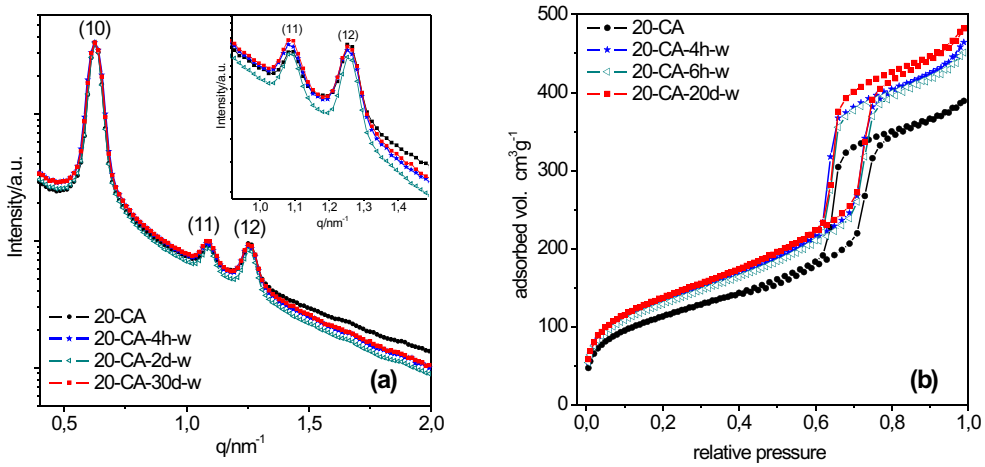

Figure 6.11: (a) SAXD profiles and nitrogen adsorption isotherms (b) for 20-CA before and after water exposure for different periods of time.

material increases with the exposure to water. This effect may be caused by the ability of water to remove some constrictions such as residual polymer in the pore system so that formerly blocked parts of the pore volume are becoming accessible. The increase of the specific surface area after water exposure can also be explained satisfactorily via this interpretation.

Table 6.4: Properties of 20-CA before and after the water exposure for different periods of time derived from the nitrogen adsorption isotherms of Fig. 6.11b.

sample	a_s/m^2g^{-1}	v_p/cm^3g^{-1}	D/nm
20-CA	400	0.60	8.1
20-CA-4h-w	470	0.72	8.1
20-CA-6h-w	462	0.70	8.2
20-CA-30d-w	489	0.75	8.2

a_s: specific surface area, $(p/p_0)_{pc}$: pore condensation pressure of nitrogen D: pore diameter (imp. KJS).

6.3 Sulfonic acid functionalization

In this section a simple one-step procedure is presented for the synthesis of sulfonic acid functionalized SBA-15 based on the co-condensation of TEOS and 3-(trihydroxysilyl)-1-propane-sulfonic acid (STHS) in the presence of block copolymers under acidic condi-

tions. For optimizing the degree of the surface functionalization of the pore walls and the yield of the synthesis, several parameter were varied, such as the functional silane/TEOS molar ratio in the synthesis mixture (ϕ), delay time for prehydrolyzing (prehydrolysis time) and prehydrolyzed component. Notice that in case of STHS, the term 'hydrolysis' is not really appropriate because STHS is already in hydrolyzed state and does not posses alkoxy-moieties to hydrolyze. Rather, we are dealing with precondensation of the functional silane. For the sake of a uniform notation the term will nevertheless be used.

6.3.1 Study of template content

As a first step of the characterization of sulfonic acid functionalized SBA-15 (SA-SBA-15), the polymer content before acid removal was studied by TGA measurements. TGA curves of polymer-containing samples synthesized with different amount of functional group are displayed in Figure 6.12.

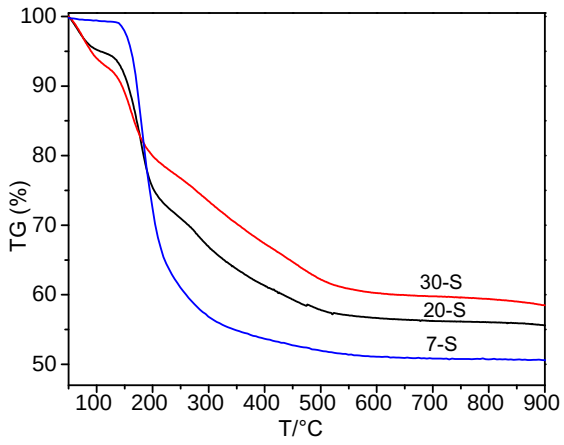

Figure 6.12: TGA curves of three sulfonic-acid-containing samples before polymer removal: 30-S: 30-S-1480-F, 20-F: 20-S-00, 7-S: 7-S-60-F.

The graph shows that the content of organic component decreases when increasing the amount of functional silane ϕ in the synthesis. The weight loss of 48% for 7-S which is similar to the polymer content in as-SBA-15 (see Section 6.1), decreases to 39% for 20-S and to 32% for 30-SA. Moreover, for the samples with ϕ= 20 and 30 a second step in the TGA curve appears, which gets higher when raising the percentage ϕ of functional reagent. According to the height of this second step, the sample 30-S contains approximately 20% of sulfonic acid, and the sample 20-S contains ca. 17% of sulfonic acid

groups. This observation shows that the P123 content decreases when increasing ϕ in the synthesis mixture. In fact, 20-S-60-F contains ca. 30 % P123 whereas 30-S-1480-F contains only 12% P123. This in turn suggests, as in case of CN-SBA-15, a smaller number of monomers in the micelles of P123.

6.3.2 Morphology, structure and porosity

The mesoscopic order of the materials was studied by nitrogen adsorption, SAXD and scanning electron microscopy (SEM). Figure 6.13 shows SEM images of different sulfonic acid functionalized SBA-15 materials prepared by premixing the functional reagent. The images reveal that the silica particles have long bent worm-like character which is typical for SBA-15 materials in which ϕ is small. When ϕ is increased the particles become shorter and more curved. The SEM image of the 30-SA-1480-F sample reveals that this sample has almost no order which is most likely due to the high percentage of functional silane ϕ in the initial synthesis mixture. These results are consistent with nitrogen

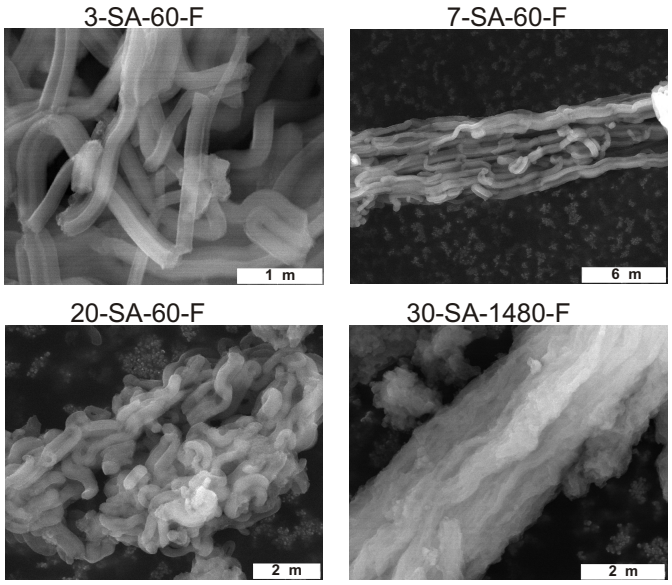

Figure 6.13: SEM images of sulfonic acid functionalized SBA-15 prepared by prehydrolysis of the functional reagent.

adsorption isotherms and SAXD profiles of these samples, which are displayed in Figure 6.14. They show that neither the order of the materials nor their pore diameter is changed significantly by increasing ϕ up to 20. Only when ϕ is increased to 30, the order of the material deteriorates. Here the pore condensation is smeared out and the SAXD curve does not show any higher peaks. The adsorption isotherms indicate that the increase of

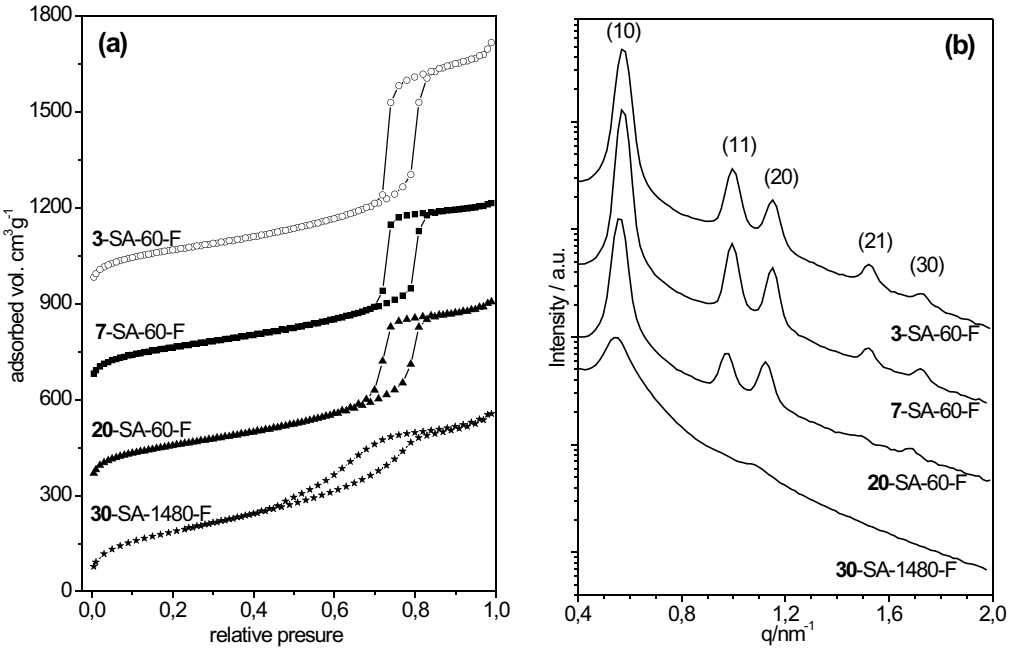

Figure 6.14: Nitrogen adsorption isotherms (a) and SAXD spectra (b) of sulfonic acid functionalized SBA-15 materials prepared by premixing the functional reagent. The isotherms and the SAXD profiles are shifted against each other.

ϕ causes a decrease of the steepness of the isotherms which in turn indicates a broader pore size distribution and thus less order. The SAXD measurements indicate that the acid treatment causes no shrinkage of the matrix. In some cases even a slight increase of the lattice constant is observed after acid treatment. Thus acid treatment can cause an expansion of the silica matrix whereas calcination at temperatures higher than 250°C induce a contraction. The results derived from nitrogen adsorption and SAXD measurements are summarized in Table 6.5. The results indicate an increase of the lattice constant and wall thickness when increasing the molar percentage of functional reagent ϕ to 20 and 30. This is very different from CA-SBA-15 materials, where the lattice constant decreases when increasing ϕ. The relative intensities of the individual Bragg reflexes are changing with the content of functional silane, as it was found for the CA-SBA-15 samples. In particular the (11), (20) and (21) peaks undergo strong changes. These can be explained when the results of Si-NMR are considered, which will occur in Section 6.3.3. In order to check whether the properties of the materials or the yield of the synthesis depend on the prehydrolysis of one of the silica sources two further samples were prepared. 20-SA-00 synthesized with no prehydrolysis time, i.e., TEOS and functional silane were added at the same time, and 20-SA-55-T where TEOS was the prehydrolyzed component. The SEM

Table 6.5: Properties of pure and sulfonic acid functionalized SBA-15 silica.

sample	a_s/m^2g^{-1}	v_p/cm^3g^{-1}	v_m/cm^3g^{-1}	$(p/p_0)_{pc}$	D/nm	a_0/nm	w/nm
3-SA-60-F	579	1.26	0.02	0.799	10.0	12.6	2.6
7-SA-60-F	572	0.92	0.05	0.800	10.0	12.6	2.6
20-SA-60-F	577	1.01	0.02	0.784	9.6	12.9	3.3
30-SA-1480-F	672	0.86	0	0.765	9.1	13.4	4.3
20-SA-00	564	0.93	0.02	0.791	9.7	13.0	3.3
20-SA-55-T	419	0.72	0.03	0.797	9.9	12.8	2.9
SBA-15cal550	561	0.89	0.10	0.757	8.9	11.5	2.6
SBA-15cal250	807	1.35	0.11	0.807	10.2	12.8	2.6

a_s: specific surface area, v_p: pore volume, v_m: micropore volume, $(p/p_0)_{pc}$: pore condensation pressure of nitrogen, D: pore diameter, a_0: lattice parameter.

images of the samples 20-SA-00 and 20-SA-55-T in Figure 6.15 show the typical worm-like habitus of SBA-15 materials. The samples are hexagonally ordered, and the length of worms is short in comparison to pure SBA-15. The nitrogen adsorption isotherms and

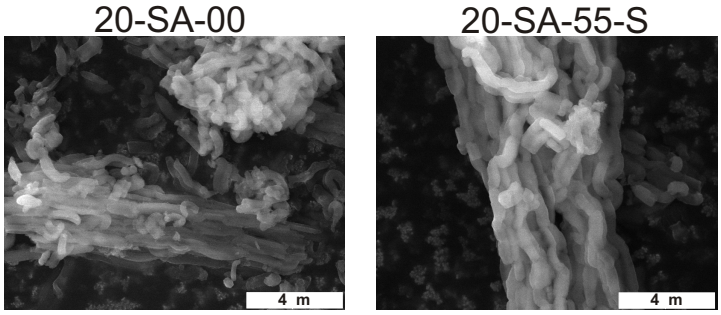

Figure 6.15: SEM images of sulfonic acid functionalized SBA-15 prepared by premixing the functional reagent.

SAXD profiles of these two samples are displayed in Figure 6.16 together with 20-SA-60-F, and the resulting data are included in Table 6.5. All isotherms are of type IV with an H1 type hysteresis loop, as is typical for well-ordered SBA-15 silicas. The isotherms reveal materials with similar pore sizes and pore size distributions independent from pre-hydrolyzed silica source (STHS or TEOS). The isotherms of 20-SA-60-F (prehydrolyzed component is functional silane (F)) and 20-SA-00 (no prehydrolyzed component, TEOS and F added simultaneously) indicate similar pore volume and specific surface area, but

these parameter are larger than for 20-SA-55-T (prehydrolyzed component is TEOS, (T)) (Table 6.5). SAXD profiles corroborate these behavior: The three samples have similar

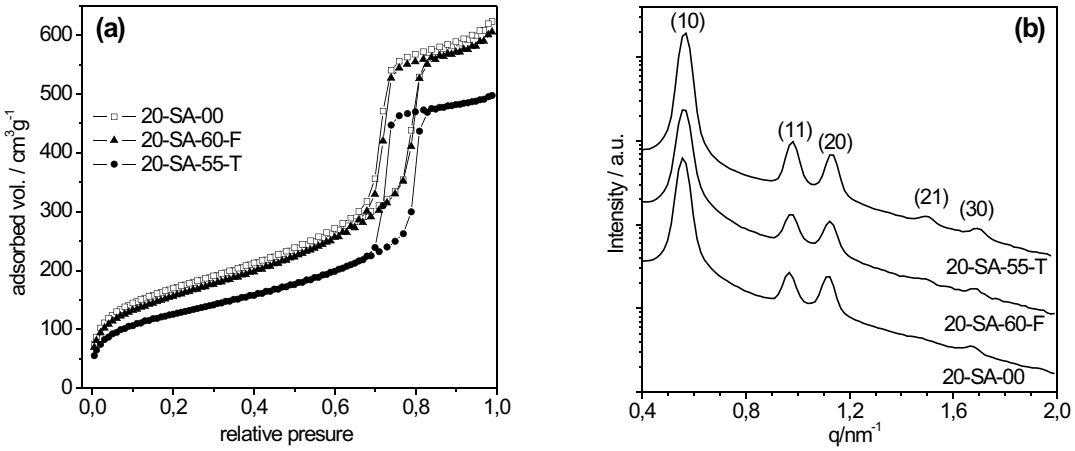

Figure 6.16: Nitrogen adsorption isotherms (a) and SAXD spectra (b) of sulfonic acid functionalized SBA-15 prepared by variation the prehydrolyzed component: 20-SA-55-T (TEOS prehydrolyzed), 20-SA-60-F (STHS prehydrolyzed), 20-SA-00 (STHS and TEOS added simultaneously); SAXD spectra are shifted against each other.

pore diameters, but the lattice constant and the wall thickness of the samples 20-SA-60-F and 20-SA-00 are somewhat larger than that of 20-SA-55-T. The relative Bragg peak intensities are also different in three samples. Closer inspection shows that the intensities of the (11) and (21) peak decrease in the order 20-SA-55-T $>$ 20-SA-60-F $>$ 20-SA-00 whereas the intensity of the (20) peak increase in that sequence. These changes of the relative intensities of the Bragg peaks correlate with the degree of surface coverage of SBA-15 by functional groups as determined by ^{29} Si MAS NMR measurements. This is explained in the following section.

6.3.3 Reaction yield and the degree of functionalization

Quantitative determinations of the content of functional groups after removal of the block copolymer were performed with TGA/DTA and ^{29}Si MAS NMR measurements. ^{29}Si MAS NMR spectra of samples synthesized by 'precondensation' of the functional silane (STHS) are shown in Figure 6.17a. They indicate that an increase of functional reagent concentration ϕ in the initial mixture yields increasing amounts of organo-functionalized moieties in the silica wall. A gradual increase in the intensities of organosiloxane T^m is readily observed. The relative integrated intensities of the siloxane (Q^n) and organosilox-

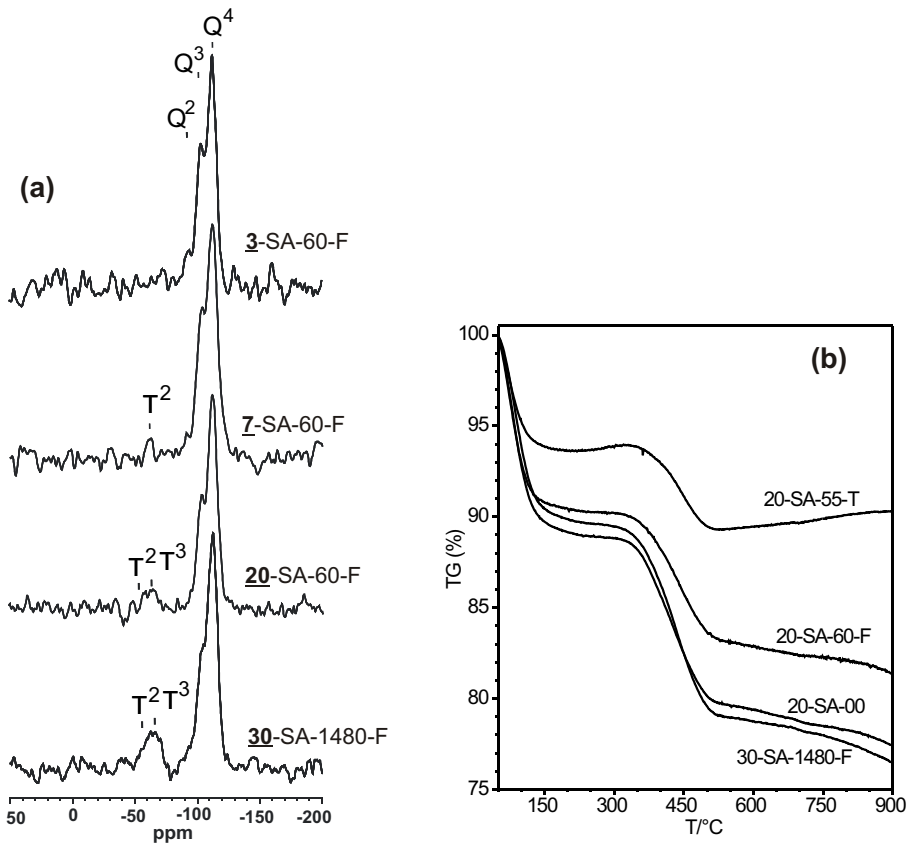

Figure 6.17: (a) ^{29}Si MAS NMR spectra of four SA-SBA-15 materials with increasing molar ratios of functional reagent ϕ; (b) TGA curves of four different SA-SBA-15 samples.

ane (T^m) NMR signals (T^m/Q^n) allow a quantitative assessment of the incorporation degree of the organic moiety. The calculated yields of the synthesis presented in Table 6.6 show that less than 50% functional silane applied in the initial synthesis mixture was incorporated into the silica. Quantitative integration of the T^m signals was not possible for the samples 3-SA-60-F and 7-SA-60-F for which only small proportion of functional reagent were used in the synthesis. A comparison of the reaction yields of 30-SA-1480-F (37%) and its pre-stage 30-S-1480-F (33%) shown in Table 6.6 reveals that this low yield is not caused by washing out of the functional groups during the acid treatment, but has already occurred before acid treatment. According to the ^{29}Si MAS NMR results, the degree of surface coverage increases when increasing the portion of functional reagent in the synthesis, where it is used as prehydrolyzed component. However, the order of the materials is lost when applying 30 mol% functional silane.

The extent of incorporation of functional silane into the silica matrix was also mon-

Table 6.6: Expected quantities and the corresponding experimental values obtained from ^{29}Si NMR, TGA/DTA and potentiometric titration.

	expected		NMR			TGA		titration	
sample	(T/Q)	n	x	(T/Q)	Y	n	Y	n	Y
20-SA-60-F	0.25	3.32	25%	0.09	37%	0.95	28%	0.69	21%
30-S-1480-F	0.43	4.98	33%	0.14	33%				
30-SA-1480-F	0.43	4.98	37%	0.16	37%	1.18	24%		
20-SA-00	0.25	3.32	31%	0.12	46%	1.10	33%	1.13	34%
20-SA-55-T	0.25	3.32	16%	0.06	25%	0.42	13%		

(T/Q): Expected and experimental ratio of organosiloxane (T) and siloxane (Q) groups; n: Expected and experimental amount of functional silane per unit mass of SiO_2 (in mmol g^{-1}); x: Degree of surface functionalization; Y: Reaction yield.

itored by TGA/DTA measurements. The amount of sulfonic acid contained in different samples was calculated from the TGA curves displayed in Fig. 6.17b. The results including the resulting reaction yields are summarized in Table 6.6. More details about the TGA/DTA measurements will be discussed in Section 6.3.4. As can bee seen in Table 6.6, for all samples TGA/TDA gives smaller yields than ^{29}Si-MAS-NMR measurements.

A further method used for the determination of the extent of incorporation of functional silane into the silica matrix was potentiometric titration. The samples 20-SA-00 and 20-SA-60-F were titrated against diluted NaOH solution. For experimental details see Section 4.2. The experimental amounts of functional silane and reaction yields determined by potentiometric titration are rather low and similar to those obtained from TGA/TDA measurements (see Table 6.6).

To summarize, for synthesis of ordered SA-SBA-15 materials the highest reaction yields obtained from NMR, TGA and potentiometric titration measurements are 30-40%, 30%, and 20-30%, respectively. Thus, the good agreement of the yields of CA-SBA-15 samples determined from NMR and TGA cannot be observed here. We investigated whether the small yield of the TGA experiments is caused by the sulfur remnants in the matrix after the heating to 1000°C. The presence of sulfur remnants in the matrix would increase its unit mass and decrease the computed yield from TGA. Elemental analysis of the sample 20-SA-00 after heating to 1000°C has shown that no sulfur is present in the silica matrix. Thus, a corruption of TGA measurements by the presence of sulfur residues in the silica matrix can be ruled out. Nevertheless, among the methods applied

the solid-state NMR is the more exact one. The relative error caused by the integration of the resonance peaks is about 5-10%. In case of TGA and potentiometric titration methods repeated measurements have shown that the relative error is about 20%.

The results in Table 6.6 also reveal the effect of the prehydrolysis. In fact the yield is highest when the functional silane (STHS) and TEOS are added simultaneously, and it is lowest when TEOS is prehydrolyzed. Another interesting feature of SA-SBA-15 samples revealed by the TGA measurements is their high water content. According to TGA, the samples release about 10% water which is three times higher than the water content in CA-SBA-15 samples.

By combining the results of Si-NMR presented in Table 6.6 with those from SAXD profiles and nitrogen adsorption isotherms the following results are obtained:

1. It appears that the sulfonic acid reagent (STHS) is not incorporated in the silica matrix in amounts as high as in CA-SBA-15 materials. Even if the percentage of functional silane is increased to ϕ=30 the loading remains low (1.18 mmol g^{-1} SiO_2) and the silica matrix loses its order at this proportion of the functional silane.

2. Samples containing high amounts of sulfonic acid, i.e. 20-SA-60-F, 30-SA-60-F and 20-SA-00, have a larger lattice parameter than samples whose surface coverage are less than 15%. On the other hand, the pore size is not significantly changed when the percentage of functional silane increases. Accordingly, the wall thickness of the samples containing high amounts of sulfonic acid is larger than that of the latter (see Table 6.5). In contrast, Margolese et al. [53] found a gradual decrease of the $d-spacing$ for SBA-15 samples synthesized with higher concentrations of functional reagent [53]. However, in their study mercaptopropyltrimethoxysilane was used as functional silane, and it was possible to incorporate higher amounts of functional silane in the pore walls.

3. The relative intensities of the (11) and (21) Bragg peaks in SAXD profiles (Fig. 6.14b and Fig. 6.16b) decrease and that of the (20) peak increases when surface coverage of SBA-15 by sulfonic acid groups increases. Similar changes of relative peak intensities in SAXD profiles have been observed in $in\text{-}situ$ SAXD gas adsorption measurements in SBA-15 [74], where relative peak intensities change as thickness of the adsorbed film increases in each gas adsorption step. Since the pore diameters of the sulfonic acid functionalized SBA-15 materials are similar, the differences in the relative intensities of the Bragg peaks of the present samples must be related to the thickness of the film formed by the propyl-sulfonic acid on the pore walls.

6.3.4 Polymer removal and microporosity

^{13}C CPMAS NMR spectra of the samples 7-S-60-F, 20-SA-55-T, 20-SA-00 and 30-SA-1480-F are displayed in Figure 6.18a. The polymer containing sample 7-S-60-F shows carbon peaks assigned to P123 at 76, 74, 71 and 18 ppm, and in addition peaks at 12 ppm, 18 ppm and 56 ppm which come from carbon chains of the functional group. However, the peak at 18 ppm (C2) overlaps with the carbon peak stemming from P123. In the spectra of 20-SA-55-T, 20-SA-00 very small peaks assigned to P123 are detectable. In the spectrum of 30-SA-1480-F, however, the peaks attributed to P123 are missing. This resembles the case of CA-SBA-15 materials, namely the higher the molar percentage of the functional silane ϕ in the sample the better the access of sulfuric acid to block copolymer to remove it. Figure 6.18b shows DTG curves of different sulfonic acid containing

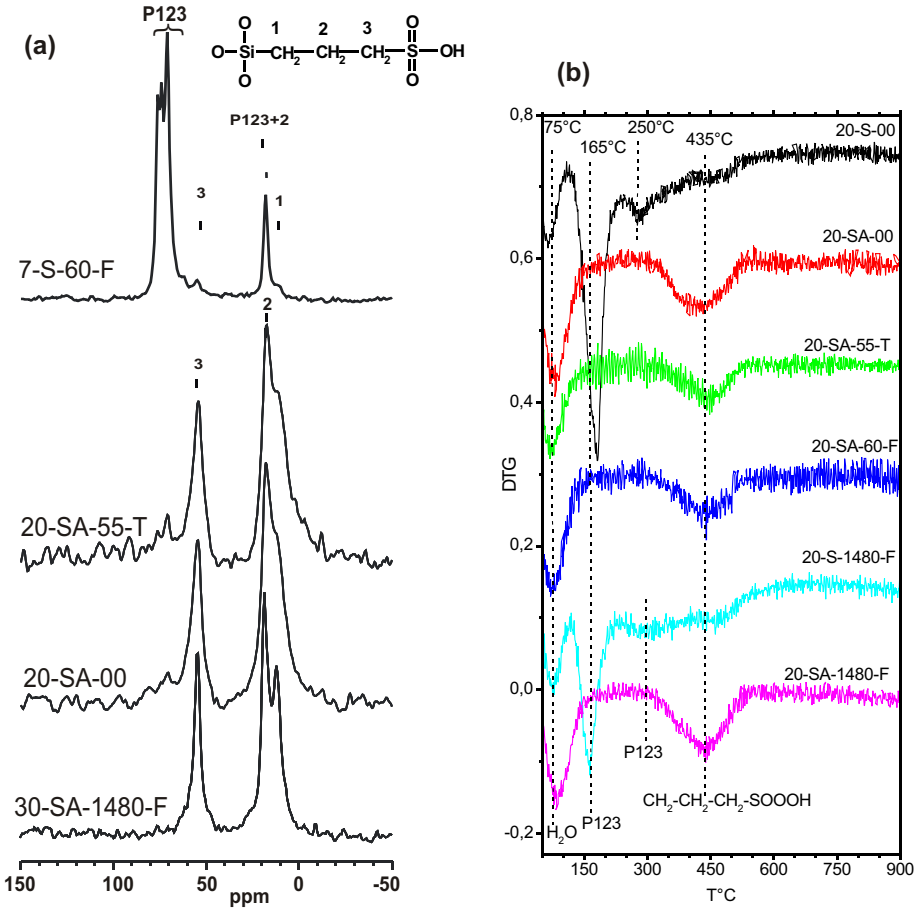

Figure 6.18: (a): ^{13}C CPMAS NMR spectra of the samples 7-S-60-F, 20-SA-55-T, 20-SA-00 and 30-SA-1480-F; (b): DTG curves of different sulfonic acid containing SBA-15 samples.

SBA-15 samples. Here four different peaks are observed: The peak at ca. 75°C results from physically adsorbed water. The peaks at 165°C and 250°C are assigned to P123 and appear only for the samples 20-S-00 and 30-S-1480-F, i.e., samples without H_2SO_4 treatment. The remaining samples which are all treated with sulfuric acid show only the peak at about 435°C attributed to the functional groups. Hence, here one cannot detect the small amount of template after sulfuric acid treatment that was detected by ^{13}C NMR in samples having 20% functional reagent in the synthesis mixture. Therefore, in SA-SBA-15 samples with $\phi \geq 20$ the block copolymer template is almost fully accessible to sulfonic acid, independently of which component (TEOS or STHS) was prehydrolyzed first. This easy access may be due to a weak penetration of the EO chains in the silica matrix. It is well known that during the hydrothermal treatment at higher temperature (ca. 100°C) the EO chains of P123 become more and more hydrophobic. The sulfonic acid head group is a stronger acid and more hydrophilic than carboxylic acid. This difference may lead to a weaker interaction between silica matrix and EO chains of block copolymer. If that is the case it should lead to a low microporosity. To check this conjecture, a t-plot analysis of all sulfonic acid functionalized samples was performed (see Figure 6.19). In the micropore region between t=0.4 and t=0.64 nm, these plots give a straight line.

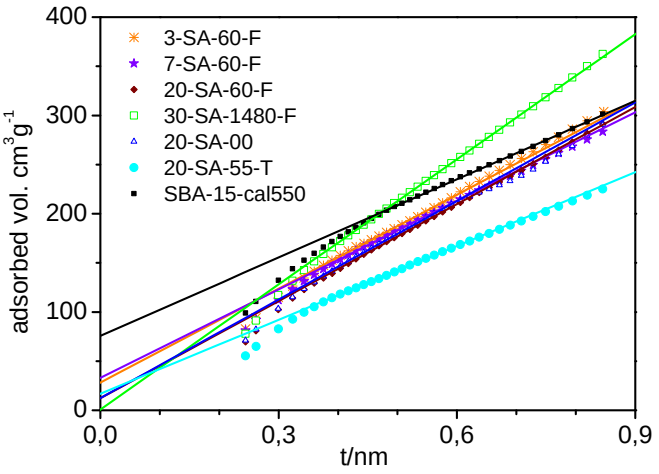

Figure 6.19: t-plot analysis of nitrogen adsorption isotherms for different sulfonic acid functionalized SBA-15 in comparison with native SBA-15 calcined at 550°C.

Figure 6.19 shows that the y-intercepts of all SA-SBA-15 samples are smaller than those of pure SBA-15 calcined at 550°C. This indicates that, similar to CA-SBA-15 ma-

terials, all SA-SBA-15 samples have indeed a much lower microporosity than pure SBA-15. The weakly ordered sample 30-SA-1480-F even has no micropores. The calculated micropore volumes are included in Table 6.5.

In Figure 6.20 the TGA and DTA curves of the samples 20-S-00 (a) and 20-SA-00 (b) are displayed which are typical for all sulfonic acid functionalized SBA-15 samples. For 20-S-00 the TGA curve shows two steps. The corresponding DTA curve indicates an

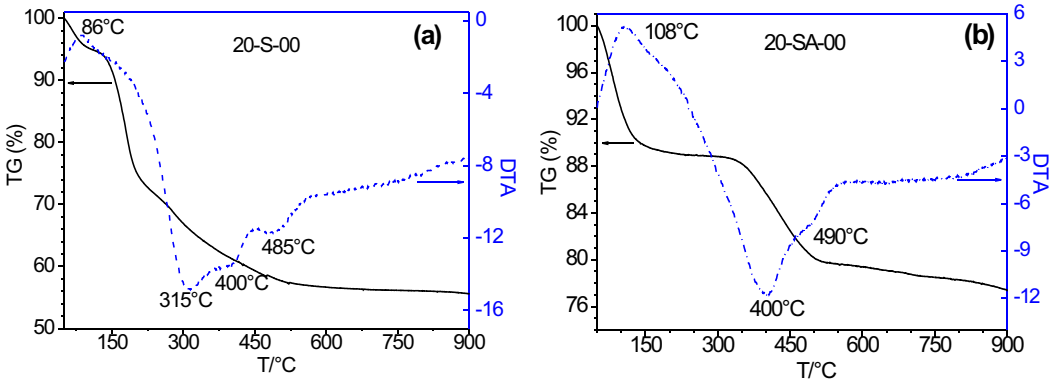

Figure 6.20: Typical TGA-DTA curves of sulfonic acid functionalized SBA-15 before and after acid treatment. The samples presented here are 20-S-00 and 20-SA-00.

exothermic peak at ca. 86°C assigned to the physically adsorbed water inside the pores, followed by three endothermic peaks at 315°C, 400°C and 485°C which can be attributed to the decomposition of organic components (block copolymer and sulfonic acid groups). In contrast, the TGA curve of 20-SA-00 sample (Fig. 6.20b) shows only one step. In the DTA curve the peak at 315°C disappears. Hence, this peak is to be attributed to the degradation of P123, whereas the two residual peaks are to be assigned to the sulfonic acid groups.

6.3.5 The mechanism of the self-assembly

The functional reagent 3-(trihydroxysilyl)-1-propane-sulfonic acid (STHS) has a hydrophobic propyl chain with a polar sulfonic acid head group. However, the propyl chain is probably not sufficiently hydrophobic enough to make the functional silane act as a cosurfactant. A cosurfactant would be preferentially adsorbed close to the hydrophobic PPO portion of the P123 micelles and therefore cause a decrease in the interfacial curvature and thus lead to an increase in the pore diameter or even cause a transformation to a different structure as observed in other systems [55, 75]. However, under the synthesis conditions applied in this work such phenomenon has never been observed but always either

hexagonal ordered, or non-ordered materials were obtained. The pore size of synthesized SA-SBA-15 materials was never larger than that of pure SBA-15 but usually smaller.

The reaction yield achieved in the functionalization of SBA-15 with sulfonic acid (30-40%) is much lower than the reaction yield in the carboxyl acid functionalization of SBA-15 (ca. 80%). In addition, the surface coverage with sulfonic acid is lower than in the case of carboxylic acid: It is between 40 and 50% for 20-CA, but only approx. 30% for 20-SA. By increasing the mol percentage of functional silane ϕ in the synthesis, the surface coverage can be increased up to ca. 40%, but in this case the hexagonal order of SBA-15 gets lost. So 30-S-1480-S/SA does not show a 2D hexagonal order. Most probably the high proportion of functional group in the synthesis mixture decreases the interfacial curvature of P123 micelles leading to a less well-ordered structure. On the

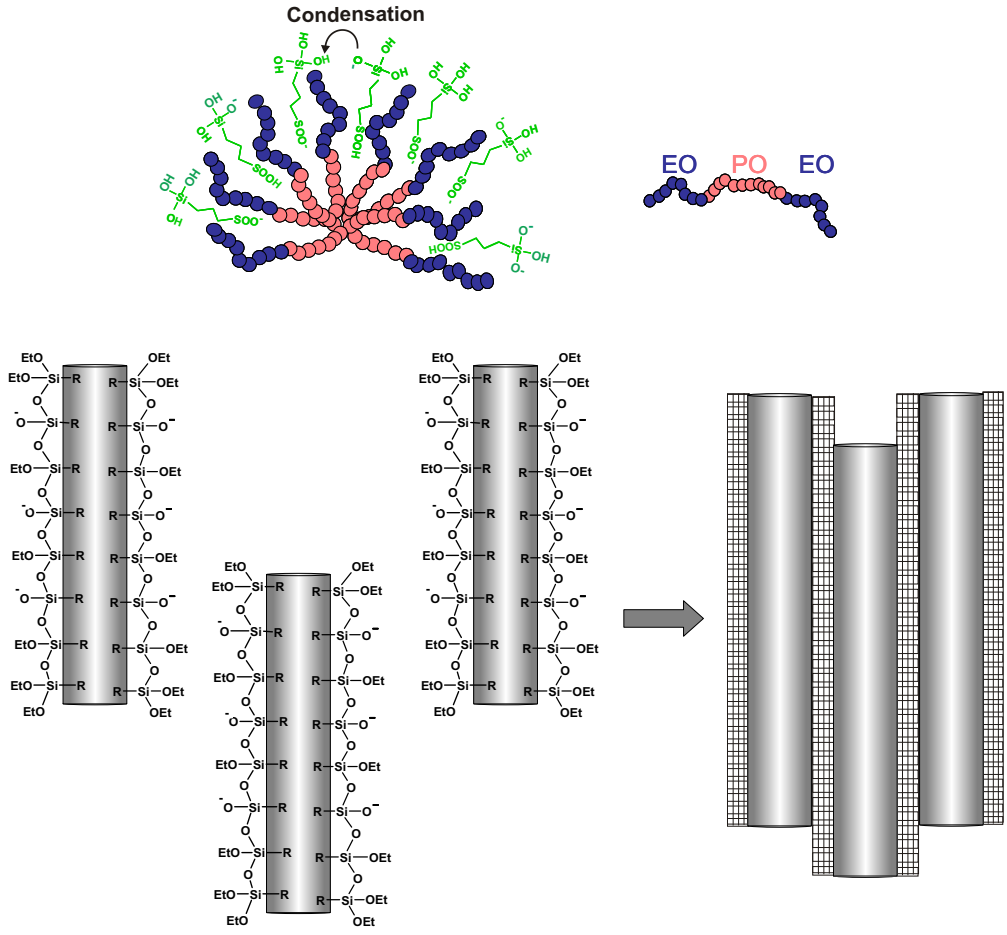

Figure 6.21: Proposed arrangement of functional silane in the periphery of P123 micelles during the formation of sulfonic acid functionalized SBA-15; R=propyl sulfonic acid.

basis of these results, the following formation mechanism is proposed (see Figure 6.21).

As mentioned before, the sulfonic acid reagent we used is rather hydrophilic. Therefore, due to the attractive interaction between the polar propyl-SOOH groups and hydrophilic PEO chains of the block copolymer the trihydroxysilyl groups can uniformly organize on the surface of the micelles and their increased length will assist in the rapid cross-linking/condensation between the micelle-oriented trihydroxysilyl groups, as depicted in Fig. 6.21. The resulting 'side-on' packing of the silicate coated cylindrical micelles will give rise to long rod-like nanoparticles. A similar mechanism was proposed by Cai et al. and Huh et al. in the functionalization of MCM-41 by different functional groups via co-condensation method [76, 77, 50].

In the synthesis of CA-SBA-15, 2D-hexagonal order of SBA-15 can only be obtained if the functional silane is prehydrolyzed. Prehydrolysis of TEOS or simultaneous addition of TEOS and functional silane (CTES) leads to disordered silica materials [71]. On the other hand, the functional silane (STHS) used in the synthesis of SA-SBA-15 has no hydrolytic sensitivity and forms stabile aqueous solutions in the hydrolyzed form. Thus it does not need a prehydrolysis time. For this reason we always obtained 2D-ordered materials with this functional silane, independent of which silica source (TEOS or STHS) was added first. Moreover the highest reaction yield is obtained when sulfonic acid reagent and TEOS are added at the same time. It can probably be explained by the slow condensation rate of the hydroxyl groups of the highly acidic functional silane. Very likely the functional silane organizes uniformly at the surface of P123 micelles due to the attractive interactions, and its condensation is enhanced by the hydrolysis and condensation of TEOS.

6.4 Phosphonic acid functionalization

In this section the synthesis of phosphonic acid functionalized SBA-15 silica materials by the co-condensation method is presented. Diethoxyphosphorylethyltriethoxysilane (PTES) was used as the functional reagent. The synthesis of such materials was reported already by Corriu et al. [78], but these authors used different reaction conditions than presented here. Specifically, they used NaF as an additional reaction component. Fluoride ions are a well-known catalysts for the hydrolysis and polymerization of silica species and have been employed in the synthesis of mesoporous silica materials under various conditions in order to improve structural order [38]. Corriu et al. prepared phosphonic acid functionalized materials with a constant mol percentage of ϕ = F/(F+T) = 9.9 in the starting mixture. In the present work, phosphonate ester containing SBA-15 materials

with different molar composition of ϕ were synthesized. Free phosphonic acid functionalities could then be formed by dealkylation of these phosphonate ester groups through refluxing the samples in concentrated HCl. Additionally, the effect of prehydrolysis was investigated, when either functional silane or TEOS was added first, or both components were added simultaneously. Results of this study are presented in this section.

6.4.1 Morphology, structure and porosity

As with the CA-SBA-15 and SA-SBA-15 materials, the mesoscopic order and morphology of phosphonic acid containing SBA-15 samples were investigated by SEM, SAXD and nitrogen adsorption. SEM images of the samples 10-P-60-F and 10-POEt-60-F (phos-

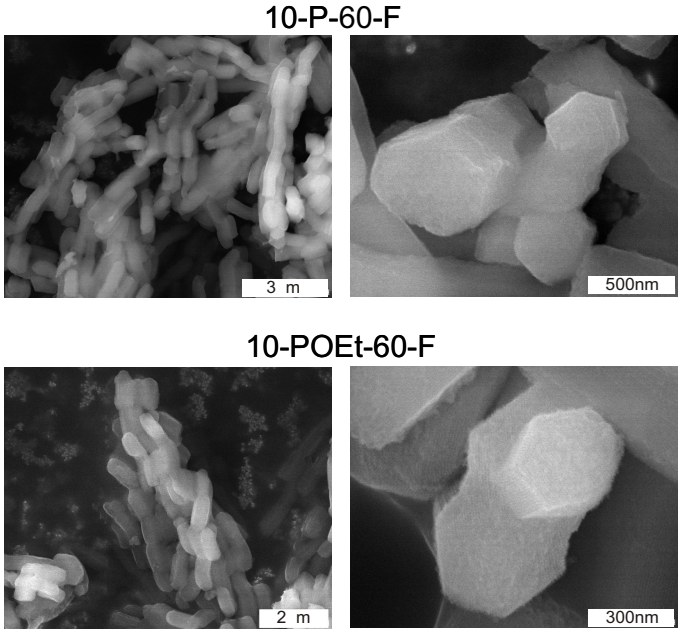

Figure 6.22: SEM images of phosphonate ester functionalized SBA-15 samples prepared by prehydrolysis of the functional reagent (ϕ=10) before and after polymer removal.

phonic acid ester contained SBA-15 before and after template removal with sulfuric acid) are displayed in Figure 6.22. These samples were synthesized with ϕ=10% of functional silane and a prehydrolysis time of functional silane of 60 minutes. The images clearly show the hexagonal habitus and elongated worm-like character of the particles before and after polymer removal, which is typical for highly ordered SBA-15 materials. From this it follows that the treatment with sulfuric acid does not cause any morphological changes of the particles.

However, as seen in the SEM images displayed in Figure 6.23, the morphology of the materials changes when increasing the percentage of functional silane. For example if the percentage of functional silane is increased to 15% (samples 15-P-95-F and 15-POEt-95-F) much shorter particles result (Fig. 6.23a). Bent worm-like structures can only be seen partially, and they seems to lump together forming cluster-like structures. But the hexagonal cross-sections of individuell particles are still recognizable in the images. When

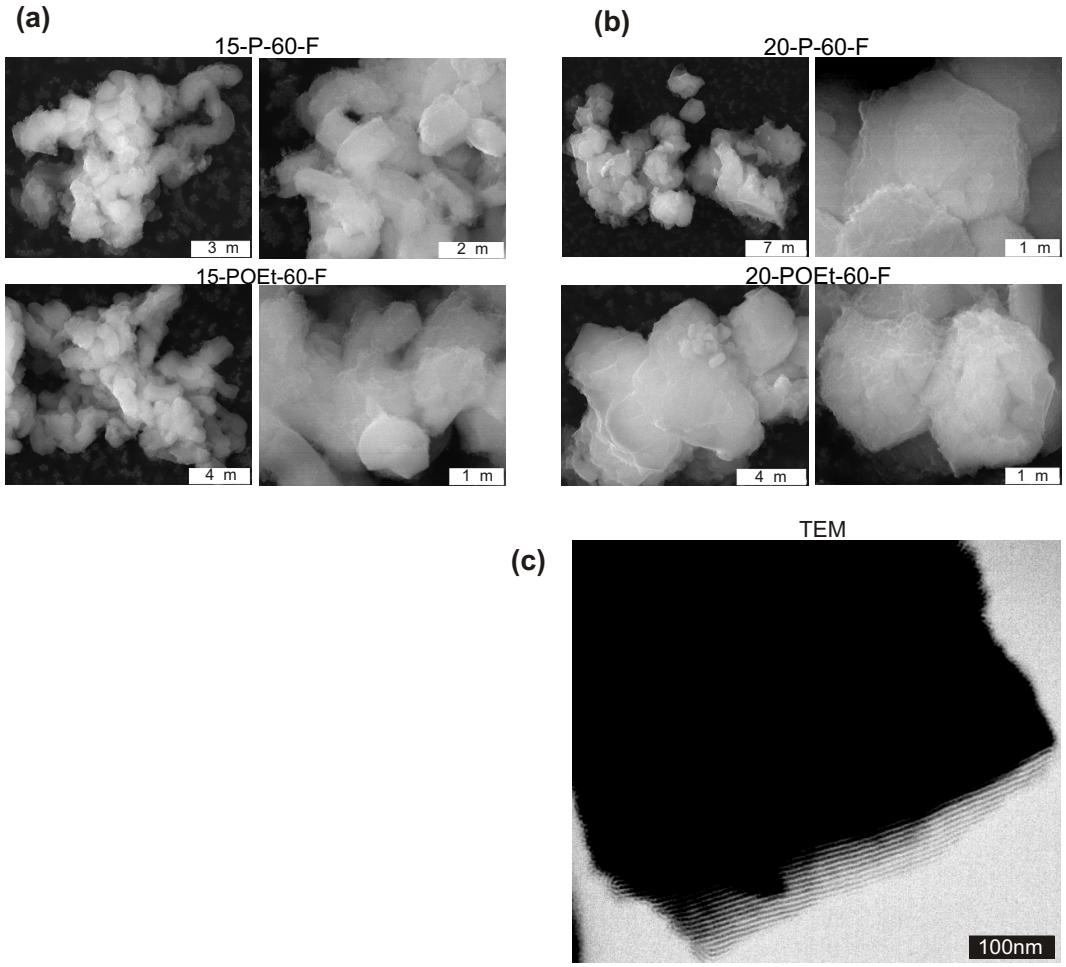

Figure 6.23: SEM images of two phosphonate ester functionalized SBA-15 prepared by prehydrolysis of functional silane, before and after polymer removal: (a) 15-P-60-F and 15-POEt-60-F; (b) 20-P-60-F and 20-POEt-60-F; (c) TEM image of 20-P-60-F exhibiting pores running parallel to each other.

increasing the percentage of functional silane to ϕ=20, particles become more shorter. As seen in the SEM images in Fig. 6.23b the samples 20-P-60-F and 20-POEt-60-F do not form elongated rod-like particles, but rather broad hexagonal disks which tend to stick

together. In any case the disks constitute arrays of ordered pores as seen in the TEM micrograph of the sample 20-P-60-F displayed in Fig. 6.23c.

Figure 6.24 shows SEM images of the samples 15-P-40-T and 15-POEt-40-T in which TEOS was the prehydrolyzed silica precursor. The images show exclusively elongated worm-like structures. However, the length of the worm-like particles is only about 1 μm, i.e., are shorter than in pure SBA-15 samples that have particle lengths of several μm. SEM images show that a simultaneously addition of TEOS and functional silane (ϕ=15)

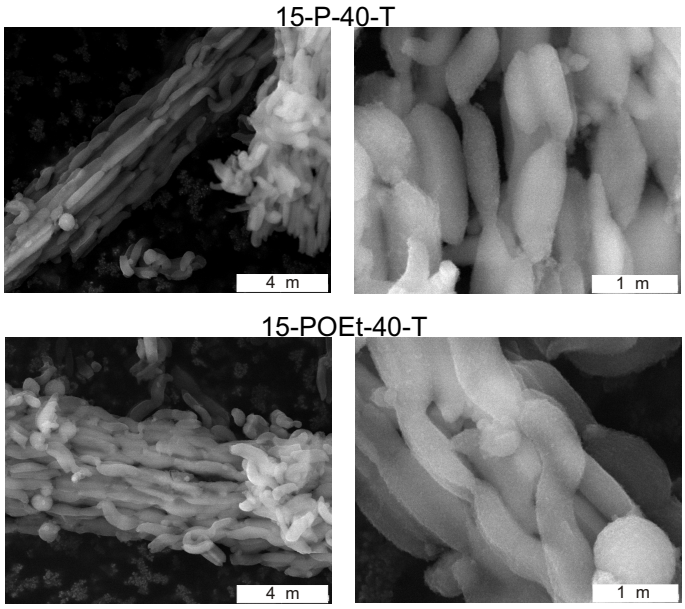

Figure 6.24: SEM images of a phosphonate ester functionalized SBA-15 material prepared by prehydrolysis of TEOS before polymer removal (15-P-40-T) and after polymer removal (15-POEt-40-T).

leads to completely disordered silica materials. Further characterizations of this sample were therefore not performed.

Nitrogen adsorption isotherms and SAXD profiles of phosphonate ester functionalized SBA-15 samples are displayed in Figure 6.25, and the results of the data analysis are summarized in Table 6.7. The results are consistent with the conclusions drawn from the SEM images. The type IV nitrogen adsorption isotherm of sample 10-POEt-60-F resembles that of pure SBA-15. They exhibit a steep pore condensation step indicating a narrow pore size distribution accompanied by a H1 type hysteresis loop. The material has a high pore volume and large pore diameter. The SAXD profile of this sample shows four resolved peaks that can be assigned to the 2D hexagonal unit cell of ordered cylindrical pores. The nitrogen adsorption isotherms of the samples 15-POEt-95-F and

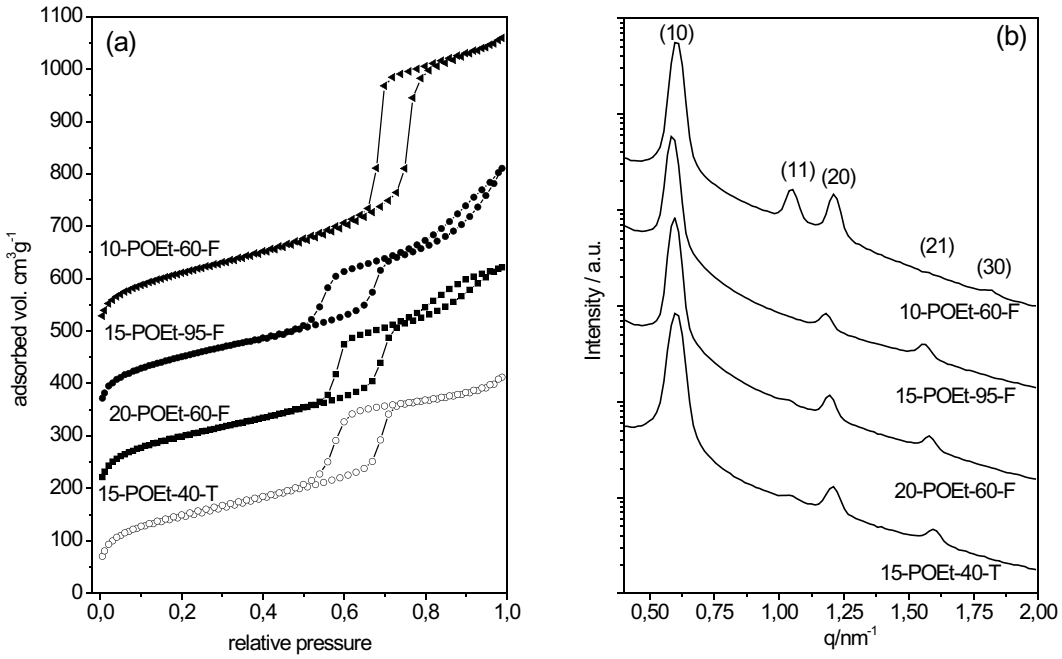

Figure 6.25: Nitrogen adsorption isotherms (a) and SAXD profiles (b) of phosphonate ester functionalized SBA-15 materials by prehydrolysis of the functional reagent. Adsorption isotherms and SAXD spectra are shifted against each other for clarity.

20-POEt-60-F show features which are not typical for pure SBA-15. Their low-pressure region corresponds to type IV isotherms with a not very steep pore condensation step accompanied by H1 type hysteresis loop. However, after this step the adsorption continues to increase and is accompanied by a secondary hysteresis of type H3 which is typical for agglomerates of disk-like particles. The sample 15-POEt-40-T, on the contrary, exhibits a typical type IV isotherm with a H1 type hysteresis, but no significant further increase of adsorption or a secondary hysteresis is observed. Hence the morphological characteristics found in the SEM images are also seen in the nitrogen adsorption measurements. The Table 6.7 shows that the specific surface area, the mesopore volume, and pore diameter of the latter three samples are considerably smaller than for 10-POEt-60-F, whereas the lattice parameter a_0 is approx. 12 nm for all phosphonate ester functionalized samples. This implies that the pore walls of these samples are thicker than that of 10-POEt-60-F and pure SBA-15. However, when increasing the percentage of functional silane ϕ from 15 and 20 no pronounced changes in pore volume and diameter are observed, i.e., the expected decrease in pore diameter and pore volume does not occur. Concerning these parameters there are no pronounced differences between these samples. The larger wall thickness of the PA-SBA-15 samples can be attributed either to a wider SiO_2 layer be-

Table 6.7: Properties of phosphonate ester-functionalized and pure SBA-15 silica.

sample	a_s/m^2g^{-1}	v_p/cm^3g^{-1}	v_m/cm^3g^{-1}	$(p/p_0)_{pc}$	D/nm	a_0/nm	w/nm
10-POEt-60-F	571	0.94	0.05	0.753	8.8	12.0	3.2
10-PA-60-F	595	0.95	0.05	0.758	8.8	12.0	3.2
15-POEt-95-F	530	0.79	0.03	0.676	7.2	12.3	5.1
20-POEt-60-F	520	0.73	0.06	0.694	7.6	12.1	4.5
15-POEt-00	disordered						
15-POEt-40-T	502	0.64	0.04	0.691	7.5	12.0	4.5
15-PA-40-T	531	0.66	0.05	0.693	7.5	12.0	4.5
SBA-15cal550	561	0.89	0.10	0.757	8.9	11.5	2.6
SBA-15cal250	807	1.35	0.11	0.807	10.2	12.8	2.6

a_s: specific surface area, v_p: pore volume, v_m: micropore volume, $(p/p_0)_{pc}$: pore condensation pressure of nitrogen, D: pore diameter, a_0: lattice parameter.

tween two neighboring pores, or to the organic film of the functional groups at the pore walls. Probably both effects play a role. A closer examination of SAXD profiles of the samples displayed in Fig.6.25b reveals that the relative intensities of the leading peaks are quite similar in the samples 15-POEt-95-F, 20-POEt-60-F and 15-POEt-40-T, but different from the relative peak intensities in the SAXD spectrum of 10-POEt-60-F. Most likely, this is due to the constant value of the lattice parameter a_0 but different pore sizes of these two groups of samples. The lattice parameter determines the peak positions in the SAXD spectrum. The pore diameter of the cylindrical pores has a direct influence on the form factor which for cylindrical pores is given by Bessel functions. The latter exhibit sharp maxima and minima depending on pore diameter. The intensity of the Bragg reflexes is modulated by these maxima and minima of the form factor [74].

In the SAXS profiles of the samples 15-POEt-95-F, 20-POEt-60-F and 15-POEt-40-T with similar pore sizes, the (11) and (30) Bragg-reflexes are purged because of the minimum of Bessel function at this positions, whereas in the profile of 10-POEt-60-F the (21) reflex is purged for the same reason. Thus the similarity of the SAXD profiles of the samples 20-POEt-60-F and 15-POEt-40-T can be explained by their similar pore sizes and lattice parameters. Hence, the relative intensities of the Bragg-peaks in a SAXD spectrum are not only effected by long-range order of the samples but also by the relation of lattice parameter and pore size (and film thickness).

6.4.2 Reaction yield and degree of the functionalization

In this section the results of examination of the functional group content in the different samples are presented. ^{29}Si MAS NMR and TGA/DTA methods were used for the quantitative determination of the functional group content in the silica samples after template removal. ^{29}Si MAS NMR spectra and TGA/DTA curves of the phosphonate ester containing samples are displayed in Figure 6.26. Results of the NMR and TGA are summarized in the Table 6.8.

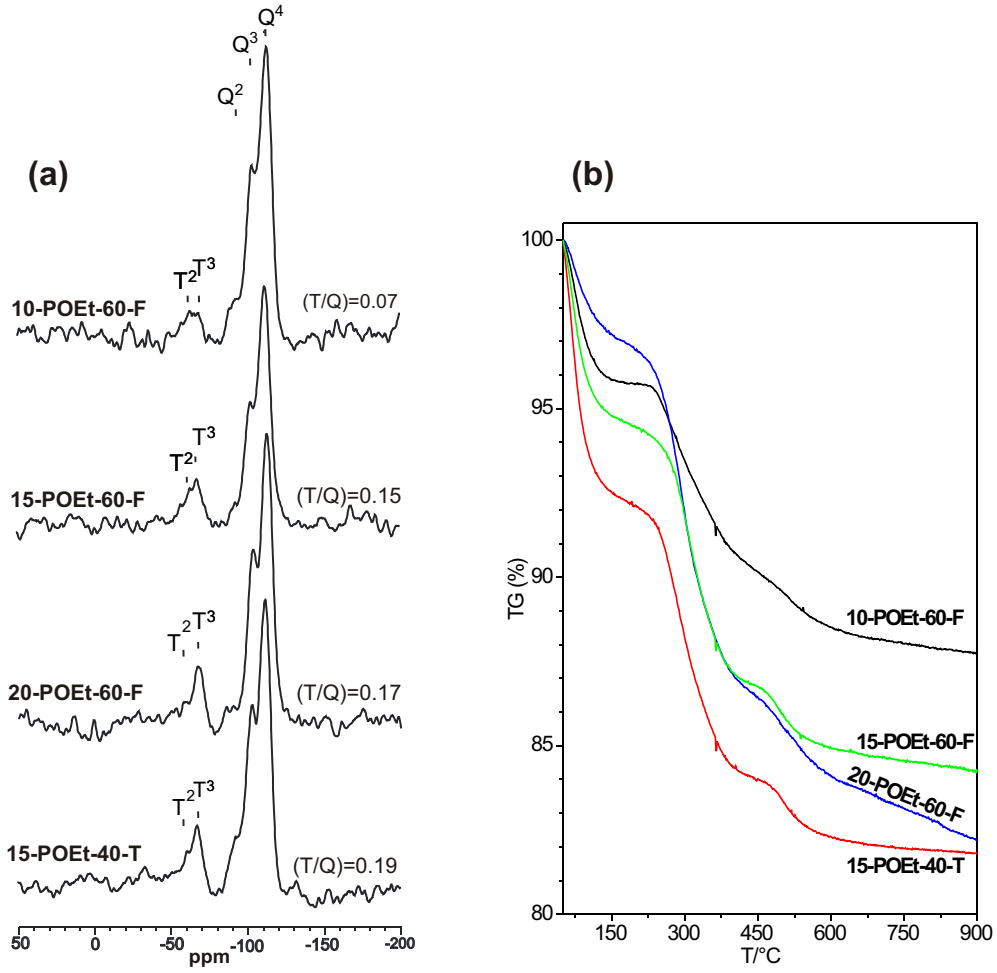

Figure 6.26: (a) ^{29}Si MAS NMR spectra and (b) TGA curves of phosphonate ester containing SBA-15 samples with increasing content of functional reagent ϕ in the initial mixture.

The gradual increase of the (T/Q) ratio in the spectra of samples synthesized by prehydrolysis of the functional silane shows that an increase of the percentage of functional reagent ϕ in the synthesis mixture yields increasing numbers of functional groups at the

silica walls. This is vindicated by TGA measurements (see Table 6.8). Closer examination of the experimental (T/Q) and n values reveals that an increase of ϕ from 10 to 15 effects an 100% increase of the number functional groups at the wall, while a further increase of ϕ from 15 to 20 causes an increase of functional groups by about 7% (NMR) or about 20% (TGA) indicating that an upper limit of the functionalization degree has been reached. Moreover, both methods show that when TEOS is the prehydrolyzed component, as is the case for the sample 15-POEt-40-T, a slightly higher (T/Q) value is observed than for the sample 15-POEt-60-F.

Table 6.8: Expected quantities and the corresponding experimental values obtained from ^{29}Si NMR, TGA/DTA and potentiometric titration.

	expected		NMR			TGA	
sample	(T/Q)	n	x	(T/Q)	Y	n	Y
10-P-60-F	0.11	1.66	0.07	16%	63%		
10-POEt-60-F	0.11	1.66	0.065	17%	59%	0.63	38%
10-PA-60-F	0.11	1.66			18%	0.30	
15-P-95-F	0.18	2.49	0.15	34%	85%		
15-POEt-95-F	0.18	2.49	0.15	37%	84%	1.13	45%
20-POEt-60-F	0.25	3.32	0.17	31%	66%	1.39	42%
15-POEt-40-T	0.18	2.49	0.16	32%	87%	1.18	47%
15-PA-40-T	0.18	2.49	0.11	38%	63%	0.91	36%

(T/Q): Expected and experimental ratio of organosiloxane (T) and siloxane (Q) groups; n: Expected and experimental amount of functional silane per unit mass of SiO_2 (in mmol g^{-1}); x: Degree of surface functionalization; Y: Reaction yield.

Though the NMR (Fig. 6.26a) and TGA (Fig. 6.26b) experiments show the same tendencies the reaction yields calculated from these methods (Table 6.8) differ from each other. Namely, NMR gives higher yields than the TGA. Reactions yields calculated from NMR spectra range from 60% to 90% whereas those calculated from the TGA curves range from 40% to 50%.

Also here we investigated whether the small yield of the TGA experiments is caused by the formation of a crystalline Si-P mixed-oxide phase in the matrix during the heating. The presence of phosphor remnants in the matrix would increase its unit mass and decrease the computed yield from TGA. The WAXS (wide angle X-ray scattering) spectra measured after heating the samples to 1000°C showed that the amorphous structure

of the PA-SBA-15 indeed becomes partially crystalline. The reflexes of the crystalline phase, however, could only be associated with 'cristobalite', the high-temperature modification of SiO_2 (see spectra in Appendix). In the crystalline phase they are no structures containing phosphor. But this does not rule out the presence of phosphor in the amorphous phase. Here the presence of phosphor could be examined, e.g., through phosphor elemental analysis. This, however, was beyond the scope of this thesis.

The reactions yields for phosphonic acid are higher than the corresponding values of sulfonic acid functionalization but smaller than the reaction yields obtained for carboxylic acid functionalization. For the sample 10-POEt-60-F the degree of the surface functionalization, x, is 16% whereas for samples prepared with a higher percentage of functional silane x ranges from 30 to 40%. The latter values are similar to the values for surface coverage x of sulfonic acid functionalized materials.

6.4.3 Polymer removal and microporosity

TGA curves of the polymer-containing samples 15-P-40-T, 20-P-60-F, 10-P-60-F are shown in Figure 6.27. The contents of organic components in these samples are 28%, 36%, and 51%, respectively. The fact that the main part of the organic component forms the block copolymer template indicates that the polymer content in the samples decreases as the degree of surface functionalization increases. The same trend was also observed in

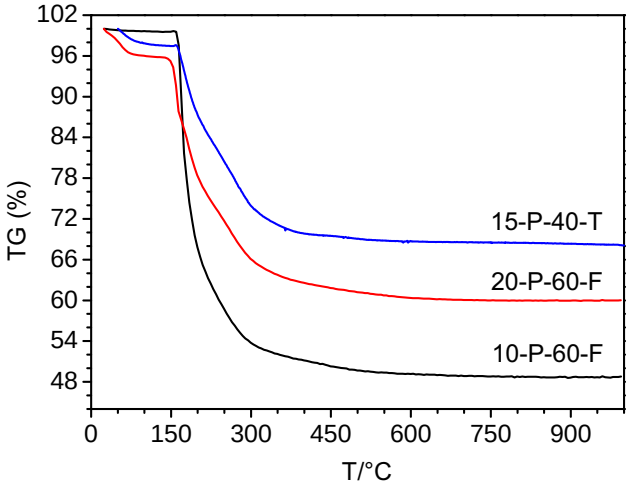

Figure 6.27: TGA curves of polymer containing 15-P-40-T, 20-P-60-F, 10-P-60-F samples.

CA-SBA-15 and SA-SBA-15 materials. Hence, it appears that the number of the block copolymer micelles decreases as the number of functional groups is increased.

Figure 6.28 compares the DTA curves of the polymer-containing phosphonate ester functionalized sample (15-P-40-T), after polymer removal by sulfuric acid (15-POEt-40-T), and after phosphonate ester cleavage by HCl treatment (15-PA-40-T). The exotherme peak at ca. 100°C is attributed to physically adsorbed water. The pronounced endothermic peak at 185°C seen in the polymer-filled sample has disappeared after sulfuric acid treatment. Therefore this peak is attributed to the block copolymer template. The peak at ca. 300°C has disappeared after HCl treatment, indicating that this peak is caused by phosphonic acid ester groups. Finally, the DTA curve of the sample containing free phosphonic acid groups (15-PA-40-T) shows only two peaks at 400°C and 500°C.

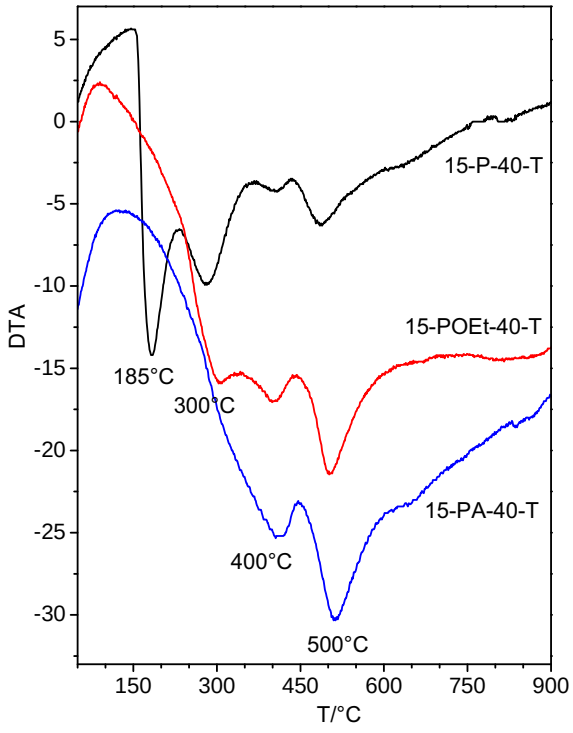

Figure 6.28: DTA curves of 15-P-40-T, 15-POEt-40-T and 15-PA-40-T.

Figure 6.29a shows the ^{13}C CPMAS NMR spectra of 10-P-60-F, 10-POEt-60-F and 15-POEt-95-F. The spectrum of the polymer containing sample 10-P-60-F displays resonances at 76, 74, 71, and 17 ppm which are attributed to the block copolymer template. Two additional carbon signals at the positions 5 ppm and 63 ppm exists that are assigned

to the functional group. After polymer removal with sulfuric acid no resonance signals from block copolymer can be seen anymore, indicating the complete template removal.

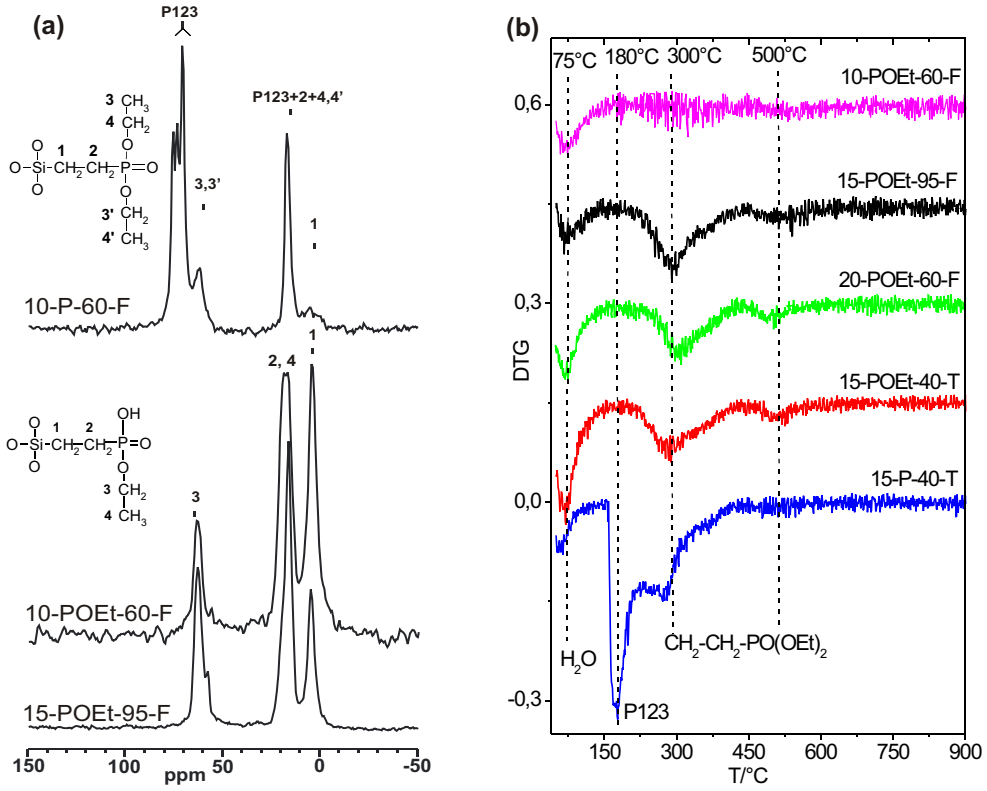

Figure 6.29: (a) ^{13}C CPMAS NMR spectra of the samples 10-P-60-F, 10-POEt-60-F and 15-POEt-95-F; (b) DTG curves of different phosphonate ester and phosphonic acid contained SBA-15 samples.

The ^{13}C CPMAS NMR spectra of 10-POEt-60-F and 15-POEt-95-F are very similar representing three resonances at the positions 5 ppm, 17 ppm and 63 ppm. In Figure 6.29a these were assigned to the different carbon atoms of the functional group. According to these spectra, the samples after polymer removal still contain phosphonic acid ester. Thus 48% sulfuric acid is not strong enough to hydrolyze the phosphonic acid ester groups completely. In Figure 6.29b DTG curves of different samples are displayed. The curves show four peaks. The peak at 75°C comes from physically adsorbed water. The peak at 180°C is attributed to the decomposition of block copolymer and the remaining two peaks at 300°C and 500°C are assigned to the degradation of functional group. No peak from polymer appears after sulfuric acid treatment. Thus the results from TGA are in full agreement with those from ^{13}C CPMAS NMR. As mentioned earlier, cleavage of phosphonic acid ester is performed by refluxing the samples in concentrated HCl for 24h.

The ^{13}C CPMAS NMR spectra of 15-POEt-40-T and 15-PA-40-T are displayed in Figure 6.30a. As can be seen the peak at 63 ppm attributed to phosphonic acid ester

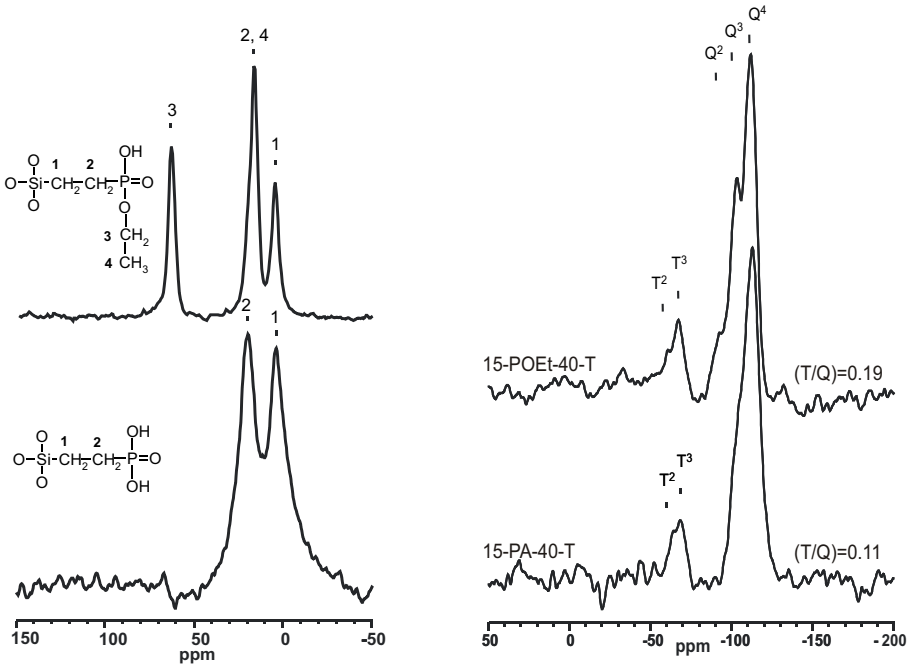

Figure 6.30: (a) ^{13}C CPMAS NMR spectra and (b) ^{29}Si MAS NMR spectra of the samples 15-POEt-40-T (before HCl treatment) and 15-PA-40-T (after HCl treatment).

groups disappears completely after HCl treatment for 24 h. Thus, SBA-15 containing free phosphonic acid groups at the pore walls can be produced in this way. Figure 6.30b shows the ^{29}Si MAS NMR spectra of the samples. The (T/Q) ratio becomes smaller after the treatment with HCl. The amount of functional groups in the pore walls decreases from 1.18 mmol g^{-1} to 0.91 mmol g^{-1} after HCl treatment. The respective data are included in Table 6.8. According to these results, ca. 20% of functional groups are cleaved after HCl treatment. Moreover, the number of Q^2 and Q^3 Si atoms relative to Q^4 decrease after HCl treatment indicating further condensation of silicon species. For this reason despite the lost of functional groups, the degree of surface functionalization x, given by $x = \frac{T^2+T^3}{Q^2+Q^3+T^2+T^3}$, increases from 32% to 38% in the sample 15-PA-40-T. On the other hand, nitrogen adsorption and SAXD data of 15-POEt-40-T and 15-PA-40-T are very similar (see Table 6.7). The data show that the lattice spacing and pore size remain constant whereas pore volume and specific surface area slightly increase in the case of 15-PA-40-T. The micropore volume of the samples was determined by t-plot analysis (see Figure 6.31). The values are ranging from 0.03 to 0.06 cm^{3}g^{-1}. Hence, though they are bigger than the micropore volumes of CA-SBA-15 and SA-SBA-15 materials, they are

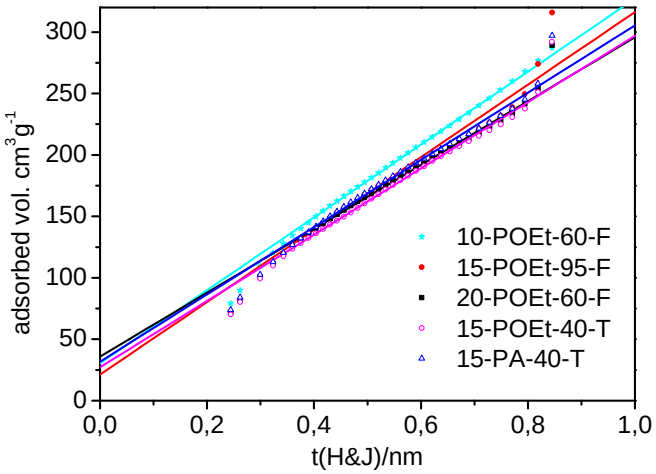

Figure 6.31: t-plot analysis of nitrogen adsorption isotherms for different phosphonic acid ester functionalized SBA-15 samples and for a SBA-15 sample containing free phosphonic acid groups (15-PA-40-T).

still smaller than those of native SBA-15.

6.4.4 The mechanism of the self-assembly

The diethoxyphosphorylethyltriethoxysilane (PTES) has two rather hydrophobic phosphone ester groups attached to the triethoxysilane via an ethyl group (see Fig. 1.1). Due to the strong P-O bond the phosphonic acid ester groups are stable in the initial synthesis conditions and thus the dealkylation does not take place. Hence, one expects that they are adsorbed close to the hydrophobic PPO part of the block copolymer. However, under the same reaction conditions the organosiloxane groups are hydrolyzed partially. Therefore they are hydrophilic and can interact with the hydrophilic PEO moieties. Because of the similar solubilities of PTES in PEO and PPO blocks of the block copolymer these molecules may cause reduced microphase separation of the two blocks and thus a decreased mesoporous ordering. Such a behavior was proposed by Margolese et al. in the preparation of propyl-thionyl functionalized SBA-15 using mercaptopropyltrimethoxysilane [53]. This functional silane is rather hydrophobic and thus resembles the functional silane PTES used in the present work.

Our investigations showed that when PTES is the prehydrolyzed silica source the presence of a molar percentage of functional silane ϕ greater than 10 in the co-condensation

perturbs self-assembly of block copolymer aggregates since the worm-like structure of SBA-15 disappears and stuck-together particles are generated. When TEOS is allowed to prehydrolyze the initial stage in nanoparticle formation involves the formation of individual silica coated P123 aggregates and materials with improved mesoscopic order are formed. In this way it is possible to increase ϕ up to 15 by retaining the worm-like mesostructure of SBA-15.

6.5 Acidity measurements

6.5.1 Measurements in non-aqueous environment by ^{15}N NMR

Acid-base interactions in aqueous solutions can be described in terms of conventional chemical reaction equilibria. This situation is quite different from that of acid-base interactions in 'dry' systems, when the acid and base are in direct contact via hydrogen bonds. Solid state NMR is a method which can be applied to investigate such interactions. Proton acceptors such as pyridine can be used to probe the proton donor ability of Brønsted acids. For instance, Shenderovich et al. have characterized the interactions of ^{15}N-labeled pyridine, a simple proton acceptor, with silica hosts using solid state NMR spectroscopy [5]. Earlier ^{15}N MAS solid-state NMR experiments showed that the isotropic ^{15}N chemical shift of pyridine is modulated when the molecule is incorporated at different sites of acid zeolites [79] or amorphous alumina [80]. In particular, a strong high-field shift occurs when pyridine is protonated.

Low-temperature NMR studies of the influence of hydrogen bonding and protonation of pyridine on NMR parameters have shown that for 1:1 hydrogen bonded complexes of an acid (AH) with pyridine (B) an increase of the acidity of AH leads to a gradual transformation of the molecular hydrogen bonded complex A-H$\cdots$B via a proton-sharing complex A$^{\delta-}\cdots$H$\cdots$B$^{\delta+}$ to a zwitterionic complex A$^{-}\cdots$H-B^{+}, where A$^{\delta-}\cdots$H$\cdots$B$^{\delta+}$ exhibits the shortest distance A$\cdots$B. In order to understand the influence of a variation of the relative acidity on the acid-base hydrogen bonds, Lorente et al. carried out low-temperature measurements on a series of hydrogen-bonded crystallized 1:1 acid-base complexes of ^{15}N-labeled collidine (2,4,6-trimethylpyridine) with a number of different carboxylic acids and their deuterated analogues [81]. They observed a correlation of the ^{15}N isotropic and anisotropic chemical shifts with the dipolar ^{1}H-^{15}N couplings and hence the nitrogen-hydrogen distances and pK_a values. A graph showing this correlation, taken from the work of Lorente et al., is displayed in Figure 6.32b. Using this correlation, the O-H$\cdots$N distances in the pyridine and surface hydroxyl pairs of MCM-41 and SBA-15 silicas were determined [5]. The O-H$\cdots$N distance found in the solid state corresponds to acids exhibiting in water a pK_a of about 4. Thus, the surface hydroxyl groups of MCM-41 and SBA-15 materials are weakly acidic.

In Figure 6.32a the ^{15}N NMR spectra of our carboxylic acid, phosphonic acid and sulfonic acid functionalized SBA-15 materials obtained after ^{15}N-pyridine adsorption into the pores are shown. The peak at ca. 0 ppm is assigned to an excess of free (not bonded) pyridine in the pores. The peak at ca. -25 ppm is assigned to pyridine hydrogen bonded

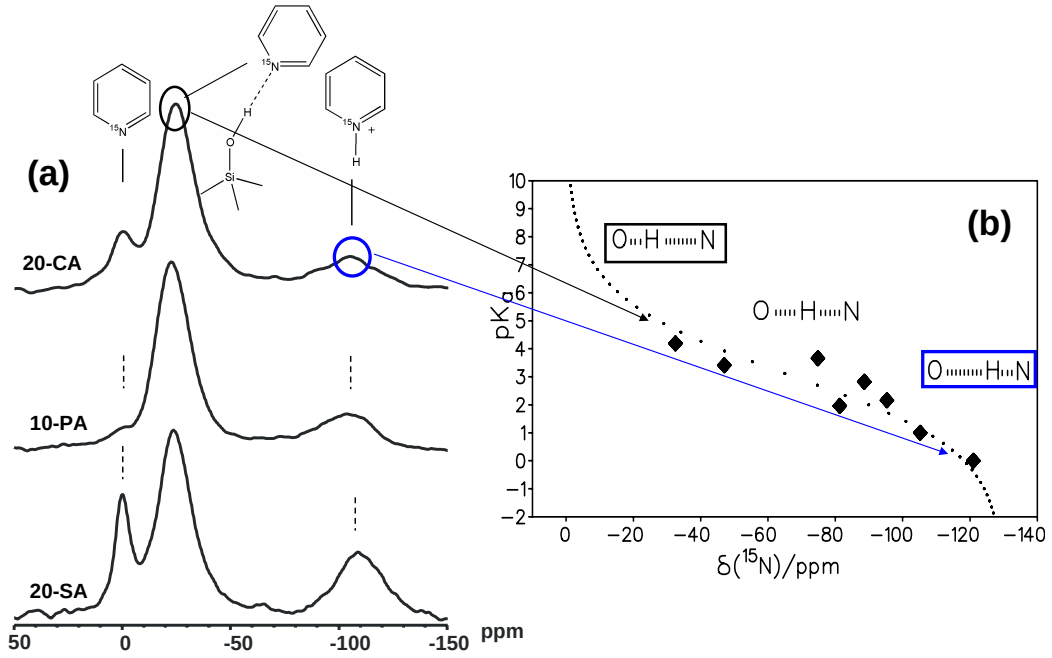

Figure 6.32: (a) ^{15}N MAS NMR spectra of 20-CA, 10-PA (10-POEt-60-F) and 20-SA (20-SA-60-F) after pyridine adsorption in the pores; (b) pK_a values of different acids AH as a function of ^{15}N chemical shift in acid-collidine solid-state complexes. The graph is taken from the work of Lorente et al. [81].

to the surface SiOH groups and in case of CA-SBA-15 also to the single COOH groups ($A^{\delta-}\cdots H\cdots B^{\delta+}$ state). The peak at -110 ppm is attributed to pyridine completely protonated from acid groups ($A^{-}\cdots H\text{-}B^{+}$ state). Figure 6.32a shows that this peak is most pronounced in the case of 20-SA, in agreement with the expected highest acidity of the sulfonic acid groups, and weakest but still clearly recognizable in the case of CA-SBA-15. The existence of totally protonated pyridine is unexpected in the case of carboxylic-acid functionalized SBA-15 which is a weak acid in aqueous solution (acid dissociation constant pK_a=4.7). The surface silanol groups have a similar acidity as carboxylic acids in water but are not protonated by pyridine in the dry state at the pore wall. The high proton-donor ability of carboxylic acid functional groups at the pore walls may be due to the formation of hydrogen-bonds between several carboxylic acid groups at the surface. It is known that in solutions the formation of hydrogen-bonded chains of carboxylic acid molecules leads to an enhanced acidity of the terminal proton [7]. The high local concentration of carboxylic acid groups in the CA-functionalized SBA-15 material (more than 40% of the surface, see Section 6.2) may lead to a similar conjugation effect in the pores. Additional ^{15}N NMR measurements are being performed to check this conjecture.

According to the present state of our study all three solid acids can be deprotonated by pyridine. The pK_a values corresponding to the ^{15}N chemical shifts for the protonated pyridine indicate a high proton donor ability of all three solid acids. The acidity measurements of the acid-functionalized SBA-15 silicas reported in this section were performed at Free University Berlin as a part of the PhD thesis of Daniel Mauder. Accordingly, the results will be discussed more detailed in his PhD thesis [82].

6.5.2 Measurements in aqueous environment by FT-IR

The proton donor ability of the COOH groups of 10-CA and 20-CA materials in aqueous solutions was studied by means of FT-IR measurements. Experimental details of these measurements were given in Section 4.2. FT-IR spectra of 10-CA and 20-CA samples in the dry state are shown in Figure 6.33. Drying was performed by exposure of the samples to dry air in the sample cell. The drying time for 20-CA and 10-CA was one week and 2 days, respectively. Because of the shorter drying time a peak at ca. 1633 cm^{-1} appears in the FT-IR spectrum of 10-CA, which is attributed to the O-H bending mode (δ(O-H)) of H_2O.

Figure 6.33 shows two spectral ranges of particular interest, namely the C-H stretching

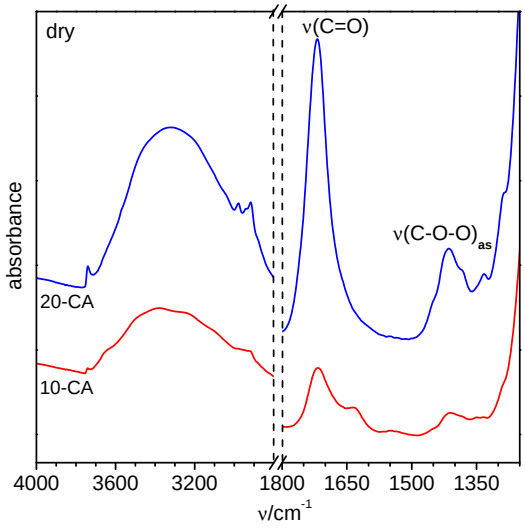

Figure 6.33: FT-IR spectra of 10-CA and 20-CA samples in the dry state.

region from 2900 to 3800 cm^{-1}, and the finger-print region from 1800 to 1250 cm^{-1}. The weak band at 3740 cm^{-1} is due to quasi isolated SiOH groups, whereas the broad band

centered at 3319 cm^{-1} is due to hydrogen-bonded silanols. These interactions can come from hydrogen bonding of SiOH groups with each other, or with the COOH groups at the surface, or with residual H_2O physisorbed at the surface. The weak band at 2979 cm^{-1}, assigned to the CH_3 stretching mode, indicates the presence of residual amounts of block copolymer template. These residues contribute also to the bands at 2939 and 2916 cm^{-1}. The latter are attributed to the CH_2 stretching mode and come mostly from ethyl chains of the functional groups. The existence of small amounts of residual template in these samples was also seen by means of ^{13}C CPMAS NMR measurements (Section 6.2).

In the finger-print region, a strong band at 1718 cm^{-1} is assigned to the C=O stretching mode, ν(C=O), of the COOH head group. Concomitant with this band, a band at 1413 cm^{-1} appears, which is assigned to the C-O stretching mode of the carboxyl group, that coupled to the O-H bending mode.

The dependence of the proton-donor ability of the 10-CA and 20-CA silicas on the pH of the solution was investigated by exposing the samples to pure D_2O of pH 5.5 and to a phosphate buffer in D_2O of pH 8. The resulting spectra in the finger-print region are shown in Figure 6.34 in comparison with the spectra of the dry materials. The fact that

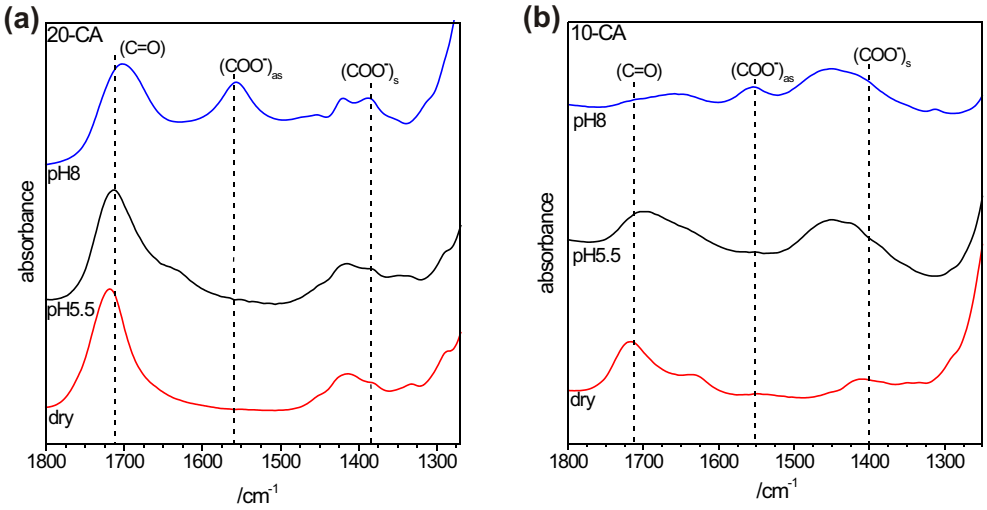

Figure 6.34: FT-IR spectra of (a) 20-CA and (b) 10-CA samples in dry state, in D_2O with pH 5.5, and in phosphate buffer ($K_3PO_4 \rightleftharpoons K_2HPO_4$) in D_2O with pH 8.

spectra show nearly no difference between the dry state and in D_2O at pH 5.5, indicates that exposure to D_2O at pH 5.5 does not cause significant deprotonation of the COOH groups. After exposure to the D_2O solution of pH 8, two new bands at 1557 and 1387 cm^{-1} appear which are attributed to the asymmetric (ν_{as}) and symmetric (ν_s) stretching vibration of carboxylate groups (COO^-), respectively. At the same time the intensity

of the band at 1718 cm^{-1} decreases. These changes indicate that a deprotonation of COOH groups has occurred. However, the decrease of the intensity of the band at 1718 cm^{-1} does not occur to the same extent in the 10-CA and 20-CA materials. In 10-CA the signal nearly disappears indicating that most of the COOH groups have been deprotonated whereas the signal intensity is reduced only to about one half in case of 20-CA. This suggests that in the 10-CA material with 20% surface coverage nearly all COOH groups are separated and accessible, while in the 20-CA material with 50% surface coverage only part of the COOH groups are accessible.

6.6 Conclusions

Co-condensation route was used for the functionalization of SBA-15 with carboxylic acid (CA), phosphonic acid (PA) and sulfonic acid (SA) groups in order to study the acidity in the confined geometry of the nanopores. Reaction conditions for maximizing functionalization of SBA-15 under retention of the structural order of the silica are strongly affected by assembly kinetics. To understand the involved hydrolysis and the condensation of silica sources and their interaction with template, the percentage of the functional silane ϕ, the prehydrolyzed silica source (TEOS or F) and the prehydrolysis time are varied.

In case of carboxylic acid functionalization using CTES hexagonally ordered materials are obtained only if CTES is prehydrolyzed. The increase of the functional silane up to 20 mole% is possible without disordering the SBA-15. The yield of the functionalization is approx. 80% indicating a substantial incorporation of the functional silane. The situation is different in the phosphonic acid functionalization. Applying functional silane PTES as the prehydrolyzed component, ordered SBA-15 materials with worm-like morphology can be obtained up to ϕ= 10. Increasing ϕ to 15 and 20 leads to a stepwise shortening of the worm-like particles up to the formation of disk-like structures under preservation of the 2D hexagonally order. The amount of PTES in the synthesis mixture can be increased to ϕ=15 mole% under retention of the elongated worm-like morphology of SBA-15 by prehydrolyzing of TEOS. The simultaneous addition of PTES and TEOS in the synthesis mixture, however, leads to the formation of disordered materials. The surface coverage of SBA-15 by phosphonic acid groups ranges from 30 to 40%. The yields of the functionalization reactions obtained from ^{29}Si-MAS NMR measurements are high (60-90%). Nevertheless, the yields decrease nearly 50% after the additional treatment of the products (SBA-POEt) with concentrated HCl to cleave the phosphate-ester groups for producing free phosphonic acid species. In the synthesis of sulfonic acid functional-

ized SBA-15 the prehydrolysis of STHS does not play a role because it already exists in the hydrolyzed form. As a hydrophilic functional reagent because of the sulphonic acid groups it preferentially interact with the hydrophilic PEO part of the block copolymer allowing a good microphase separation. Accordingly, an amount of STHS in the synthesis mixture up to ϕ=20 mole% yields SBA-15 materials with the typical well-known order and morphology, and this independently of the silica source (TEOS or STHS) added first. Nevertheless, the degree of the incorporation of the sulfonic acid reagent using STHS is the lowest among other functionalization reactions. Increasing the mole fraction of functional silane ϕ to 30% results in formation of disordered silica. The surface coverage of SBA-15 by sulfonic acid groups ranges from 20 to 30%. The yields of the functionalization reactions obtained from ^{29}Si-MAS NMR measurements are high (30-50%). The lower degree of the incorporation of the STHS compared to the other functionalization reactions can probably be explained by the slow condensation rate of the hydroxyl groups of the highly acidic functional silane.

The acidity measurements of functionalized SBA-15 materials in water free conditions were performed via ^{15}N CPMAS NMR after adsorption of pyridine into the pores. The pK_a values corresponding to the ^{15}N chemical shifts for the protonated pyridine indicate a high proton donor ability of all three solid acids. The proton donor ability of the COOH groups of 10-CA and 20-CA materials in aqueous solutions was studied by means of FT-IR measurements. These show the deprotonation of COOH groups in 10-CA and 20-CA materials at pH 8. The results suggest that in the 10-CA material with 20% surface coverage nearly all COOH groups are separated and accessible, while in the 20-CA material with 50% surface coverage only part of the COOH groups are accessible.

Part II

Functionalized SBA-15 Silica as a Host

Chapter 7

Background

7.1 Supramolecular polymers

Loosely defined, supramolecular polymers are polymers in which the monomers are held together by weak noncovalent reversible interactions. Noncovalent interactions with little specificity or directionality are present in all condensed molecular materials. However, when highly directional forces dominate the interaction between neighboring molecules, long chains or networks of concatenated molecules can be formed, resulting in many of the (mechanical) properties that have made polymeric materials so successful. Long chains, which lead to polymer-like behavior, are only formed when the interactions between the monomeric units are strong enough. The presence of linear chains, which persist when a material is heated or dissolved, is what guarantees a successful design of strong and directionally interacting functionalities. In a fundamental research context, where the goal is to understand the relation between molecular structure and macroscopic properties, strength and directionality are of prime importance. For supramolecular polymers there are many examples in nature. For example, globular proteins in biological cells, such as tubulin, actin, and fibrinogen, are known to polymerize into long filaments by means of non-covalent interactions. This polymerization plays an important role in the cell rigidity and motility, and in intercellular transport.

Another well-known example of supramolecular assembly is that of amphiphilic surfactant molecules or polymers. These molecules can form a variety of aggregate structures such as isotropic micellar and vesicle phases, or hexagonal and lamellar mesophases. As we have seen in Part I such systems can be used as structure directing agents for the synthesis of ordered mesoporous materials. In order to create a linear supramolecular polymer, bifunctional monomers are needed possessing two binding sites that have a spe-

cific interaction with other binding sites. Most design of supramolecular polymers are based on hydrogen bonding [83]. Due to their specific and highly directional character, hydrogen bonds are ideally suited for the assembly of supramolecular polymers. The strength of the interactions correlates with the number hydrogen bonds of a bonding site.

An important further class of supramolecular polymers is formed by coordination polymers. In a coordination polymer the bonds between monomers are based on metal ligand interactions as shown in Figure 7.1 in the following Section.

7.1.1 Fe-MEPE

The supramolecular coordination polymer Fe-MEPE studied in this work is an organometallic complex assembled from Fe(II)-acetate and 1,4-bis-(2,2´:6´2´´-terpyridine-4´-yl)-benzene by coordinative bonds (see Figure 7.1) which results in a stereochemically well-defined octahedral coordination with D_{2d} symmetry [84]. Because of the ditopic character of the ligand, Fe-MEPE forms a linear rigid-rod-like structure (1.2 nm diameter) in which the Fe(II) ions are periodically positioned along the backbone at a distance of 1.55 nm. The rigidity results from the short length of the spacer, in our case phenyl, by which the terpyridine ligands are connected. More flexible coordination polymers are obtained by using longer spacer chain lengths.

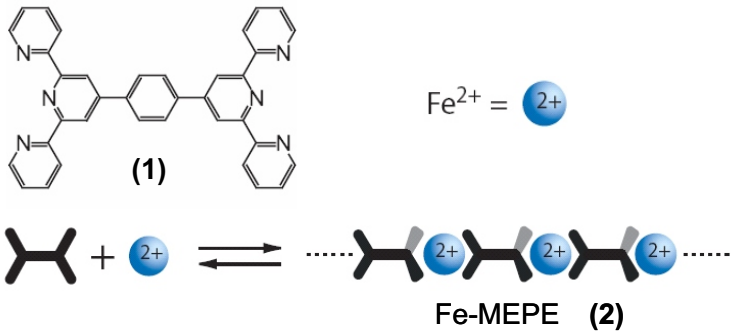

Figure 7.1: Metallo-supramolecular coordination polyelectrolyte (Fe-MEPE) (**2**) formed by self-assembly of Fe(II) ions with the ditopic ligand 1,4-bis-(2,2´:6´2´´-terpyridine-4´-yl)-benzene (**1**).

Fe^{2+} having the electron configuration [Ar]$3d^6$ has 24 electrons. In an octahedral ligand field the 6 valence electrons in the 3d orbitals split to form two sets of degenerated orbitals. These are the t_{2g} orbitals d_{xz}, d_{xy}, d_{yz}, and the e_g orbitals d_{z^2} and $d_{x^2-y^2}$ as illustrated in Figure 7.2. The energy difference between the t_{2g} and e_g orbitals depends on

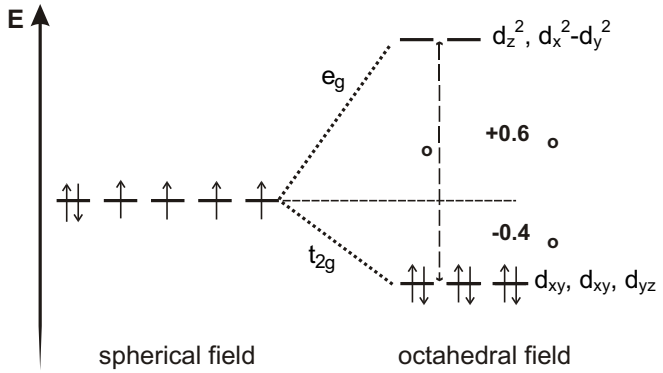

Figure 7.2: Splitting of the d-orbitals of Fe^{2+} in an octahedral ligand field.

the strength of the ligand field and is denoted by Δ_O, the ligand field splitting. Relative to the spherical ligand field, t_{2g} orbitals are lowered by $0.4\Delta_O$, and the e_g orbitals increased by $0.6\Delta_O$. Accordingly, for an octahedral complex with electronic configuration $t_{2g}^m e_g^n$ the ligand field stabilization energy (LFSE) is given by

$$LFSE_{okt} = (-0.4m + 0.6n)\Delta_O. \tag{7.1}$$

In its ground state, Fe^{2+} forms a low-spin complex with electronic configuration $t_{2g}^6 e_g^0$. Thus the LFSE of Fe(II)-MEPE is $-2.4\Delta_O$.

The transition metal complexes are most stable when they fulfill the 18-electron rule. according to this rule, those configurations are stable in which the sum of the metal valence electrons and the ligand electrons offered in dative bonds exactly add up to the valence electron number of next following noble gas atom. In Fe-MEPE each Fe(II) is coordinated by 6 nitrogen atoms of two terpyridine ligands. Because Fe(II) has 6 d-electrons and each nitrogen atom contributes 2 electrons into the coordinative bond, Fe(II)-MEPE fulfil the 18 electron rule, making it an especially stable complex.

For the octahedral coordination of the Fe(II) ion, contorting of the two terpyridine molecules by 90° against each other is necessary. This is illustrated in Figure 7.3. In this coordination not all Fe-N bond distances are equal: The bond distances of the two N-atoms in the central pyridine rings is 1.89 Å, while the bond distance of the four N-atoms of the terminal pyridine rings is 1.99 Å[86]. These values correspond to an octahedral coordination geometry with two N-atoms being in the central and four being in the terminal positions of the octahedron. In Fe-MEPE films obtained by drying of MEPE-solutions at solid surfaces like quartz the octahedral coordination geometry becomes distorted, leading to a partial paramagnetic high-spin complex of Fe(II)-MEPE. Magnetic susceptibility measurements of such Fe(II)-MEPE films at room temperature has shown that the 15-30

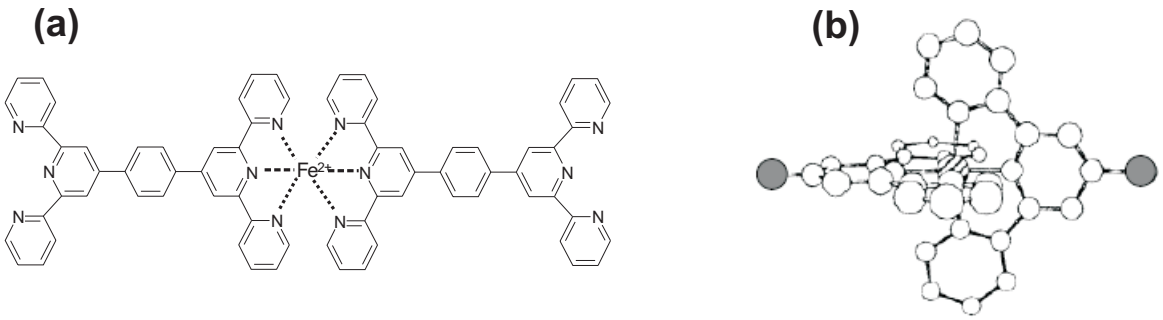

Figure 7.3: (a) Coordination of Fe^{2+} with ditopic ligand 1,4-bis-(2,2´:6´2´´-terpyridine-4´-yl)-benzene in an octahedral ligand field; (b) real space illustration of Fe-MEPE in which the two terpyridine molecules are contorted by 90° against each other [85].

% of Fe-complex is transformed to the paramagnetic high-spin state [87].

7.2 Lifetime of a supramolecular bond

Supramolecular polymers consist of bifunctional monomers that each have two functional groups **F**. If a functional group of one monomer is linked to that of another monomer a bond **B** between these two monomers is formed [83].

$$\cdots F + F \cdots \underset{k_d}{\overset{k_a}{\rightleftharpoons}} \cdots B \cdots$$

where k_a and k_d are the rate constants of bond formation and dissociation, respectively. The dynamic properties of supramolecular polymers are mainly determined by the lifetime of a bond

$$\tau_B = \frac{1}{k_d}. \tag{7.2}$$

τ_B is practically infinite for covalent polymers. For supramolecular polymers however, it is usually much smaller. It may vary from less than a nanosecond up to thousand of years, depending on the type of supramolecular bond.

7.2.1 Lifetime of a coordinative bond

As explained above, in coordination polymers each metal ion (M) is coordinated by two ligand groups (L) in form of a complex:

$$M + L \underset{k_{d1}}{\overset{k_{a1}}{\rightleftharpoons}} ML$$

$$ML + L \underset{k_{d2}}{\overset{k_{a2}}{\rightleftharpoons}} ML_2$$

with the stability constants

$$K_1 = \frac{[ML]}{[M][L]} \quad \text{and} \quad K_2 = \frac{[ML_2]}{[ML][L]} \tag{7.3}$$

The ML complexes and free ligand groups L form the chain end whereas the ML_2 complexes constitute the bonds between monomers. The dissociation rate of ML_2 complexes k_{d2} determines the lifetime of a bond. It is given by $k_{d2} = k_{a2}/K_2$ where K_2 is the stability constant of an ML_2 complex.

In most cases for ML complexes in aqueous solutions the binding of a ligand to a metal ion involves the rapid formation of an intermediate outer sphere complex, which is an ion pair between the ligand and hydrated metal, and the expulsion of a water molecule. Because of the slowness of the latter the formation of ML depends on the water-exchange rate of the metal ion [88]. Accordingly, this is the rate limiting step and the rate constant of complex formation can be written as

$$k_{a1} = \frac{K_{os}}{k_{-w}} \tag{7.4}$$

where k_{-w} is the rate constant of dehydration and K_{os} is the equilibrium constant of the intermediate outer sphere complex. The dehydration rate is characteristic for a given metal ion at a given temperature. Table 7.1 presents the approximate dehydration rates of some ions, taken from Morel and Hering [89]. The equilibrium constant K_{os} primarily

Table 7.1: Approximate rate constants of dehydration for different metal ions at room temperature [89].

metal ion	k_{-w}/s^{-1}	metal ion	k_{-w}/s^{-1}
Pb^{2+}	7.10^9	Fe^{2+}	4.10^6
Cu^{2+}	1.10^9	Ni^{2+}	3.10^4
Cd^{2+}	3.10^8	Fe^{3+}	2.10^2
Zn^{2+}	7.10^7	Cr^{3+}	5.10^{-7}

depends on the charges of the ligand and the metal ion and on the ionic strength. It can be

calculated from statistical considerations [89]. For divalent metal ions and neutral ligands such as Fe^{2+} and 1,4-bis-(2,2´:6´2´´-terpyridine-4´-yl)-benzene used for the formation of Fe-MEPE in this work, K_{os} is approximately 3.10^{-1} M^{-1} [83]. Thus, the rate constant k_{a1} is primarily determined by the metal ion and not by the ligand. For an ML_2 complex, the association rate constant k_{a2} is determined by removal of a water molecule from an ML complex. This is generally faster than the dehydration of a free metal ion, so that $k_{a2} > k_{a1}$. Thus, Equation 7.4 gives a lower limit for k_{a2}. A rough estimate yielding a upper limit for the life time of a coordinative bond can be obtained as $\tau_B = 1/k_{d2} \approx K_2/(k_{-w}K_{os})$. As can be seen from the values of k_{-w} presented in Table 7.1 the kinetics of dehydration varies strongly from one metal ion to another. Because of these large differences the properties of coordination polymers depend strongly on the metal ion used. The dynamics also changes drastically if the valence state of the ion changes, as seen in the Table by comparison of Fe^{2+} and Fe^{3+}.

In the literature the stability constants K_1 and K_2 for the Fe(II)-MEPE complex are given as 10^7 M^{-1} and 10^{14} M^{-1}, respectively. These values were determined in 1966 by Holyer et al. for the monotopic ligand Fe-Terpy (Fig. 1.2b) by means of stopped-flow measurements [88] and are adopted also for Fe-MEPE. We note that although the association rate constant $k_{a2} > k_{a1}$ for the reasons explained above, for most coordination complexes the stability constant $K_2 < K_1$ because the first ligand group causes some repulsions for the second ligand group. The value for K_2 of 10^{14} M^{-1} for Fe(II)-Terpy given by Holyer et al. is unusually high and new measurements are needed for verifying this value. On the other hand, these values were commonly used in the literature for calculations of the chain length of Fe-MEPE in solution [14, 90]. A lower value of K_2 would result in a lower estimate of the chain length of Fe-MEPE.

7.2.2 Living polymers

The behavior of supramolecular polymers depends strongly on the lifetime of a bond τ_B as compared to the time scale of interest t. For $\tau_B \gg t$, polymers behave as ordinary, covalent polymers with a fixed length distribution. For $\tau_B \ll t$, however, every functional group changes frequently between the free and bonded state within a time t, so that a state of dynamic equilibrium is reached. If this is the case, the supramolecular polymer represents a living polymer (or equilibrium polymer).

In many cases, living polymers have the characteristics of ordinary polymers such as low osmotic pressure, high viscosity and viscoelasticity at higher concentrations. On the other hand, the possibility of the chains to break and recombine on experimental time

scale also introduces new features. For instance, the chain length distribution is not fixed but changes with variable conditions. Because of this, tuning the properties of these polymers is possible by varying the concentration, the solvent, the pH and the temperature. Whereas living polymers exhibit typical polymer properties at low temperature, such as a high viscosity and elasticity, the chains break into shorter units at elevated temperature and behave more liquid-like. Another difference with ordinary polymers is the thixotropic behavior of living polymers: When a solution of living polymers is sheared, some bonds may break, leading to a lower viscosity. When the shear is stopped, the bonds are restored and the viscosity reaches its initial state again after some time.

Fe-MEPE used in this work is a water-soluble living polymer consisting of coordinative bonds. It shows all characteristics mentioned above. These are examined in the group of Kurth and Möhwald in the Max-Planck Institut für Kolloid- und Grenzflächenforschung in Potsdam/Golm. In the present work the uptake of Fe-MEPE in the mesopore channels of SBA-15 by adsorption from solution has been studied. Basic aspects of the adsorption from solution are introduced in the next section.

7.3 Sorption

Liquids and solids can bind molecules from their environment. This process is referred to as *sorption*. The substances can penetrate into the interior of the condensed phase (sorbent) or can accumulate at its surface. The former process called *absorption*, the latter process *adsorption*. In that case, a gas or component of liquid mixture forms a molecular or atomic film at the surface. Thus, sorption is a generic name for adsorption and absorption [91]. Following Falbe [92] the term sorption can be extended to a general concept encompassing adsorption, absorption, ion exchange, and precipitation. In all these processes, a substance is taken up (immobilized) by another substance that is in contact with it. The general term sorption is used if the immobilization is based on more than one of these processes or is not precisely known. Below, some forms of sorption that are relevant in this work will be introduced.

7.3.1 Adsorption

Adsorption is the most important process among all forms of sorption and represents an accumulation of substances at the surface of a solid or liquid. Let us first introduce the key definitions. The material in the adsorbed state is called *adsorbate* and the substance to

be adsorbed is called the *adsorptive*. The substance, onto which adsorption takes place, is the *adsorbent*. In general adsorption is an exothermic process ($\Delta H < 0$). Depending on the magnitude of the adsorption enthalpy and on the type of bonding involved, adsorption can be classified as follows:

1. *Physical sorption or physisorption*. Here the adsorbate is held to the surface by relatively weak van der Waals forces and multiple layers may be formed with nearly the same heat of adsorption. The heat of physisorption of gases and vapors is of the same order of magnitude as the heat of condensation of the vapor. Therefore this type of adsorption is stable only at temperatures below 150°C.

2. *Chemical sorption or chemisorption*. This involves an exchange of electrons between specific surface sites and adsorbed molecules and, as a result, a chemical bond is formed. Chemisorption is characterized by interaction energies between the surface and adsorbate comparable to the strength of chemical bonds and is therefore much stronger and stable up to higher temperatures than physisorption.

7.3.2 Electrostatic sorption (ion exchange)

At a fist glance, adsorption and ion exchange are two different phenomena with diverse characteristics. Nevertheless ion exchange is similar to adsorption, since mass transfer from a fluid to a solid phase is common in both process, i.e. they are both diffusion processes. Ion exchange is a term reserved for Coulomb attractive forces between ions and charged functional groups. The exchange of ions of the same charge sign takes place between a solution and an insoluble solid in contact with it, or between two immiscible solvents one of which contains a soluble material with immobilized ionic groups. In most cases the term is used for purification, separation, and decontamination processes of aqueous and other ion-containing solutions with solid polymeric or mineralic ‘ion exchangers’. Commonly, the latter are solid materials (stationary phase) capable of taking up charged ions from a solution and releasing an equivalent amount of other ions into the solution (mobile phase). The ability to exchange ions is due to the properties of the structure of the materials. The exchanger consists of a so-called matrix with positive or negative excess charge. This excess charge is immobilized in specific locations on the stationary phase and is compensated by the *counter ions*, which can move within the free space of the matrix and can be replaced by other ions of equal charge sign [93]. Typical ion exchangers are ion exchange resins (functionalized porous or gel polymers), zeolites,

clays, and soil humus. Normally, an exchanger has a large surface area and pores of variable size and shape. Few inorganic exchangers contain pores of uniform cross section. An example for this kind of exchangers are zeolites. Ordered mesoporous silicas such as MCM-41 or SBA-15 containing aluminum in the framework also have good application potentials as an exchanger in separation processes. Ion exchangers can be unselective or have binding preferences for certain ions or classes of ions depending on their chemical structure.

The characteristic difference between adsorption and ion-exchange is that the latter is a stoichiometric process, i.e., for every ion that is removed, an ion of the same sign is released into the solution. Adsorption from solution can also be considered as a displacement process at the surface, but this is not strictly stoichiometric as in ion exchange.

Ion exchange can be seen as a reversible reaction involving chemically equivalent quantities [94]. A typical ion exchange is represented in the following equation

$$\mathbf{R}^- A^+ + B^+ = \mathbf{R}^- B^+ + A^+ \tag{7.5}$$

In Equation 7.5 $\mathbf{R}^-$, represents the matrix. The ion exchange takes place if the matrix has a selectivity for B^+ ions. The cation A^+, which was originally balancing the negative charge on the matrix, must not be too strongly held by the matrix as otherwise no exchange will occur. The process of Eq. 7.5 form the basis of cation exchange chromatography. If the matrix contains cationic sites, it is capable of exchanging anions, and the process is applied in anion exchange chromatography. The characterization of an ion exchange as a chemical process is rather misleading. Ion exchange is in principle a redistribution of ions between two phases by diffusion, and chemical factors are less significant or even absent. For this reason the heat evolved in the course of ion exchange is usually very small to negligible, often less than 2 kcal mol^{-1} [93]. Only when an ion exchange is accompanied by a reaction such as neutralization can the the process be characterized as 'chemical'.

7.4 Sorption equilibrium

7.4.1 General description

Adsorption from solution onto inert surfaces represents a displacement process at the surface and follows the general principles of thermodynamic reaction equilibria. If there is only one adsorbable component in the solution, as is the case in this work, the equilibrium can be characterized by three factors. These are the equilibrium concentration in the solution, the surface concentration at equilibrium, and temperature. Accordingly, at constant

temperature one has the equilibrium condition

$$a_{eq} = f(c_{eq})_{T=const} \tag{7.6}$$

where a_{eq} is some measure of the surface concentration of the sorptive at equilibrium, and c_{eq} is the equilibrium concentration of sorptive in the solution. After achieving equilibrium at a given temperature, a plot of the surface concentration of sorbent vs. the equilibrium concentration of solution yields the so-called *sorption isotherm*. In an adsorption process, if the adsorbent represents a powder of well-defined specific surface area, the equilibrium amount of adsorbent is commonly expressed as the amount per unit mass of adsorbent (specific adsorption) and is obtained from

$$a_{eq} = \frac{V}{m}(c_0 - c_{eq}), \tag{7.7}$$

where c_0 is the initial concentration in solution, V is the volume of the solution, and m is the mass of the solid (adsorbent).

7.4.2 Isotherm equations

Experimental adsorption isotherms may be represented by a mathematical isotherm equation, but there is no single equation universally describing all experimental isotherms. Instead, a series of different equations exits and the applicability of them is to be checked on a case-by-case basis. Three simple isotherm equations are commonly used in adsorption from solution: Henry equation, Freundlich equation, and Langmuir equation. These isotherms are sketched in Figure 7.4.

7.4.2.1 Henry adsorption isotherm

The Henry equation assumes a linear relation between the loading of the adsorbent and the equilibrium concentration in the solution. Accordingly, the adsorbed amount of a substance per unit of adsorbent (a_{eq}) is directly proportional to the equilibrium concentration of the solution (a_{eq}) and depends only on the so-called Henry coefficient (K_H).

$$a_{eq} = K_H \cdot c_{eq}. \tag{7.8}$$

Thus the Henry coefficient is the ratio of the loading of the adsorbent and the equilibrium concentration of the solution and is constant for an achieved equilibrated state. Henry isotherm applies to any adsorption equilibrium as a limiting law for low concentrations, i.e,

$$\lim_{c \to 0}(a_{eq}/c_{eq}) = K_H(T).$$

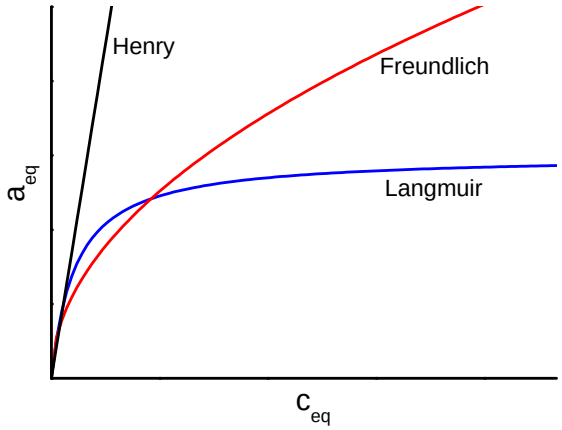

Figure 7.4: Schematic plot of three most common adsorption isotherms; a_{eq}: The loading of adsorbent at the equilibrium; c_{eq}: The concentration of the solution at the equilibrium.

7.4.2.2 Freundlich adsorption isotherm

This isotherm equation is an empirical relation developed by Freundlich and Küster to describe a non-linear dependency of the loading on the equilibrium concentration in the solution (see Fig. 7.4). It is mathematically expressed as

$$a_{eq} = K_F \cdot c_{eq}^{1/n} \tag{7.9}$$

where K_F is the Freundlich constant and $1/n$ is an arbitrary constant ($n > 1$) for a given adsorbate and adsorbent at a particular temperature. In a double-logarithmic plot Equation 7.9 leads to a straight line in form $lna_{eq} = lnK_F + 1/n \cdot lnc_{eq}$. The parameter K_F and n can be determined by a linear regression. The Freundlich equation, though commonly used, is thermodynamically inconsistent as it does not give Henry's law for $c \rightarrow 0$. This is evident from the fact that in the plot of $\ln a_{eq}$ vs. $\ln c_{eq}$ the slope does not approach 1 as c_{eq} is decreased.

7.4.2.3 Langmuir adsorption isotherm

The Langmuir equation relates the surface concentration of the adsorptiv to equilibrium concentration in the solution at a fixed temperature. It was first derived by Irving Langmuir in 1916 on the following assumptions.

1. The molecules are adsorbed into discrete binding sites at the surface of the adsorbent.

2. Each site can bind only one molecule.

3. The binding energy is independent of the presence of the other bound molecules.

The Langmuir equation has following form:

$$a_{eq} = a_m \frac{K_L \cdot c_{eq}}{1 + K_L c_{eq}} \tag{7.10}$$

where a_m is the maximum loading of sorbent with sorptive (monolayer capacity). K_L is the Langmuir adsorption coefficient which increases with the adsorption strength and with a decrease in temperature.

Equation 7.10 reduces to Henry's law in the limit of low concentrations. At high concentrations it approaches a maximum of the sorption a_m (see Fig.7.4) and thus accounts for the finiteness of the sorption space, which is not the case in the Henry and Freundlich equations.

7.5 Sorption kinetics

The time dependent devolution of the sorption process up to achieving the equilibrium is referred to as sorption kinetics. It is determined by the character and magnitude of transport resistances which counteract the mass transfer of sorptive from the solution up to the sorption centers at the outer or inner surfaces of the adsorbent. Commonly, the following steps are considered [95].

1. Film diffusion: diffusion of the sorptive through a boundary layer or film adjacent to the external surface of the sorbent (interphase diffusion).

2. Pore diffusion: diffusion of the sorptive through the porous interior of the sorbent where the local sorption centers are located (intraparticle diffusion)

3. Sorption: accumulation of sorptive on the sorption centers of the inner sorbent surface.

The sorption is normally a fast processes. Therefore dependent on the hydrodynamic conditions, either the film diffusion and/or the pore diffusion is the rate determining step. The driving force for film diffusion and pore diffusion is the resulting concentration gradient of the adsorptive.

For quantitative studies of the sorption kinetics, a solution of initial concentration c_0 and volume V is brought into contact with the sorbent powder of mass m, and the residual

concentration in the supernatant is measured as a function of time t. For each time t there is a mass balance analogous to equilibrium (Eq. 7.7).

$$a_t = \frac{V}{m}(c_0 - c_t) \tag{7.11}$$

where a_t is the loading of sorbent at time t and c_t is the sorptive concentration in solution until the point in time t.

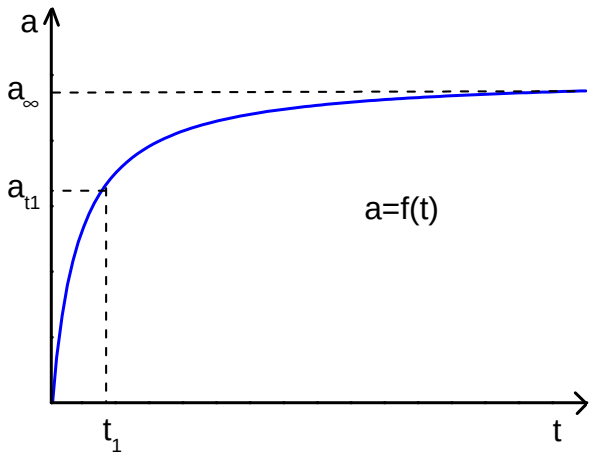

Figure 7.5: Schematic plot of a kinetic curve.

A kinetic curve can be expressed in the form $a = f(t)$ (see Figure 7.5). At the point in time t an average loading of the sorbent a_{t1} is then calculated. The loading a_∞ is only reached for sufficiently long sorption times.

In this work the uptake kinetics of Fe-MEPE in SBA-15 is analyzed according to standard kinetic models for diffusion controlled- systems proposed by J. Crank [96]. For a system in which the sorption is controlled by the diffusion through the surface layer (controlling resistance) the uptake curve following a step change in concentration is given by

$$\frac{a_t - a_*}{a_\infty - a_*} = 1 - e^{-\alpha k t} \tag{7.12}$$

where a_∞ is the final loading at equilibrium with the solution, a_t is the sorbate loading time t, a_* is the initial loading before the step change in concentration, α is the mass transfer rate coefficient and k is the ratio of the external area to volume. After its conversion and linearization Equation 7.12 take the form $ln(1 - (a_t - a_*)/(a_\infty - a_*)) = -\alpha k t$.

Hence, the plot $ln(1-(a_t-a_*)/(a_\infty-a_*))$ vs. time (t) should give a straight line through the origin with slope (-α k) allowing straightforward extraction of the mass transfer coefficient α if the sorption is controlled by the diffusion through the surface layer. Equation 7.12 can be applied regardless of the dimensionality of the adsorbent pore system. If the sorption rate is controlled by internal diffusion (diffusivity D), the following kinetic equations apply:

for sphere (diffusion in 3 dimensions)

$$\frac{a_t - a_*}{a_\infty - a_*} = 1 - \frac{6}{\pi^2}\sum_{n=1}^{\infty}\frac{1}{n^2}exp(-n^2\pi^2 Dt/R^2), \tag{7.13}$$

for slab (one-dimensional diffusion)

$$\frac{a_t - a_*}{a_\infty - a_*} = 1 - \frac{8}{\pi^2}\sum_{n=0}^{\infty}\frac{exp[-(2n+1)^2\pi^2 Dt/4l^2]}{(2n+1)^2} \tag{7.14}$$

where R is the radius of the sphere and l the half thickness of the parallel sided slab. Up to about 50% uptake the Equations 7.13 and 7.14 are well approximated by the limiting form for the short times

$$\frac{a_t - a_*}{a_\infty - a_*} \approx 2k\sqrt{\frac{Dt}{\pi}}. \tag{7.15}$$

If the sorption process is controlled by the internal diffusion process the plot $(a_t - a_*)/(a_\infty - a_*)$ vs. $\sqrt{t}$ should give a straight line through the origin with slope $2k\sqrt{D/\pi}$. It is worth noting that a sorption rate measurement can yield only the diffusional time constant R^2/D or l^2/D. The estimation of diffusivity requires either knowledge or an assumption about the dimensionality and extension of the pore system. For our cylindrical pore systems these quantities can be estimated from nitrogen adsorption measurements.

Chapter 8

Materials and Methods

8.1 Materials

8.1.1 Fe-MEPE

The ligand 1,4-bis(2,2´:6´2´´-terpyridine-4´-yl) benzene **(1)** and Fe-MEPE **(2)** (see Figure 1.2a) were synthesized as described elsewhere [97, 98, 99]. Terephthaldialdehyde, acetylpyridine, ammonia solution (25%), and ethanol were purchased from Sigma-Aldrich and used without further purification. Throughout this work Fe-MEPE was used in the form of the acetate salt. The assembly of ligand **(1)** (Fig. 1.2a) and $Fe(OAc)_2$ (Sigma-Aldrich, 99.995%) was carried out in 75% acetic acid. In view of the oxidation sensitivity of $Fe(OAc)_2$ after contact with air, the Fe-MEPE material used in most of this work (material I) was prepared with a small excess of the iron salt. The ^{15}N NMR measurements aimed at determining the average chain length of Fe-MEPE before and after uptake in the pores were performed with a Fe-MEPE sample (material II) assembled under inert conditions from freshly prepared $Fe(OAc)_2$ and ^{15}N labeled ligand at an initial metal-to-ligand stoichiometry of 0.8:1. The NMR measurements revealed that the stoichiometry of the product was close to 0.9:1. Complementary ^{15}N NMR measurements to characterize the Fe-MEPE in the solid state were made with two unlabeled Fe-MEPE samples (material III) and (material IV) of 1:1 and 0.8:1 metal-to-ligand stoichiometry, respectively.

8.1.2 Fe-Terpy

The ligand 2,2´:6´2´´-terpyridine (Terpy) **(3)**, (see Figure 1.2b) was purchased from Sigma-Aldrich (98%) and used without further purification. Fe-Terpy **(4)**, $Fe(Terpy)_2(OAc)_2$ (Fig.

1.2b), was prepared according to standard procedures published by Margan and Burstall using freshly prepared $Fe(OAc)_2$ and Terpy in 75% acetic acid [100].

8.1.3 Uptake isotherms

8.1.3.1 UV-vis calibration curves

For determining the adsorbed amount of Fe-MEPE and Fe-Terpy from solution in the silica by UV-vis measurements data were collected first to draw UV-vis calibration curves. For this purpose different concentrations of Fe-MEPE (in H_2O and in KOAc) and Fe-Terpy (in H_2O) were prepared and the absorbance of the MLCT band, which is very specific for the complexes, was plotted against the concentrations as shown in Figure 8.1. The equations obtained through linear regression of the calibration curves (see Table

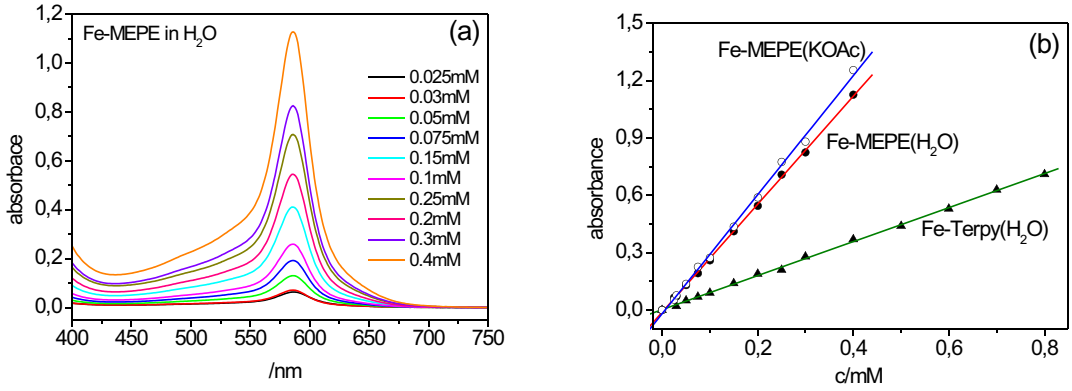

Figure 8.1: (a) Absorbance of the MLCT band of Fe-MEPE solved in H_2O (milli-Q) in different concentrations; (b) calibration curves of Fe-MEPE in H_2O and in KOAc and of Fe-Terpy in H_2O.

8.1) were used for the determination of the remaining concentration of the complexes in solution after adsorption in silica. The main information obtained from the calibration curves is listed in Table 8.1. Thus the frequency of UV transition bands of Fe-MEPE depends on the pH of solution. So the frequency of MLCT band of Fe-MEPE in milli-Q water (pH 5.5) shifts by 15 nm if Fe-MEPE is dissolved in 0.1M KOAc solution (pH 7.25)

Table 8.1: Information obtained from the calibration curves

sample	λ_{MLCT}/nm	ε/L mol^{-1} cm^2	equation
Fe-MEPE in H_2O	586	26100	$y = 2.83x - 0.011$
Fe-MEPE in KOAc	601	27200	$y = 3.11x - 0.002$
Fe-Terpy in H_2O	552	9490	$y = 0.889x + 0.003$

λ: wave length of MLCT transition, ε: molar absorption coefficient

8.1.3.2 Uptake in the silica

The uptake of the MEPE in the silica matrix was studied by bringing a mass m_s of silica into contact with a volume V_l of aqueous MEPE solution of an initial concentration c_0. The mass m_t of the MEPE complex included in the matrix after a time t was calculated from the corresponding solution concentration c_t by the relation

$$a_t = \frac{m_t}{m_s} = \frac{MV_l(c_0 - c_t)}{m_s} \tag{8.1}$$

where M is the molar mass of the entity embedded in the pores ($M = 714.6$ g mol^{-1} for Fe-MEPE acetate). The concentration c_t was obtained from UV-vis measurements of the MLCT band of Fe-MEPE in the supernatant solution using the equations listed in Table 8.1. Experiments were made at initial concentrations c_0 of MEPE in a range from 0.4 to 1.2 mM and with different MEPE-to-silica silica mass ratios $\mu = m_{MEPE}/m_s$ with $m_{MEPE} = MV_lc_0$ by dissolving appropriate amounts of Fe-MEPE in the volume V_l (50 ml) of milli-Q-water (pH=5.5) or 0.1 M potassium acetate solution (KOAc, pH= 7.25). For studying the time dependence of the uptake, the suspensions were slowly rotated in a test tube rotator at the chosen temperature and the concentration was measured after centrifugation (4000 rpm for 15 min) and taking small aliquots of the supernatant for UV-vis analysis. At the end of the uptake time, when m_t/m_s had reached a steady value (a_∞), the solid product, having an intense violet color, was washed two times with 50 ml H_2O and dried at 60°C before further analysis.

8.1.3.3 Settling of Fe-MEPE during centrifugation

Blank measurements in the absence of the silica (but otherwise under identical conditions as in the determination of the uptake isotherms) were made in order to see if centrifugation is causing gravitational settling of Fe-MEPE, which would cause systematic errors in the

determination of the uptake. Results for Fe-MEPE in milli-Q water at 50°C are presented in Figure 8.2, where the depletion of the solution (in percent of its original concentration) due to gravitational settling is plotted as a function of time t elapsed since the beginning of the experiment (start of rotation of the sample at the chosen temperature). Open symbols

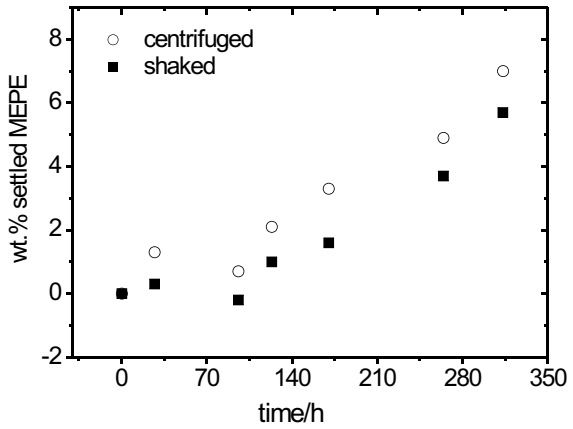

Figure 8.2: Blank measurement showing the effect of gravitational settling induced by centrifugation of a 0.4 mM Fe-MEPE solution in water at 50°C. The data give the w % of settled MEPE after 15 min centrifugation (open circles) and after centrifugation and subsequent shaking of the samples (full symbols) as a function of the time elapsed since sample preparation and rotation at 50°C.

give the depletion measured immediately after centrifugation, full symbols the respective depletion after centrifugation and subsequent shaking of the sample. Figure 8.2 shows that the depletion effect caused by settling of MEPE is increasing with the time over which the samples had been rotated at the elevated temperature. This effect is attributed tentatively to a gradual increase of the mean molar mass of Fe-MEPE in the aqueous medium. In quantitative terms, this effect is rather small (less than 3%) for times up to 150 h, i.e., for all data in the fast-uptake regime. However, progressively greater settling effects were observed at longer times (nearly 20% after 800 h). The uptake data for the slow-uptake regime presented in Chapter 9 (samples CA-MEPE-7 and CA-MEPE-8) extend to uptake times of or up to 300 h. They were corrected for the effect of gravitational settling.

8.2 Methods

8.2.1 XPS

XPS measurements were carried out in Fritz-Haber Institut using a modified LHS/SPECS EA200 MCD system equipped with a Mg Kα source (1253.6 eV, 168 W). The binding energy scale of the system was calibrated using Au4f$_{7/2}$ = 84.0 eV and Cu2p$_{3/2}$ = 932.67 eV from foil samples. The powder samples were placed in a stainless steel sample holder with a 0.6 mm deep rectangular well, covering an area of (12×8) mm^2. During the XPS experiments the pressure in the UHV analysis chamber increased to about 1×10^{-9} mbar. The binding energies of the SBA-15 based samples were referred to the Si2p signal of silica at 103.6 eV to correct for charging. Data reduction included satellite deconvolution, and subtraction of a Shirley background. Quantitative data analysis was performed on the basis of peak areas by fitting with 30/70 Gauss-Lorentz product functions. Atomic ratios were calculated using empirical cross sections [101].

8.2.2 AAS

Atomic absorption spectroscopy (AAS) measurements of Fe in the silica matrix were made in the analytic chemistry department of TU-Berlin by a 1100B Perkin-Elmer Flame AAS spectrometer after dissolving the silica matrix in 25 ml of 0.1 M NaOH. To dissolve the Fe-MEPE which precipitates in this high pH region, 2 ml of each sample solution was acidified with concentrated HCl and filled up to 10 ml with milli-Q water. After this pretreatment flame atomization was performed in air-acetylen gas mixture. Calibration was done by 0.1 M $FeCl_3$ standard (titrisol) by means of the standard addition method.

8.2.3 UV-Vis

UV-vis absorption spectra were recorded on a Carry 50 UV-vis spectrometer by Varian using quartz glass cells of 1 mm thickness.

8.2.4 ^{15}N solid-state NMR

The solid-state ^{15}N NMR measurements were performed in the chemistry department of FU-Berlin on a Bruker MSL-300 instrument operating at 7 Tesla, equipped with a Chemagnetics-Varian 6 mm pencil CPMAS probe. The samples were spun at 6-8 kHz under magic angle spinning (MAS) conditions. The ^{15}N MAS spectrum was recorded

employing $\pi/2$ pulse-sequence, with a 90°-pulse length of 4.5 sec. The $\{^{1}H\}$-^{15}N CPMAS spectra were recorded using a cross polarization contact time of 5 ms, the typical ^{1}H-90°-pulse lengths were 3.5-4.5 sec. All ^{15}N chemical shift values are referenced to solid $^{15}NH_4Cl$.

Chapter 9

CA doped SBA-15 as a host for MEPE*

Abstract

The adsorption of a metallo-supramolecular coordination polymer (Fe-MEPE) in the cylindrical pores of SBA-15 silica with pure and carboxylic acid (CA) carrying pore walls has been studied. Fe-MEPE is an intrinsically stiff polycation formed by complexation of Fe(II)-acetate with an uncharged ditopic bis-terpyridine ligand. The adsorption affinity and kinetics of the Fe-MEPE chains is strongly enhanced when the pore walls are doped with CA, and when the pH of the aqueous medium or temperature is increased. The initial fast uptake is connected with a decrease of pH of the aqueous solution, indicating an ion-exchange mechanism. It is followed by a slower (presumably diffusion-controlled) further uptake. The maximum adsorbed amount of Fe-MEPE in the CA doped material corresponds to a monolayer of Fe-MEPE chains disposed side-by-side along the pore walls. The stoichiometry of Fe-MEPE in the pores (determined by XPS) was found to be independent of the loading and similar to that of the starting material. The mean chain length of Fe-MEPE before and after embedding in the CA doped matrix was studied by solid-state ^{15}N NMR using partially ^{15}N-labeled Fe-MEPE. It is shown that the average chain-length of Fe-MEPE is reduced when the complex is incorporated in the pores.

*In modified form published as: Akcakayiran, D.; Mauder, D.; Hess, C.; Sievers, T. K.; Kurth, D. G.; Shenderovich, I. G.; Limbach, H.-H.; Findenegg, G. H. *J. Phys. Chem. B.*, **2008**, *112*, 14637

9.1 Introduction

A new era in inclusion chemistry began with the discovery of periodic mesoporous materials such as SBA-15 [4] which constitutes a 2D-hexagonal arrangement of cylindrical pores with diameters in a range 6-12 nm. Because of their wide pore openings, narrow pore size distribution and their large internal surface area, these materials have a high potential as catalyst supports [102], [103], adsorbents and host materials for organic guest molecules. Incorporation of functional molecular components or metal ions into such a mesoporous oxide matrix can be carried out by different ways, namely by a one-pot synthesis [104], ion-exchange in as-synthesized material [105, 106, 107], covalent grafting followed by ion exchange [108], solid state grinding [109] or by direct loading sorption [110, 111]. Among the incorporated functional molecular components dyes and related molecules represents an important class. For instance, Fe-MEPE [110], methylen blue, rhodamin, thionine dyes [112], coumarine derivate dyes [113], fluorescein [114], direct blue 71 dye [115] and chromophores [116] have been incorporated into mesoporous silica matrices. In many cases, the interaction between the dye molecules and the host system causes a shift of UV-vis absorption bands. Due to this interaction with the host, a higher degree of organization and increased diffusion stability of the guest can be achieved, which is of importance for potential applications in lasers, optical sensors, photochromic materials and photocatalysts [117, 116, 118].

This Chapter diels with the uptake of a **me**tallo supramolecular coordination **p**oly-**e**lectrolytes (MEPE) in SBA-15 type silica matrices. MEPE materials are prepared by a metal-ion induced self-assembly of two-valent transition metal ions with ditopic terpyridine ligands. The resulting materials exhibit several potentially useful properties such as electro-chromic behavior [119, 120, 121], molecular magnetism [122], as well as dynamic properties due to the labile metal ion ligand interaction [14]. The properties of MEPE are readily manipulated by simply changing the ligands or metal ions. The substance studied in this work, Iron-(II)-MEPE **(2)** (see Fig. 7.1 in Section 7.1) is assembled from Fe-(II)-acetate and 1,4-bis (2,2´:6´2´´-terpyridine-4´-yl) benzene **(1)**, which results in stereochemically well-defined octahedral coordination geometry with D_{2d} symmetry [84]. At an exact 1:1 stoichiometry of Fe-(II) to ligand, the average length of the Fe-MEPE chains in aqueous solution can grow to very high values, depending on concentration, temperature, and pH. Small deviations from 1:1 stoichiometry are causing a reduction of chain-length [14]. Hence, the metal-to-ligand stoichiometry is another important parameter affecting the properties of the resulting assemblies and the amount of MEPE adsorbed in the pores.

A prominent feature of Fe-MEPE is the positive charge along the backbone. This implies that screened electrostatics plays an important role in the interaction of MEPE with the silica pore wall, which at ambient pH is negatively charged due to the weakly acidic surface silanol groups. It is of interest to see if this charge effect can be boosted by decorating the pore walls with acidic groups. For this purpose, a chemically modified SBA-15 material with short-chain carboxylic acid groups grafted to the pore walls (CA-SBA-15) was prepared (see Fig. 1.2c). The carboxylic acid (CA) functionality was chosen because the ionized form of these groups is similar to the acetate ions which form the counter ions of MEPE in solution. The transfer of the MEPE polycations from solution into the pores may represent an ion exchange process, involving either the ionization of carboxylic acid groups at the pore wall and a release of protons or the release of the counterions of MEPE polycations. In either case, the ion exchange represents an entropic driving force for the adsorption of MEPE in the pores. To test this possible mechanism we made a comparative study of the uptake of Fe-MEPE in pure ('native') and CA-doped SBA-15 materials. We also studied the effect of temperature and pH on the uptake of MEPE, as both can affect the sorption process.

Another interesting question concerns the mechanism of the MEPE uptake and the mean chain-length of MEPE in the pores. It is known that in aqueous media, due to the labile nature of the metal ion ligand interaction, MEPE represent dynamic equilibrium polymers, i.e., assemblies of different length coexist in solution [123]. It is feasible that short chains adsorb more easily into the pores, or that longer chains break up into shorter chain segments when entering the pore. These processes would lead to a shorter chain length of MEPE in the pores as compared to the solution. Alternatively, short chain segments may merge into longer ones in the pores if the pore walls stabilize the chains. Two ways for studying the chain length of MEPE in the pores are used in this work: (I) Indirect information is derived from the number ratio of metal ions to carbon or nitrogen atoms in the pore, which can be determined by X-ray photoelectron spectroscopy (XPS). (II) A more direct way is to measure the ratio of terminal and internal terpyridine groups of the Fe-MEPE using solid state NMR spectroscopy. This latter method requires ^{15}N NMR measurements, which made it necessary to synthesize a ^{15}N-labeled ligand.

A combination of experimental techniques was used to characterize pure and CA doped SBA-15 materials and the state of Fe-MEPE in the pores. The silica samples before MEPE incorporation were characterized by nitrogen adsorption, small angle X-ray diffraction (SAXD), solid state ^{29}Si and ^{13}C NMR, whereas Fe-Terpy, Fe-MEPE and Fe-MEPE incorporated in the silica materials were studied by UV-vis-spectroscopy, atomic

absorption spectroscopy (AAS), X-ray photoelectron spectroscopy (XPS) and ^{15}N solid-state NMR. The materials and methods used in this study have been already introduced in Chapter 2 and in Chapter 8, and the results are presented in Section 9.2. The Discussion (Section 9.3) is focused on the driving forces for the uptake of MEPE in the pores, the maximum uptake, and the stoichiometry and average chain length of Fe-MEPE in the pores of pure and CA doped SBA-15. Finally, Section 9.4 winds up the main findings of the work.

9.2 Results

9.2.1 Characterization of silica hosts

The synthesis of SBA-15, 10-CA and 20-CA silica materials used as hosts for Fe-MEPE were described in Section 4.1. The physical properties of silica materials used are summarized in Table 9.1.

Table 9.1: Characterization of pure and-COOH-functionalized SBA-15 by nitrogen adsorption SAXD and ^{29}Si NMR

sample	a_s/m^{2}g^{-1}	v_p/cm^{3}g^{-1}	D/nm	a_0/nm	x_{COOH}
SBA-15	650	0.89	8.9	11.50	–
10-CA	513	0.97	9.8	12.13	0.19
20-CA	400	0.60	8.0	11.61	0.42

a_s: BET specific surface area, v_p: specific pore volume D: pore diameter (imp. KJS algorithm), a_0: lattice constant, x_{COOH}: mole fraction of carboxylic acid groups on the surface

9.2.2 Characterization of coordination compounds by NMR

The synthesis of Fe-MEPE and Fe-Terpy, the record of UV-adsorption isotherms and the methods used were explored in Chapter 8. The free terpyridine (Terpy) ligand and the Fe-Terpy complex were investigated by ^{15}N CPMAS NMR spectroscopy to determine the chemical shift of the different nitrogen atoms, which is needed for peak assignment of the Fe-MEPE complex. For free Terpy in its energetically preferred trans-configuration two signals at chemical shifts of 252 ppm and 267 ppm appear, resulting from nitrogen atoms on the central ring (◯) and the outer rings (dashed ◯), respectively (Figure 9.1a).

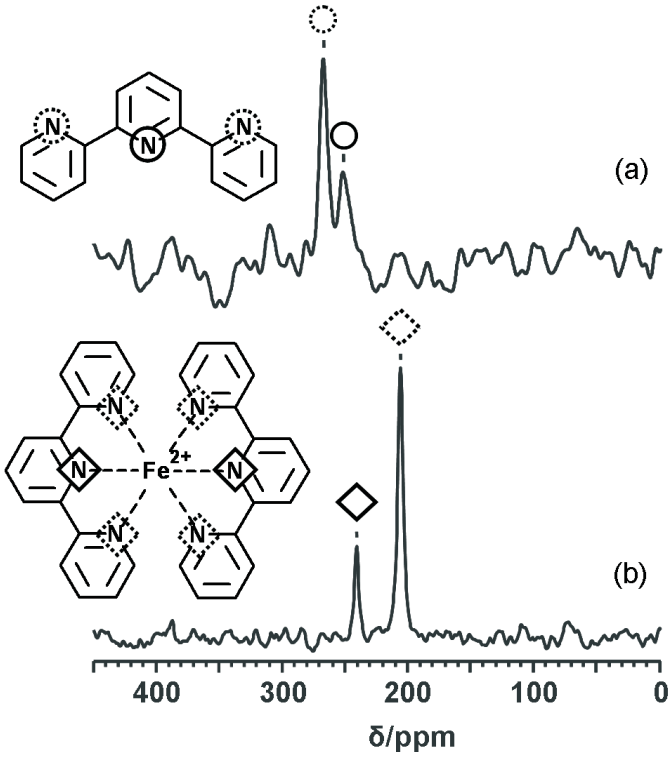

Figure 9.1: Solid-state ^{15}N CPMAS NMR spectra of (a) free ligand Terpy and (b) Fe(Terpy)$_2$OAc$_2$. The signals are assigned to atoms by symbols as follows: ◯ free Terpy; ◊ complexed Terpy. Solid symbols indicate N atoms of the central ring, dashed symbols N atoms of the outer rings.

Figure 9.1b shows the ^{15}N CPMAS NMR spectrum of Fe-Terpy, which is taken as a simple model of a Fe-MEPE unit. For complexation with Fe(II) ions, Terpy molecules have to change their configuration from trans to cis to allow octahedral coordination of the ligands to the center. The presence of the Fe(II) ion and the different ligand configuration have an effect on the chemical shift for the different nitrogen species in the Fe-Terpy complex. The signal at 242 ppm is assigned to the central nitrogen atom of Fe-Terpy, slightly shifted to high field, and the signal at 207 ppm is assigned to the outer nitrogen atoms of Fe-Terpy, shifted 60 ppm to high field, compared to the free ligand.

^{15}N CPMAS NMR spectra of solid Fe-MEPE materials III and IV, having different stoichiometric Fe:ligand ratios (see Section 8.1), are displayed in Figure 9.2. By comparison with the ^{15}N CPMAS NMR spectra of free Terpy and Fe-Terpy (Fig. 9.1) we can assign each peak to the either of the two types of nitrogen atoms. In the Fe-MEPE material with a Fe:ligand ratio of 1:1 only signals from Fe(II)-coordinated ligands (238 and 205 ppm) are detected (Figure 9.2a). This implies that nearly all ligands are coor-

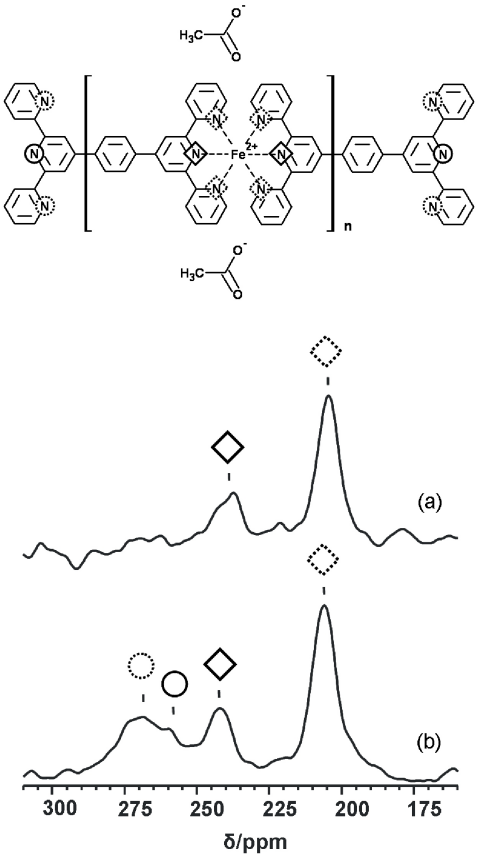

Figure 9.2: Solid state ^{15}N CPMAS NMR spectra of (a) Fe-MEPE material III with an Fe:ligand ratio 1:1; (b) Fe-MEPE material IV with an Fe:ligand ratio of 0.8:1. Fe-MEPE chains of 1:1 stoichiometry (spectrum a) are long and thus end groups are detected. In the material having a ligand excess (spectrum b), uncoordinated N atoms are present at an appreciable concentration.

dinated to two Fe(II) ions, so that the number of non-coordinated nitrogen atoms at the chain ends is too small to be detected by solid state ^{15}N NMR. From this, we conclude that Fe-MEPE with an Fe:ligand ratio of 1:1 consists of long chains. However, as such long chains are hardly soluble in aqueous media, they are unsuitable for uptake studies into the porous matrix. Accordingly, a Fe-MEPE sample with an Fe:ligand stoichiometry of approximately 0.8:1 (material IV) is used because an excess of ligand results in shorter Fe-MEPE chains [14]. The ^{15}N NMR spectrum of this Fe-MEPE sample (Fig. 9.2b) shows two additional signals corresponding to N-atoms in free ligands at chain ends (269 and 259 ppm) besides the signals from coordinated ligands (242 and 206 ppm). This result illustrates that ^{15}N solid-state NMR can be used to estimate the chain-length of

Fe-MEPE by analyzing the signal intensities of coordinated and free N atoms of the ligand. An estimate of the mean chain length of Fe-MEPE before and after inclusion into the pores by signal deconvolution of the respective signals is presented in Section 9.2.5

9.2.3 Effect of CA functionalization on the Fe-MEPE uptake

The uptake of Fe-MEPE (material I) in the silica matrix as a function of time was determined by UV-vis spectroscopy as explained in Section 8.1. The strong MLCT band is ideally suited to quantify the concentration of Fe-MEPE. The uptake of Fe-MEPE into the cylindrical pores of pure and CA doped SBA-15 was studied at different mass ratios of Fe-MEPE and silica matrix μ in a range from 0.05 to 0.3.

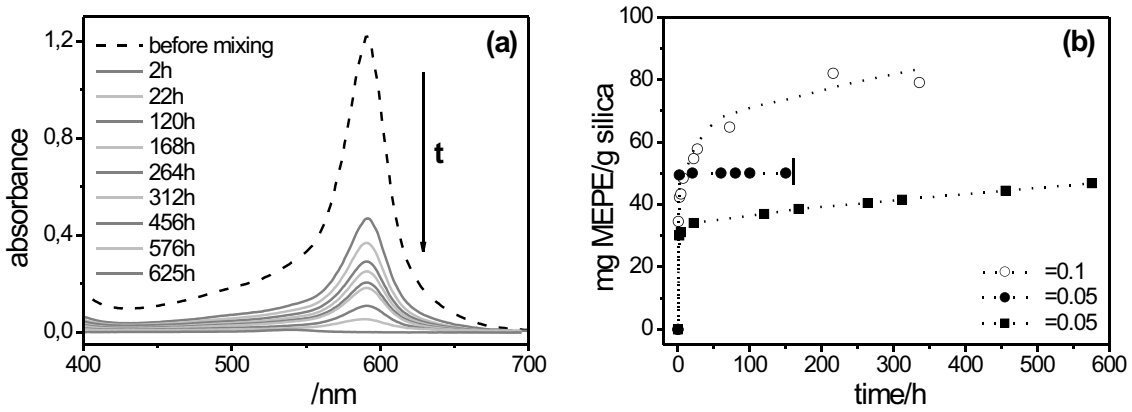

Figure 9.3: Example of the uptake of Fe-MEPE from 0.1 M KOAc into pure SBA-15 and the CA doped material 20-CA: (a) Decrease of the MLCT band of the supernatant solution during an uptake experiment with pure SBA-15; (b) corresponding uptake isotherms into pure SBA-15 (■) and 20-CA (●) at a MEPE/silica mass ratio μ = 0.05, and into 20-CA at μ = 0.1 (○). Curves are drawn to guide the eye.

Figure 9.3 shows a typical example for the decreasing intensity of the MLCT band in the supernatant solution as a function of time (a) , and the respective uptake isotherms (b) for Fe-MEPE in pure SBA-15 and 20-CA. For both samples, we observe a fast initial uptake of Fe-MEPE. This fast process is most pronounced for 20-CA: At a MEPE-to-silica mass ratio μ=0.05, it leads to nearly quantitative uptake of MEPE within 2 h, indicated by a change of the initially deep blue color of the Fe-MEPE solution to completely colorless, while the initially colorless silica turned violet. For pure SBA-15 at the same MEPE-to-silica mass ratio the fast process leads to a lower uptake, but is followed by a much slower

second uptake process that leads to nearly quantitative uptake of MEPE after about 600 h. This slow process also takes place with Fe-MEPE in 20-CA at a higher MEPE-to-silica mass ratio (μ=0.10), where it leads to an increase in the MEPE uptake from 50% to more than 80% of the overall amount after about 200 h (Fig. 9.3b).

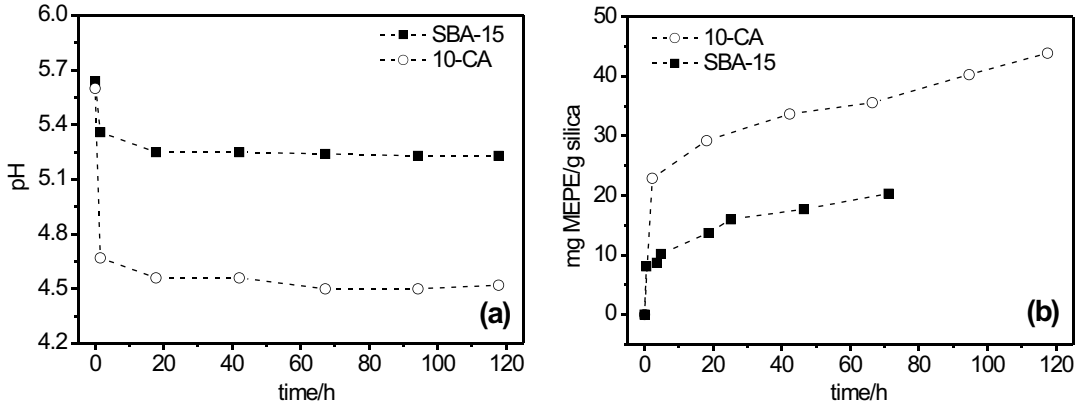

Figure 9.4: Uptake of Fe-MEPE in pure SBA-15 and 10-CA (20°C): (a) Evolution of pH in the aqueous solution before (t=0) and after addition of the silica (t>0); (b) uptake isotherms in the two materials (MEPE-to-silica mass ratio μ=0.10, room temperature). Dashed curves are drawn as a guide to the eye.

It is well-known that SBA-15 materials with carboxylate groups have cation-exchange properties [124]. In order to check whether ion exchange is a driving force in the uptake of Fe-MEPE in the present materials, time dependent measurements of pH were performed with freshly prepared suspensions of the silica materials in aqueous Fe-MEPE solutions in the absence of KOAc. Results for 10-CA and pure SBA-15, both at μ=0.10, are displayed in Figure 9.4a, and the respective uptake isotherms are shown in Figure 9.4b. The initial pH (5.6) represents the value of the MEPE solution in milli-Q water. Addition of the silica causes a decrease in pH, from 5.6 to 5.2 for pure SBA-15 and from 5.6 to 4.5 for 10-CA, during the first 1.5-2 h, that is, in the period of the fast uptake process. Later, during the slow uptake process, the pH of the suspensions remains constant. The finding that the pH change is linked with the fast uptake process of MEPE indicates that ion exchange is indeed involved in this step. Moreover, the larger pH change induced by 10-CA, as compared to the pure SBA-15, is in line with the larger initial uptake of MEPE in 10-CA (Fig. 9.4b).

To assess the influence of pH, and thus the degree of dissociation of the CA groups at the pore wall, a comparison of the uptake of Fe-MEPE from pure water (initial pH 5.5) and from 0.1 M KOAc solution (pH 7.3) was made. Uptake isotherms for MEPE at an

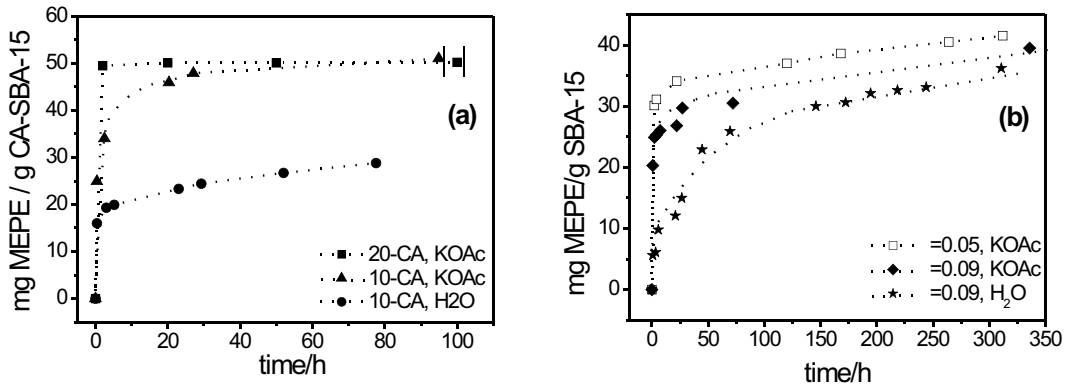

Figure 9.5: (a) Effect of pH on the uptake isotherms of Fe-MEPE in carboxylic-acid doped SBA-15: Fe-MEPE uptake in • 10-CA at pH 5.5; ▲ 10-CA at pH 7.3; ■ 20-CA at pH 7.3; (b): Effect of pH and μ on the uptake isotherms of Fe-MEPE in pure SBA-15: □ at pH 7.3 and μ=0.05, ♦ at pH 7.3 and μ=0.09, and ★ at pH 5.5 and μ=0.09; dashed lines are drawn as a guide to the eye.

initial concentration c_0=0.4 mM, and a MEPE-to-silica mass ratio μ =0.05 are shown in Figure 9.5a. It can be seen that in 10-CA both the fast and the slow uptake process are more effective at the higher pH, at which complete uptake is accomplished within about 50 h. At the lower pH, at which one expects a lower degree of ionization of the CA groups at the pore wall, the fast process leads to a lower initial uptake and the slow process proceeds at a significantly lower rate than at higher pH. Figure 9.5a also indicates that at a given pH (7.3) the uptake of MEPE in 10-CA is less effective than in 20-CA, for which complete uptake is accomplished within 2 h at the given MEPE-to-silica mass ratio. Figure 9.5b shows the uptake isotherms for MEPE in pure SBA-15 at pH 5.5 and pH 7.3. As in the case of CA-SBA-15, at a given MEPE-to-silica mass ratio (μ=0.09) an increase of pH leads to an increase of the adsorbed amount of Fe-MEPE. However, in the case of pure SBA-15 the effect is much smaller than observed in case of CA-SBA-15. Figure 9.5b also shows that the adsorbed amount of Fe-MEPE (nearly 40 mg/g) does not increase when increasing μ, but the uptake at μ=0.05 is rather higher than the uptake at μ=0.09. This is distinctly different from the MEPE uptake in CA-SBA-15, where an increase of μ leads to an increase in the adsorbed amount of MEPE. This shows clearly that the adsorption affinity of MEPE in pure SBA-15 is much less than in CA-SBA-15.

We also studied the effect of temperature on the rate of uptake of Fe-MEPE into the pores of pure and CA doped SBA-15. Results for Fe-MEPE in 20-CA at 20°C and 45°C are shown in Figure 9.6a. In this example (μ =0.09) at 45°C, nearly quantitative uptake

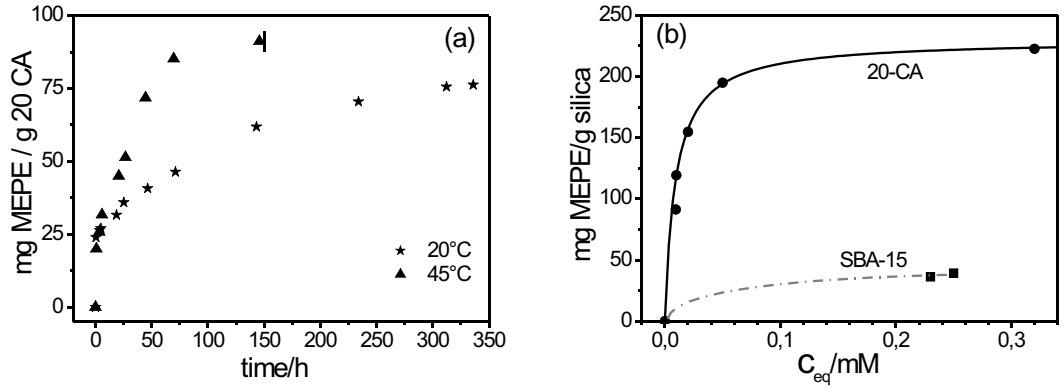

Figure 9.6: (a) Effect of temperature on the uptake rate in 20-CA (μ =0.1); the vertical bar indicate complete uptake; (b) Adsorption isotherms of Fe-MEPE from aqueous solution (without added salt) in 20-CA (●) and in pure SBA-15 (■); results for different MEPE-to-silica ratios μ at 50°C. The solid line represents a fit of the 20-CA data by the Langmuir equation; the dashed-dotted line for the data in SBA-15 is drawn to guide the eye.

was reached after 150 h while at 20°C uptake was not complete after 350 h. This behavior indicates a significant kinetic resistance for the slow process. For this reason, measurements of the equilibrium adsorption isotherm were performed at an elevated temperature. Figure 9.6b shows data for the uptake of Fe-MEPE in 20-CA up to 300 h as a function of the concentration in the supernatant solution. The individual data points correspond to different initial MEPE-to-silica ratios μ. Also shown in this figure are two points for the adsorption of Fe-MEPE in pure SBA-15, to indicate the large difference in adsorption affinity between pure and carboxylic-acid doped SBA-15. A detailed account of the adsorption kinetics of Fe-MEPE in 20-CA will be presented in Chapter 10.

9.2.4 Characterization of Fe-MEPE in CA-SBA-15

To characterize the state of Fe-MEPE in the pores of pure and CA doped SBA-15 materials, some of the composite samples were studied by a combination of different techniques. The effect of the MEPE uptake on the properties of the matrix was determined by nitrogen adsorption isotherms and SAXD measurements, while the Fe-MEPE content was determined by atomic absorption spectroscopy (AAS) and X-ray photoelectron spectroscopy (XPS). Composite samples were prepared by exposing the silica to Fe-MEPE solutions (50 mL) of different initial concentrations c_0 and different MEPE-to-silica mass ratios μ, and centrifugation after 300 h. (The terms bare silica and composite sample are used for the silica samples without and with embedded Fe-MEPE, respectively.) Table 9.2 gives

the Fe-MEPE content of these samples, expressed as adsorbed mass of Fe-MEPE per unit mass of silica, and as the mean number of MEPE chains accommodated side-by side in a pore. Both quantities were derived from the UV-vis depletion measurements. The samples specified as CA-MEPE-4 to CA-MEPE-6 come from the high-affinity regime of the MEPE uptake by the silica. The samples CA-MEPE-7, CA-MEPE-8 and CA-^{15}N-MEPE result from the highest initial MEPE concentrations c_0 and highest MEPE-to-silica mass ratios μ, at which the uptake was not complete after 300 h. Values of the Fe-MEPE content of these samples were corrected for the effect of sedimentation of Fe-MEPE during the centrifugation step (see Section 8.1).

Table 9.2: Fe-MEPE (material I) in SBA-15 (SBA-MEPE) and in 20-CA (CA-MEPE-4-8) prepared for comparative studies.

sample	c_0/mM	μ	$m_{Fe-MEPE}/_{SiO2}$	S
SBA-MEPE	0.37	0.094	0.033	3
CA-MEPE-4	0.37	0.094	0.091	10
CA-MEPE-5	0.48	0.112	0.119	13
CA-MEPE-6	0.62	0.159	0.156	17
CA-MEPE-7	0.81	0.207	0.195	21
CA-MEPE-8	1.20	0.305	0.223	24
CA-^{15}N-MEPE†	1.127	0.225	0.219	18

c_0: initial MEPE concentration; μ: MEPE to silica mass ratio; $m_{Fe-MEPE}/_{SiO2}$: specific uptake of Fe-MEPE acetate; S: Number of MEPE chains accommodated side-by-side in the pores. † prepared from a different 20-CA charge using Fe-MEPE material II.

The effect of embedding Fe-MEPE on the pore structure and pore volume pure and CA-doped SBA-15 samples was studied by small-angle X-ray diffraction (SAXD) and nitrogen adsorption. In this way it can be checked if the silica matrix was affected by the exposure to aqueous solutions and elevated temperatures during the embedding of Fe-MEPE. The SAXD measurements were also made in order to see if a layer of Fe-MEPE adsorbed at the pore walls causes characteristic changes in the scattering curves. Nitrogen adsorption isotherms for a CA-MEPE composite and the respective bare CA-doped silica sample are presented in Figure 9.7a. Also shown is the isotherm of the bare CA-doped sample after exposure to water under similar conditions as during the MEPE uptake procedure.

The pore diameters, specific surface area and specific pore volume derived from these isotherms are given in Table 9.3. It can be seen that the pore diameter is not significantly

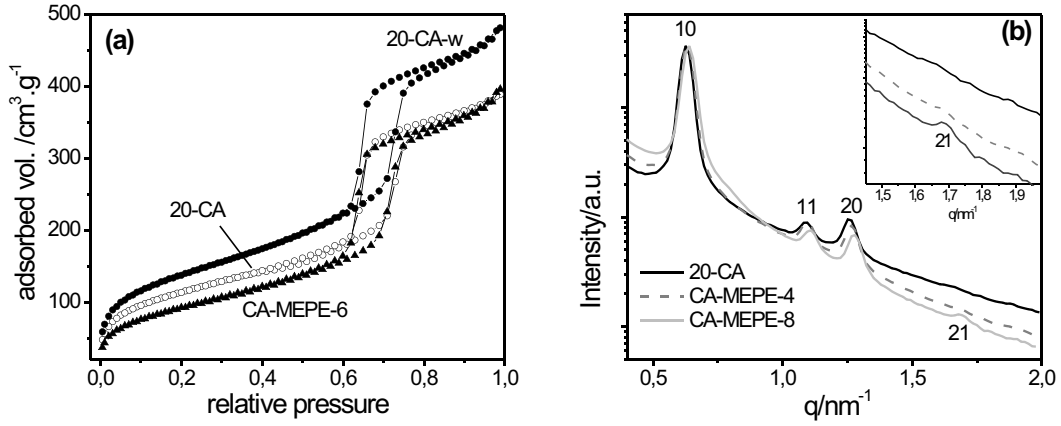

Figure 9.7: (a) Nitrogen adsorption isotherms for sample 20-CA in its original state (○), after exposure to water for 30 d (20-CA-w) (●), and after uptake of Fe-MEPE (sample CA-MEPE-6) (▲); for all samples the amount of adsorbed nitrogen is referenced to unit mass of the 20-CA matrix; (b) SAXD profiles for 20-CA and the composite samples CA-MEPE-4 (μ =0.09) and CA-MEPE-8 (μ =0.3). The profile for the sample with μ =0.3 is moved up by a factor 1.4 in order to have the same intensity at the position of the 10 reflection for all samples.

changed by the exposure to water nor by the incorporation of Fe-MEPE. On the other hand, the pore volume of the bare 20-CA material is increased by the exposure to water. Hence, the similar pore volumes of the samples CA-MEPE and bare 20-CA before water exposure can be attributed to a compensation of two effects. (i) an increase of v_p due to the exposure to water and (ii) a reduction of v_p due to the incorporation of Fe-MEPE. The former effect may be caused by the ability of water to remove some constrictions in the pore system and thus to improve the accessibility of the pores of 20-CA. The decrease of the pore volume by ca. 0.14 $cm^3\ g^{-1}$ in step (ii) for the uptake of 0.16 g MEPE/g of silica is of the expected order of magnitude assuming a density of about 1 g/cm^3 for Fe-MEPE. Systematic measurements on the effect of water exposure on the pore volume and specific area of CA-doped SBA-15 materials corroborating this effect were presented in Section 6.2.4. As was shown there, the pore volume of CA-SBA-15 silica increased by exposure to water without a significant change of the pore diameter.

The SAXD profiles of two composite samples, CA-MEPE-4 (μ=0.09) and CA-MEPE-8 (μ =0.3), and of the respective bare 20-CA (μ=0) are shown in Figure 9.7b . One finds that the leading Bragg reflections (10, 11, 20) are shifted to larger q with increasing loading, indicating some shrinkage of the lattice spacing with the incorporation of Fe-MEPE. Presumably this effect is caused by immersing the silica sample into water during the

Table 9.3: Specific surface area a_s, specific pore volume v_p, and mean pore diameter D as derived from the nitrogen adsorption isotherms of Figure 9.7a.

sample	a_s/m^2g^{-1}	v_p/cm^3g^{-1}	D/nm
20-CA	400	0.60	8.1
20-CA-w	489	0.75	8.2
CA-MEPE-6	331	0.61	8.0

sample preparation, which took 6 days for the sample with μ=0.09 and 35 days for the sample with μ=0.3. The relative intensities of the three leading Bragg peaks (10, 11 and 20) do not change significantly as the amount of MEPE in the matrix is increased. This indicates that the MEPE chains are not forming a layer of uniform thickness and electron density at the pore wall. On the other hand, one observes a significant lowering of the diffuse scattering at large q (above the 20 Bragg peak) as the content of MEPE is increased. Due to the decreased diffuse scattering the 21 Bragg reflection becomes detectable for the sample with μ=0.3, although this peak is not detectable at lower loadings of the pores. This point is discussed in Section 9.3.3 of this Chapter.

The samples CA-MEPE-4, CA-MEPE-6 and CA-MEPE-8 were characterized by taking XPS spectra of carbon, nitrogen and iron. Figure 9.8A shows C1s XPS spectra of bare 20-CA (a) and of the samples CA-MEPE-4 (b) and CA-MEPE-6 (c). The peaks at 285.1 and 289.6 eV of bare 20-CA are assigned to the carbon atoms of the alkyl and carboxyl groups, respectively, of the propionic acid groups at the pore wall. Upon loading with Fe-MEPE, a shift of the 285.1 eV peak to 285.4 eV is observed. To compare the spectral features of embedded Fe-MEPE with bulk Fe-MEPE, difference spectra were calculated by subtraction of spectrum (a) from the spectra (b) and (c). The resulting difference spectra are displayed in Fig. 9.8B as spectra (a) and (b). Regarding the peak position of the signal at 285.4 eV, the C1s spectra of embedded Fe-MEPE closely resemble the respective spectrum of bulk Fe-MEPE which is shown as spectrum (c) in Fig. 9.8B. The observed binding energy of 285.4 eV is in good agreement with the literature value of 285.5 eV for pyridine [19]. Figure 9.8B also shows that the intensity of the C1s signal of the embedded Fe-MEPE increases from CA-MEPE-4 to CA-MEPE-6.

Figure 9.8C shows X-ray photoelectron $Fe2p_{3/2}$ spectra of Fe-MEPE in the samples CA-MEPE-4 (a) and CA-MEPE-6 (b); the respective $Fe2p_{3/2}$ spectrum of bulk Fe-MEPE normalized in intensity to spectrum (b) is shown as spectrum (c). All spectra are characterized by an asymmetric peak with an intensity maximum at 709.3 eV. This value of

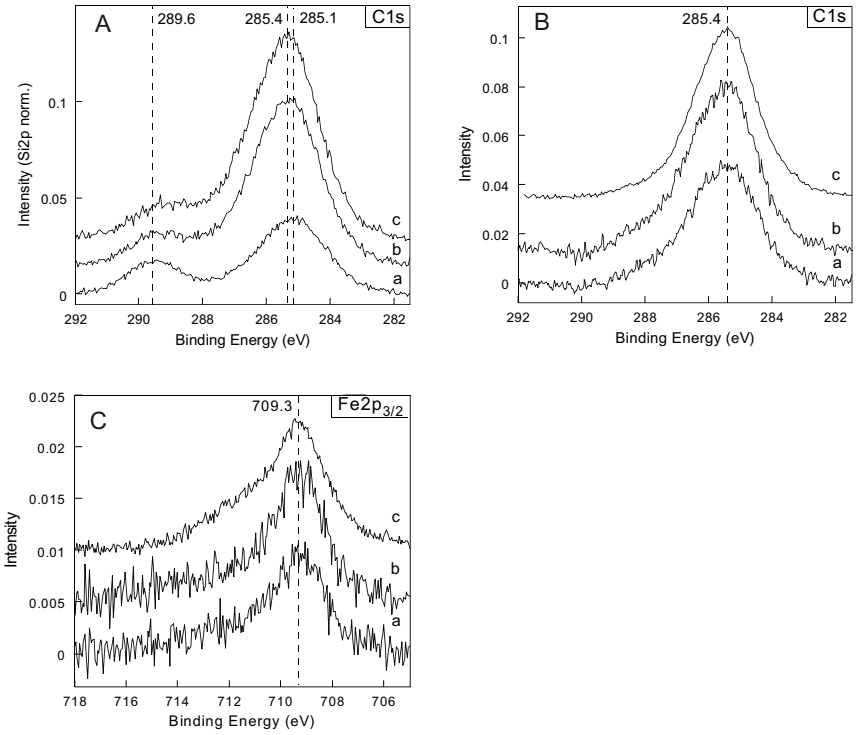

Figure 9.8: (A) Si2p normalized X-ray photoelectron C1s spectra of bare 20-CA (a) and 20-CA loaded with Fe-MEPE at μ =0.10 (b) and μ =0.16 (c); (B) X-ray photoelectron C1s difference spectra of 20-CA loaded with Fe-MEPE at μ =0.10 (a) and μ =0.16 (b) as well as bulk Fe-MEPE (c) normalized in intensity to spectrum (b); (C) X-ray photoelectron $Fe2p_{3/2}$ spectra of 20-CA loaded with Fe-MEPE (a) μ = 0.10 and (b) μ =0.16 as well as (c) bulk Fe-MEPE normalized in intensity to spectrum b. For details see text. Spectra in each graphic are shifted for clarity.

the binding energy as well as the shape of the asymmetric tail are consistent with results reported for other Fe(II) compounds such as Fe(phthalocyanine) [125] or FeO [126]. However, due to the complexity of the X-ray photoelectron Fe2p spectra, a contribution of Fe(III) ions cannot be ruled out. X-ray photoelectron N1s spectra of the samples CA-MEPE-4 and CA-MEPE-6 and bulk Fe-MEPE were also determined. From the normalized intensities of the N1s and $Fe2p_{3/2}$ signals the atom ratio N/Fe of the MEPE complexes in the pores was determined (Table 9.4).

Table 9.4 compares the iron content of the 20-CA-MEPE composite samples as determined by three methods, viz. depletion of the supernatant solution (UV-vis), AAS and XPS. The AAS and UV-vis data are in reasonably good agreement (deviation of AAS from UV-vis no greater than 12%), except for the sample with the highest loading (CA-

Table 9.4: Characterization of CA-MEPE samples specified in Table 9.2: Fe content and N/Fe atomic ratio.

	wt % Fe*			XPS		
sample	UV-vis	AAS	XPS	at.%Fe	at.%N	N/Fe
CA-MEPE-4	0.65	–	0.60	0.30	1.90	5.3
CA-MEPE-5	0.83	0.93	–			
CA-MEPE-6	1.06	0.96	1.36	0.43	2.30	5.4
CA-MEPE-7	1.27	1.14	–			
CA-MEPE-8	1.42	1.12	1.96	0.61	3.30	5.4

wt % Fe* of the Fe-MEPE loaded samples as determined by UV-vis, AAS, and XPS

MEPE-8) for which the AAS values are significantly lower than that obtained by the depletion method. For the sample of lowest Fe-MEPE content (CA-MEPE-4), the iron content obtained by XPS also agrees with that obtained by the depletion method. At higher loadings, however, XPS yields significantly higher values of the iron content than the two other methods. Higher Fe concentrations obtained by XPS than by AAS may indicate higher concentrations of Fe-MEPE near the surface than in the core of the silica grains, because XPS is a surface-sensitive technique while the other methods are integrating over the whole sample. Specifically, the very high value for CA-MEPE-8 obtained by XPS may indicate that part of the Fe-MEPE was not included in the pores but formed a multilayer film at the outside of the silica grains. Table 9.4 also shows that the number ratio of nitrogen and Fe atoms has the same value (5.4 ± 0.3) for all composite samples studied by XPS. This indicates that the composition of Fe-MEPE was the same in these three samples, which is remarkable in view of their very different loadings. For octahedral coordination of the metal centers and infinitely long Fe-MEPE chains one expects an atom number ratio $N/Fe = 6$. The somewhat lower experimental value indicates an excess of iron. This result is consistent with the fact that the Fe-MEPE used in these experiments (material I) was prepared with a small metal excess. It thus appears that the stoichiometry of the Fe-MEPE in the pores is similar to that of the original material, in line with the fact that most of the Fe-MEPE is adsorbed in the pores in the high-affinity region of the uptake isotherm.

9.2.5 Characterization by solid-state ^{15}N NMR

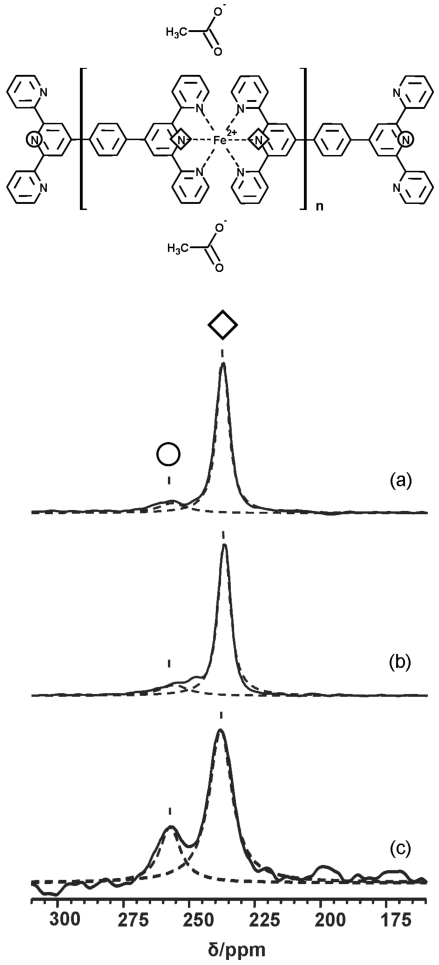

Figure 9.9: (a) ^{15}N MAS NMR and (b) ^{15}N CPMAS NMR of bulk solid ^{15}N Fe-MEPE and (c) ^{15}N CPMAS NMR of ^{15}N Fe-MEPE (material II) embedded in the pores of 20-CA silica.

^{15}N solid-state NMR was used to estimate the mean chain-length of Fe-MEPE (material II) in bulk and in the pores of 20-CA. This analysis is based on signal deconvolution and observing the change in signal intensities of the Fe-coordinated and free nitrogen atoms (N_{coor}/N_{free}) in the ligand molecules before and after uptake of Fe-MEPE in the host material. Because of the relatively low amount of Fe-MEPE in these samples (compared to the bulk Fe-MEPE materials; cf. Figure 9.2) it was necessary to use ^{15}N-labeled material to enhance the ^{15}N NMR sensitivity. Only the nitrogen atom in the central ring of the ligand was accessible for ^{15}N labeling, although labeling of the nitrogen atoms in the outer rings would be advantageous because they exhibit a bigger difference in chem-

Table 9.5: Number ratio of coordinated and free ^{15}N atoms, N_{coor}/N_{free}, and mean chain length,n, of Fe-MEPE (material II) in the bulk state and in the pores of 20-CA.

sample	NMR method	N_{coor}/N_{free}	n
bulk MEPE	MAS	$15 \pm 1)/2$	7-8
bulk MEPE	CP MAS	$15 \pm 1)/2$	7-8
CA-MEPE	CP MAS	$7 \pm 1)/2$	3-4

ical shift between free and coordinated ligand. However, the difference in chemical shift of the central ^{15}N nuclei between free and coordinated ligand is still sufficient to clearly distinguish these two signals. Figure 9.9 shows the ^{15}N MAS NMR and ^{15}N CPMAS NMR spectra of the ^{15}N-labeled bulk Fe-MEPE, and the ^{15}N CPMAS NMR spectrum of a 20-CA-MEPE composite.

The spectrum of ^{15}N-labeled Fe-MEPE in the bulk state was recorded by ^{15}N MAS NMR (Fig. 9.9a). This technique directly gives the ratio of coordinated and free nitrogen atoms, N_{coor}/N_{free}, from the relative intensities of the corresponding signals. However, this method could not be used for Fe-MEPE embedded in the silica matrix, because of the relatively low concentration of the Fe-MEPE in the samples and the need to use a long recycle delay time (10 min), which would lead to excessive measurement times. Hence, the cross-polarisation transfer technique (^{15}N CPMAS NMR) was used to study Fe-MEPE both in bulk and embedded in the pores (Figure 9.9b and 9.9c). A disadvantage of this method is that the relative intensities of the peaks in a spectrum may not precisely reflect the relative concentration of the individual species. This problem was reduced by applying a sufficiently long contact time (5 ms) in the pulse sequence. Hence, the relative intensities of the peaks could be mutually compared, and the relative concentrations of the two nitrogen species were estimated from the respective peak intensities of the CPMAS NMR spectra. Assuming that the MEPE chains are terminated on both sides by ligand (as to be expected in the case of ligand excess), then $N_{coor}/N_{free} = 2n/2$, where n is the mean chain length. Results for N_{coor}/N_{free} and n are summarized in Table 9.5. For bulk solid Fe-MEPE (Fig. 9.9a and Fig. 9.9b) signal deconvolution yields N_{coor}/N_{free}=(15±1)/2 for both methods, corresponding to an average chain length n=7−8. The fact that the MAS and CPMAS techniques give concordant result for bulk Fe-MEPE indicates that the CPMAS method may indeed be used for estimating the concentration of the two nitrogen species. On this basis, signal deconvolution of the CPMAS spectrum for Fe-MEPE embedded in silica (Figure 9.9c) yields N_{coor}/N_{free}=(7±1)/2, corresponding to an average

chain length $n = 3 - 4$. Hence, the results of Table 9.5 indicate that the mean length of Fe-MEPE chains in the pores of 20-CA is smaller than in the bulk state. The significant broadening of the signal corresponding to the Fe-coordinated nitrogen species in Fig. 9.9c can be attributed to the confined pore geometry, which reduces the possible orientations of the Fe-MEPE-chains inside the pores of 20-CA.

9.3 Discussion

The present study shows that the uptake of Fe-MEPE into the pores of SBA-15 is strongly enhanced when the pore walls are decorated with a layer of CA. This enhancement can be attributed to an ion exchange process and to electrostatic interactions of the Fe-MEPE polycations with the negatively charged pore walls. These two driving forces of the fast uptake process, and the relation between high-affinity adsorption and the arrangement of the MEPE chains in the pores, are discussed below. Finally, the relation between stoichiometry and mean chain length of Fe-MEPE before and after uptake in the pores will be taken up briefly.

9.3.1 MEPE uptake by ion exchange

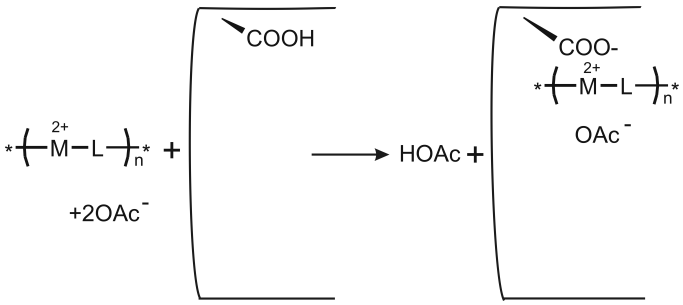

Figure 9.10: Cartoon of the ion exchange transfer of MEPE polycations (indicated as $-(-M^{2+} - L-)_n-)$ from the solution into the CA functionalized pores. The acetate counterions are partly neutralized by the released protons.

From the pH change accompanying the initial fast uptake of MEPE from aqueous MEPE it can be concluded that this process involves an ion exchange in which protons of the silanol or CA groups at the pore walls of the CA-SBA-15 are replaced with Fe-MEPE polycations. In the proposed ion exchange process of Figure 9.10, the uptake of a MEPE polycation of n chain segments is accompanied by a release of n protons from

undissociated or dissociated carboxylic acid groups at the pore wall. These protons leave the pore space and cause a shift of pH according to the pK_a value of acetic acid. Similarly, in the uptake of MEPE from KOAc solutions, when a fraction α of the carboxylic acid groups at the pore wall exists in deprotonated form, $n\alpha$ potassium ions and $n(1-\alpha)$ protons are released on the uptake of a single polycation of n segments. In either case, the release of a larger number of small ions causes an entropic driving force for the uptake and binding of the polycations in the pore. This offers an explanation for the high rate of the initial uptake. The finding that the ion exchange process with 10-CA causes a larger pH change than with pure SBA-15 (Fig. 9.4) indicates that the CA doped material has a higher proton donor ability than pure SBA-15, because the overall proton exchange capacities of the two materials are similar. Tentatively, this higher proton donor ability is attributed to steric effects caused by the flexibility of the propionic acid chains, which allows the COOH groups to get in closer contact with the metal ions of the Fe-MEPE chains than the silanol groups of the surface. The overall proton exchange capacity of 10-CA is estimated as 3.2 mmol g^{-1}, about 20% of which are carboxylic acid groups (see Table 9.1). In the following section a simple estimate is presented, which shows that the number of protons released from the 10-CA matrix during the fast uptake step of Fe-MEPE from a salt-free solution (Fig. 9.4) amounts to only a few percent of the proton exchange capacity of this material.

9.3.1.1 Estimation of pH change

In the uptake measurement of Fe-MEPE from aqueous solutions into 10-CA shown in Fig. 9.4, 50 mL of a Fe-MEPE solution of initial concentration c_0=0.4 mM were brought in contact with 145 mg of 10-CA silica, corresponding to a MEPE-to-silica mass ratio μ=0.1. Hence, the number of CA groups in this sample was about 1.10^{-4} mol. The fast uptake step was connected with a pH change from 5.6 to 4.5, corresponding to a change in the proton concentration of $\Delta c_{H+} = 2.9 \times 10^{-5} M$. Further protons are consumed by the protonation of acetate counterions of Fe-MEPE in the solution. From the Henderson-Hasselbalch equation it follows

$$\log \frac{[HA]}{[A^-]} = pK_a - pH^f = 4.75 - 4.50 = 0.25$$

where HA and A^- represent undissociated acetic acid and acetate ions, $pK_a = 4.75$ is the acid dissociation constant of acetic acid and pH^f =4.5 is the pH of the solution after ion exchange. Since $[A^-] = c_0 - [HA]$, where c_0 =0.8 mM is the overall acetate concentration (counter ions of Fe-MEPE), we find $[HA] = 0.64 c_0 = 5.2 \times 10^{-5} M$ for the concentration

of undissociated acetic after ion exchange. Hence, the overall increase in the number of protons released is given by

$$\Delta n_{H+} = (0.05L)(2.9mM + 5.2mM) = 4 \times 10^{-6} mol.$$

This result implies that only about 4% of the CA groups at the pore wall are contributing to ion exchange in the case of pure aqueous MEPE acetate, since for 10-CA the amount of CA-groups at the pore wall is estimated as 0.6 mmol g^{-1}. This estimate is based on the assumption that the overall density of surface groups (silanol + carboxylic acid) in the CA doped materials is equal to the density of the silanol groups in SBA-15 (3.7 nm^{-2})[5]. From the values of the specific surface area (a_s) and mol fraction of CA groups (x_{COOH}) in Table 9.1 one than obtains the amount of CA groups at the pore wall as 0.6 mmol g^{-1} (10-CA) and 1.0 mmol g^{-1} (20-CA). Somewhat higher values are obtained by titration with NaOH by the method described by Bruzzoniti et al. [127].

Accordingly, the ion exchange mechanism process appears to play only a relatively small role in the uptake of the Fe-MEPE polycations at the weakly acidic pH of the salt-free solution.

9.3.2 Effect of electrostatic interactions

Beyond ion exchange, electrostatic interactions will play an important role in the uptake of the Fe-MEPE polycations in the pores. In the aqueous medium, the pore walls of both pure and carboxylic-acid functionalized SBA-15 are negatively charged, but the acid-functionalized silicas have a higher surface charge density than the pure SBA-15 samples in the pH range of the present study. In particular, whereas the surface charge density of pure silica is only weakly dependent on pH between 4 and 8 [128], a more pronounced pH dependence of the surface charge density is found for the carboxylic-acid functionalized SBA-15 materials. This is concluded from FT-IR measurements (see Section 6.5.2) which revealed that the ratio of the COO^-/COOH peak intensities of 10-CA and 20-CA clearly increase with pH from pH 5.5 (D_2O) to pH 8 (phosphate buffer in D_2O). On this basis, the difference in MEPE uptake in 10-CA from milli-Q water (pH 5.5) and 0.1 M KOAc (pH 7.25) shown in Fig. 9.5a may be explained by the interplay of two effects: (i) attractive electrostatic interactions between a MEPE polycation and the pore wall; and (ii) repulsive electrostatic interactions between the adsorbed MEPE polycations. Initial adsorption is dominated by the attractive interaction of individual MEPE molecules with the pore wall, which is higher at higher pH due to the higher surface charge density. Electrostatic repulsion between adsorbed MEPE chains becomes significant at higher surface coverage,

where it tends to limit the maximum adsorption. However, the range of these repulsive interactions is reduced as the ionic strength of the system is increased by the addition of electrolyte. Accordingly, the repulsive interactions between the adsorbed MEPE chains are expected to be weaker in KOAc than in milli-Q water, leading to a higher adsorption in the presence of KOAc. Hence, both effects are causing a higher adsorption in the presence of KOAc. These conclusions are in line with observations by other authors. Bruzotti et. al. [127] have found that the retention of Fe(III) ions in CA-SBA-15 increases with increasing pH, and Katiyar et al. [129] observed that the adsorption of a positively charged protein (lysoczyme) in SBA-15 is increased by a factor 2 from pH 5 to 8 in appropriate buffers.

9.3.3 Adsorption affinity and chain packing

The adsorption isotherm of Fe-MEPE in 20-CA (Fig. 9.6b) indicates that the high-affinity regime extends to a loading of about 150 mg Fe-MEPE acetate per 1 g of the matrix. In the study of the uptake kinetics, a similar value was found for the upper limit of the fast-uptake regime. It is of interest to see how this borderline value of the adsorbed amount is related to possible adsorption geometries of the MEPE chains in the pores. The number of adsorbed MEPE units per unit mass of the silica matrix is the respective number for single occupancy of the pores, σ, multiplied with S, the number of chains accommodated side-by-side in each pore [110]. The former number is given by $\sigma = 4v_p/lD^2\pi$, where v_p is the specific pore volume, D the pore diameter, and ℓ=1.5 nm is the length of a MEPE unit (distance between Fe^{2+} ions along the chain). Accordingly, the number of chains arranged side-by-side can be calculated from the experimental data as

$$S = \frac{N_A}{M}\sigma(m_{Fe-MEPE}/m_{silica}) \tag{9.1}$$

where $m_{Fe-MEPE}/m_{silica}$ is the mass of Fe-MEPE per unit mass of silica matrix, M is the molar mass of Fe-MEPE, and N_A is the Avogadro's constant. The maximum number of MEPE chains, S_{max}, that can be accommodated side-by-side in a close-packed monolayer at the pore wall can be estimated from the diameter of the MEPE chain (d =1.2 nm) and the pore diameter D. For 20-CA (D=8.0 nm), this yields $S_{max} = 18$. Table 9.2 indicates that this value is attained at loadings between sample CA-MEPE-6 and CA-MEPE-7, that is, near the upper limit of the high-affinity adsorption regime of Fe-MEPE in the silica matrix. This supports the conjecture that high-affinity adsorption occurs as long as the Fe-MEPE chains are accommodated in the monolayer in direct contact with the pore

wall. Values of S>18, as they are obtained for the samples CA-MEPE-7 and CA-MEPE-8, then indicate the formation of a second layer of Fe-MEPE in the pores or at the outside of the silica grains, or both.

As mentioned earlier, some of the CA-MEPE composite samples of Table 9.2 were also studied by SAXD. No significant changes in the intensities of leading Bragg reflections (10, 11, 20; cf. Fig. 9.7b) were observed, as they were found for physisorbed films of vapors at the pore wall of SBA-15 [130, 26]. However, the MEPE-loaded samples exhibit a significantly lower level of diffuse scattering than the empty material in the region of higher q, so that the 21 Bragg reflection that was masked by diffuse scattering in the empty material is detectable in the material of highest loading with MEPE. Because diffuse scattering is partly due to the roughness of the pore wall, we may conclude that the formation of a layer of MEPE chains reduces the effective roughness of the pore walls. On the other hand, the fact that no significant modulation of the Bragg intensities is observed for the CA-MEPE materials indicates that the layer of MEPE chains is less uniform than a physisorbed fluid film at the pore walls.

9.3.4 Stoichiometry and chain length of MEPE in the pores

Information about the stoichiometry and chain length of Fe-MEPE in the pores was derived from the number ratio of nitrogen and iron atoms (N/Fe) as determined by XPS, and from the number ratio of coordinated and free nitrogen atoms of the ligand (N_{coor}/N_{free}) as determined by ^{15}N solid-state NMR. The XPS measurements, which were made with Fe-MEPE material I, give the same N/Fe atom ratio for the three CA-MEPE composites studied. This indicates that the stoichiometry of Fe-MEPE in the pores is independent of the degree of loading which differs strongly for the three samples (Table 9.4). The experimental atom ratio N/Fe of 5.4 $\pm$ 0.3 instead of 6 indicates an excess of metal over ligand in the complex, as to be expected for Fe-MEPE material I (see Section 8.1). Because the number of segments, n, of a chain terminated by metal at both sides ($M_{n+1}L_n$) is related to the atom number ratio as $N/Fe = 6n/(n+1)$, the XPS data indicate a mean chain length n≈9 or greater for Fe-MEPE material I in the CA-MEPE composite materials. However, this value must be taken with caution, as it relies on the assumption that the MEPE chains are terminated by metal on both ends. Lower values of n would result on the assumption that a fraction of the chains are of type M_nL_n instead of $M_{n+1}L_n$.

The ^{15}N MAS NMR measurements were performed with a ^{15}N-labeled Fe-MEPE (material II) having a ligand excess (see Section 8.1), for which one expects that the chains are terminated by ligand on both sides (M_nL_{n+1}). From the measured ratio of

coordinated and free nitrogen atoms, N_{coor}/N_{free}, it was concluded that this Fe-MEPE material has a mean chain length n=7-8 in the bulk state, and a value of about n=3-4 in the pores of 20-CA. Because the measurements were made with the same MEPE material, this result implies that the chains are breaking into two or more fragments when the material is dissolved in the aqueous phase or during the uptake into the pores. For instance, if a MEPE chain M_nL_{n+1} breaks into two fragments,

$M_nL_{n+1} \longrightarrow M_mL_{m+1} + (ML)_{n-m}$,

one of the fragments will not be terminated by ligand on both sides, and thus the relation $N_{coor}/N_{free} = n$ is not strictly applicable for estimating the chain length in the pores. Instead, for the mixture of the fragments, one finds, for any $m < n$, $N_{coor}/N_{free} = (2n-1)/3$, which is smaller than n. Hence, the important finding that N_{coor}/N_{free} in the pores is smaller than in the bulk state clearly implies that the MEPE chains are breaking into smaller entities when transferred into the pores. A direct complexation of Fe ions by the surface acid groups might also be envisaged in view of the relatively strong binding of Fe ions to these groups [127]. However, since direct complexation involves a release of ligand L, this alternative seems rather unlikely in view of the high complex formation constants of Fe(II) with the Terpy-type ligands [88].

9.4 Conclusions

This work has shown that intrinsically stiff metallo-supramolecular polyelectrolytes like Fe-MEPE are adsorbed into the cylindrical nanopores of SBA-15 and that the adsorption affinity is strongly enhanced when the pore walls are functionalized with carboxylic acid groups. Two uptake mechanisms have been identified: a fast process and a slower subsequent process. The fast process is connected with a lowering of pH in the supernatant solution, indicating an ion exchange mechanism. It is favored by increasing the pH which causes stronger dissociation of the surface functional groups and thus stronger electrostatic interactions of the polycations with the negatively charged pore walls. The nature and rate-determining resistance of the slow process is not fully understood. Generally, an increase of temperature from 20 to 50°C causes an increase of the uptake rate and leads to higher levels of uptake of Fe-MEPE in the pores. For the material 20-CA, in which nearly one-half of the surface silanol is replaced by propionic acid groups, the maximum adsorbed amount corresponds to more than a densely packed layer of Fe-MEPE-chains aligned side-by-side along the pores.

Except for the high uptake regime, the results of the uptake measurements by UV-vis analysis of the supernatant are consistent within the error limits with AAS determinations of the iron content in the dry samples. However, XPS measurements gave significantly higher values at high Fe-MEPE loadings. Because XPS is a surface sensitive probe, this may indicate that at high loadings Fe-MEPE is accumulating near or at the surface of the grains. The metal-to-ligand stoichiometry and average chain length of Fe-MEPE in the matrix was characterized by XPS and ^{15}N solid-state NMR spectroscopy. XPS measurements of the atomic ratio of nitrogen to iron showed that the stoichiometry of the Fe-MEPE complex was independent of the level of uptake in the matrix. This result suggests that the Fe-MEPE chains are transferred into the pores as they exist in the solution. ^{15}N solid-state NMR measurements of the ratio of coordinated and free nitrogen (N_{coor}/N_{free}) were made with a ^{15}N-labeled Fe-MEPE sample with ligand excess. Assuming that in the Fe-MEPE material obtained under these conditions the chains are terminated by ligand at both ends, the mean chain length was taken as $N_{coor}/N_{free} = n$. For the bulk material, a value $n = 7 - 8$ was obtained. For the same Fe-MEPE material in the pores of 20-CA, $N_{coor}/N_{free} = n = 3 - 4$ was found. From the increase of the relative number of free (noncoordinated) nitrogen atoms of the ligand it was concluded that the Fe-MEPE chains break into smaller entities in the pores, because fragmentation leads to a higher proportion of uncoordinated nitrogen.

Chapter 10

Kinetic Study of Fe-MEPE Uptake

Abstract

In this section a quantitative analysis of the adsorption kinetics and adsorption equilibrium of Fe-MEPE in the pores of carboxylic-acid functionalized SBA-15 (CA-SBA-15) is presented. The starting point is a comparison of the uptake kinetics of Fe-Terpy and Fe-MEPE. As in the case of Fe-MEPE, the affinity of Fe-Terpy for CA-SBA-15 is greater than for pure SBA-15. The uptake of Fe-Terpy is much faster than the uptake of Fe-MEPE and equilibrium is reached within a few hours, whereas equilibrium adsorption of Fe-MEPE is attained only after several hundred hours. The equilibrium adsorption isotherm of Fe-MEPE can be described satisfactorily by the Langmuir model. A fit of the equilibrium data yields a high adsorption constant and a high monolayer capacity of 230 mg MEPE /g silica which is in fact higher than the value estimated for a monolayer of Fe-MEPE chains at the pore wall. The uptake curves of Fe-MEPE can be represented by a sum of two exponential decay functions for the fast initial process, and a subsequent slow uptake process leading to the adsorption equilibrium. The analysis suggests that the uptake of Fe-MEPE into the pores is controlled by surface layer resistance and not by internal diffusion inside the pore channels. The estimated mass transfer coefficient α of 10^{-9}-10^{-10} m s^{-1} indicates a slow entering process of Fe-MEPE chains into the pores.

10.1 Fe-Terpy-uptake vs. Fe-MEPE-uptake

We studied the uptake of Fe-Terpy, a simpler system than Fe-MEPE because of its monomeric character, to confirm the higher affinity of carboxylic acid functionalized SBA-15 for these kind of complexes compared with pure SBA-15. Figure 10.1 shows uptake isotherms of Fe-Terpy into pure SBA-15 and 20-CA under the same experimental conditions. As can be seen, the amount of adsorbed Fe-Terpy in 20-CA is grater by a factor four than the adsorbed amount in pure SBA-15. Since the surface area of 20-CA is not greater (but in fact smaller) than that of pure SBA-15, this result is a clear evidence for the higher adsorption affinity of 20-CA for the Fe-Terpy- complexes. In both cases the uptake took place in pure water at pH 5.5. Under these conditions the surface of pure SBA-15 is negatively charged because the isoelectronic point of SBA-15 is near pH 2. Still, its affinity for the positively charged Fe-Terpy complex is much less than 20-CA. This observation could be ascribed to (i) the higher negative surface charge of 20-CA material in comparison to pure SBA-15 because of its higher proton donor ability in solution, and (ii) the higher entropy during the adsorption in 20-CA due to the release of acetate counter ions of Fe-Terpy in solution as a consequence of their replacement by wall carboxylic acid groups after the adsorption.

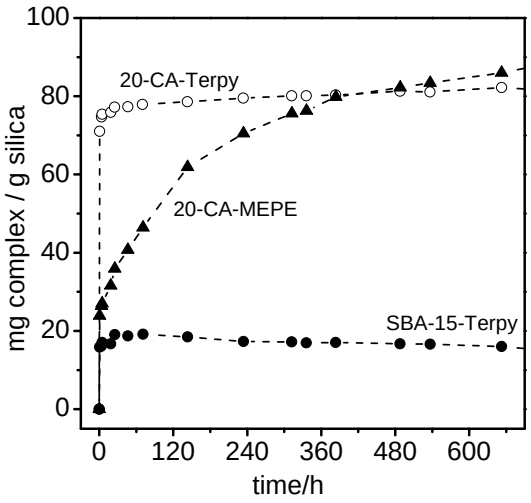

Figure 10.1: Uptake isotherms of Fe-Terpy in pure SBA-15 (•), in 20-CA (○) and of Fe-MEPE in CA-20 (▲). The preparations were performed in milli-Q-water and with a complex to silica ratio of μ=0.1. Curves are drawn to guide the eye.

Also shown in Figure 10.1 is a comparison of the uptake of Fe-Terpy and Fe-MEPE

in 20-CA silica material. A pronounced difference in the adsorption kinetics of Fe-Terpy and Fe-MEPE into the pores of 20-CA can be seen. Although in the final equilibrium state after 300 h the amount of adsorbed MEPE and Terpy is nearly the same, the uptake kinetics of the two complexes is grossly different: The uptake curve of Fe-Terpy shows a fast initial increase followed by a plateau, indicating a rapid achievement of the equilibrium. The uptake curve of Fe-MEPE also exhibits a rapid initial increase but to a much lower extend than for Fe-Terpy, and this fast process is followed by a much slower uptake extending over several hundred hours. We believe that this difference in the uptake behavior is caused by the the polymeric character of Fe-MEPE. The grossly different equilibration

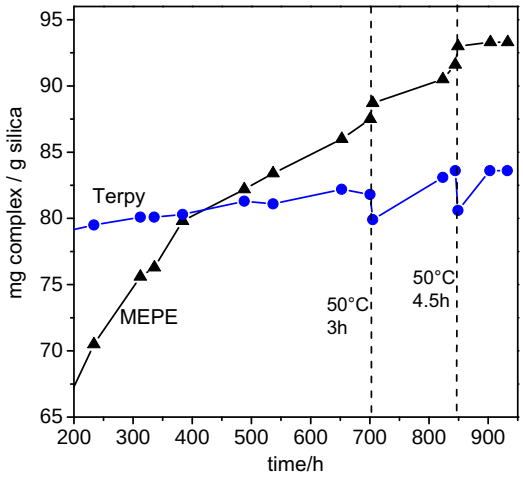

Figure 10.2: Uptake isotherms of Fe-Terpy (▲) and Fe-MEPE (■) in 20-CA at 20°C. The vertical lines show the times, at which the temperature was raised from 20°C to 50°C for a period of 3h and for a period of 4.5 h, respectively. Curves are drawn to guide the eye.

times for the adsorption of Fe-Terpy and Fe-MEPE is also revealed by temperature jump experiments shown in Figure 10.2. In these experiments the temperature of the systems was taken from 20°C to 50°C and back to 20°C after 3-4 h. The adsorbed amounts determined by UV-vis measurement of the supernatant solution immediately after the heating step indicated that temperature increase leads to a decrease of Terpy adsorption and to an increase of MEPE adsorption. After cooling to 20°C, the adsorbed amount of Fe-MEPE remains at the higher level of adsorption while the adsorption of Fe-Terpy returns to the higher adsorption level attained before the temperature jump. Figure 10.2 shows that this temperature jump experiment could be repeated at a later time, when the adsorption of Fe-MEPE in the matrix had attained a higher level while the adsorption of Fe-Terpy had

remained at a nearly constant value.

The reversible changes in the adsorbed amount observed in the case of Terpy/20-CA system suggest that these changes are induced by a temperature-induced shift of the adsorption equilibrium to a lower level of adsorption at higher temperature, as to be expected for an exothermic adsorption process. Accordingly, the adsorbed Fe-Terpy molecules diffuse out of the pores to establish the new equilibrium at the higher temperature. After cooling the system back to 20°C , the system returns to the original equilibrium state. In the case of Fe-MEPE adsorption, equilibrium has not yet been attained at he time of the temperature jump. In this case an increase of the temperature increases the adsorption rate, and therefore, the adsorption remains at the higher level after return to 20°C. Possibly, this behavior comes from the supramolecular coordination polymer character of Fe-MEPE (see section 7.1). An increase of the temperature, i.e. kinetic energy supply, leads to shorter chain lengths making the entering and diffusion of the chains in the pore channels easier.

10.2 Adsorption kinetics of Fe-MEPE

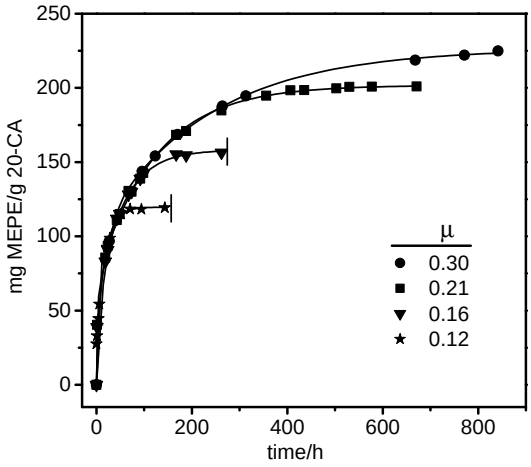

Figure 10.3: Effect of the initial Fe-MEPE concentration (MEPE to 20-CA mass ratio μ) on the adsorption rate. All preparations were performed in 50 ml pure water. The solid lines are fits. The short vertical lines indicate the complete adsorption of Fe-MEPE by 20-CA.

In order to clarify the mechanism of Fe-MEPE adsorption into the pores of CA-SBA-

Table 10.1: Parameters from fitting the MEPE adsorption curves to the Equation 10.1

μ	c_0/mM	A_1/mg g^{-1}	t_1/h	A_2/mg g^{-1}	t_2/h	R
0.12	0.5	25±2	0.004±0	94±1	18±1	0.99932
0.16	0.6	52±2	1.3±0.1	106±2	54±2	0.99968
0.21	0.8	70±2	1.8±0.2	131±2	122±4	0.99924
0.30	1.2	80±6	2.1±0.3	143±4	178±12	0.99875

μ: Fe-MEPE to silica mass ratio; c_0: initial Fe-MEPE concentration

15 silica systematic studies were performed by measuring the uptake rate with different initial concentrations of Fe-MEPE, that is, at different silica to MEPE mass ratios μ (see Figure 10.3). In order to attain acceptable equilibration times for the uptake of Fe-MEPE, these adsorption measurements were conducted at 50°C because we found that the adsorption rate of Fe-MEPE increases by increasing the temperature (see Section 9.2.3). 20-CA was used as adsorbent because of its higher MEPE adsorption capacity. In view of the high stability of Fe-MEPE in salt free solution the adsorption studies were made in pure water. The uptake curves displayed in Figure 10.3 can be fitted by a sum of two exponential decay functions

$$y = y_0 - A_1 e^{-t/t_1} - A_2 e^{-t/t_2} \tag{10.1}$$

where y is the uptake at time t and y_0 is the limiting uptake at $t \rightarrow \infty$. Hence, the uptake curves may be described as the combination of two first-order processes with different relaxation times. The uptake time t_1 is short in comparison to the uptake time t_2. The parameters obtained from the fit of the MEPE uptake curves to the Equation 10.1 are summarized in Table 10.1. Table 10.1 reveals that the time constant t_1 is of the order of 1 h or less, while the time constant t_2 is of the order of 100 h. Hence the time scales of the two processes are separated by two orders of magnitude. Both time constants increase with increasing MEPE-to-silica mass ratio μ.

In order to interpret these experimental data by means of the kinetic standard models for diffusion-controlled systems discussed in Section 7.5 viz. diffusion control through the surface layer (Eq. 7.12) and internal diffusion control (Eq. 7.15) the parameters a_∞ and a_* of Eq. 7.12 have to be extracted from Eq. 10.1. We consider this relation for three different times

(i) at t=0 : y=0 and Eq. 10.1 yields $y_0 = A_1 + A_2$

(ii) at t= t^* so that $t_1 \ll t^* \ll t_2$: y= a_*

$$a_* = y_0 - A_2$$

(iii) at t $\gg$ t* : y=a_∞

$$a_\infty = y_0$$

Accordingly, we find $a_\infty = A_1 + A_2$ and $a_* = A_1$. By substituting a_∞ and a_* into Eq. 10.1 and changing y to a_t one obtains

$$a_t = a_\infty - a_*\, e^{-t/t_1} - (a_\infty - a_*)\, e^{-t/t_2}. \tag{10.2}$$

Since t=t* and $t_1 \ll t^*$ in case (ii), $e^{-t/t_1} \approx 0$. Thus

$$a_t = a_\infty - (a_\infty - a_*)\, e^{-t/t_2} \tag{10.3}$$

$$\frac{a_t - a_*}{a_\infty - a_*} = 1 - e^{-t/t_2}. \tag{10.4}$$

This analysis is based on the fact that the time scale of the two processes are well-separated so that the quantity a_* introduced by (ii) is well-defined.

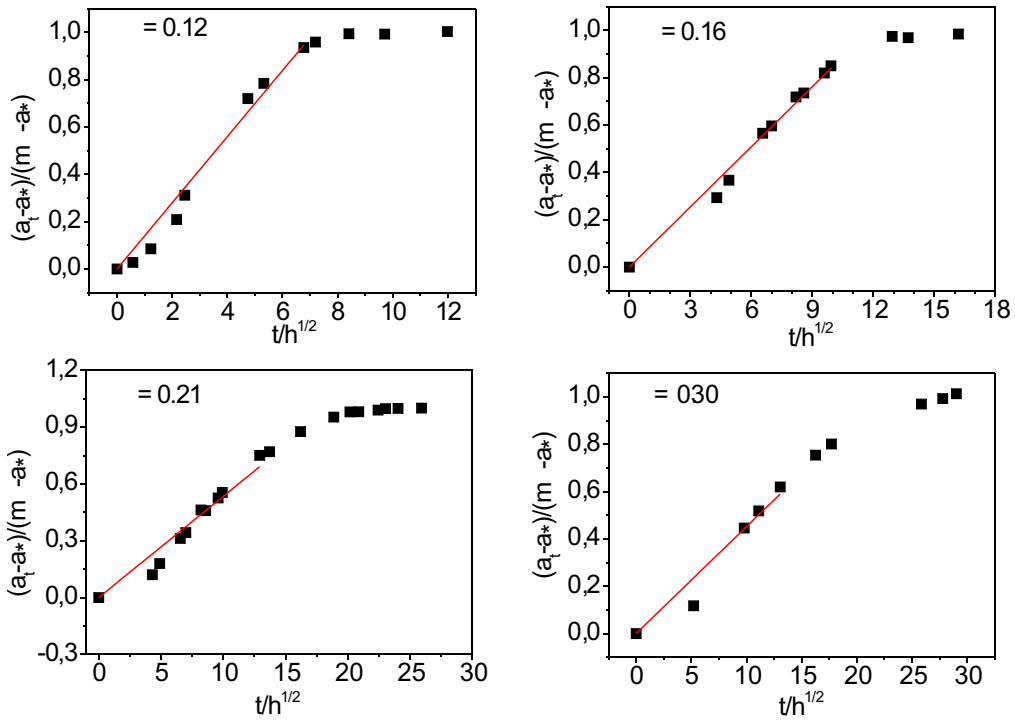

Figure 10.4: Fe-MEPE uptake curves fitted with internal diffusion model.

If the Fe-MEPE sorption is controlled by the internal diffusion process (see Eq. 7.15), the plot $(a_t - a_*)/(m_\infty - m_*)$ vs. $\sqrt{t}$ should give a straight line through the origin with slope $2k\sqrt{D/\pi}$. Figure 10.4 shows that the data points cannot be fitted well by Equation 7.15 indicating that the adsorption process is not controlled by the internal diffusion.

After its linearization Equation 10.4 takes the form $ln(1 - (a_t - a_*)/(a_\infty - a_*)) = -(1/t_2)t$. Hence, if the adsorption is controlled by the diffusion through the surface layer, the plot of $ln(1 - (a_t - a_*)/(a_\infty - a_*))$ vs. time (t) should give a straight line through the origin with slope (-1/t_2) which is equal to (-αk), where α is the mass transfer rate coefficient and k is the ratio of the external area to volume (see Section 7.5). Plots for all four MEPE-to-silica mass ratios μ are displayed in Figure 10.5. As can be seen, the data

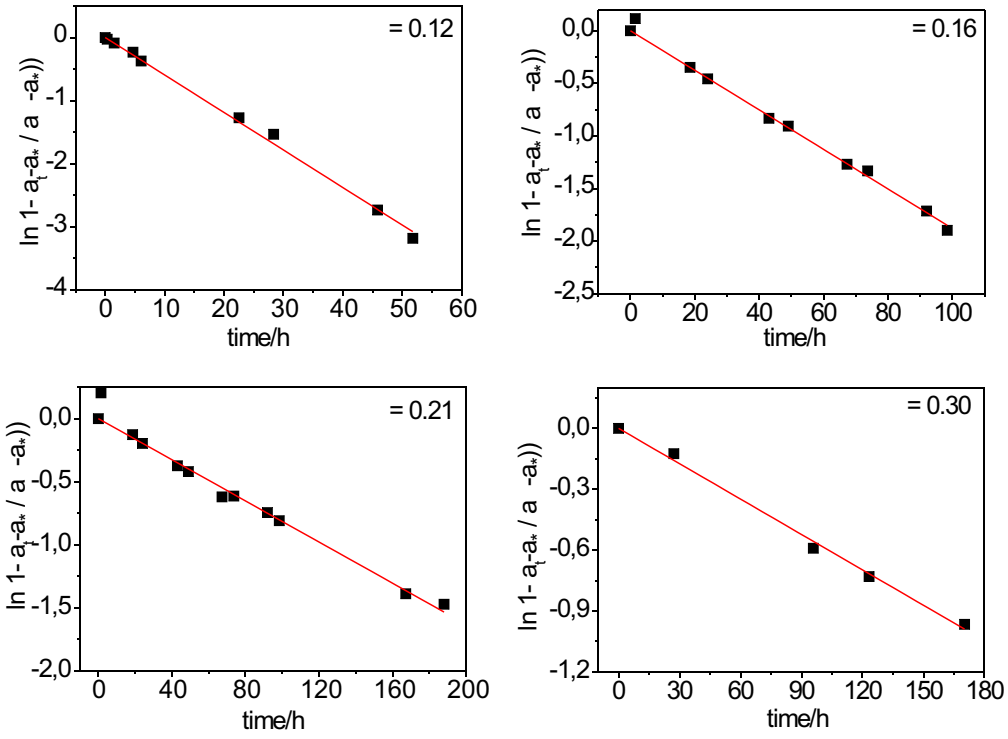

Figure 10.5: Fe-MEPE uptake curves fitted with surface-layer resistance model.

can be represented well by the surface-layer resistance model. The parameters obtained from the fits are summarized in Table 10.2.

To estimate the external surface area (A_{ext}) we assume a hexagonal cylindrical shape of SBA-15 particles as indicated in Figure 10.6. The ratio of external area to volume $k\approx$ 2.06×10^7 m^{-1} is calculated using geometrical considerations (cf. Equation 10.8 below).

In order to determine the mass transfer rate coefficient α, we need to know the ratio of the external surface area to total pore volume $k = A_{ext}/V_p$. For this purpose we assume

Table 10.2: Parameters from fitting the MEPE uptake curves to the Equation 10.1

μ	slope	R	kα/s^{-1}	α/m s^{-1}
0.12	-0.0595±0.0009	0.998425	17	2.3×10^{-10}
0.16	-0.0188±0.0003	0.997573	53	7.2×10^{-10}
0.21	-0.0082±0.0002	0.989572	122	1.6×10^{-9}
0.30	-0.0058±0.0001	0.997821	172	2.3×10^{-9}

μ: Fe-MEPE to silica mass ratio; k: external area to volume ratio $\approx 2.06\times10^{7}$ m^{-1}; α: mass transfer rate coefficient

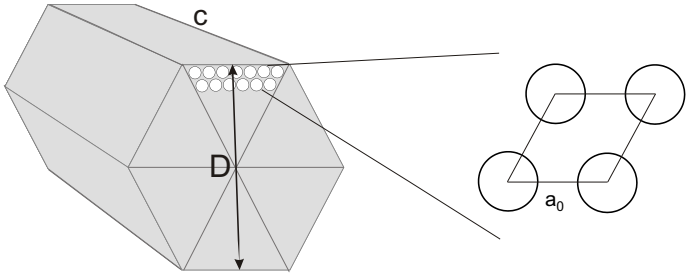

Figure 10.6: left: Scheme of a hexagonal cylindrical SBA-15 particle, consisting of cylindrical mesopores, for estimation of the external surface area; right: Unit cell of 2D hexagonally ordered pores with lattice parameter a_0.

that the SBA-15 particles have an ideal hexagonal cross section and a high aspect ratio, i.e., the length c of the cylinder is large in comparison to the cross sectional diameter D of the cylinder. In this case A_{ext} can be approximated as

$$A_{ext} \approx 6c\frac{D}{\sqrt{3}} = 2\sqrt{3}c \cdot D \tag{10.5}$$

where the diameter D of the cross sectional area of the cylinder is estimated as 450 nm from the SEM micrographs (see Figure 10.6 left). The total pore volume V_p of the particle is given by

$$V_p = \frac{\pi d^2}{4} N \cdot c \tag{10.6}$$

where d is the diameter of the mesopores and N is the number of pores in the cylindrical particle, which is approximately given by

$$N = \frac{A_Q}{A_U} = \frac{\sqrt{3}/2D^2}{\sqrt{3}/2a_0^2} = \frac{D^2}{a_0^2} \tag{10.7}$$

Here A_Q denotes the cross sectional area of the cylinder and A_U denotes the area of a unit

cell of the 2D hexagonally arranged pore lattice (lattice parameter a_0). By substituting Equation 10.7 into Equation 10.6 and using Equation 10.5 one gets

$$k = \frac{A_{ext}}{V_p} \approx \frac{8\sqrt{3}\ a_0^2}{\pi\ d^2 D} \approx\ 0.02\ \text{nm}^{-1} \tag{10.8}$$

where we have used a_0=11.6 nm (from SAXD), d=8 nm (from nitrogen adsorption) and D=450 nm (from SEM micrographs of CA-SBA-15 particles). This relation applies to long worm-like particles for which the front and the back cross-sectional areas of the hexagonal cylinder are disregarded in Eq. 10.8. In this case the unknown quantity c which appears as a factor both in the approximation of A_{ext} and V_p cancels out. For shorter particles the external area-to-volume ratio of the adsorbent will be larger, when the cross section of particles is taken into the account. Thus we expect that k will be in a range $0.02 < k < 0.05$ nm^{-1}. With the known value of k the mass transfer coefficient α can be extracted directly. Values of α (based on $k = 0.02nm^{-1}$) for each initial Fe-MEPE concentration are included in Table 10.2.

As can be seen the mass transfer rate coefficient increases as the initial Fe-MEPE concentration is increased. A comparison with the mass transfer rate of methanol vapor in Ferrite, for which $\alpha = 4.2 \times 10^{-8}$ m s^{-1}) [131], shows that the mass transfer of Fe-MEPE in CA-SBA-15 is a rather slow process.

10.3 Adsorption equilibrium of MEPE

The Langmuir isotherm (Eq. 7.10) was used to represent the adsorption equilibrium relationship (see Figure 10.7). The data for a_{eq} (equilibrium loading of Fe-MEPE at the surface of CA-SBA-15) and c_{eq} (equilibrium concentration of Fe-MEPE in solution) are taken from the uptake curves of Fig. 10.3 for equilibration times of 300-350 h.

After linearization the Langmuir equation takes the form

$$\frac{1}{a_{eq}} = \frac{1}{a_m} + \frac{1}{a_m K_L}\frac{1}{c_{eq}}. \tag{10.9}$$

The plot of $1/a_{eq}$ vs. $1/c_{eq}$ gave a straight line. From the slope and y-intercept one finds a_m=230 mg g^{-1}, and K_L=107.5 l mmol^{-1} which corresponds to 150.5 l g^{-1}. Figure 10.7 shows that the data for a_{eq} are well represented by the Langmuir equation. The high value of K_L indicates a high adsorption affinity of Fe-MEPE in 20-CA. High adsorption affinity is often observed for polymer or protein adsorption from solution [132]. In this type of adsorption the molecules bind so strongly that no remnant can be detected in solution,

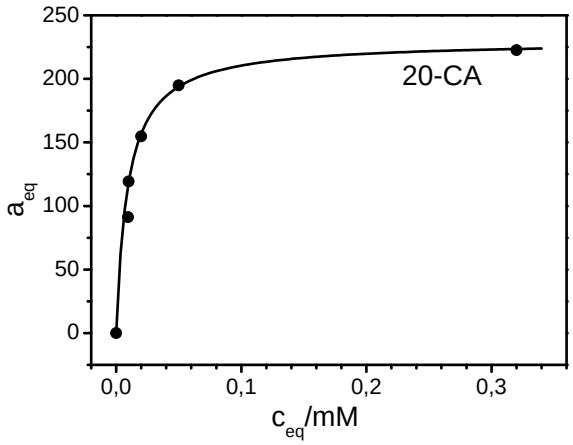

Figure 10.7: Langmuir isotherm of samples prepared with different μ at 50°C.

which is exactly what we observed for the adsorption of Fe-MEPE in the carboxylic acid functionalized SBA-15.

20-CA has a pore diameter of 8 nm and a pore volume of 0.60 cm^3 g^{-1}. On the other hand, Fe-MEPE can be considered as a cylinder of diameter 1.2 nm. A schematic illustration true to scale shows that a maximum of 18 Fe-MEPE chains can be accommodated side-by-side in a 8 nm pore (see Figure 10.8). On the basis of the model discussed in Section 9.3.3, 18 Fe-MEPE chains correspond to an adsorbed amount of 183 mg MEPE/g silica, which on the basis of the geometrical model should represent the monolayer capacity. However, this value is smaller than the value a_m=230 mg g^{-1} derived on the basis

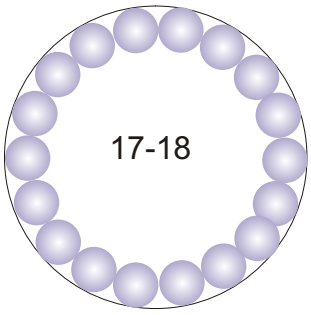

Figure 10.8: The schematic illustration of Fe-MEPE in a 8 nm pore. According to the illustration a maximum of 18 Fe-MEPE chains can be accommodated side-by-side in a 8 nm pore. The illustration is true to scale.

of the Langmuir adsorption isotherm which would correspond to ca. 25 Fe-MEPE chains

side-by-side in the pores. Values higher than 18 may indicate the formation of a second layer of Fe-MEPE in the pores, or at the outside of the silica particles, or both. An alternative explanation of the high value of a_m derived from the Langmuir isotherm is suggested by nitrogen adsorption measurements of pure 20-CA silica, which indicated an enlargement of the pore volume of silica after exposure to water (see Section 6.2.4). From the fact that the pore diameter remained constant while the pore volume was increased, it was suggested that the exposure to water makes part of the pores which were formerly blocked accessible to adsorption. This would imply that the silica can adsorb more Fe-MEPE than estimated on the basis of the nitrogen adsorption data obtained prior to the exposure to water.

10.4 Conclusions

In this chapter, comparative adsorption measurements of Fe-Terpy and Fe-MEPE in pure and carboxylic-acid functionalized SBA-15 (20-CA) were performed. These showed (i) the adsorption affinity of Fe-Terpy in 20-CA is much higher than in pure SBA-15; (ii) under comparable conditions the adsorption of Fe-Terpy is much faster than the adsorption of Fe-MEPE. Result (i) confirms the outcomes of the uptake study of Fe-MEPE in the pure and carboxylic acid doped silica materials (Chapter 9). Most likely this can be ascribed to the higher negative surface charge of 20-CA in comparison to pure SBA-15 and to a higher entropic driving force connected with ion exchange in 20-CA. The difference in the uptake kinetics of Fe-MEPE and Fe-Terpy are attributed to the polymeric character of Fe-MEPE. The uptake curve of Fe-Terpy shows a fast initial increase leading directly to a plateau, indicating a rapid achievement of the adsorption equilibrium. The uptake curve of Fe-MEPE also exhibits a fast initial uptake. But this is followed by a much slower second uptake process extending for many days. The uptake curves of Fe-MEPE could be modelled by a combination of two exponential decay functions, the first with a short relaxation time t_1 (corresponding to the fast adsorption process), the second with a much longer relaxation time t_2, accounting for the slow uptake process that leads to the adsorption equilibrium. An analysis of the kinetic data on the basis of models for surface-layer-resistance or internal diffusion as rate determining process showed that the diffusion during the uptake of Fe-MEPE into the pores is controlled by surface layer resistance and not by internal diffusion inside the pore channels. This means that the rate-limiting step of adsorption during the uptake is the entering of the Fe-MEPE chains into the pores and not the diffusion of the MEPE chains inside of the pore channels. The estimated mass

transfer coefficient α of 10^{-9}-10^{-10} m s^{-1} is small, indicating a slow entering process of Fe-MEPE chains into the pores.

The different equilibration times for the adsorption of Fe-Terpy and Fe-MEPE are also revealed by repeated temperature jump experiments. A temperature increase (50°C) leads to a decrease of Terpy adsorption and to an increase of MEPE adsorption. After cooling (20°C), the adsorbed amount of Fe-MEPE remains at the higher level of adsorption while the adsorption of Fe-Terpy returns to the higher adsorption level attained before the temperature jump. The reversible changes in the adsorbed amount observed in the case of Terpy uptake suggests that these are induced by a temperature-induced shift of the adsorption equilibrium to a lower level of adsorption at higher temperature, as to be expected for an exothermic adsorption process. In the case of Fe-MEPE adsorption equilibrium has not yet been attained at the time of the temperature jump. In this case an increase of the temperature increases the adsorption rate, and therefore, the adsorption remains at the higher level after returning to 20°C. Moreover, the Langmuir adsorption isotherm turned out to describe the solid-liquid equilibrium of Fe-MEPE satisfactorily. The high value of the Langmuir constant K_L indicates a high adsorption affinity of Fe-MEPE in 20-CA.

Chapter 11

Summary and Outlook

In this Thesis, pure and functionalized 2D-hexagonally ordered mesoporous silica materials have been synthesized and characterized by a large variety of methods. The functionalization was performed by two different routes:

1. post-modification by surface grafting
2. functionalization by co-condensation (one-pot synthesis)

The functionalized materials were used (i) for examination of the surface properties of mesoporous MCM-41 and SBA-15 silicas; (ii) for acidity measurements in water-free confined geometry; (iii) as hosts for metallo-supramolecular coordination polymers (MEPE).

Grafting route was used for modifying the surface of MCM-41 and SBA-15 silicas using $(CH_3)_2$-Si$(OCH_3)_2$ and (CH_3)-Si$(OCH_3)_3$ as grafting reagents. In the next step the arrangement of surface silanol groups at the silica surfaces was studied by solid-state ^{15}N NMR method after pyridine adsorption into the pores. We found that the number of covalent bonds to the surface formed by the functional reagents is affected by the surface morphology. It was concluded that for high-quality MCM-41 silicas the distance between neighboring surface silanol groups at the pore walls is greater than 0.5 nm. As a result, the di- and tripodical functional reagents can form only one covalent bond to the surface. In the case of SBA-15, however, the formation of two covalent bonds to the surface is possible as well. The residual hydroxyl groups of surface-bonded functional reagents either remain free or interact with other reagent molecules. Accordingly, the number of surface silanol groups at a given MCM-41 or SBA-15 silica needs not decrease but may increase after grafting with $CH_3Si(OH)_3$ reagent.

Co-condensation route was used for functionalization of the SBA-15 silica with acidic groups of different pK_a values in the liquid phase. These were carboxylic acid, phospho-

nic acid and sulfonic acid. This synthesis route was chosen because the high surface coverage of silica by acid groups which is needed for the acidity measurements cannot be reached by the grafting method. The following features are common to all acid-functionalized SBA-15 materials prepared by the co-condensation route:

1. The higher the proportion of the functional silane ϕ in the silica precursor, the lower is the amount of polymer template in the as-synthesized functionalized SBA-15 and the higher is the degree of the polymer removal achieved by the sulfuric acid treatment.

2. The microporosity of acid-functionalized SBA-15 samples is lower than that of pure SBA-15.

3. Well-ordered SBA-15 materials are obtained with a maximum molar percentage of functional silane $20 < \phi < 30$.

The maximum surface coverage of the pore walls and the yield of the functionalization reaction reached by the co-condensation method are different for the three acids. The highest surface coverages of SBA-15 by carboxylic acid, phosphonic acid, and sulfonic acid groups are 50%, 40% and 30%, respectively. The reaction yields of the functionalization reactions show a similar tendency. The optimum reaction conditions for producing ordered SBA-15 type materials with a high functionalization degree are different, and they strongly depend on the (hydrophilic or hydrophobic) nature of the functional silane used. An ideal functional silane should be able to interact attractively both with the hydrophilic silica precursor TEOS and with the hydrophilic PEO block of the blockcopolymer (P123) template. However, it must not interact equally well with the hydrophobic PPO and hydrophilic PEO blocks of the copolymer as this would affect the microphase separation of the two blocks which is needed for the formation of ordered materials. Our studies showed that these requirements become increasingly important at higher mole percentages ϕ of the functional silane used in the reaction mixture, and thus for the synthesis of SBA-15 with a high degree of functionalization. Moreover, the hydrolysis and condensation rate of the functional silane relative to that of TEOS plays a crucial role for the ordering of silica material obtained. Ideally, the hydrolysis and condensation rates of TEOS and functional silane should be similar. Furthermore, at the chosen reaction conditions the rate of condensation of the silica sources must not be faster than their hydrolysis rates. Presumably, the hydrophilicity of the functional silanes decrease in the order STHS > CTES > PTES. In the case of carboxylic acid functionalization, CTES is expected to become more hydrophilic during the synthesis due to the partial hydrolysis of the CN head

group, whereas the phosphonic acid silane PTES with its not-cleavable phosphonic acid ester groups remains rather hydrophobic. Thus, for CTES and the sulfonic acid silane STHS an attractive hydrophilic interaction with PEO and TEOS is suggested during the synthesis. However, simultaneous addition of TEOS and CTES leads to the formation of disordered silica materials, indicating different hydrolysis/condensation rates of these silica sources. Two probable explanations for this behavior are (i) the hydrolysis rate of the CTES is slower than that of TEOS, and (ii) hydrolysis of CN-groups to COOH-groups increases the hydrophilicity of the functional reagent and yields a better interaction with both the hydrophilic POE block of copolymer and TEOS and a weak interaction with the hydrophobic PPO block of copolymer which effects a better microphase separation. This suggests that a prehydrolysis of CTES before the addition of TEOS will improve the formation of functionalized products, which indeed leads to ordered composite materials up to ϕ= 20 of CTES in the silica precursor mixture. In the case of sulfonic acid functionalization using STHS, prehydrolysis does not play a role, because STHS already exists in the hydrolyzed form. Simultaneous addition of TEOS and STHS yields ordered functionalized SBA-15 material. However, the degree of incorporation of the sulfonic acid reagent is low compared to the other functionalization reactions. Probably this can be explained by the slow condensation rate of the hydroxyl groups of the highly acidic functional silane. In contrast, the interactions of hydrophobic phosphonic acid silane PTES both with the block copolymer and TEOS are unfavorably. Presumably PTES interacts both with PEO and PPO blocks of the block copolymer, and thus reduces the microphase separation necessary for the formation of ordered silicas. Nevertheless, the system seems to tolerate this up to PTES contents of ϕ= 10. Increasing ϕ to 15 and 20 causes a shortening of the worm-like structures and leads to the forming of disk-like stuck-together structures under preservation of the 2D-hexagonally order. The amount of PTES in the precursor mixture can be increased to ϕ =15 without destruction of the worm-like morphology of SBA-15 by prehydrolysis of TEOS. This probably indicates that the hydrolysis of TEOS is slow in comparison to that of PTES.

Acidity measurements of the functional groups at the pore wall were performed by ^{15}N solid-state NMR after adsorbing pyridine into the silica materials. These measurements performed in cooperation with the NMR Group in Freie Universität Berlin in the framework of SFB 448 showed that all three acids can be deprotoned pyridine. This is unexpected in the case of carboxylic-acid functionalized SBA-15 which is a weak acid in aqueous solution (acid dissociation constant pK_a=4.7). The surface silanol groups have a similar acidity as carboxylic acids in water but are not protonated by pyridine in the dry

state at the pore wall. The high proton-donor ability of carboxylic acid functional groups at the pore walls may be due to the formation of hydrogen-bonds between several carboxylic acid groups at the surface. It is known that in solutions the formation of hydrogen-bonded chains of carboxylic acid molecules lead to an enhanced acidity of the terminal proton. The high local concentration of carboxylic acid groups in the CA-functionalized SBA-15 material may lead to a similar conjugation effect in the pores. Further measurements within the PhD thesis of Daniel Mauder (FU-Berlin) are in progress to check this conjecture. In addition to these experiments, comparative pH dependent proton donor ability measurements of 10-CA-SBA-15 (10-CA) and 20-CA-SBA-15 (20-CA) samples were performed by FT-IR spectroscopy. An increase of the pH from 5.5 to 8.0 leads to the appearance of the asymmetric and symmetric stretching bands of carboxylate anions, while the intensity of the C=O stretching band of COOH group decreases. The FT-IR measurements reveal an interesting difference between 10-CA and 20-CA: Whereas for 10-CA the C=O stretching has almost disappeared at pH 8, it is only weakened in the case of 20-CA. This suggests, that in 10-CA, where the surface is covered by COOH groups to 20%, all COOH groups are separated and accessible while in 20-CA with 50% surface coverage only a part of COOH groups are accessible.

The adsorption behavior of metallo-supramolecular polyelectrolytes (MEPE) in the pores of pure and CA-functionalized SBA-15 was studied for the case of Fe-MEPE. The adsorption of Fe-MEPE acetate from aqueous solutions was studied under different conditions of pH, ionic strength, temperature and chemical properties of the pore wall. The uptake kinetics and the adsorption equilibrium in water was studied in detail. Electrostatic interactions play an important role in the interaction of Fe-MEPE with the silica pore wall, because Fe-MEPE has positive charges along the backbone, whereas the walls of the silica at ambient pH are negatively charged due to the weakly acidic surface silanol groups. This charge effect can be boosted by using carboxylic-acid functionalized SBA-15. The amount of adsorbed Fe-MEPE at the pore walls of CA-functionalized SBA-15 corresponds to a close-packed monolayer of Fe-MEPE chains disposed parallel to each other at the pore walls. The increase of the amount adsorbed in CA-doped silica relative to pure SBA-15 can be verified by using the monotopic Fe-Terpy complex formed by complexation of Fe(II) ions with 2,2´:6´2´´-terpyridine. The equilibrium of Fe-Terpy uptake in silica occurs in less than one hour. By contrast, the uptake of Fe-MEPE extends over a long period of time and can be represented by a sum of two first order processes, a fast initial process with relaxation time t_1 and a second much slower process with relaxation time t_2. The decrease of pH during the initial-fast uptake implies an ion exchange be-

tween the protons on the wall-carboxyl groups and Fe-MEPE. The slow process extends over hundred of hours until the adsorption equilibrium is reached. The adsorption equilibrium of Fe-MEPE can be described by a Langmuir isotherm with a large adsorption constant K_L indicating strong interactions between the carboxylic acid decorated silica wall and Fe-MEPE. The kinetic study indicates that Fe-MEPE adsorption in the pores is a diffusion-controlled process, where diffusion is controlled by the surface-layer resistance. Presumably, this resistance is due to reduction of configurational freedom of the chains on entering the pores. Solid-state NMR method has proved to be a useful method for estimating the chain length of Fe-MEPE before and after the adsorption into the pores. Comparative measurements showed that Fe-MEPE chains incorporated into the pores are shorter than those in solution, indicating that the chains break into smaller entities in the pores.

In conclusion, the present work has shown that the interactions between the polymer template, functional silane and TEOS during the synthesis are crucial for the formation of well-ordered functionalized SBA-15 silicas. However, a detailed examination of these complex interactions requires more systematic studies in the future. For example, determining the relative hydrolysis and condensation rates of both functional silane and TEOS in diluted aqueous systems will cast new light on the formation mechanism. The investigation of these entities by spectroscopic methods such as UV-Vis or IR spectroscopy provides a challenge for future work.

Surface charge titrations of the pure SBA-15 and CA-SBA-15 at well-defined pH values may be very useful for resolving the question of the difference in surface charge between pure SBA-15 and CA-SBA-15. In this context it would also be interesting to study the adsorption of Fe-Terpy and Fe-MEPE in the stronger acidic PA-SBA-15 and SA-SBA-15 samples that are expected to have higher surface charge. If the acids act as oxidizing agents, this would destroy the complexes which in turn would be detectable by the color change of the complex.

The time and concentration dependent precipitation of Fe-MEPE chains in solution as well as during the adsorption in SBA-15 also calls for further investigation. Specially, it should be clarified to what extent the slow uptake process of Fe-MEPE is affected by this precipitation.

Bibliography

[1] MUMPTON, F. A.: *La roca magica : Uses of natural zeolites in agriculture and industry*. Proc. Natl. Acad. Sci. USA, 96:3463, 1999.

[2] MUELLER, U.; SCHUBERT, M.; TEICH F.; PUETTER H.; S.-ARNDT K.; PASTRÉ J.: *Metal-organic frameworks- prospective industrial applications*. J. Mater. Chem., 16:626, 2005.

[3] KRESGE, C. T.; LEONOWICZ; M. E.; ROTH, W. J.; VARTULI J. C.; BECK J. S.: *Ordered mesoporous molecular sieves synthesized by aliquid-cyristal template mechanism*. Nature, 359:710, 1992.

[4] ZHAO, D.; FENG, J.; HUO Q.; MELOSH N.; FREDRICKSON G. H.; CHMELKA B. F.; STUCKY G. D.: *Triblock copolymer syntheses of mesoporous silica with periodic 50 to 300 Angstrom pores*. Science, 279:1998, 1998.

[5] SHENDEROVICH, I. G.; BUNTKOWSKY, G.; SCHREIBER A.; GEDAT E.; SHARIF S.; ALBRECHT J.; GOLUBEV N. S.; FINDENEGG G. H.; LIMBACH H.-H.: *Pyridine-15N- A mobile NMR sensor for surface acidity and surface defects of mesoporous silica.* J. Phys. Chem. B, 107:11924, 2003.

[6] CLARK, J. H.; MACQUARRIE, D. J.; TAVENER S. J.: *The application of modified mesoporous silicas in liquid phase catalysis*. Dalton Trans., 4297, 2006.

[7] SMIRNOV, S. N.; GOLUBEV, N. S.; DENISOV G. S.; BENEDICT H.; S.-MOHAMMEDI P.; LIMBACH H.-H.: *Hydrogen/Deuterium isotope effects on the NMR chemical shifts and geometries of intermolecular low-barrier hydrogen-bonded complexes*. J. Am. Chem. Soc., 118:4094, 1996.

[8] MELERO, J.A.; VAN GRIEKEN, R.; MORALES G.: *Advances in the synthesis and catalytic applications of organosulfonic-functionalized mesostructured materials*. Chem. Rew., 106:3790, 2006.

[9] SCOTT, B. J.; WIRNSBERGER, G.; STUCKY G. D.: *Mesoporous and mesostructured materials for optical Applications*. Chem. Mater., 13:3140, 2001.

[10] YIU, H. P.; WRIGHT, P. A.; BOTTING N. P.: *Enzyme immobilisation using SBA-15 mesoporous molecular sieves with functionalised surfaces*. J. Mol. Catal. B, 15:81, 2001.

[11] MOLLER, K.; BEIN, T.: *Inclusion chemistry in periodic mesoporous hosts*. Chem. Mater., 10:2950, 1998.

[12] SCHÜTTE, M.; KURTH, D. K.; LINFORDT M. R.; CÖLFEN H.; MÖHWALD H.: *Herstellung und Charakterisieung von metallosupramolekularen dünnen Polyelektrolytfilmen*. Angew. Chem., 110:3058, 1998.

[13] BRAY, D.: *Cell movements: from molecules to motility*. Garland Publishing, New York, 2001.

[14] KURTH, D. G.; HIGUCHI, M.: *Transition metal ions: Weak links for strong polymers*. Soft Matter, 2:915, 2006.

[15] GADE, L. H.: *Koordinationschemie*. Wiley-VCH, Weinheim, 1998.

[16] WELZ, B.; SPERLING, M.: *Atomabsorptionsspektrometrie*. Wiley-VCH, Weinheim, 1999.

[17] ZELLMER, D. L.: *http://zimmer.csufresno.edu/ davidz/Chem106/StdAddn/StdAddn.html*. website, 1998. California State University, Fresno.

[18] BRIGGS, D.; GRANT, J. T.: *Surface Analysis by Auger and X-ray Photoelectron Spectroscopy*. IM Publications, Chichester, 2003.

[19] BABER, M.; CONNOR, J. A.; GUEST M. F.; HILLIER I. H.; SCHWARZ-M.; STACEY M.: *Bonding in some donor acceptor complexes involving boron trifluoride. Study by means of ESCA and molecular orbital calculations*. J. Chem. Soc. Faraday Trans. II, 69:551, 1973.

[20] SEAH, M. P.; DENCH, W. A.: *Quantitative electron spectroscopy of surfaces: A standard data base for electron inelastic mean free paths in solids*. Surf. Interface Anal., 1:2, 1979.

[21] HORNAK, J. P.: *Basics of NMR*. website. http://www.cis.rit.edu/htbooks/nmr/.

[22] SCHURKO, R.: *http://mutuslab.cs.uwindsor.ca/schurko/ssnmr/ssnmr_schurko.pdf*.

[23] SOLOVYOV, L. A.; KIRIK, S. D.; SHMAKOV A. N.; ROMANNIKOV V. N.: *X-ray structural modeling of silicate mesoporous mesophase material*. Microporous Mesoporous Mater., 44:17, 2001.

[24] SOLOVYOV, L. A.; MOLOKEEV, M. S.; VASILEV A. D.: *Powder diffraction crystal structure analysis using derivative difference minimization: example of the potassium salt of 1-(tetrazol-5-yl)-2-nitroguanidine*. Acta Crystallogr. B, 61:435, 2005.

[25] IMPÈROR-CLERC, M.; DAVIDSON, P.; DAVIDSON A.: *Existence of a microporous corona around the mesopores of silica-based SBA-15 materials templated by triblock copolymers*. J. Am. Chem. Soc., 122,:11925, 2000.

[26] ZICKLER, G.A.; JÄHNERT, S.; WAGERMAIER W.; FUNARI S.S.; FINDENEGG G.H.; PARIS O.: *Physisorbed films in periodic mesoporous silica studied by in situ synchrotron small-angle diffraction*. Phys. Rev. B, 73:184109, 2006.

[27] SING, K. S. W.: *Characterization of porous materials: past, present and future*. Colloids and surfaces A, 241:3, 2004.

[28] GREGG, S. J.; SING, K. S. W.: *Adsorption, Surface Area and Porosity*. Academic Press, London, 1982.

[29] GALARNEAU, A.; CAMBON, H.; DI RENZO F.; FAJULA F.: *True microporosity and surface area of mesoporous SBA-15 silicas as a function of synthesis temperature*. Langmuir, 17:8328, 2001.

[30] MIYAZAWA, K.; INAGAKI, S.: *Control of the microporosity within the pore walls of ordered mesoporous silica SBA-15*. Chem. Commun., 2121, 2000.

[31] HARKINS, W. D.; JURA, G.: *Extension of the attractive energy of a solid into an adjacent liquid film, the decrease of energy with distance, and the thickness of films*. J. Am. Chem. Soc., 66:919, 1944.

[32] DOLLIMORE, D.; HEAL, G. R.: *An improved method for the calculation of pore size distribution from adsorption data*. J. Appl. Chem., 14:109, 1964.

[33] AKCAKAYIRAN, D.: *Funktionalisierung der Porenwaende und Einlagerung von Metall-Koordinations-Polyelektrolyten in SBA-15 Silika*. Diplom Arbeit, TU-Berlin, 2004.

[34] KRUK, M.; JARONIEC, M.: *Application of large pore MCM-41 molecular sieves to improve pore size analysis using nitrogen adsorption measurements*. Langmuir, 13:6267, 1997.

[35] JARONIEC, M; SOLOVYOV, L. A.: *Improvement of the Kruk-Jaroniec-Sayari method for pore size analysis of ordered silicas with cylindrical mesopores*. Langmuir, 22:6757, 2006.

[36] EHRENSTEIN, G. W.; RIEDEL, G.; TRAWIEL P.: *Thermische Analyse von Kunststoffen*. Carl Hanser Verlag, München, 2003.

[37] LI, Y., ZHANG W.; ZHANG L.; YANG Q.; WEI Z.; FENG Z.; LI C.: *Direct sytnhesis of Al-SBA-15 mesoporous materials via hydrolysis-controlled approach*. J. Phys. Chem. B, 108:9739, 2004.

[38] KIM, J. M.; HAN, Y.-J.; CHMELKA B. F.; STUCKY G. D.: *One-step synthesis of ordered mesocomposites with non-ionic amphiphilic block copolymers: implications of isoelectric point, hydrolysis rate and fluoride*. Chem. Commun., 2437, 2000.

[39] YU, C.; TIAN, B.; FAN-J.; STUCKY G. D.; ZHAO D.: *Salt effect in the synthesis of mesoporous silica templated by non-ionic block copolymers*. Chem. Commun., 2726, 2001.

[40] WEI, Y. L.; WANG, Y. M.; ZHU J. H.; WU Z. Y.: *In-situ coating of SBA-15 with MgO: Direct synthesis of mesoporous solid bases from strong acidic systems*. Adv. Mater., 15(22):1943, 2003.

[41] LI, Y.; FENG, Z.; LIAN Y.; SUN K.; ZHANG L.; JIA G.; YANG Q.; LI C.: *Direct synthesis of highly ordered Fe-SBA-15 mesoporous materials under weak acidic conditions*. Micropor. Mesopor. Mater., 84:41, 2005.

[42] ZHANG, W.; GLOMSKI, B.; PAULY T. R.; PINNAVAIA T. J.: *A new nonionic surfactant pathway to mesoporus molecular sieve silicas with long range framework order*. Chem. Commun., 1803, 1999.

[43] BRUNEL, D.; CAUVEL, A.; DI RENZO F.; FAJULA F.; FUBINI B.; ONIDA B.; GARRONE E.: *Preferential grafting of alkoxysilane coupling agents on the hydrophobic portion of the surface of micelle-templated silica*. New. J. Chem., 24:807, 2000.

[44] BURKETT, S.L.; SIMS, S. D.; MANN S.: *Synthesis of hybrid iorganic-organic mesoporous silica by co condensation of siloxane and organosiloxane precursors*. Chem. Commun., 1367, 1996.

[45] FIORILLI, S.; ONIDA, B.; BONELLI B.; GARRONE E.: *In situ infrard study of SBA-15 functionalized with carboxylic groups incorporated by a co-condensation route*. J. Phys. Chem. B, 109:16725, 2005.

[46] YOKOI, T.; YOSHITAKE, H.; TATSUMI T.: *Synthesis of amino-functionalized MCM-41 via direct co-condensation and post-synthesis grafting methods using mono-, di- and tri-amino-organoalkoxysilanes*. J. Mater. Chem., 14:951, 2004.

[47] MACQUARRIE, D. J.: *Direct preparation of organically modified MCM-type materials. Preparation and characterization of aminopropyl-MCM and 2 cynoethyl-MCM*. Chem. Commun., 1996.

[48] HALL, S. R.; FOWLER, C. E.; LEBEAU B.; MANN S.: *Template-directed synthesis of bi-functionalized organo-MCM-41 and phenyl-MCM-48 silica mesophases*. Chem. Commun., 201, 1999.

[49] MERCIER, L.; PINNAVAIA, J.: *Direct synthesis of hybrid organic-inorganic nanoporous silica by a neutra amine assembly route: Structure-function control by stoichiometric incorparation of organosiloxane molecules*. Chem.Mater., 12:188, 2000.

[50] HUH, S.; WIENCH, J. W.; YOO J.-C.; PRUSKI M.; LIN V. S.-Y.: *Organic functionalization and morphologie control of mesoporous silicas via a co-condensation synthesis method*. Chem. Mater., 15:4247, 2003.

[51] FOWLER, C: E.; BURKETT, S. L.; MANN-S.: *Synthesis and characterization of ordered organo-silica-surfactant mesophases wih functionalized MCM-41-type architecture*. Chem. Commun., 1769, 1997.

[52] LIM, M. H.; BLANFORD, C. F.; STEIN-A.: *Synthesis of ordered microporous silicates with organosulfur surface groups and their aplication as solid catalyst*. Chem. Mater., 10:467, 1998.

[53] MARGOLESE, D.; MELERO, J. A.; CHRISTIANSEN S. C.; CHEMELKA B. F.; STUCKY G. D.: *Direct synthesis of ordered SBA-15 mesoporous silica containing sulfonic acid groups*. Chem. Mater., 12:2448, 2000.

[54] LIM, M. H.; BLANFORD, C. F.; STEIN A.: *Comparative Studies of grafting and direct syntheses of inorganic-organic hybrid mesoporous materilas*. Chem. Mater., 11:3285, 1999.

[55] WANG, Y. Q.; YANG, C. M.; ZIBROWIUS B.; SPLIETHOFF B.; LINDÉN M.; SCHÜTH F.: *Directing the formation of Vinyl-functionalized silica to the hexagonal SBA-15 or large-pore Ia3d structure*. Chem. Mater., 15:5029, 2003.

[56] CHONG, A. S. M.; ZHAO, X. S.: *Functionalization of SBA-15 with APTES and chracterization of functional materials*. J. Phys. Chem. B, 107:12650, 2003.

[57] RICHER, R.; MERCIER, L.: *Direct synthesis of functionalized mesoporous silica by non-ionic alkylpolyetyleneoxide surfactant assembly*. Chem. Commun., 1775, 1998.

[58] CHONG, A.S.M.; ZHAO, X.S.: *Functionalized nanoporous silicas for the immobilization of penicillin acylase*. Appl. Surf. Sci., 237:398, 2004.

[59] YIU, H. P.; BOTTING, C. H.; BOTTING N. P.; WRIGHT P. A.: *Size selective protein adsorption on thiol-functionalised SBA-15 mesoporous molecular sieve*. PCCP, 3:2983, 2001.

[60] VAN RHIJN, W. M.; DE VOS, D. E.; SELS B. F.; BOSSAERT W. D.; JACOBS P. A.: *Sulfonic acid functionalised ordered mesoporous materials as catalysts for condensation and esterification reactions*. Chem. Commun., 317, 1998.

[61] BOSSAERT, W. D.; DE VOS, D. E.; VAN RHJIN W. M.; BULLEN J.; GROBET P. J.; JACOBS P. A.: *Mesoporous sulfonic acids as selective heterogeneous catalysts for the synthesis of monoglycerides*. J. Catal., 182:156, 1999.

[62] MELERO, J. A.; STUCKY, G. D.; VAN GRIEKEN R.; MORALES G.: *Direct synthesis of ordered SBA-15 mesoporous materials containing arenesulfoic acid groups*. J. Mater. Chem., 12:1664, 2002.

[63] MELERO, J.; VAN GRIEKEN, R.; MORALES G.; NUNO V.: *Friedel Crafts acylation of aromatic compounds over arenesulfonic containing mesostructureed SBA-15 materials*. Catal. Commun., 5:131, 2004.

[64] GRIEKEN, R.; MELERO, J. A.; MORALES G. VAN: *Fries rearrangement of phenyl acetate over sulfonic modified mesostructured SBA-15 materials*. Appl. Catal., A, 289:143, 2005.

[65] WANG, X.; CHEN, C. C.; CHEN S. H.; MOU Y.; CHENG S.: *Arenesulfonic acid functionalized mesoporous silica as a novel acid catalyst for the liquid phase Beckmann rearrangement of cyclohexanone oxime to var epsilon-caprolactam*. Appl. Catal. A, 281:47, 2005.

[66] GRIEKEN, R.; MELERO, J. A.; MORALES G. VAN: *Etherification of benzyl alcohols with 1-hexanol over organosulfonic acid mesostructured materials*. J. Mol. Catal. A: Chem., 256:29, 2006.

[67] KAWI, S.; SHEN, S. C.; CHEW P. L.: *Generation of Bronsted acid sites on Si-MCM-41 by grafting of phosphorus species*. J. Mater. Chem., 12:1582, 2002.

[68] LE, Y.; YANG, X.; DAI W. L.; GAO R.; FAN K.: *Unexpected mononuclear W(VI) complexes containing phosphonate ligands anchored on mesoporous silica. Another strategy for immobilization*. Catal. Commun., 9:1838, 2008.

[69] GRUEN, M.; UNGER, K. K.; MATSUMOTO A.; TSUTSUMI K.: *Novel pathways for the preparation of mesoporous MCM-41 materials: control of porosity and morphology*. Microporous Mesoporous Mater., 27:207, 1999.

[70] SCHREIBER, A.: *Phasenverhalten reiner Stoffe in mesoporösen Silika-Materialien*. PhD Thesis, TU-Berlin, 2002.

[71] YANG, C. M.; ZIBROWIUS, B.; SCHMIDT W.; SCHÜTH F.: *Formation of cyanide-functionalized SBA-15 and its transformation to carboxylate functionalized SBA-15*. Phys. Chem. Chem. Phys., 6:2461, 2004.

[72] ZHANG, C.; ZHOU, W.; LIU S.: *Synthesis and characterization of organofunctionalized MCM-41 by the original stepped templated sol-gel technology*. J. Phys. Chem., 109:24319, 2005.

[73] KUMAR, R.; CHEN, H. T.; ESCOTO J. L. V.; LIN V. S. Y.; PRUSKI M.: *Template Removal and Thermal Stability of Organically Functionalized Mesoporous Silica Nanoparticles*. Chem. Mater., 18:4319, 2006.

[74] JÄHNERT, S.: *Untersuchung von reinen Stoffen in periodisch mesoporösen Silikamaterialien mit thermophysikalischen Methoden und in-situ Röntgenkleinwinkelstreuung*. PhD Thesis, TU-Berlin, 2008.

[75] KLEITZ, F.; CHOI, S. H.; RYOO R.: *Cubic Ia3d large mesoporous silica: synthesis and replication to platinium nanowires, carbon nanoroads and carbon nanotubes*. Chem. Commun., 2136, 2003.

[76] CAI, Q.; LUO, Z.-S.; PANG W.-Q.; FAN Y.-W.; CHEN X.-H.; CUI F.-Z.: *Dilute solution routes to various controllable morphologies of MCM-41 silica with a basic medium*. Chem. Mater., 13:258, 2001.

[77] SAJANIKUMARI, S.; KHUSHALANI, D.; MANN S.: *Synthesis and shape modification of organo-functionalized silica nanoparticles with ordered mesostructured interiors*. Chem. Mater., 13:1023, 2003.

[78] CORRIU, R. J. P.; DATAS, L.; GUARI-Y.; MEHDI A.; REYÉA C.; THIEULEUXA-C.: *Ordered SBA-15 mesoporous silica containing phosphonic acid groups prepared by a direct synthetic approach*. Chem. Commun., 763, 2001.

[79] MACIEL, G. E.; HAW, J. F.; CHUANG-I-S.; HAWKINS B. L.; EARLY-T. A.; MCKAY-D. R.; PETRAKIS L.: *NMR studies of pyridine on silica-alumina*. J. Am. Chem. Soc., 105:5529, 1983.

[80] RIPMEESTER, J. A.: *Surface acid site characterization by means of CP/MAS nitrogen-15 NMR*. J. Am. Chem. Soc., 105:2925, 1983.

[81] LORENTE, P.; SCHENDEROVICH I. G.; GOLUBEV, N. S.; DENISOV G. S.; BUNTKOWSKY G.; LIMBACH H.-H.: *1H/15N NMR chemical shift shielding, dipolar 15N,2H coupling and hydrogen bond geometry correlations in a novel series of hydrogen-bonded acid-base complexes of collidine with carboxylic acids*. Magn. Reson. Chem., 39:18, 2001.

[82] MAUDER, D.: *PhD Thesis in preparation*. 2009.

[83] GUCHT, J.; VAN: *Equilibrium polymers in solution and at interfaces*. phD Thesis, Wageningen University, Holland, 2004.

[84] C., CONSTABLE E.: *The coordination chemistry of 2,2':6',2"-terpyridine and higher oligopyridines*. Adv. Inorg. Chem. Radiochem., 30:69, 1987.

[85] CONSTABLE, E. C.; THOMPSON ALEXANDER, M. W. C.: *Multinucleating 2,2´:6´, 2´´-terpyridine ligands as building blocks for the assembly of co-ordination polymers and oligomers*. J. Chem. Soc. Dalton Trans., 3467, 1992.

[86] BODENTHIN, Y.; PIETSCH, U.; MÖHWALD H.; KURTH D. G.: *Inducing spin crossover in metallo-supramolecular polyelectrolytes through an amphiphilic phase transition*. J. Am. Chem. Soc., 125:3110, 2005.

[87] SCHWARZ, G.: *Charakterisierung von Eigenschaften und Struktur Metallo-supramolekularer Funktionseinheiten*. PhD Thesis, Potsdam Universitaet, Potsdam, 2008.

[88] HOLYER, R. H.; HUBBARD, C. D.; KETTLE S. F. A.; WILKINS R. G.: *The kinetics of replacement Reactions of complexes of the transition metals with 2,2',2"-Terpyridine*. Inorg. Chem., 5:622, 1966.

[89] MOREL, F. M. M.; HERING, J. G.: *Principles and applications of aquatic chemistry*. John Wiley, New York, 1993.

[90] SIEVERS, T.: *Multischichten aus vernetzten Koordinationspolyelektrolyten*. Diplom Arbeit, MPI-Golm and FU-Berlin, 2005.

[91] M., MILLER. J.: *Chromatography: Concepts and Contrast*. John Wiley and Sons, Inc., USA, New Jersey, 2nd , 2005.

[92] FALBE, J.; REGITZ M.: *Roempp-Chemie-Lexikon*, Band 5. Thieme, Stutgart, 1992.

[93] HELFFERICH, F. G.: *Ion Exchange*. Dover Publications, New York, 1995.

[94] INGLEZAKIS. V. J.; POULOPOULOS, S. G.: *Adsorption, ion exchange and catalysis: Design of operations and environmental applications*. Elsevier, Amsterdam, 2006.

[95] DITTMEYER, R.; EMIG, G.: *Simultaneous heat and mass transfer and chemical reaction.*, 8, 1727. Wiley-VCH, Weinheim, G. Ertl. et al. , 2008.

[96] CRANK, J.: *The mathematics of diffusion*. Clarendon Press, Oxford, second , 1975.

[97] KRÖHNKE, F.: *The specific synthesis of pyridines and oligopyridines*. Synthesis, 1, 1976.

[98] VADUVESCU, S.; POTVIN, P. G.: *Synthesis and Characterization of a Novel Linear Trinuclear Ruthenium(II) Complex: Variation of Photosensitization Ability with Chain Length in a Homologous Series*. Inorg. Chem., 41:4081, 2002.

[99] VADUVESCU S.; POTVIN, P.G.: *Linear Multinuclear Ru(II) Photosensitizers*. Eur. J. Inorg. Chem, 2004:1763, 2004.

[100] MARGAN, G., BURSTALL F.H.: *347. Researches on residual affinity and co-ordination. Part XXXVII. Complex metallic salts containing 2 : 6-di-2-pyridylpyridine (2 : 2 : 2-tripyridyl)*. J. Chem. Soc., 1649, 1937.

[101] BRIGGS, D.; SEAH, M. P.: *Practical Surface Analysis*. Wiley, Chichester, 1990.

[102] KIM, D. J.; DUNN, B. C.; HUGGINS F.; HUFFMAN G. P.; KANG M.; YIE J. E.; EYRING E. M.: *SBA-15-supported iron catalysts for Fische-Tropsch production of diesel fuel*. Energy and fuels, 20:2608, 2006.

[103] ERNST, S.; GLASER, R.; SELLE M.: *Pogress in zeolite and microporous materials*. H. CHON, S.-K. IHM, Y.S. UH (EDS) (): *Stud. Surf. Sci. Catal.*, 105B, 1021, Amsterdam, 1997. Elsevier.

[104] HONMA, I.; SASABE, H.; ZHOU H. S.: *Synthesis of self-assembled functional molecules in mesoporous materials*. KOMARNENI, S.; PARKER, J. C.; WOLLENBERGER H. J. (EDS) (): *Symposium V: Nanophase and Nanocomposite Materials II*, vol. 457, 525, USA, 1997. Mater. Res. Soc. Symp. Proc., MRS.

[105] ZHU, J.; KÓNYA, Z.; PUNTES V. F.; KIRICSI E.; MIAO C. X.; AGER J. W.; ALIVISATOS A. P.; SOMORJAI G. A.: *Encapsulation of Metal (Au, Ag, Pt) Nanoparticles into the Mesoporous SBA-15 Structure*. Langmuir, 19:4396, 2003.

[106] HOLLAND B. T.; WALKUP C.; STEIN, A.: *Encapsulation, stabilization, and catalytic properties of flexible metal porphyrin compolexes in MCM-41 with minimal electronic perturbation by environment*. J. Phys. Chem. B, 102:4301, 1998.

[107] GANSCHOW, M.; WARK, M.; WÖHRLE D.; SCHULZ-EKLOFF G. *Angew. Chem.*, 112:167, 2000.

[108] HESS, C.; HOEFELMEYER, J. D.; TILLEY T. D.: *Spectroscopic characterization of highly dispersed vanadia supported on SBA-15*. J. Phys. Chem. B, 108:9703, 2004.

[109] WANG, Y. M.; WU, Z. Y.; WANG H. J.; ZHU J. H.: *Fabrication of metal oxides occluded in mesoporous hosts via a solid-state grinding route: The influence of host-guest interacions*. Adv. .Func. Mater., 16:2374, 2006.

[110] AKCAKAYIRAN, D.; KURTH, D. G.; RÖHRS S.; RUPPRECHTER G.; FINDENEGG G. H.: *Self-assembly of a metallosupramolecular coordination polyelectrolyte in the pores of SBA-15 and MCM-41*. Langmuir, 21:7501, 2005.

[111] ERNST, S.; SELLE, M. *Micropor. Mesopor. Mater*, 27:355, 1999.

[112] ZANJANCHI M. A.; EBRAHIMIAN, A.; ALIMOHAMMADI Z: *A spectroscopich study on the adsorption of cationic dyes into mesopoous AlMCM-41 materials*. Optical Materials, 29:794, 2007.

[113] LI, D. M.; ZHAO, W. J.; SUN X. D.; ZHANG J. L.; ANPO M.; ZHAO J.C.: *Photophysical properties of coumarin derivates incorporated in MCM-41*. Dyes and pigments, 68:33, 2006.

[114] YAO, Y. F.; ZHANG, M. S.; SHI J. X.; GONG M. L.; ZHANG H. J.; YANG Y. S.: *Encapsulation of fluorescein into MCM-41 mesoporous molecular sieve by a sol-gel method.* Materials Letters, 48:44, 2001.

[115] REN, T. Z.; YUAN, Z. Y.; SU B. Y.: *Encapsulation of direct blue dye into mesoporuos silca based materials*. Colloids and Surfaces A, 300:79, 2007.

[116] S.-EKLOFF, G; WÖHRLE, D.; VAN DUFFEL B.; SCHOONHEYDT R. A.: *Chromophores in porus silicas and minerals: preparation and optical properties*. Micropor. Mesopor. Mater., 51:91, 2002.

[117] REN, T. Z.; YUAN, Z. Y.; SU B. Y.: *Direct blue dye encapsulatated mesostructured MCM-41 composites: Microwave asisted preparation and characterization*. Colloids and Surfaces A, 300:88, 2007.

[118] ASEFA, T.; MACLACHAN, M. J.; COOMBS N.; OZIN G. A.: *Periodic mesoporous organosilicas with organic groups inside the hannel walls.* Nature, 402:867, 1999.

[119] KURTH, D. G.; LÓPEZ, J. P.; DONG W. F.: *A new Co(II)-metalloviologen-based electrochromic material integrated in thin multilayer films*. Chem. Commun., 2119, 2005.

[120] HAN, F. S.; HIGUCHI, M.; KURTH D. G.: *Metallosupramolecular polyelectrolytes self-assembled from various pyridine ring-substituted bisterpyridines and metal Ions: photophysical, electrochemical, and electrochromic properties*. J. Am. Chem. Soc., 130:2073, 2008.

[121] HAN, F. S.; HIGUCHI, M.; KURTH D. G.: *Metallo-supramolecular polymers based on functionalized bis-terpyridines as novel electrochromic materials*. Adv. Mater., 19:3928, 2007.

[122] BODENTHIN, Y.; SCHWARZ, G.; GUTBERLET T; GEUE T.; STAHN J.; MÖHWALD H.; KURTH D.G.; PIETSCH U.: *Molecular magnetism in thin metallo-supramolecular films: A combined neutron and soft x-ray reflectometry study*. Superlattices and Microstructures, 41:138, 2007.

[123] VERMONDEN, T; VAN DER GUCHT J.; DE WAARD, P.; MARCELIS A. T. M.; BESSELING N. A. M.; SUDHÖTER E. J. R.; FLEER G. J.; COHEN STUART M. A.: *Water-soluble reversible coordination polymers: chains and rings*. Macromolecules, 36:7035, 2003.

[124] YANG, C. M.; ZIBROWIUS, B.; SCHMIDT W.; SCHÜTH F.: *A novel synthetic route for negatively charged ordered mesoporous silica SBA-15*. Chem. Commun., 1772, 2003.

[125] MAROIE, S.; SAVY, M.; VERBIST J.: *ESCA and EPR studies of monomer, dimer, and polymer iron phthalocyanines: involvements for the electrocatalysis of molecular oxygen reduction*. Inorg. Chem., 18:2560, 1979.

[126] JOSEPH, Y.; KETTELER, G.; KUHRS C.; RANKE W.; WEISS W.; SCHLÖGL R.: *On the preparation and composition of potassium promoted iron oxide model catalyst films*. Phys. Chem. Chem. Phys., 3:4141, 2001.

[127] BRUZZONITI, M. C.; PRELLE, A.; SARZANINI C.; ONIDA B.; FIORILLI S.; GARRONE: *Retention of havy metal ions on SBA-15 mesoporous silica functionalized with carboxylic groups*. J. Sep. Sci., 30:2414, 2007.

[128] ILER, R. K.: *The chemistry of Silica*. Wiley, New York, 1978.

[129] KATIYAR, A.; JI, L.; SMIRNIOTIS P.; PINTO N. G.: *Protein adsoption on the mesoporous molecular sieve silicate SBA-15: effects of pH and pore size*. Journal of chromatography A, 1069:119, 2005.

[130] HOFFMANN, T.; WALLACHER, D.; HUBER P.; BIRRINGER R.; KNORR K.; SCHREIBER A.; FINDENEGG. G.H.: *Small-angle x-ray diffraction of Kr in mesoporous silica: Effects of microporosity and surface roughness*. Phys. Rev. B, 72:064122, 2005.

[131] KORTUNOV, P.; CHMELIK, C.; KÄRGER J.; RAKOCZY R. A.; RUTHVEN D. M.; TRAA Y.; VASENKOV S.; WEITKAMP J.: *Sorption kinetics and intracrystalline diffusion of methanol in ferrite: An example of disguised kinetics*. Adsorption, 11:235, 2005.

[132] BUTT, H. J.; GRAF, K.; KAPPL M.: *Physics and Chemistry of Interfaces*. Wiley-VCH Verlag and Co. KGaA, Weinheim, 2003.

Appendix

UV-Spectrum of Fe-Terpy

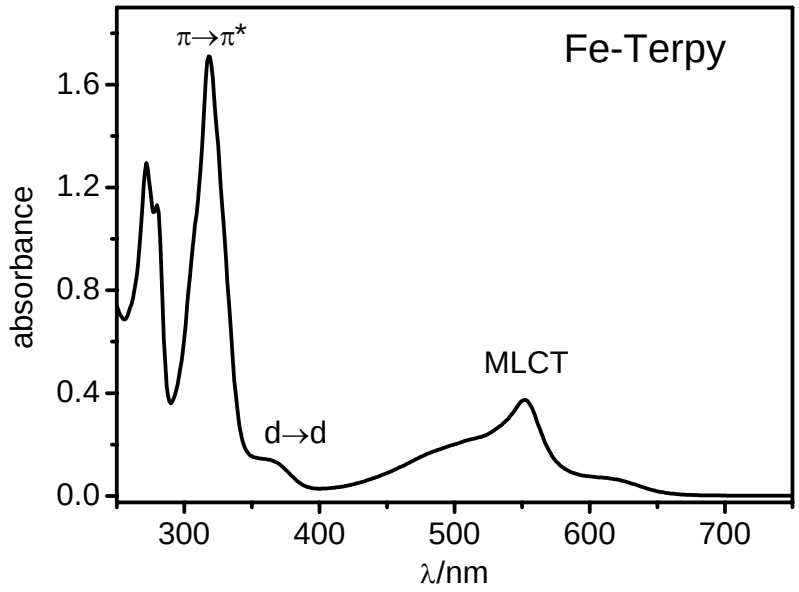

Figure A 1: UV-vis spectrum of Fe-Terpy.

The MLCT-band in the UV-vis spectrum at 552 nm is responsible for the pink-red colour of the Fe-Terpy complex.

Wide Angle X-Ray diffractions of Acid-Functionalized Silicas

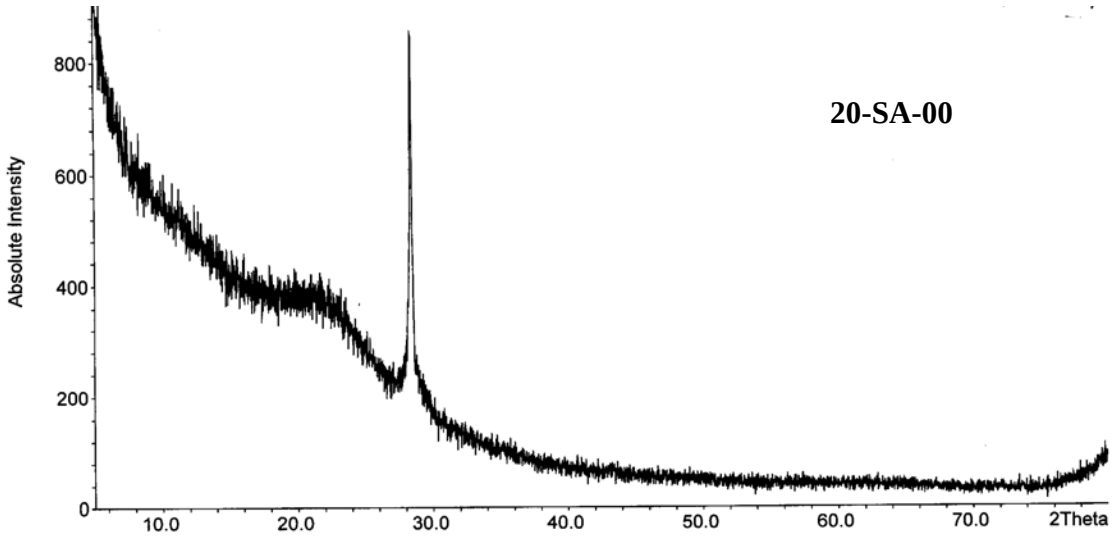

Figure A 1: XRD spectrum of 20-SA-00. The sharp reflex at 2θ=28° comes from the silicon in the sample carrier. The broad reflex at approx. 2θ=22° is assigned to the amorphous structure of the 20-SA-00 sample.

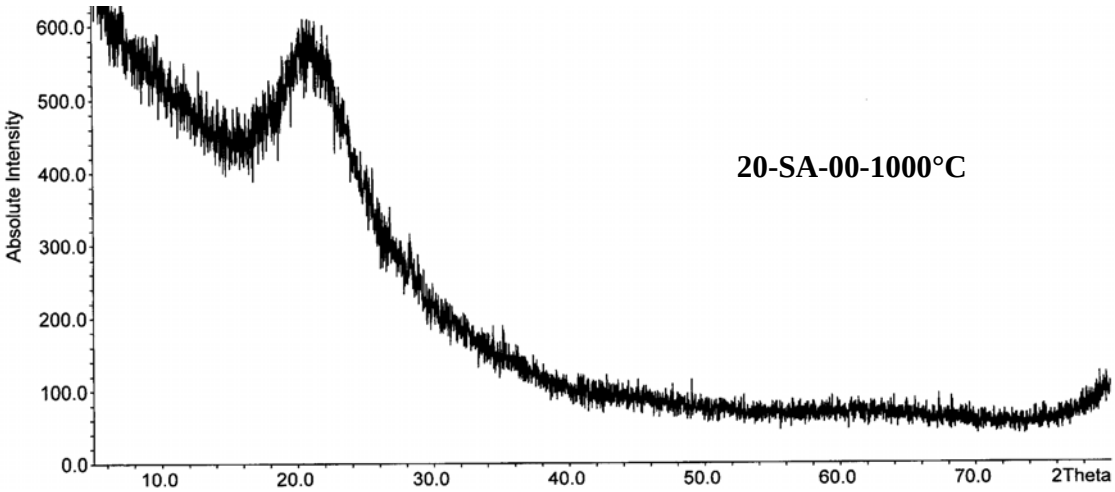

Figure A 2: XRD spectrum of 20-SA-00 heated to 1000°C with a heat rate of 10Kmin^{-1}. The broad reflex at approx. 2θ=22° is assigned to the amorphous structure of the 20-SA-00 sample.

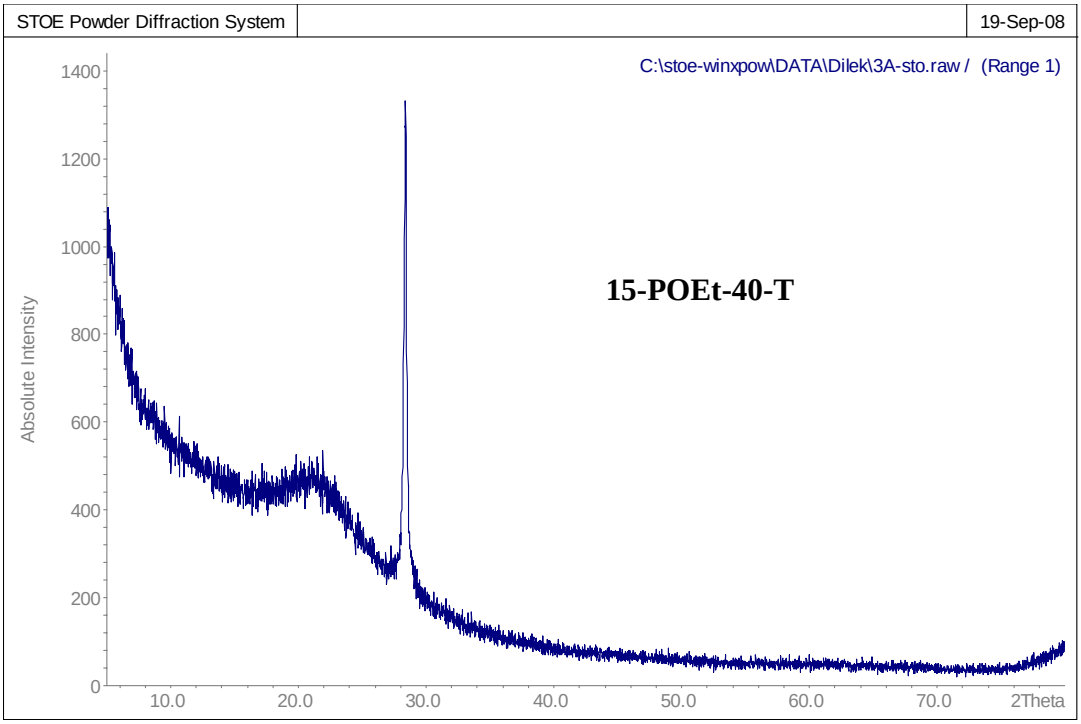

Figure A 3: XRD spectrum of 15-POEt-40-T. The sharp reflex at 2θ=28° comes from the silicon in the sample carrier. The broad reflex at approx. 2θ=22° is assigned to the amorphous structure of the 15-POEt-40-T sample.

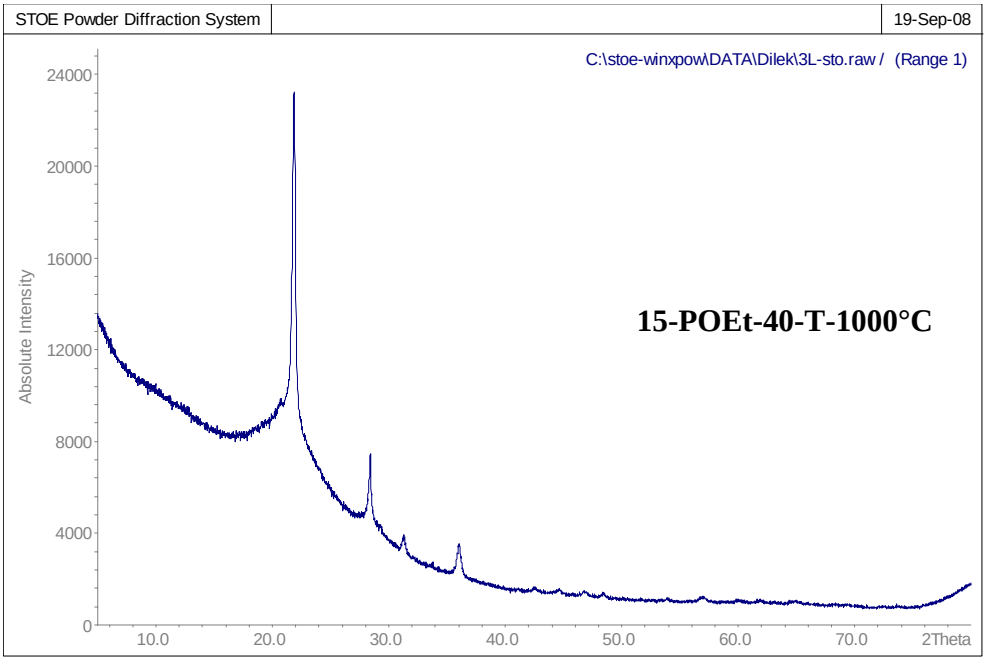

Figure A 4: XRD spectrum of 15-POEt-40-T heated to 1000°C with a heat rate of 10Kmin^{-1}. In this case some sharp reflexes appear in the spectrum coming from a crystalline structure.

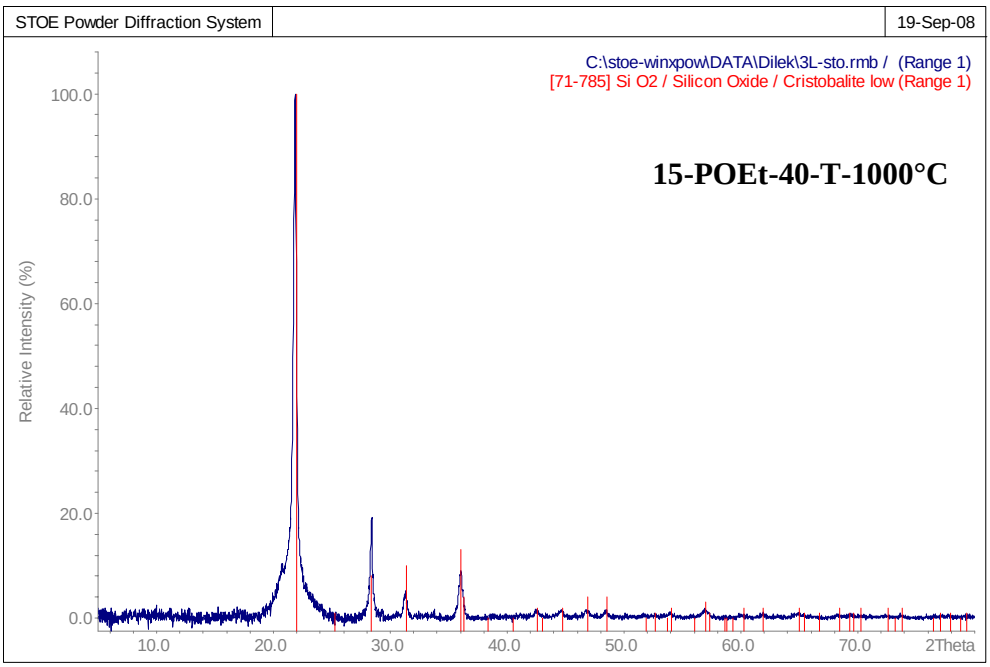

Figure A 5: The background subtracted spectrum in Fig. A 4. The reflexes can be associated with cristobalite which is a high temperature modification of SiO_2.

^{29}Si Solid-State NMR Results

Carboxylic-Acid Functionalized SBA-15

sample	new names	T^2	T^3	Q^2	Q^3	Q^4	$(T/Q)_{exp}$	$(T/Q)_{NMR}$	Y	x
90-60-20-CN(1)	20-CN-60-F(1)	21.2	4.99	36.6		100	0.25	0.19	77%	42%
90-60-20-CA(1)-2	20-CA-60-F(1)-2	29.4		33.6		100	0.25	0.22	88%	50%
90-60-20-CA(1)-3	20-CA-60-F(1)-3	4.7	16.8	30.3		100	0.25	0.17	66%	42%
90-60-20-CA(1)-4	20-CA-60-F(1)-4	14.78	14.37	40.7		100	0.25	0.21	83%	42%
100-60-10-CA(1)-2cal	10-CA-60-F(1)-2	10.6	1.1	40.6		100	0.11	0.08	75%	20%

Table A 1: Expected $(T/Q)_{exp}$ and experimental $(T/Q)_{NMR}$ ratio of organosiloxane (T) and siloxane (Q) groups; Y: Reaction yield; x: Degree of surface functionalization. All samples are discussed in the main text.

Phosphonic-Acid Functionalized SBA-15

sample	new names	T^2	T^3	Q^2	Q^3	Q^4	$(T/Q)_{exp}$	$(T/Q)_{NMR}$	Y	x
90-60-10-PEt	10-P-60-F	0.57	10.1	54.1		100	0.11	0.07	63%	16%
90-60-10-PA(1)-1	10-POEt-60-F(1)-1	9.4		2.2	42.8	100	0.11	0.065	59%	17%
90-60-10-PA(1)-1-H_2SO_4-24h	10-PA-60-F(1)-1									
90-60-10-PA(1)-2	10-POEt-60-F(1)-2	4.28	7.08	0.96	39.6	100	0.11	0.03	73%	22%
90-60-20-PEt(1)	20-P-60-F(1)	25.1	16.7	68.3		100	0.25	0.25	99%	38%
90-60-20-PA(1)-1	20-POEt-60-F(1)-1	5.1		46.2		100	0.25	0.035	14%	10%
90-60-20-PEt(2)	20-P-60-F(2)	19	23.1	73.8		100	0.25	0.24	97%	36%
90-60-20-PA(2)-1	20-POEt-60-F(2)-1	26.6		60.5		100	0.25	0.17	66%	31%
100-95-15-Pet	15-P-95-F(1)	7.3	14	41.2		100	0.18	0.15	85%	34%
100-95-15-PA	15-POEt-95-F(1)-1	6.5	13.3	33.6		100	0.18	0.15	84%	37%
100-95-15-PA-EtOHsox-cal250	15-POEt-95-F(1)-2	15.3	6.3	90.8		100	0.18	0.11	64%	19%
100-95-15-PA-EtOHkolb	15-POEt-95-F(1)-3	12.1	14.4	65.1		100	0.18	0.16	91%	29%
100-00-15-PEt	15-P-00	disordered!								
100-(-40)-15-PA	15-POEt-40-T(1)	12.7	12.6	3.82	56.90	100	0.18	0.19	89%	29%
100-(-40)-15-PA-HCl-24h	15-PA-40-T(1)	6.1	7.5	22		100	0.18	0.11	73%	38%

Table A 2: Expected $(T/Q)_{exp}$ and experimental $(T/Q)_{NMR}$ ratio of organosiloxane (T) and siloxane (Q) groups; Y: Reaction yield; x: Degree of surface functionalization. Marked samples are discussed in the main text.

Sulfonic-Acid Functionalized SBA-15

sample	new names	T^2	T^3	Q^2	Q^3	Q^4	$(T/Q)_{exp}$	$(T/Q)_{NMR}$	Y	x
90-60-20-SA	20-SA-60-F	4.6	8.7	43		100	0.25	0.093	37%	24%
90-1480-30-S	30-S-1480-F		20.4	42.3		100	0.43	0.143	33%	33%
90-1480-30-SA	30-SA-1480-F	14	7.4	35.6		100	0.43	0.158	37%	38%
100-00-20-SA	20-SA-00	5.87	8.73	0.71	31.72	100	0.25	0.116	46%	31%
100-(-55)-20-SA	20-SA-55-T		8.75	0.29	44.19	100	0.25	0.063	25%	16%

Table A 3: Expected $(T/Q)_{exp}$ and experimental $(T/Q)_{NMR}$ ratio of organosiloxane (T) and siloxane (Q) groups; Y: Reaction yield; x: Degree of surface functionalization. All samples are discussed in the main text.

TGA Results

sample	new names	w % F TGA	w % SiO_2 TGA	n_{TGA}	n_{exp}	Y
90-60-20-CA(1)-2	20-CA-60-F(1)-2	16.43	78.8	2.86	3.32	86%
90-60-20-CA(1)-3	20-CA-60-F(1)-3	15	83	2.48	3.32	75%
90-60-20-CA(1)-4	20-CA-60-F(1)-4	15.9	78.1	2.79	3.32	84%
100-60-10-CA(1)-1	10-CA-60-F(1)-1	8.4	86.5	1.33	1.66	80%
100-60-10-CA(1)-2	10-CA-60-F(1)-2	9.6	88.4	1.49	1.66	90%
100-60-10-CA(1)-2cal	10-CA-60-F(1)-2cal	8.7	86.3	1.38	1.66	83%
90-60-20-SA(2)-1	20-SA-60-F(1)-1a	10	85.7	0.95	3.32	29%
90-60-20-SA(2)-1a	20-SA-60-F(1)-1b	11	83.4	1.07	3.32	32%
90-60-20-SA(2)-1b	20-SA-60-F(1)-1c	8	80.3	0.81	3.32	24%
Average:	20-SA-60-F(1)-1	9.7	83.1	0.95	3.32	28%
100-(-55)-20-SA	20-SA-55-T	4.64	89.3	0.42	3.32	13%
100-00-20-SA	20-SA-00	10.3	75.8	1.10	3.32	33%
90-1480-30-SA	30-SA-1480-F	10.93	75	1.18	4.98	24%
90-60-10-POEt(1)a	10-POEt-60-F(1)-a	6	88.6	0.63	1.66	38%
90-60-10-POEt(1)b	10-POEt-60-F(1)-b	5.6	90	0.58	1.66	35%
90-60-10-PA(1)-H_2SO_4	10-PA-60-F	2.97	92.6	0.30	1.66	18%
90-60-20-POEt(1)-1	20-POEt-60-F(1)-1	7.2	89.6	0.74	3.32	22%
90-60-20-POEt(2)-1	20-POEt-60-F(2)-1	12.2	81	1.39	3.32	42%
100-95-15-POEt	15-POEt-95-F(1)-1	10.28	84	1.13	2.49	45%
100-(-40)-15-POEt	15-POEt-40-T	10.4	81.7	1.18	2.49	47%
100-(-40)-15-PA(HCl)	15-PA-40-T	8.48	86.4	0.91	2.49	36%

Table A 4: F: functional group; w % F TGA: weight percentages for F and for SiO_2 obtained from TGA; expected n_{exp} and experimental amount n_{TGA} of F per unit mass of SiO_2 (in mmol g^{-1}); Y: Reaction yield of functionalization. Marked samples are discussed in the main text.

N_2 Adsorption Data

Table A 1: $(p/p_0)_{pc}$: pore condensation pressure of nitrogen; D: pore diameter; v_p: pore volume; a_s: BET specific surface area; v_m: micropore volume, C: BET constant.

Sample-old name	new name	$(p/p_0)_{pc}$	D/nm	v_p/ $cm^3 g^{-1}$	a_s / $m^2 g^{-1}$	v_m /$cm^3 g^{-1}$	C
90-SBA-15a	S-acid	0.799	10.0	0.98	464	-0.015	75
90-SBA-15-b	S-acid	0.799	10.0	0.96	449	-0.022	66
90-SBA-15-c-gr	S-acid	0.797	9.9	0.96	459	-0.020	70
90-SBA-15-d-m	S-acid	0.794	9.8	1.00	483	-0.033	55
90-SBA-15 cal 550	S-cal	0.7425	8.5	1.26	947	0.099	-978
90-SBA-15 cal 250.3h-b-m	S-acid-cal	0.807	10.2	1.35	807	0.082	-1346
P123s05	SBA-15	0.757	8.9	0.89	648	0.05	1371
90-60-20-CA(1)-1-a	20-CA-60-F(1)-1	0.718	8.0	0.79	506	-0.001	102
90-60-20-CA(1)-1-b	20-CA-60-F(1)-1	0.72	8.1	0.79	471	44.405	
90-60-20-CA(1)-2	20-CA-60-F(1)-2	0.72	8.1	0.82	526	-0.010	86
90-60-20-CA(1)-1/2	20-CA-60-F(1/2)	0.716	8.0	1.20			
90-60-20-CA(1)-1/2-cal250	20-CA-60-F(1/2)cal250	0.716	8.0	0.87	571	0.0093	129
90-60-20-CA(1)-3	20-CA-60-F(1)-3	0.718	8.0	0.60	389	0.006	130
90-60-20-CA(1)-4	20-CA-60-F(1)-4	0.716	8.0	0.82	533	0.026	206
100-60-20-CA(1)1	20-CA-20-F(2)	0.644	6.7	0.49	399	-0.001	104
100-90-20-CA(1)1	20-CA-20-F(3)	0.726	8.2	0.88	549	-0.003	98
100-60-10-CA(1)-1 cal250-2h	10-CA-60-F(1)cal250	0.778	9.4	0.98	544	0.018	166
100-60-10-CA(1)-2	10-CA-60-F(2)	0.793	9.8	0.98	490	0.029	248
100-60-10-CA(1)-2-cal250-2h	10-CA-60-F(2)cal250	0.794	9.8	0.97	513	0.005	121
90_60_20_Pet(1)	20-P-60-F(1)			0.14	42	-0.008	26
90_60_20_Pet(1) Cal(250 C- 5 h)	20-P-60-F(1)cal250	0.678	7.3	0.73	666	0.061	6449
90_60_20_PA(1) [(1-a) 48% H2SO4]	20-POEt-60-F(1)-1	0.815	10.5	1.39	687	0.031	213
90_60_20_PA(1)-2a (40% H2SO4)	20-POEt-60-F(1)-2-						
90_60_20_PA(1)-2-cal250-3h	20-POEt-60-F(1)-2-cal250	0.819	10.6	1.20	588	0.022	189
90_60_20_Pet(1)-cal550°C	20-P-60-F(1)cal550	0.624	6.5	0.26	123	-0.001	89

Sample-old name	new name	$(p/p_0)_{pc}$	D/nm	v_p/ cm^3g^{-1}	a_s / m^2g^{-1}	v_m /cm^3g^{-1}	C
90_60_20_Pet(2)	20-P-60-F(2)			0.12	50	-0.004	46
90_60_20_Pet(2)-cal550°C	20-P-60-F(2)cal550	0.601	6.2	0.31	220	0.003	130
90_60_20_PA(2)-1	20-POEt-60-F(2)-1	0.694	7.6	0.73	520	0.032	322
90_60_10_Pet(1)	10-P-60-F(1)	0.656	6.9	0.15	80	-0.021	20
90_60_10_PA(1)-1a [48%H2SO4]	10-POEt-60-F(1)-1	0.753	8.8	0.94	571	0.035	319
90_60_10_PA(1)-1b [48%H2SO4]	10-POEt-60-F(1)-1	0.758	8.9	0.94	559	0.031	292
90_60_10_PA(1)-1 cal250.3h	10-POEt-60-F(1)-1-cal250	0.770	9.2	0.94	572	0.038	386
90-60-10-PA(1)-2	10-POEt-60-F(1)-2	0.740	8.5	0.94	617	0.026	209
90-60-15-PA	15-POEt-60-F(1)-1	0.683	7.4	0.80	553	0.022	201
90-60-15-Pet-550°C	15-POEt-60-F(1)-1-cal550	0.592	6.0	0.31	219	0.004	139
100-95-15-PA(1)	15-POEt-95-F(2)-1	0.676	7.2	0.79	530	0.021	197
100-95-15-PA(1)-EtOH-Soxlet	15-POEt-95-F(2)-2	0.656	6.9	0.73	503	0.040	583
100-95-15-PA(1)-EtOH-Kolben	15-POEt-95-F(2)-3	0.646	6.8	0.55	350	-0.021	60
100-(40)-15-PA	15-POEt-40-T(1)-1	0.691	7.5	0.64	502	0.042	619
100-(40)-15-PA-HCl	15-PA-40-T(1)-1	0.693	7.5	0.66	531	0.025	234
100-(40)-15-POEt(1)-2	15-POEt-40-T(1)-2	0.709	7.8	0.36	244	0.010	203
90_60_20_S(1)	7-S-60-F(1)	0.735	8.4	0.18	87	-0.014	30
90_60_20_S(1)-cal(250°C_5 h)	7-S-60-F(1)cal250	0.765	9.1	1.23	904	0.064	489
90_60_20_SA(1)-1 48% H2SO4	7-SA-60-F(1)-1	0.692	7.5	0.76	560	0.046	938
90_60_20_SA(1)-2 40% H2SO4	7-SA-60-F(1)-2	0.796	9.9	0.79	438	0.005	124
90_60_20_SA(1)-2 40% H2SO4cal250	7-SA-60-F(1)-2cal250	0.8	10.0	0.95	572	0.034	306
90_60_20_SA(2)	20-SA-60-F(2)-1	0.7935	9.8	0.94	557		126
100-00-20-SA	20-SA-00(1)	0.791	9.7	0.96	593	0.029	218
100-00-20-SA(1)-2	20-SA-00(1)-1	0.79	9.7	0.93	564	0.007	125
100-(-55)-20-SA	20-SA-55-T	0.798	10.0	0.77	443	0.022	205
90-1480-30-SA	30-SA-1480-F	0.765	9.1	0.86	672	-0.007	92

Sample-old name	**new name**	$(p/p_0)_{pc}$	D/nm	v_p/ cm^3g^{-1}	a_s / m^2g^{-1}	v_m / cm^3g^{-1}	C
90_60_10_S(1)	3-S-60-F(1)	0.721	8.1	0.19	81		27
90_60_10_S(1) cal(250 C. 5 h)	3-S-60-Fcal250	0.7553	8.8	1.17	836		2170
90-60-10-SA(1)-1	3-SA-60-F(1)1	0.799	10.0	1.26	579	0.045	590

Acknowledgements

This Thesis was written at the Stranski Laboratory for Physical and Theoretical Chemistry at the Technical University Berlin, in the framework of Sonderforschungbereich 448 "Mesoskopisch struktruierte Verbundsysteme" as a part of the the subproject B1*Phasenübergänge und Self-assembly in Mesoporen*.

First, I would like to thank my supervisor, Professor Gerhard H. Findenegg, for the opportunity to work in his group, for many stimulating discussions, for all the time he devoted to my thesis, and for his invaluable advice and guidance. My thanks also go to Professor Reinhard Schomäcker for agreeing to be my second supervisor, and for critical comments and encouragement. Moreover I thank Prof. Regine von Klitzing for agreeing to be the chairlady in my PhD defence.

The experimental work was carried out in cooperation with several groups of the SFB-448 and the Fritz-Haber Institut, various inorganic chemistry departments of TU-Berlin, and with BAM. I am deeply indebted to the following persons:

Stranski co-workers for such a convenient and harmonic working atmosphere.

Our cooperation partner and NMR specialists Dr. Ilja Shenderovich and Daniel Mauder from FU-Berlin. Dear Ilja, I thank you for many useful suggestions during our long discussions. Dear Daniel I thank you for performing all the solid state NMR measurements, and for such a close and productive cooperation. I think our cooperation within the SFB will set a paradigm! Now it's your turn. I wish you all the best in writing your thesis.

Dr. Dirk Kurth (MPI-Golm) for the opportunity to work with MEPE's, and also for numerous suggestions and discussions.

Torsten Sievers (MPI-Golm) for time-consuming synthesis of the MEPE's and for his cooperativeness and assistance.

Dr. Christian Hess (FHI-Berlin) for performing the XPS measurements and also for long and valuable discussions.

Prof. Hildebrandt (TU-Berlin) for the opportunity to work in his group with different devices. I thank Dr. Inez Weidinger for helping me with the FT-Raman measurements of Fe-MEPE in the pores. The spectra were not very predicative due to the complexity of the system. But that's science! Special thanks for Dr. Ingo Zebger for his help by performing the FT-IR measurements.

Dr. Oskar Paris (MPI-Golm) for the opportunity to perform the SAXD measurements in his group, and Ingrid Zenke for carrying out the SAXD measurements always very quickly.

Dr. Matthias Koch (BAM-Berlin) for giving me the opportunity to perform CHN elemental analysis in his group.

Prof. Martin Lerch (TU-Berlin) for giving me the opportunity to measure in his group and Brigitte Hahn for conducting the TGA/DTA measurements.

Prof. Thorsten Ressler (TU-Berlin) for the opportunity to measure in his group, and Dr. Ingo Piotrowski for performing the Fe-AAS measurements.

Our indefatigable secretary Christiane Abu-Hani for her helpfulness, and always being there with a contagious smile.

Thanks are also due to Dersy Lugo for her proof-reading and her companionship in our sports sessions.

I would especially like to thank my friends and colleges in the office; Susanne Jähnert for always radiating high sprits, and Stefan Wellert for his proof-reading and for lending a sympathetic ear every time when I had something important to tell.

I owe a special debt of gratitude to Kasia Ciunel-Hänni and Tatjana Mauser for motivating me and for helping me to stay in a good mood.

And many cordial thanks go to Kai, for his huge support during all the years, and for the readiness to listen to me at any time, and for all the good advice.

Publications

Schemmel, S.; Akcakayiran, D.; Rother, G.; Brulet, A.; Farago, B.; Hellweg, Th.; Findenegg, G. H., *Phase Separation of a Binary Liquid System in Controlled-Pore Glass*, Mat. Res. Soc. Symp. Proc., **2004**, *790*, P7.2.1.

Akcakayiran, D.; Kurth, D.; Röhrs, S.; Rupprechter, G.; Findenegg, G. H., *Self assembly of a Metallo-Supramolecular Coordination Polyelectrolyte in the Pores of SBA-15 and MCM-41 Silica*, Langmuir **2005**, *21*, 7501.

Shenderovich, I. G.; Mauder, D.; Akcakayiran, D.; Buntkowsky, G.; Limbach, H.-H.; Findenegg, G. H., *NMR Provides Checklist of Generic Properties for Atomic-Scale Models of Periodic Mesoporous Silica*, J. Phys. Chem. B, **2007**, *111*, 12088.

Akcakayiran, D.; Mauder, D.; Hess, C.; Sievers, T.; Kurth, D. G.; Shenderovich, I. G.; Limbach, H.-H.; Findenegg, G. H., *Carboxylic Acid-Doped SBA-15 Silica as a Host for Metallo-Supramolecular Coordination Polymers*, J. Phys. Chem. B, **2008**, *112*, 14637.

Findenegg, G.H.; Jähnert, S.; Akcakayiran, D.; Schreiber, A., *Freezing and Melting of Water Confined in Silica Nanopores*, ChemPhysChem, **2008**, *9*, 2651.

Akcakayiran, D.; Findenegg, G. H., Adsorption Kinetics of *Metal Coordination Polymers into Acid-functionalized SBA-15*, in preparation.

Akcakayiran, D.; Mauder, D.; Tabak, A.; Lerch, M. Shenderovich, I. G.; Kurth, D. G.; Limbach, H.-H.; Findenegg, G. H., *Properties of Acid- functionalized SBA-15.* ***Part I****: Carboxylic, Phosphonic and Sulfonic Acid Containing Materials Synthesized by Co-condensation*, in preparation.

Mauder, D.; Akcakayiran, D.; M. Shenderovich,; D. G.; Findenegg, G. H.; Limbach, H.-H., *Properties of Acid- functionalized SBA-15.* ***Part II****: Acidity Measurements by* ^{15}N *Solid-State NMR*, in preparation.